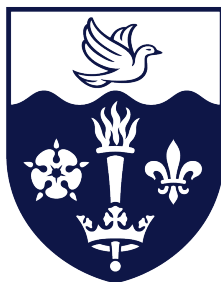


THE UNIVERSITY OF HULL



**UNIVERSITY
of HULL**

Chemical Elements as Tracers of the Evolution of the Milky Way

being a Thesis submitted for the Degree of Doctor of Philosophy in Physics
in the University of Hull

by

Kate Alice Womack M.Sc.

October 2024

“I am not afraid of storms, for I am learning how to sail my ship.”

– Louisa May Alcott, *Little Women*

Acknowledgements

I would like to start by thanking my supervisors for all their support throughout my PhD. I want to express my deepest thanks and appreciation to Dr Fiorenzo Vincenzo for his encouragement and valuable advice, especially through the final stages of my work. Getting to this point would not have been possible without his unwavering confidence in me. A special thank you to Dr Elke Roediger for graciously becoming my second supervisor and providing thorough feedback throughout the writing process. I would also like to acknowledge the support of our head of department Dr Gareth Few, his help and guidance has had such an impact over the last few years and I am grateful for the support he has shown me.

I acknowledge the support of the European Union's Horizon 2020 research and innovation programme (ChETEC-INFRA - Project no. 101008324), for funding this research and for providing me with opportunities I could only have dreamed of at the start of my studies. Many thanks go to Dr Benoit Côté whose GCE code OMEGA+ is used to perform the work in this thesis and whose help, especially in the early days of my research, was invaluable. Without the help of Dr Andrés Yagüe López, I would not be able to make code public - thank you for teaching me the ways of GitHub.

Thanks also to Dr Marco Pignatari for all of the help and advice over the years and for welcoming me to Konkoly Observatory, Budapest for a week during my PhD. A mention here must also go to Dr Maria Lugaro for funding my trip and to Dr Lorenzo Roberti for being an excellent tour guide.

Special thanks also go to Dr Richard Stancliffe, the confidence I gained as a result of my MSc was often what carried me through the early struggles of my PhD. My colleagues at the E.A.Milne Centre for Astrophysics are too many to name them all, but know that you have all had a profound influence on me as a researcher and a human being. Shout out to the best little group of women in STEM I could ask for: Georgia, Kiri and Laura, thank you for your friendship and for not laughing at my terrible painting skills. Also to the Friday pub pals:

Tom, James, Leah and Claire, seeing you all at the end of the week was exactly what I needed after many long weeks of writing. I have had many wonderful office-mates over the years who also deserve a mention for putting up with me in my most stressed states: Aaron, Dom, Iraj, Kiri, Laura, Leah, Oliver and Ryan.

I would also like to show my appreciation for three of my lifelong friends: Emily, Jess and Kate. Every time I see each one of you, its as though no time has passed, thank you for listening to me ramble about this PhD every time I've seen you for the last few years.

To my family: Mum, Dad and Ella, who knew I could do it even if I didn't, thank you for your belief in me. Your support as I put myself through yet more education never faltered, thank you for being there always. Finally, to my partner Jack, your confidence in me throughout the whole process, but especially as I was writing helped me so much to keep going. Listening to me talk about how my writing was going every day in excruciating detail kept me sane, thank you for everything.

Declaration of Originality

This thesis is submitted in partial fulfilment of the degree of Doctor of Philosophy from the University of Hull. I declare that the work undertaken in this thesis is original and my own and was carried out under the supervision of Dr Fiorenzo Vincenzo and Dr Elke Roediger. Some of the work in this thesis has been used as part of peer-reviewed publications either led or co-authored by myself while completing my PhD research at the University of Hull. Where this is the case, it is clearly stated in the prologue of the relevant Chapter. Where work, results, or ideas have been taken from other sources, those sources are explicitly referenced.

Candidates signature: Kate A. Womack

Date: 2nd October 2024

Abstract

To better understand the processes that have formed the Milky Way and enriched the galactic gas, we can study galactic chemical evolution (GCE). When we study GCE we combine our understanding of galaxy formation with stellar evolution to trace the chemical composition of the galactic gas.

Using the semi-analytical GCE codes OMEGA and OMEGA+ to study the evolution of the Milky Way interstellar medium (ISM), we first perform two single element studies investigating the evolution of fluorine and phosphorus abundances. Second, we develop OMEGA to study the evolution of abundance gradients in the Milky Way with both time and radius, using a sample of open clusters in the galactic disc.

The origins of fluorine are investigated by employing a variety of yield sets in our chemical evolution models. We find rotating massive stars are important to reproduce observations, while also ruling out Wolf-Rayet winds as a dominant source of galactic fluorine. We use a similar technique to try to determine the origins of a sample of phosphorus-rich stars. Again, we use a range of yield sets, in this case focussing on massive stars. We are not able to reproduce the full abundance trends of the P-rich sample with any of the models, pointing to the presence of additional physical processes, which are discussed in this Thesis.

We move on to develop a multi-zone version of OMEGA, known as ALPHA. Using ALPHA we develop two Milky Way models, one model includes radial gas flows and the other does not. We go on to use these models to study some chemical clock ratios found in the literature, especially considering $[s/\alpha]$ ratios. We find we can go some way to qualitatively reproducing the abundance gradient trends seen in open clusters. We use the models to show the predictive power of chemical evolution modelling.

Contents

1	Introduction	1
1.1	Structure and Formation of the Milky Way Galaxy	2
1.1.1	Halo	3
1.1.2	Bulge	6
1.1.3	Thin disc	7
1.1.4	Thick disc	9
1.2	Nucleosynthesis	10
1.3	Galactic Chemical Evolution	21
1.3.1	Key Ingredients	21
1.3.2	Advancements in GCE modelling	26
1.4	Summary of thesis content	29
2	Galactic Chemical Evolution Code	31
2.1	OMEGA/OMEGA+	31
2.1.1	Defining Inflows	34
2.2	Applications of OMEGA and OMEGA+	35
3	Chemical Evolution of Fluorine in the Milky Way	38
3.1	Introduction	38
3.2	Observations	43
3.3	Galactic Chemical Evolution Model	44
3.3.1	Stellar Yields	46
3.4	Results	48
3.4.1	Fluorine and s-process elements	52
3.5	Discussion	61
3.5.1	Wolf-Rayet stars as a significant source of fluorine?	65

3.5.2	Sources of Uncertainty in GCE	68
3.6	Conclusions	70
4	Chemical evolution of Phosphorus in the Milky Way with a Focus on Phosphorus-Rich Stars	72
4.1	Introduction	72
4.2	Observational Data	76
4.2.1	Sample selection	76
4.2.2	Notable features of the P-rich sample	77
4.3	Galactic Chemical Evolution Model	78
4.3.1	Stellar Yields	78
4.4	Results	80
4.5	Discussion	82
4.6	Conclusions	84
5	Developing Multi-zone OMEGA(ALPHA) for Chemical Evolution Modelling	86
5.1	Introduction	86
5.2	Methods and Simulations	89
5.2.1	Initial GCE model - OMEGA/+	89
5.2.2	Multi-zone extension	91
5.3	Milky Way model development	97
5.3.1	Effect of radial gas flows	105
5.4	Sensitivity Study	113
5.4.1	Varying the key parameters	113
5.4.2	Varying radial flow velocity	121
5.5	Conclusions	123
6	‘Chemical Clocks’ and Milky Way Radial Gradients	124
6.1	Introduction	124
6.2	Methods	130
6.2.1	Observations	132

6.3	Results	133
6.3.1	Age Gradients as Chemical Clocks	133
6.3.2	Abundance Gradients as a Function of Radius	140
6.4	Discussion and Conclusions	148
7	Conclusions and Future Work	150
	Bibliography	153
A	Appendix - Extra Model Information	173
B	Appendix - Multi-zone Development	176

List of Figures

1.1	Schematic diagram of the Milky Way	2
1.2	Solar abundance pattern	18
1.3	s and r process on the nuclide chart	19
3.1	Panel a: [F/Fe] versus [Fe/H] Panel b: [F/O] versus [O/H]	50
3.2	As Figure 3.1 but using the Ventura yields	51
3.3	[s/Fe] versus [Fe/H]	54
3.4	[F/s] versus [Fe/H]	55
3.5	[F/Ba] versus [Fe/H]	56
3.6	Contribution of each stellar source for model CLC300	58
3.7	Contribution of each stellar source for model CLC 300 in a narrower metallicity range	59
3.8	Contribution of each stellar source at solar metallicity using a variety of rotational velocities	60
3.9	Comparison of non-rotating, solar metallicity massive star wind fluorine yields	66
3.10	IMF weighted fluorine yield as a function of [Fe/H]	67
4.1	[P/Fe] versus [Fe/H]	80
4.2	[Mg/O] versus [Fe/H]	81
4.3	[Si/S] versus [Fe/H]	82
5.1	Schematic diagram of the multi-zone galactic disc	94
5.2	Multi-zone disc with gas flows shown	96
5.3	Diagnostic plots when filtering for a good Milky Way like model	102
5.4	As Figure 5.3 but with a 1 km s^{-1} radial flow	107
5.5	As Figure 5.4 but with the two final Milky Way like models	110
5.6	Diagnostic plots varying M_{inf}	115

5.7	Diagnostic plots varying f_{\star}	117
5.8	Diagnostic plots varying a	118
5.9	Diagnostic plots varying b	120
5.10	Diagnostic plots varying v_{rad}	122
6.1	[Y/Mg] versus Time with and without radial gas flows	134
6.2	[Y/Mg] versus Time with observations	135
6.3	[Y/Fe] and [Mg/Fe] versus Time with observations	137
6.4	[Ba/Mg] versus Time with and without radial gas flows	138
6.5	[Ba/Mg] and [Ba/Fe] versus Time with observations	139
6.6	Radial abundance profiles for each age band	141
6.7	[Ba/Fe] versus R alongside observations for age bands 1 and 2	143
6.8	[Ba/Fe] versus R alongside observations for age bands 3 and 4	145
6.9	Radial abundance slopes for each yield set at each age band	147
A.1	Evolution of star formation rate, inflow rate, gas mass and supernovae rates with galactic age for the model. The shaded regions are present day observa- tional constraints from Kubryk et al. (2015)	174
B.1	SFR versus age at 4 kpc, 8 kpc and 12 kpc	177
B.2	Rejected [O/H] gradient	178
B.3	Rejected SFR density	179
B.4	Rejected surface gas density	180
B.5	Rejected MDF	181
B.6	Rejected age-metallicity relation	182
B.7	Infall rate density at 8 kpc and 12 kpc varying a	183
B.8	Infall rate density at 8 kpc and 12 kpc varying b	184

List of Tables

3.1	Parameters of the chemical evolution model	47
3.2	Yield sets used to explore the chemical evolution of fluorine	48
4.1	Yield sets used to explore the chemical evolution of phosphorus	79
5.1	Properties of the no flows and flows model	100
5.2	Present day SFR, and supernovae rate values from the model compared with observational constraints from Kubryk et al. (2015)	113
6.1	Properties of the models used in Chapter 6	131
6.2	Age bands for the Viscasillas Vázquez et al. (2022) OCs	140
A.1	Present day SFR, inflow rate, gas mass and supernovae rate values from the model compared with observational constraints from Kubryk et al. (2015) . . .	173
A.2	[X/Fe] or [Fe/H] abundance ratios for the model using Asplund et al. (2009) solar abundances.	175

1. Introduction

“There’s a whole world at your feet and who gets to see it but the birds, the stars and the chimney sweeps.”

– Mary Poppins (1964 film)

The primordial gas produced by the Big Bang was primarily composed of hydrogen, helium and trace amounts of lithium. It was from this gas that the first generation of stars was born. These metal-free population three (Pop III) stars generated the first traces of heavier elements in their interiors. Models of the first generation of star formation suggest Pop III stars were very short lived, meaning they are no longer visible today (e.g. [Frebel & Norris 2015](#), [Clarkson et al. 2018](#)), but the heavier elements that they formed will have enriched the surrounding gas, polluting the primordial composition as they died. It was from that polluted gas that the next generation of stars formed. The next generation of stars then went through the same process of synthesising new elements in their interiors and on their death the galactic gas was once again polluted. This process of star formation, element synthesis, stellar death, gas enrichment and subsequent formation of new stars from the enriched gas is the process of galactic chemical evolution (GCE). The study of GCE aims to combine our understanding of both galaxy formation and stellar evolution and nucleosynthesis in order to better understand the processes that have formed the Milky Way. Therefore, in order to study GCE we must be familiar with the structure of the Milky Way (section [1.1](#)), stellar nucleosynthesis (section [1.2](#)) and the history of galactic chemical evolution modelling (section [1.3](#)). Here, the reader should note that each of the above sub-sections requires some knowledge of the other therefore, throughout this introduction the reader will be referred to other parts of the text where necessary.

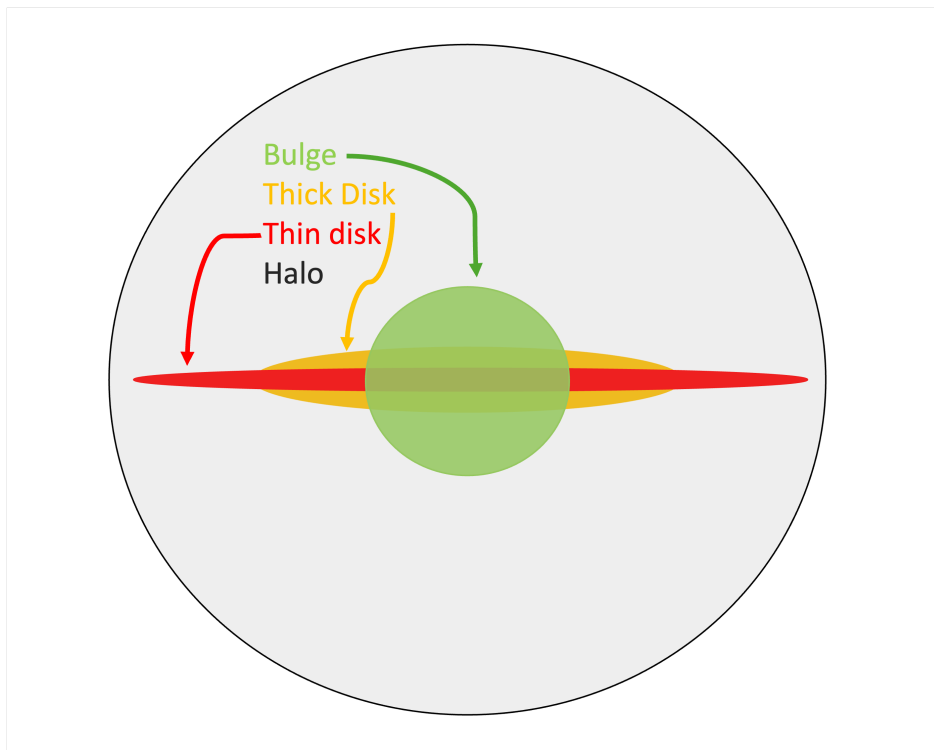


Figure 1.1: Schematic diagram of the Milky Way.

1.1 Structure and Formation of the Milky Way Galaxy

The Milky Way (MW) is a typical barred spiral galaxy with a dark matter (DM) halo surrounding the disc. The MW is comprised of four distinct stellar populations: the halo, bulge, thick disc and thin disc. Figure 1.1 shows the structure of the MW. The extended halo surrounding the galaxy is represented by the grey shaded area, the galactic bulge is in green, while the two disc components are represented by the yellow (thick disc) and red (thin disc) areas respectively. How this galactic structure formed has been debated in the literature. [Eggen et al. \(1962\)](#) proposed the Monolithic Collapse Model which suggests that the galaxy formed from a giant gas cloud which rapidly collapsed to form the first generation of stars in globular clusters (see later on in this introduction for a discussion of globular clusters). However, [Searle & Zinn \(1978\)](#) suggested the Hierarchical Clustering Model in which they argue that the clusters in the halo were formed by a series of merger events, owing to their age distribution. From the gas ejected by the cluster populations, the rest of the disc would gradually form. More recently, we have been able to study the formation of each stellar population of the galaxy in more detail using the results of spectroscopic surveys. In particular in this work, we discuss

data from the Gaia-ESO (Gilmore et al., 2012), Apache Point Observatory Galactic Evolution Experiment (APOGEE) (Majewski et al., 2017) and GALactic Archaeology with HERMES (GALAH) (Buder et al., 2018) surveys. We will now discuss each main stellar component in more detail, describing how they formed and some notable features. The reader should note here that in this Introduction and throughout this work abundances are typically represented in square-bracket notation where: $[\frac{A}{B}] = \log_{10}(\frac{X_A}{X_B})_* - \log_{10}(\frac{X_A}{X_B})_{\odot}$ where X is the abundance by mass fraction of the element in question, \odot represents the solar abundance and * represents the abundance of the gas or the star in question. Therefore, a ratio of two elements A and B of $[A/B] = 0$ is equivalent to the solar abundance ratio. When using square-bracket notation, we will also be using the units of dex. A dex is a logarithmic unit typically used in astronomy to describe an order of magnitude. For example a difference of 10 between two values would be equivalent to a difference of 1 dex.

1.1.1 Halo

Hartwick (1976) and Hartwick (1987) were the pioneering works in understanding the formation of the stellar halo. Hartwick (1976) began by investigating the metallicity distribution function (MDF) of globular clusters in the MW halo. An MDF describes the distribution of the $[Fe/H]$ abundance in a given population or populations of stars. They found the halo MDF did not match predictions from the simple model of chemical evolution (see later on in this work for details) as it predicted too few very-metal poor stars. As a solution, they proposed the removal of gas from the halo, which would form part of the disc. Hartwick (1987) furthered this by suggesting the halo is comprised of two populations, an inner and outer component. There is now growing evidence that the stars in the halo can be split into an inner and outer component (e.g. Carollo et al. 2007, 2010, Nissen & Schuster 2010). With the advent of large spectroscopic surveys such as APOGEE, the separation between the two populations has become even clearer (e.g. Hayes et al. 2018, Fernández-Alvar et al. 2018). Hayes et al. (2018) found two chemically distinct populations of halo stars from APOGEE DR13 which are clearly separated by $[Mg/Fe]$. They found the low metallicity, high Mg population showed chemistry and kinematics (net rotation) similar to that of the thick disc, while the low Mg

population has halo like kinematics and is likely an accreted population. Chemical evolution modelling is a powerful tool to understand the properties of the ISM that may have lead to these two chemically distinct populations. Therefore, following this [Fernández-Alvar et al. \(2018\)](#) use chemical evolution modelling to infer properties of the two populations, finding the high Mg population has a more intense and longer-lived star formation history and a top-heavier initial mass function (IMF). An explanation of the importance of the IMF and how it may vary between populations can be found later in this Chapter (see section 1.3).

In recent years, using main sequence star data from the Gaia mission within 10 kpc from the sun, it was discovered that some of the inner halo was formed during a merger event ([Helmi et al. 2018](#), [Belokurov et al. 2018](#)). Named the Gaia-Sausage, this metal-rich component has a peculiar ellipsoid shape in the velocity space of the halo and it represents a record of a head-on collision that the MW had with a massive dwarf galaxy (Gaia-Enceladus) more than 10 Gyr ago. [Vincenzo et al. \(2019\)](#) performed chemical evolution modelling of Gaia-Enceladus/Sausage in order to investigate its star formation history (SFH) and reproduce both the observed $[\alpha/\text{Fe}]-[\text{Fe}/\text{H}]$ ¹ and MDF. They find a median iron abundance, median stellar age, age distribution and stellar mass at the time of the merger which all agree with observations. They suggest that the merger with Gaia-Enceladus was likely the cause of a temporary quenching of star formation and gas accretion of the MW and that Enceladus was likely cannibalised by the MW after the first gas infall episode (see later in this section for more information on the gas infall which formed the MW). Once again, this demonstrates how GCE modeling can allow us to gain more information on how the galaxy may have formed by explaining the chemical abundance patterns we observe.

There are a number of stars in the halo categorised as carbon-enhanced metal-poor (CEMP). These stars have $[\text{Fe}/\text{H}] < -1$ and $[\text{C}/\text{Fe}] > 0.9$ ([Masseron et al., 2010](#)), though this varies slightly between authors with [Beers & Christlieb \(2005\)](#) defining carbon-enhanced as $[\text{C}/\text{Fe}] > 1$. CEMP stars are generally split into four classifications, CEMP-s, CEMP-r, CEMP-r/s (or CEMP-i) and CEMP-no. CEMP-s stars display an enhancement in s-process elements, with $[\text{Ba}/\text{Fe}] > 1$ and $[\text{Eu}/\text{Fe}] > 0$ and CEMP-r an enhancement of r-process ele-

¹Here α refers to α element abundances, these are elements primarily produced in massive stars via the capture of α particles (helium nuclei). More information on these elements can be found in section 1.2.

ments with $[\text{Ba}/\text{Eu}] < 0$ and $[\text{Eu}/\text{Fe}] \geq 0.3$. CEMP-r/s denotes a simultaneous enhancement of both s and r-process elements, which could come from an i-process scenario (e.g. [Abate et al. 2015](#), [Hempel et al. 2016](#)), whose signature is $[\text{Ba}/\text{Eu}] > 0$ and $[\text{Eu}/\text{Fe}] > 1$. CEMP-no here means there is no enhancement in neutron capture elements in the stellar abundances. The production of neutron capture elements (s and r process) is discussed later on in this Chapter (see section 1.2).

At only $1.4 \pm 0.4 \times 10^9 M_{\odot}$ ([Deason et al., 2019](#)), the stellar halo makes up a small portion of the stellar mass of the galaxy. However, it is evident from the above discussion that it has an important and complex history. The halo is also home to some of the Milky Way's globular cluster (GC) populations, these will be discussed below. Later in this introduction, the Milky Way's open cluster (OC) population will also be discussed (see section 1.1.3).

Globular Clusters

Globular clusters are stable, tightly bound clusters of stars in the halo. Many formation scenarios of GCs have been proposed but none have been able to explain the strange properties of GCs. GCs contain multiple populations of stars, potentially as high as seven different populations in one cluster ([Milone, 2015](#)) and GCs do not show the same chemical properties as field stars with the same age and metallicity. We also see characteristic anti-correlations of $[\text{Na}/\text{Fe}]$ versus $[\text{O}/\text{Fe}]$ and $[\text{Mg}/\text{Fe}]$ versus $[\text{Al}/\text{Fe}]$ and a homogeneity of the iron-peak elements which are difficult to explain (e.g. [Snedden et al. 1997](#), [Recchi et al. 2017](#)). As there is not much spread in the iron group elements, it has been proposed that Type Ia supernovae (SNe Ia) do not contribute strongly to the enrichment of GCs. All of these factors make finding a model of GC formation difficult. Though we do not understand how they form, GCs play a crucial part in our understanding of the formation of the MW galaxy. [Kruijssen et al. \(2019\)](#) used GCs to understand the formation of the MW through comparison of a cosmological zoom in simulation with observed GCs. They were able to reconstruct the merger tree of the MW using the age-metallicity distribution of the GCs. They found the MW assembled quickly for its mass, putting its assembly rate in the 72nd - 94th percentile compared to other galaxies in the simulation.

1.1.2 Bulge

The galactic bulge makes up the central portion of the galaxy and extends to a galactocentric radius of approximately 4.5 kpc (e.g. [Cabrera-Lavers et al. 2007](#)) with recent work suggesting the length of the bar is around 3.5 kpc with over-dense regions reaching to around 4.8 kpc ([Lucey et al., 2023](#)). The bulge has a stellar mass of approximately $2.0 \times 10^{10} M_{\odot}$ (e.g. [Valenti et al. 2016](#), [Portail et al. 2017](#)), constituting around a fifth of the total stellar mass in the Milky Way ([Zoccali & Valenti, 2016](#)).

The bulge is recognised as having at least two stellar populations: one which shows properties of a classical bulge formed via mergers; and another which suggests the formation of a bar and a ‘boxy-peanut’ structure, formed in-situ by a collapsing disc population. [Hill et al. \(2011\)](#) analysed the chemical composition of a sample of red clump stars, finding a bimodal iron distribution, with a metal-rich population centered around $[\text{Fe}/\text{H}] = 0.32$ and a metal poor population around $[\text{Fe}/\text{H}] = -0.3$. These two components are also kinematically different, with the metal poor component being compatible with a classical bulge and the metal rich component with a bar (or pseudo-bulge). More recently, [Zoccali et al. \(2017\)](#) has analysed the metallicity distribution function, again of a sample of red clump stars. They found the metal poor population to be more centrally concentrated, while the metal rich population is a boxy shape consistent with an edge-on bar. The boxy-peanut shape of the bulge component has been discussed in a number of studies (e.g. [Kuijken & Merrifield 1995](#), [Bureau & Freeman 1999](#), [Fragkoudi et al. 2017](#), [Semczuk et al. 2022](#), [Ghosh et al. 2024](#)) and is so called due to the funnel-like shape of the bulge. This structure is thought to have arisen as the metal-rich component is consistent with being formed in the inner disc but due to instabilities, it collapsed forming a bar-like structure (e.g. [Di Matteo et al. 2014](#)). The idea of two populations in the bulge has been discussed by a number of authors (e.g. [Hill et al. 2011](#), [Robin et al. 2012](#), [Zoccali et al. 2017](#), [Matteucci et al. 2019](#)), however other studies have suggested the bulge could comprise of multiple populations (e.g. [Bensby et al. 2013](#), [Ness & Freeman 2016](#), [García Pérez et al. 2018](#)).

1.1.3 Thin disc

The thin disc is likely the most well-studied component of the Milky Way galaxy and it is where the majority of the stellar mass is contained ($3.5 \pm 1 \times 10^{10} M_{\odot}$ [Bland-Hawthorn & Gerhard 2016](#)). Therefore, the thin disc is where we observe most of the star formation to be taking place. The thin disc is thin by nature with a scale height of approximately 300 pc ([Jurić et al., 2008](#)).

When modelling the Milky Way thin disc, we assume that the disc forms ‘inside-out’. By this, we mean the inner regions of the disc form first and on a much shorter timescale than the outer regions. The concept of inside-out growth was first proposed by [Larson \(1976\)](#) after finding that in order to produce a model of galaxy formation which successfully reproduced the structure of our galaxy, the inner part of the disc must always form first and the outer parts progressively later. A model for ‘inside-out’ growth has since been developed by a number of authors (e.g. [Chiosi 1980](#), [Lacey & Fall \(1985\)](#), [Matteucci & Francois 1989](#), [Chiappini et al. 1997, 2001](#)). The thin disc may also experience dynamical processes such as migration of gas (e.g. [Tinsley & Larson 1978](#), [Mayor & Vigroux 1981](#)) and stars (e.g. [Spitoni et al. 2015](#), [Vincenzo & Kobayashi 2020](#)), alongside inside-out formation, these processes may contribute to the radial abundance gradients in the disc. Radial migration of gas and Milky Way radial gradients are studied in detail in this work in Chapters 5 and 6. Radial migration of gas can affect the surface density of the gas in different regions of the disc, causing variable star formation rates across the disc. Variable star formation rate (SFR) as a function of radius may help us to be able to effectively reproduce abundance gradients using chemical evolution modelling (e.g. [Colavitti et al. 2009](#), [Spitoni & Matteucci 2011](#), [Belfiore et al. 2019](#), [Palla et al. 2020](#)). There is also the suggestion that a threshold surface gas density is required in order to reproduce a break in star formation between the formation of the halo/thick-disc and thin disc (more detail on this formation scenario can be found in section 1.1.4) that appears to exist in the observations; [Chiappini et al. \(2001\)](#) set this threshold at $7 M_{\odot} \text{pc}^{-2}$. How we model these evolutionary parameters in more detail can be found later in this introduction (see section 1.3).

The formation and evolution of the disc, especially the thin disc has been well researched

over the last decades by many authors from stellar abundances (e.g. [Kroupa et al. 1993](#), [Bensby et al. 2014](#), [Spina et al. 2018](#), [Spina et al. 2021](#)), to chemical evolution modelling (e.g. [Tinsley \(1968\)](#), [Matteucci & Francois \(1989\)](#), [Chiappini et al. \(1997, 2001\)](#), [Grisoni et al. 2017](#), [Palla et al. 2020](#)). With the advent of new surveys, we are able to understand the formation and structure of the thin disc in more detail. For example, [Miglio et al. \(2021\)](#) used asteroseismic data from Kepler and spectroscopic data from APOGEE to infer masses and ages of nearly 5400 giant stars. By analysing the age-chemo-kinematic properties of the sample, their results indicate that there is efficient radial migration of stars in the thin disc. They were also able to distinguish thick and thin disc populations in the data, we discuss this in more detail in the following sub-section (see section [1.1.4](#)).

Recently, [Gallart et al. \(2024\)](#) aimed to reconstruct the star formation history (SFH) of the Milky Way by obtaining detailed dynamically evolved star formation histories. Using the Gaia Catalogue of nearby stars they performed colour-magnitude diagram fitting in order to age date their sample of stars. This work gave a different insight into the evolution of the Milky Way at the solar neighbourhood allowing the identification of when star formation may have started (11 -10.5 Gyr ago), periods of low star formation (between 4 - 6 Gyr ago) and high star formation rate throughout the evolution of the MW.

Both of the works mentioned above rely on being able to determine stellar ages, which is not always straightforward. As demonstrated by both [Miglio et al. \(2021\)](#) and [Gallart et al. \(2024\)](#), the more precise our stellar ages, the better we can understand the formation and evolution of our galaxy using its chemical properties. Another way we might determine stellar age is via chemical clocks. Later in this work, we will return to this idea, using open clusters to investigate both stellar age and radial gradients in the galactic disc (see Chapter [6](#)).

Open Clusters

We use open clusters throughout this work as an observational comparison to galactic chemical evolution modelling. More information about their usefulness when performing chemical evolution modelling can be found in Chapter [6](#) where they are used extensively to study Milky Way abundance gradients. OCs are a population of stars formed from the same molecular

cloud at the same age, members of an open cluster can be identified via kinematic, photometric and spatial criteria (e.g. [Castro-Ginard et al. 2019, 2020](#)).

Unlike GCs, OCs do not have commonality in their abundance trends, as they are dependent on the gas cloud out of which they were born. However, they are useful in understanding the formation of the galaxy. For example, [Poggio et al. \(2021\)](#) used a sample of open clusters, young stars and Cepheids from Gaia to trace the spiral arm structure of the disc by mapping over and under dense regions. Meanwhile, [Hunt & Reffert \(2024\)](#) also used the Gaia catalogue to compile an open cluster census, with the largest catalogue of open cluster masses to date. This allowed them to investigate age and mass functions for the open clusters and predicted that the MW contains 1.3×10^5 OCs, only 4% of these are currently known.

1.1.4 Thick disc

[Gilmore & Reid \(1983\)](#) used a sample of 12,500 stars to investigate the vertical density profile of the Milky Way, from this the thick disc was identified at a scale height of 1350 pc. The thick disc is significantly less massive than the thin disc, with a stellar mass of $6 \pm 3 \times 10^9 M_{\odot}$ ([Bland-Hawthorn & Gerhard, 2016](#)).

We can identify thick disc stars based on their stellar abundances. Using $[\text{Mg}/\text{Fe}]$ or $[\alpha/\text{Fe}]$ more generally (α elements are those made by a series of α particle captures such as Mg, Si, S etc., see section 1.2 for more detailed information), some authors (e.g [Haywood et al. 2013](#), [Bensby et al. 2014](#), [Nissen 2015](#)) have identified that stars belonging to the thick disc tend to be α -enhanced compared to those of the thin disc. We can also use $[\alpha/\text{Fe}]$ abundance to infer stellar age. There has been strong suggestion in the literature that $[\text{Mg}/\text{Fe}]$ (or $[\alpha/\text{Fe}]$) can be used as a chemical clock, we discuss this further in Chapter 6 as stars in the thick disc (with enhanced α element abundances) tend to be older than stars in the thin disc.

These two distinctly different populations of the thick and thin discs are thought to have arisen due to the way gas fell onto the disc of the galaxy in two distinct episodes of infalling gas, we call this the two-infall model. [Chiappini et al. \(1997, 2001\)](#) proposed that the first of the two exponential infall episodes formed the thick disc over a short period of time, while the second infall forms the thin disc (inside-out) over a longer period of time. Recently,

[Grisoni et al. \(2017\)](#) proposed the timescales for accretion are 0.1 Gyr and 7 Gyr for the thick and thin disc components respectively, with a gap between infall episodes of around 700 Myr. Meanwhile, another revision of the two-infall model from [Spitoni et al. \(2019, 2020\)](#) suggested a model with a longer period between episodes of approximately 4.5 - 5.5 Gyr.

1.2 Nucleosynthesis

Nucleosynthesis is the production of the elements and their isotopes as a result of nuclear reactions. Nucleosynthesis in space primarily occurs in stellar interiors but there are processes that can also occur outside of stars (such as Big Bang nucleosynthesis and cosmic ray spallation). Which isotopes and elements a star produces and the abundance of those elements is dependent on the stellar properties. Mass, metallicity, temperature, density and explosion energy (if the star explodes) of the star can all play a role in the production of the chemical elements in space. However, when we group elements together, we do find general trends on where and how these elements can be produced. It is important for the study of galactic chemical evolution and galactic archaeology to understand where and how the chemical elements are produced. Where stellar abundance trends are seen in the data, we may be able to infer the dominant stellar source responsible for that trend based on our knowledge of where the chemical elements are produced or find correlations between two elements based on them being produced in similar ways. Alternatively, a ratio of two elements may be able to be used as a chemical clock if they are produced on different timescales in two different stellar sites (see Chapter 6), therefore a knowledge of the sites of production for the elements is crucial when selecting a potential chemical clock ratio. Later in this work, we will study two single elements: fluorine (Chapter 3) and phosphorus (Chapter 4), knowledge of where and how these elements are produced is what forms the basis of the two studies, allowing us to choose appropriate stellar yield sets and investigate their impact on the modelled ISM abundances.

A crucial work which underpins the field of stellar nucleosynthesis is [Burbidge et al. \(1957\)](#) (known widely as B²FH). Using their knowledge of the stellar abundance pattern, coupled with Earth-based nuclear physics experiments, the authors showed eight different types of processes were required in order to synthesise the elements in stars. The majority of

the processes discussed in B²FH are still recognised and studied today, including: hydrogen burning, helium burning, α process, e process, s process, r process, p process and x process. The e process is now recognised as the nucleosynthesis that occurs in SN Ia when producing iron group elements, while the x process has been discovered to be cosmic ray spallation. We will discuss each of these processes throughout this introduction.

Not all elements are produced in abundance by every type of star, some stellar sources are better at producing particular groups of elements than others. While some elements are not synthesised in stars at all, with two process occurring outside of stellar interiors. In the following, we will discuss seven broad groups of elements and the wider nucleosynthesis trends which lead to the production of the most abundant stable isotope of each of the elements in the group. It should be noted here that the pathways mentioned below are the most common way to produce these elements/isotopes but are not the only nucleosynthesis pathways, however for the sake of brevity and clarity we will not go into detail on each alternate pathway which can produce every stable element.

Non-stellar nucleosynthesis

Big Bang Nucleosynthesis produced the primordial composition of the galactic gas. The primordial gas was around 75 % hydrogen (¹H and ²H), 25 % helium (³He and ⁴He) and trace amounts of lithium (⁷Li). Another non-stellar nucleosynthesis process is cosmic ray spallation. There is both a direct and inverse spallation process. The direct process occurs when rays of highly energetic particles such as protons or alpha particles collide with nuclei in the interstellar medium ([Iliadis, 2015](#)). The collision causes the larger nucleus to split apart, producing smaller nuclei like beryllium and boron. Lithium can be made by inverse spallation, where instead the larger nuclei collide with protons or alpha particles in the ISM and split apart. Some He and Li as well as every other element are synthesised in stars via different burning or explosive processes.

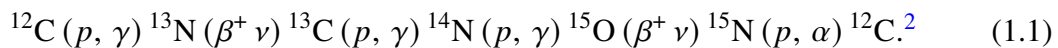
When considering the production of the pre-iron elements below, both the terms hydrostatic and explosive burning/nucleosynthesis will be used. By hydrostatic burning we mean thermonuclear burning that takes place when the star is in a state of hydrostatic equilibrium (the internal pressure of the star is balanced against gravitation). If an element is a product of

explosive nucleosynthesis, it has been made during the explosion of the star, in the majority of the below cases (α elements and other light elements), this is a core collapse supernovae (CCSN).

Helium production and CNO elements

During the hydrogen burning phase, stars can convert hydrogen to helium via two processes, either through proton-proton (pp) chains or the CNO cycle (see [Iliadis 2015](#) and references therein). There are three pp chains, each converting four protons to one alpha particle (helium nucleus) by means of different sequences of reactions. The first pp chain (pp-chain 1) uses isotopes of H and He alone, while the second and third chains utilise isotopes of Li, Be and B which are subsequently destroyed due to their high proton capture cross sections (this means they capture protons easily). It should be noted here, that it is the pp chain in novae that is responsible for the stellar origins of Li. In novae, the second pp chain produces ${}^7\text{Be}$, which we have detected in a handful of novae ([Tajitsu et al. 2015, 2016](#), [Molaro et al. 2016, 2020](#), [Selvelli et al. 2018](#), [Arai et al. 2021](#), [Izzo et al. 2022](#)). The subsequent decay of ${}^7\text{Be}$ into ${}^7\text{Li}$ is theorised to be the dominant source of Li in the galaxy (e.g. [Kemp et al. 2022](#)).

In more massive stars, the CNO cycle converts H into He by ‘cycling’ through the production of different isotopes of carbon, nitrogen and oxygen (C, N and O). For this to occur, an initial abundance of ${}^{12}\text{C}$ is needed within the stellar interior as a result of the gas from which it was born. The CNO cycle proceeds as follows:

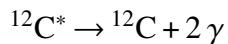


If there is an abundance of ${}^{14}\text{N}$, ${}^{15}\text{N}$ and ${}^{16}\text{O}$, either as a result of prior CNO cycle or as part of the initial abundance of the star, these isotopes can also be used as seed nuclei for other modes of operation of the CNO cycle which we will not discuss here. The result of each of the chains is the production of a He nucleus along with a seed nucleus of either ${}^{12}\text{C}$, ${}^{14}\text{N}$, ${}^{15}\text{N}$ or ${}^{16}\text{O}$, allowing the cycle to continue. This is the main way that nitrogen (especially ${}^{14}\text{N}$) is synthesised in stars.

During the helium burning phase of a star, He is converted into ${}^{12}\text{C}$ by means of the

²We use this notation to describe nuclear reactions throughout this section. Here, A(b,c)D is how we represent A + b resulting in D + c.

triple- α process:



Note here that ${}^{12}\text{C}^*$ denotes an excited state of ${}^{12}\text{C}$ and the ${}^8\text{Be}$ produced in this process is unstable. Subsequent α captures can then produce ${}^{16}\text{O}$ (via ${}^{12}\text{C}(\alpha, \gamma){}^{16}\text{O}$) and ${}^{20}\text{Ne}$ (via ${}^{16}\text{O}(\alpha, \gamma){}^{20}\text{Ne}$). In low and intermediate mass stars, the helium burning phase is the last stage of nuclear fusion reactions in the star. These stars range in mass from $0.8 M_{\odot}$ - $8 M_{\odot}$, however the transition mass from low and intermediate mass to massive stars is uncertain and may range between $8 M_{\odot}$ - $10 M_{\odot}$ (super asymptotic giant branch (AGB) stars) (see for example [Karakas & Lattanzio 2014](#), [Doherty et al. 2015](#)). After the He has been exhausted, low mass stars usually end their lives as carbon-oxygen (CO) white dwarfs but the more massive low mass stars may result in ONe white dwarfs ([Doherty et al., 2015](#)) as the core temperature allows the fusion of some carbon. Massive stars are able to undergo more burning phases, resulting in the production of heavier and heavier elements up to iron via nuclear fusion.

Alpha elements

The alpha (α) elements are a group so-called as they are produced via a series of α captures (an α particle is the same as a ${}^4\text{He}$ nucleus). They are primarily made in massive stars in both hydrostatic and explosive burning phase scenarios depending on the element, though some of the lighter alpha elements like O and Ne can be produced in low mass AGB stars (see above).

The alpha elements are generally regarded as O, Ne, Mg, Si, S, Ar and Ca. Following on from the production of ${}^{20}\text{Ne}$ described above, a series of either (α, γ) reactions or reactions between other α elements is what allows the production of ${}^{24}\text{Mg}$, ${}^{28}\text{Si}$, ${}^{32}\text{S}$, ${}^{36}\text{Ar}$ and ${}^{40}\text{Ca}$, which are the most abundant isotopes of each of these elements in the Sun ([Clayton, 2003](#)). Some also regard Ti to be an alpha element as the isotope ${}^{44}\text{Ti}$ is made via the fusion of alpha particles. However, ${}^{44}\text{Ti}$ is an unstable isotope of Ti, thus the element Ti is not generally an alpha element as stable Ti cannot be made through the alpha capture chain. This is also the case for ${}^{48}\text{Cr}$ and ${}^{52}\text{Fe}$ which are both alpha nuclei but their elemental form would not be considered an alpha element.

Neon and magnesium are primarily produced during the carbon burning phase of massive star evolution. The fusion of two ^{12}C nuclei produces both ^{20}Ne and ^{24}Mg . Massive stars make ^{20}Ne via $^{12}\text{C}(^{12}\text{C}, \alpha)^{20}\text{Ne}$, the resulting alpha particle can be captured by ^{20}Ne resulting in $^{20}\text{Ne}(\alpha, \gamma)^{24}\text{Mg}$ (see [Chieffi et al. 1998](#), [Pignatari et al. 2013](#), [Iliadis 2015](#) and [Chieffi et al. 2021](#) for more information on these burning processes and those discussed throughout this section).

Silicon and sulphur start to be produced in neon photodisintegration and continue to be produced throughout the oxygen burning phase of a massive star. In the Ne photodisintegration phase, high energy photons collide with ^{20}Ne , producing ^{16}O and the α particles required to capture onto ^{16}O and ^{20}Ne ([Iliadis, 2015](#)) for the following series of reactions: $^{20}\text{Ne}(\alpha, \gamma)^{24}\text{Mg}(\alpha, \gamma)^{28}\text{Si}(\alpha, \gamma)^{32}\text{S}$. While in O burning the collision of two ^{16}O nuclei results in $^{16}\text{O}(^{16}\text{O}, \alpha)^{28}\text{Si}$, when the resulting alpha particle can be captured once again for $^{28}\text{Si}(\alpha, \gamma)^{32}\text{S}$. Both of these isotopes can be produced in hydrostatic and in explosive oxygen burning ([Pignatari et al., 2016](#)).

Argon is mainly produced during explosive oxygen burning as the massive star undergoes core collapse resulting in a CCSN. Following previous hydrostatic oxygen burning, the shell has an abundance of ^{32}S onto which an alpha particle can be captured, giving rise to the $^{32}\text{S}(\alpha, \gamma)^{36}\text{Ar}$ reaction ([Chieffi et al., 1998](#)). Note here that though ^{36}Ar is the most abundant isotope of Ar in the Sun, ^{40}Ar is the most abundant isotope on Earth. This is owing to the large amount of radioactive ^{40}K which the Earth formed with which then decayed into ^{40}Ar ([Clayton, 2003](#)). In massive stars, the production of ^{40}Ar is uncertain, it is likely to arise via neutron captures during explosive carbon burning but could also be as a result of the radioactive decay of ^{40}K produced in explosive oxygen burning.

Ca can be produced both in the oxygen and silicon burning phases of massive stars again, in both hydrostatic and explosive burning. The chain of reactions that produces ^{40}Ca , once again arises from the initial fusion of two ^{16}O nuclei followed by three alpha captures, the final part of this chain being $^{36}\text{Ar}(\alpha, \gamma)^{40}\text{Ca}$ ([Iliadis 2015](#)).

Other notable isotopes of α elements, though not alpha nuclei themselves include ^{13}C , ^{22}Ne and ^{25}Mg which, along with ^{16}O are important elements for neutron production. Neutron

capture is the way in which elements heavier than iron are synthesised in stars, for this to occur an abundance of neutrons must be present in stellar interiors. The reactions which generate neutrons are as follows: $^{13}\text{C}(\alpha, n)^{16}\text{O}$ and $^{22}\text{Ne}(\alpha, n)^{25}\text{Mg}$ (Pignatari et al., 2016). Neutron captures and the elements they produce will be discussed in more detail later in this section.

Other light elements

The remaining pre-iron group elements not yet discussed in this section are F, Na, Al, P, Cl and K. Again, these elements are primarily produced in massive stars, though a not insignificant yield of these elements can be produced in other stellar sources, for example low and intermediate mass AGB stars can be responsible for some of the galactic fluorine abundance especially at later times in the evolution of the Milky Way (see Chapter 3). Some of the CNO cycle reactions involve the fluorine isotopes ^{17}F , ^{18}F and ^{19}F allowing its production in low mass stars (AGB stars). F is also produced in massive stars as a product of helium burning. The production and evolution of F is discussed at length in this work in Chapter 3, more detail on the stellar sites of fluorine production can be found there. Phosphorus is produced via neutron captures during the carbon, oxygen and neon burning phases of massive star evolution, though mainly in the carbon burning phase (both hydrostatic and explosive). The production and evolution of P is also discussed in detail in this work in Chapter 4. For the below introduction to the remaining elements, we will group them based on the burning phases in which they are made.

Sodium and aluminium are produced in similar scenarios. They are primarily produced alongside neon and magnesium in carbon burning (Pignatari et al., 2016). Another possible outcome of the collision of two ^{12}C nuclei is $^{12}\text{C}(^{12}\text{C}, p)^{23}\text{Na}$. ^{23}Na is the only stable isotope of sodium. Al is produced as a result of α capture onto ^{26}Mg via $^{26}\text{Mg}(\alpha, p)^{27}\text{Al}$. ^{27}Al is the only stable isotope of aluminium, though ^{26}Al has been extensively discussed in the literature owing to its usefulness in tracing the early solar system (e.g. Lugaro et al. 2022) Both ^{23}Na and ^{27}Al can also be produced in hydrogen burning via the (p, γ) reactions $^{22}\text{Ne}(p, \gamma)^{23}\text{Na}$ and $^{26}\text{Mg}(p, \gamma)^{27}\text{Al}$.

Chlorine and potassium are both produced during oxygen burning, with K made exclusively in explosive oxygen burning (Clayton, 2003). After the production of ^{32}S , ^{35}Cl is

produced via $^{32}\text{S}(\alpha, p)^{35}\text{Cl}$, while ^{37}Cl is produced via decay of ^{37}Al (which is made as a result of neutron captures). Explosive oxygen burning facilitates the production of ^{39}K , ^{40}K and ^{41}K , each by a different series of events, with neutron captures playing an important role, especially in the production of ^{40}K .

Iron Group and SNe Ia

The iron group elements are generally accepted to be the elements on the periodic table between titanium and zinc (Ti, V, Cr, Mn, Fe, Co, Ni, Cu, Zn) and are produced by type Ia supernovae (SNe Ia). Low and intermediate mass stars typically end their lives as CO white dwarfs (WDs), which are stable on timescales longer than the age of the Universe. However, if these stars are in a binary star system, they can explode as SNe Ia. For this to occur, material must be accreted onto the CO white dwarf from its binary companion, which can happen in two ways. The single degenerate model ([Whelan & Iben, 1973](#)) says the material is accreted from a normal companion star such as a main sequence or AGB star, while the double degenerate scenario proposes that the SNe Ia explosion occurs due to the merging of two white dwarfs ([Iben & Tutukov, 1984, 1987](#)). When the star reaches the Chandrasekhar limit of $1.4 M_{\odot}$, nuclear burning processes can restart within the star. However, sub-Chandrasekhar scenarios have also been proposed (e.g. [Woosley & Weaver 1994](#)). The timescale on which white dwarfs explode as a supernova is important for chemical evolution modelling, as the first generation of SNe Ias provides the first injection of iron and iron group elements into the ISM. Often, in chemical evolution studies we use $[\text{Fe}/\text{H}]$ as a proxy for stellar age, as we expect Fe to become gradually more present in the ISM as WDs explode, while H is present from the primordial composition, which becomes more diluted as the galaxy evolves.

The iron group elements are ejected during the SNe Ia explosion and are generated as a result of a number of explosive burning processes which are dependent on the temperature at different densities within the star. As the shock propagates through the central zones of the star, high temperatures (around 9 GK) are reached, causing explosive silicon burning. These temperatures are so hot that the existing nuclei are destroyed and ‘freeze-out’ occurs in which protons, neutrons and α particles are not able to recombine to form heavier elements ([Iliadis, 2015](#)). At the end of the explosion, these particles are cooled enough to recombine and α

captures occur producing the α nuclei ^{44}Ti , ^{48}Cr , ^{52}Fe and finally ^{56}Ni . The decay of these isotopes along with any other proton or neutron captures that occur during the recombination is what allows the iron group elements to be synthesised in abundance during these events.

Gallium to Rubidium

The origin of these elements can be complex, with many processes playing a role. In massive stars, the ‘freeze-out’ process described above also occurs during core-collapse. The proton rich environment can allow for proton captures up to Ga and Ge. Beyond this point neutrino interactions are required through the νp -process. In this case, antineutrinos are absorbed by proton-rich nuclei, leading to the freeing of neutrons. These neutrons are captured by neutron-deficient nuclei, allowing decays or further neutron captures to take place (e.g. [Fröhlich et al. 2006](#), [Arcones & Thielemann 2023](#)). This allows for the production of elements $A > 64$ without full neutron capture nucleosynthesis, though some authors argue that the production of Kr and Rb is the start of the weak s process in massive stars during He burning.

Neutron Capture elements

After the iron group, it is difficult for charged particle reactions to occur as the Coulomb barrier is too large to overcome. Therefore, another nucleus with charge cannot be fused to make heavier elements. It is at this point that neutron captures become the dominant way in which heavier elements can be made as neutral particles do not experience Coulomb repulsion. There are two main neutron capture processes: the slow neutron capture process (s process) or the rapid neutron capture process (r process). A third process, known as the intermediate neutron capture process (i process), has also been proposed ([Cowan & Rose, 1977](#)), though a site for this process has been a matter of debate and is still uncertain (e.g. [Asplund et al. 1999](#), [Herwig et al. 2011](#), [Lugaro et al. 2009](#), [Campbell et al. 2010](#), [Jones et al. 2016](#), [Clarkson et al. 2018](#), [Denissenkov et al. 2019](#), [Hampel et al. 2019](#)). Figure 1.2 shows the logarithmic solar abundance pattern ([Asplund et al., 2009](#)) against atomic weight in the style of figure 1.1 of [Burbidge et al. \(1957\)](#). When we consider this abundance pattern, there is clearly a peak at the iron group as a result of these nuclei having large nuclear binding energies and therefore, strong Coulomb repulsion. Beyond the iron group, there are a series of smaller peaks (labelled s and r), these are the s- and r-process peaks.

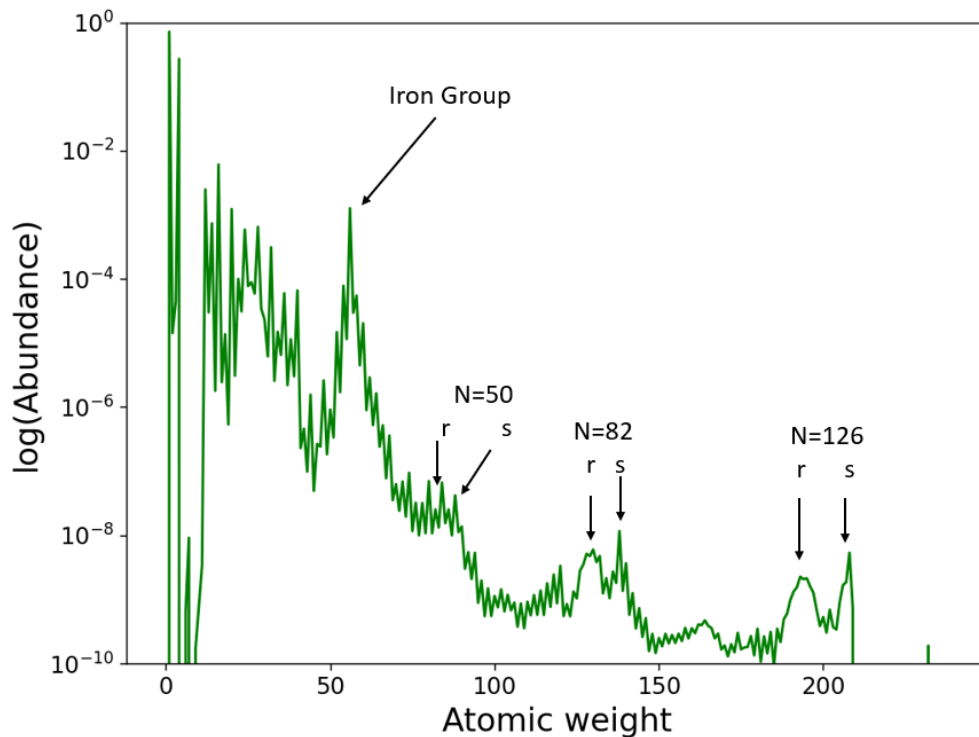


Figure 1.2: Logarithmic abundance against atomic weight for the solar abundance pattern (Asplund et al., 2009) with the iron group and s- and r-process peaks labelled on the line. This figure is from Womack (2021).

The peaks arise due to a large abundance of neutron magic nuclei ($N = 50, 82$ and 126). Neutron magic nuclei have full neutron shells, making these nuclei more stable and therefore, it is much more difficult for these nuclei to capture another neutron. Neutron shells can be thought of as analogous to electron shells in this way. As neutron magic nuclei are less likely to capture another neutron (low neutron capture cross section), bottlenecks form during the process of neutron captures and abundance peaks form.

How neutron captures proceed depends on the process in question. When a neutron is captured by a nucleus, the following nucleus will either β decay or capture another neutron. If the new isotope is stable then it cannot β decay, therefore the only option is to eventually capture another neutron. However, if the new isotope is unstable, then which one of these occurs depends on the neutron density of the environment compared with the half life of the isotope.

Figure 1.3 shows how neutron captures might proceed for the s and r process respectively using a section of the nuclide chart. The nuclide chart places isotopes as a function of their

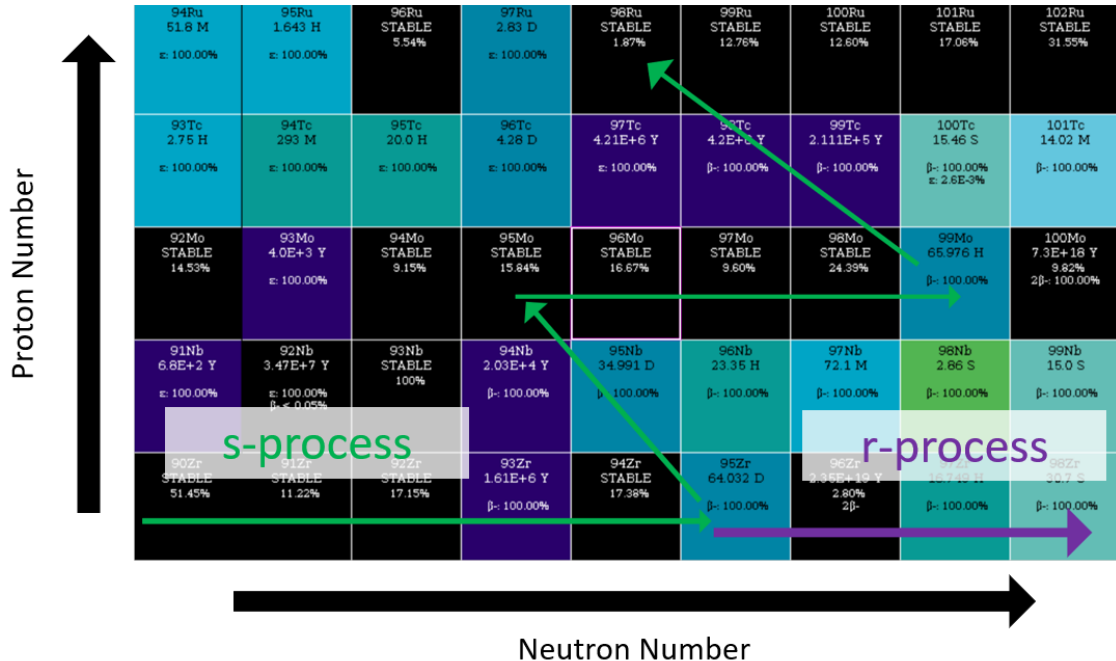


Figure 1.3: A section of the nuclide chart from The National Nuclear Data Center, Brookhaven National Laboratory (National Nuclear Data Centre, 2021). The green arrows represent the s-process path and the purple arrows show the r-process path. Figure from Womack (2021).

proton number (y-axis) and neutron number (x-axis). The s-process path (green lines) shows stable nuclei capturing neutrons until ^{93}Zr which is unstable but with a long enough half-life that neutron captures are able to proceed until ^{95}Zr , which β decays towards stable ^{95}Mo and so on. The r-process path (purple line) shows neutrons being captured until the neutron drip line (see later on in this section for a description of the neutron drip line).

s process

The s process happens at low neutron densities of approximately $10^7 - 10^{10} \text{ cm}^{-3}$ (Busso et al., 1999), therefore it is more likely a nucleus will decay than capture a neutron. This means neutrons are captured slowly in comparison with the rate of β decays. There are three different components of the s process (weak, main and strong) depending on the neutron exposure, how many neutrons a given area is exposed to over a period of time. The weak s process produces elements with $A \leq 88$ (Kappeler et al., 1989), the main $88 < A \leq 204$ and the strong $204 < A \leq 209$ (Busso et al. 1999, Sneden et al. 2008). These three components roughly correspond to the peaks observed in the solar abundance pattern (see Figure 1.2). The

first peak at $N = 50$, corresponds to the light s process (so-called because it produces lighter elements than the other two components) and produces Sr, Y and Zr, the second peak ($N = 82$) has signatures of Ba, La, and Ce, the final peak is at lead (Pb), which is the last stable element on the s -process path.

The s process can occur in both low and intermediate mass stars (AGB intershell regions) and massive stars. The s process occurs during thermal pulses of AGB stars. Protons are ingested into the intershell region (between the H and He shells) of an AGB star. The protons allow for the production of ^{13}C via $^{12}\text{C}(p, \gamma)^{13}\text{N}$, ^{13}N has a half life of around ten minutes and will decay to ^{13}C . The intershell region is He rich, so the ^{13}C is able to capture an alpha particle and produce neutrons via $^{13}\text{C}(\alpha, n)^{16}\text{O}$. This produces an abundance of neutrons which are available for further capture. Meanwhile, the s process can occur in massive stars during the helium burning phase. Here, the neutrons are mainly synthesised via the $^{22}\text{Ne}(\alpha, n)^{25}\text{Mg}$ reaction. In massive stars, we expect to produce s -process elements up to the first peak (Sr, Y, Zr) (e.g. [Limongi & Chieffi 2003](#)). However, [Frischknecht et al. \(2012\)](#) showed that the efficiency of the mixing processes in massive stars can be enhanced when they rotate, this allows for s -process element production beyond the first peak. The effect of rotating massive stars in GCE modelling is discussed at length throughout this work. As listed above typical s -process elements are Sr, Y, Zr, Ba, La, Ce and Pb though a smaller amount of these elements can be made via the r process.

r process

In contrast with the s process, the r process happens in very neutron rich environments of approximately 10^{20} cm^{-3} ([Lugaro, 2005](#)), hence neutron captures are much more likely and happen much more quickly. The r process can produce isotopes up to the neutron drip-line, this is the point at which neutron captures can no longer take place as the isotopes are too neutron rich to be able to capture another. After the drip-line is reached, the isotopes will β decay into something more stable.

A site for the r process has been difficult to narrow down. Initially, it was thought these elements would be made during a CCSNe event (e.g. [Wasserburg & Qian 2000](#)). However, it is likely these events are not energetic or neutron-rich enough to provide the appropriate

conditions for the r process to take place. Some have suggested magneto-rotationally driven supernovae are a promising site for the r process (e.g. [Ono et al. 2012](#), [Winteler et al. 2012](#), [Nishimura et al. 2015](#), [Nishimura et al. 2017](#)), while others have proposed neutron star mergers (NSMs). NSMs became more promising as an r-process site when the NSM (GW170817) was detected using gravitational waves ([Abbott et al., 2017a](#)). Alongside the NSM, there was a gamma ray burst (GRB) detection suggesting a kilonova as a result of the merger, which are powered by the decay of r-process nuclei. The NSM and GRB detection were confirmed to be signatures of the same event, confirming NSMs as a site for the r process ([Abbott et al., 2017b](#)).

It is important to understand how this knowledge of nucleosynthesis and the production of the elements feeds into chemical evolution modelling. The stellar yields that we use in our models of chemical evolution are produced by models of stellar evolution. There are many models of stellar evolution and post-processing codes which will treat the production of the elements in different ways. Generally, a code will have a ‘reaction network’ made up of a series of nuclear reactions, each assigned a reaction rate, which is dependent on a range of stellar properties such as stellar mass, temperature and density. As the model of a star at a given mass and metallicity evolves, these reactions will take place and isotopes will be created and destroyed. Isotopes can be ejected from the source in two main ways: first via stellar winds where material is lost from the outer layers of a star as it evolves or second during the explosion, either as ejecta from the inner layers of the star or as a result of explosive nucleosynthesis. At the end of the evolution of the model, the mass of each isotope ejected by these two pathways becomes the stellar yield which we use in chemical evolution modelling. Hence, understanding the nucleosynthesis which produces the elements is crucial to understand the evolution of our GCE models.

1.3 Galactic Chemical Evolution

1.3.1 Key Ingredients

The field of galactic chemical evolution explores how galaxies evolve based on the production and distribution of the chemical elements. There are basic considerations that must be

made when developing a GCE model, regardless of how complex it may become. These considerations are: the initial conditions of the gas, the star formation rate (SFR), the initial mass function (IMF), stellar nucleosynthesis and lifetimes and gas flows (i.e. inflows, outflows and radial flows).

Initial Conditions of the gas: GCE models can be closed-box or open-box. If the model is closed-box, this means no gas will enter or exit the galaxy over the course of its evolution. Therefore, the gas the stars form from has been present since the beginning of the simulation and the total mass of the galaxy (gas + stars) will be constant throughout. If the model is open-box, this allows gas to flow into (i.e. the gas has been accreted from elsewhere) and/or out of the galaxy. In modern chemical evolution modelling, it is much more common to have an open-box simulation as closed-box simulations lead to a phenomenon known as the G-dwarf problem (Schmidt 1963, Lynden-Bell 1975, Pagel & Patchett 1975, Tinsley 1980). The G-dwarf problem is an over production of metal-poor G-dwarf stars in closed-box modelling and will be discussed in more detail later in this section (section 1.3.2).

It must also be decided if the initial gas in the galaxy is of primordial composition or pre-enriched by ejecta from elsewhere. Opting for a primordial composition allows the galaxy to evolve how we might expect: from population III like stars with relatively low abundances of anything other than H and He, through to enriched stellar populations at later times. However, if one wanted to model a galaxy which formed from some pre-enriched environment then a non-primordial composition would be used and the abundances of the stellar populations would be as a result of pre-enriched chemical evolution. This is known as a prompt initial enrichment (Lynden-Bell, 1975).

Star Formation Rate: The star formation rate is a measure of how much gas is ‘locked away’ by star formation per unit time, typically measured in solar masses per year ($M_{\odot} \text{ yr}^{-1}$). The importance of star formation rate in chemical evolution modelling is two-fold. First, star formation is what will ultimately govern the chemical evolution of the galaxy, if no stars form, evolve and die, then the gas will never be enriched with chemical elements. If a significant fraction of gas is used to form stars at one time step in a model, then there would not be enough gas available to form stars at the next. Thus, the evolution of the galaxy would be

stilted. Secondly, the star formation rate in a chemical evolution model is often used to drive the outflow of gas from a galaxy (e.g. [Murray et al. 2005](#)). Once again, if the outflow is too strong, this affects the modelled galaxy’s ability to form stars at later time steps as too much gas has been removed over the course of its evolution.

The most common way to express the star formation rate is via the Kennicutt-Schmidt law ([Schmidt 1959](#), [Kennicutt 1998](#)). This expresses the SFR (ψ) as $\psi = \nu \sigma_{\text{gas}}^k$, where ν is the star formation efficiency and σ_{gas} is the gas surface density raised to the power k . Thus the SFR is proportional to the gas surface density to some power, k . [Kennicutt \(1998\)](#) suggests value of $k = 1.4 \pm 0.15$. For semi-analytical models such as OMEGA ([Côté et al., 2017](#)), which will be used in this work (see section 2.1 for a discussion), an adapted version of the Kennicutt-Schmidt law, which removes the area dependence is used (e.g. [Kauffmann et al. 1993](#), [Kauffmann et al. 1999](#), [Baugh 2006](#), [Somerville & Davé 2015](#)), allowing the star formation rate to be proportional to the mass of the gas in a galaxy, rather than its gas density. In this work (Chapters 3 and 4) we use:

$$\dot{M}_{\star}(t) = \epsilon_{\star} \frac{M_{\text{gas}}(t)}{\tau_{\star}} \quad (1.2)$$

where $\dot{M}_{\star}(t)$ is the star formation rate, ϵ_{\star} is the star formation efficiency, $M_{\text{gas}}(t)$ is the mass of the gas reservoir and τ_{\star} is the star formation timescale. See section 2.1 for a full description of the code used in this work.

Initial Mass Function: The IMF expresses the number of stars born within a given mass interval ($m - m + dm$) for a given stellar population. There are many different ways to model the IMF, for example Salpeter ([Salpeter, 1955](#)), Miller & Scalo ([Miller & Scalo, 1979](#)), Ferrini ([Ferrini et al., 1990](#)), Kroupa ([Kroupa et al., 1993](#); [Kroupa, 2001](#)), Chabrier ([Chabrier, 2003](#)) and Maschberger ([Maschberger, 2013](#)). The IMF is most commonly expressed as a power law, with the Salpeter or Kroupa 2001 IMFs being two of the most popular choices. The Salpeter IMF is a single slope power law and can be expressed as:

$$\xi(m) = A m^{(-1+\alpha)}, \quad (1.3)$$

where $\alpha = 1.35$ and A is a normalisation factor relating to the local stellar density of the population. [Kroupa et al. \(1993\)](#) suggested a three-slope power law, where:

$$\begin{aligned}
\alpha &= 0.2 \text{ for } M \leq 0.5 M_{\odot} \\
\alpha &= 1.2 \text{ for } 0.5 < M/M_{\odot} \leq 1.0 \\
\alpha &= 1.7 \text{ for } M > 1.0 M_{\odot},
\end{aligned}
\tag{1.4}$$

However, [Kroupa \(2001\)](#) then suggested a two-slope power law, called the universal IMF (UIMF) whereby stars with $M > 0.5 M_{\odot}$ have the same power law.

$$\begin{aligned}
\alpha &= 0.3 \text{ for } 0.08 < M/M_{\odot} \leq 0.5 \\
\alpha &= 1.3 \text{ for } M > 0.5 M_{\odot},
\end{aligned}
\tag{1.5}$$

Each option for the IMF will form stars in a different way so it is important to understand how they compare with each other. The main difference between the [Kroupa \(2001\)](#) IMF and other choices of IMF is its ‘top-heavy’ nature. This means, in comparison with the [Salpeter \(1955\)](#) and its predecessor [Kroupa et al. \(1993\)](#), it produces a larger number of massive stars. Therefore, the more massive stars formed will eject their material into the ISM more quickly and the gas will become enriched with elements typically made during massive star evolution or core collapse supernova explosion (like the alpha elements or first peak s-process elements), causing an earlier increase in metallicity.

Stellar Nucleosynthesis: In order to follow the chemical evolution of a galaxy using a GCE model, we need to know the chemical composition of the material that is ejected by the stars as they die. We can use sophisticated stellar modelling to study the nucleosynthesis occurring in the interiors of stars to generate predictions of stellar yields from various stellar sources (e.g. [Kobayashi et al. 2006](#), [Karakas 2010](#), [Limongi & Chieffi 2018](#)). For a discussion of where and how different groups of elements are formed, refer to section 1.2.

There are stellar yields available for a variety of stellar sources from low and intermediate mass stars (AGB stars) (e.g. [Karakas et al. 2012](#), [Fishlock et al. 2014](#), [Cristallo et al. 2015](#), [Karakas & Lugaro 2016](#), [Pignatari et al. 2016](#), [Karakas et al. 2018](#), [Battino et al. 2019](#)), to massive stars (e.g. [Kobayashi et al. 2006](#), [Nomoto et al. 2013](#), [Limongi & Chieffi 2018](#), [Ritter et al. 2018c](#)), SNe Ia (e.g. [Iwamoto et al. 1999](#), [Kromer et al. \(2015\)](#), [Townsend et al. 2016](#), [Leung & Nomoto \(2018\)](#), [Keegans et al. 2023](#)), NSMs (e.g. [Rosswog et al. 2014](#), [Holmbeck & Andrews 2024](#)), faint supernovae (e.g. [Ritter et al. 2018c](#)) and more. Which of these

sources are included in the model is dependent on the the type of galaxy being modelled or the goal of the study. However, for GCE modelling it is important that there are stellar yields available for a range of stellar masses (if appropriate) and metallicities. This allows us to continue to model the chemical evolution of the galaxy as closely as possible as the galaxy evolves and forms more metal rich stars at a range of masses as governed by the IMF. We are able to use the stellar yields to understand the chemical composition of stellar ejecta (either via stellar death or winds) and thus, how the gas is enriched through time.

Gas Flows: There are three main types of gas flows that can be considered when developing or using a GCE model: inflows, outflows and radial flows. The inflow of gas into a galaxy generally occurs via accretion of gas from elsewhere. When the accreted gas is mixed into the galaxy, the metal content of the galactic gas is diluted as the accreted gas is often of primordial composition.

As previously mentioned, star formation is often the driver of gas outflows from galaxies (see [Rupke 2018](#) for a review). When stars die and end their lives as supernovae the energy generated by the explosion, drives outflows of gas. When gas leaves the potential well of a galaxy, it is known as a galactic wind. Galactic winds carry away metal-rich material from the galaxy, thus the gas becomes diluted.

Finally, radial flows, as the name suggests, are the movement of gas in a radial direction i.e. gas that migrates within the galaxy itself. In disc galaxies, this allows gas from metal-poor regions of the galaxy (e.g. the halo and outer regions of the disc) to be mixed with metal-rich regions ([Kubryk et al., 2015](#)). For an in depth introduction into the inclusion of radial gas flows in chemical evolution modelling see section [5.1](#).

It should be noted that the formation of the Milky Way and other disc galaxies was likely hierarchical. This means the Milky Way was formed by a series of mergers and accretion of smaller building blocks ([Matteucci, 2012](#)). This ‘lumpy’ nature of galaxy formation cannot be replicated by GCE models. Therefore, though including gas flows in GCE models is important, it only gives us a first order approximation in terms of modelling the gas flows that lead to the formation of spiral galaxies like our Milky Way.

How we use these key ingredients to model the chemical evolution of galaxies has varied

between authors over the last few decades with different parameterisations and types of models used to model different scenarios. The field of GCE modelling was greatly advanced in the 1970s and 1980s with the works of Beatrice Tinsley (e.g. [Tinsley 1968, 1974, Tinsley & Larson 1978](#)), Talbot and Arnett (e.g. [Talbot & Arnett 1971, 1973](#)), Bernard Pagel (e.g. [Pagel & Patchett 1975, Pagel 1989](#)) and many others (e.g. [Schmidt 1963, Larson 1972](#)). However, it was in the 1950s and 1960s when the groundwork for chemical evolution modelling was laid.

1.3.2 Advancements in GCE modelling

The Simple model of galactic chemical evolution was the first model of GCE and originated from the works of [Van den Bergh \(1958, 1962\)](#) and [Schmidt \(1959, 1963\)](#), which considered star formation rate in the galaxy, studying the frequency of stars of different masses and/or abundances.

Works by [Talbot & Arnett 1971, Larson \(1972\), Pagel & Patchett \(1975\), Lynden-Bell \(1975\)](#) and many others (see references therein), helped to develop the Simple model further. The Simple model uses four basic assumptions:

1. The system is an isolated closed-box (i.e. there are no flows of gas in or out of the system and the total mass remains constant).
2. The initial gas in the system is of primordial composition.
3. The gas is well mixed at all times so that the mixing of the stellar ejecta and the ISM is instantaneous.
4. The initial mass function (IMF) is constant with time.

The assumptions allow for a model which can follow the evolution of the galactic gas, the metallicity of the gas, the stellar death rate and their yields. However, these assumptions also allow for the occurrence of unphysical scenarios.

By assuming a closed-box model, more metal-poor stars are predicted by the model than we observe. This is known as the G-dwarf problem ([Schmidt 1963, Lynden-Bell 1975, Pagel & Patchett 1975](#)). A G-dwarf is a low metallicity star belonging to the thin disc which exists

within a 1 kpc radius of the Sun. The problem is solved by allowing gas to infall onto the galaxy, especially in the solar neighbourhood. By assuming the galaxy does not start with all the mass it is ever going to have, the first generation of stars are born metal-poor but in fewer number, due to the low gas surface density. As the gas becomes enriched, gas is also being accreted onto the disc adding mass to the galaxy, allowing the next generation of slightly more metal-rich stars to form. Thus, by the end of the evolution, the most metal poor stars are formed only at the beginning of the evolution of a galaxy (Tinsley, 1980).

The review by Tinsley (1980) was pioneering in the field of galactic chemical evolution: summarising the key ingredients of chemical evolution modelling and explaining the basic equations to perform the modelling. Tinsley (1980) explained the Simple model in detail, providing a basis for modern chemical evolution modelling, despite its unphysical assumptions.

Following on from this work, the field of chemical evolution was advanced through the 1980s and 1990s by various authors exploring new ways of modelling the chemical evolution of the Milky Way. Firstly, the ‘instantaneous recycling approximation’ could be relaxed, this allowed models to account for stellar lifetimes, rather than all stars with $M < 1 M_{\odot}$ living forever and all stars with $M \geq 1 M_{\odot}$ dying instantaneously and mixing into the ISM. By relaxing these rules Chiosi (1980) and Tosi (1982) were able to study the chemical enrichment of lower mass stars and more accurately trace the chemical evolution of the galaxy. Modelling Milky Way evolution was advanced further with the inclusion of SNe Ia by Greggio & Renzini (1983), Matteucci & Tornambe (1985) and Matteucci & Greggio (1986), allowing the authors to trace $[\alpha/\text{Fe}]$ ratios for the first time. During this time, the way the galaxy formed in these models was also changing. Matteucci & Francois (1989) created a model which formed inside-out, as is now conventional. While, Mayor & Vigroux (1981) were the first to include radial gas flows in their models on the suggestion of Tinsley & Larson (1978).

In section 1.1, the two-infall model was discussed, this was a crucial development in chemical evolution modelling. By exploring the idea that the MW formed by means of two distinct gas infall episodes, Chiappini et al. (1997, 2001) were able to predict a gap in star formation later confirmed by other authors (e.g. Fuhrmann 1998, Gratton et al. 2000).

Models of chemical evolution are still being developed in recent times. For example, [Grisoni et al. \(2017\)](#) compared the traditional two-infall model to a new parallel model which forms the thick and thin disc via two episodes of infall occurring in parallel rather than one after the other. By comparing each of the models to data from the AMBRE (which stand for Archéologie avec Matisse Basée sur les aRchives de l'ESO) project they found the parallel model could reproduce the observed [Mg/Fe] and metallicity distribution better than the traditional two-infall model. The field of GCE modelling is rich with a variety of models and authors, each performing their modelling in different ways with the same goal: to better understand the evolution of the ISM. We have already touched on the two-infall model, which was subsequently adapted by [Spitoni et al. \(2019, 2020\)](#) who found a delay of approximately 4 Gyr between the two episodes of gas infall is needed to explain the dichotomy between the APOKASC (APOGEE+ Kepler Asteroseismology Science Consortium, [Pinsonneault et al. 2014](#)) sample for the solar neighbourhood ([Silva Aguirre et al., 2018](#)) and APOGEE-DR16 stars. [Spitoni et al. \(2020\)](#) even employs MCMC models to fit the two-infall model to the APOKASC observational data, finding a delay of between 4.5 - 5.5 Gyr between infalls for the best fit models. Recently, [Spitoni et al. \(2023\)](#) has gone beyond the two-infall model and developed a three-infall model in which the disc has more recently undergone a third infall of gas. They were able to reproduce α element abundances from Gaia DR3 ([Recio-Blanco et al., 2023](#)) showing a young population of stars with chemical impoverishment (low- α) which had not previously been explained. Chemical evolution modelling can also be multi-zone, as illustrated in Chapters 5 and 6 of this work. An example of a multi-zone model is that of [Ferrini et al. \(1992, 1994\)](#) who model the galaxy as a series of N coaxial cylinders each divided into two zones (halo and disc). This model was then employed by a variety of works to study gradients in both the Milky Way and other galaxies (e.g. [Magrini et al. 2007](#), [Magrini et al. 2009](#), [Casali et al. 2020](#), [Magrini et al. 2021](#)). The work of Weinberg and his collaborators uses observational evidence to inform their GCE studies, using data from surveys like APOGEE, SDSS and GALAH. Their work finds abundance ratios trends are most dependent on stellar yield set (e.g. [Andrews et al. 2017](#), [Weinberg et al. 2017](#)), while distribution functions are more sensitive to star formation history and stellar migration (e.g.

[Schönrich & Binney 2009a](#), [Hayden et al. 2015](#), [Loebman et al. 2016](#), [Johnson et al. 2021](#)). Meanwhile, [Kobayashi et al. \(2006, 2020\)](#) has found great success in studying the chemical evolution of the elements across the periodic table, performing chemical evolution modelling of a variety of scenarios in an attempt to identify the origins of the elements. Specifically, both studies include a number of stellar nucleosynthesis sources (e.g. hypernovae, electron capture supernovae, failed supernovae) in their one zone model creating a number of scenarios to be able to find the best match for each element. These studies also assist in determining the frequency of some of these rarer events ([Kobayashi et al., 2020](#)). Most of the models we have discussed so far draw on the idea that the gas is of homogenous chemical composition, i.e. the stellar ejecta is well mixed across the galaxy. However, it is also possible to model chemical evolution inhomogeneously (e.g. [Argast et al. 2000, 2002](#), [Cescutti 2008](#), [Alexander et al. 2023](#)). Inhomogeneous chemical evolution modelling can be advantageous as it can account for the stochastic formation of supernovae progenitors and allows for the study of how SN ejecta and stellar winds disperse in the ISM. Recently, [Alexander et al. \(2023\)](#) used the inhomogeneous chemical evolution code I-GETOOL to model two ultra-faint dwarf galaxies finding they are successful in reproducing α and odd-Z element abundance patterns.

The models of chemical evolution used in this work are constructed using the OMEGA ([Côté et al., 2017](#)) and OMEGA+ ([Côté et al., 2018b](#)) chemical evolution codes, as well as a multi-zone version of OMEGA called ALPHA developed as part of this work (Chapter 5). We use these codes because they are flexible, user-friendly and can run quickly, allowing the user to create many models of chemical evolution, exploring a variety of scenarios. Details of the modelling used in this thesis, the advantages of these codes and how the codes have been implemented in other studies can be found in the following Chapter (Chapter 2).

1.4 Summary of thesis content

This thesis focuses on the galactic chemical evolution of the Milky Way Galaxy. OMEGA and OMEGA+ are used to model the evolution of the Milky Way and the models are compared with a variety of observations to try to understand the production and evolution of the chemical elements. In Chapter 2 the chemical evolution code is described and its uses and benefits

discussed.

In the first half of the thesis, two single elements are explored, these are fluorine (Chapter 3) and phosphorus (Chapter 4). Understanding the origin and evolution of fluorine in the galaxy is a challenge, as there are many proposed sites of fluorine production in the literature. We also have limited observations of fluorine due to difficulties with fluorine lines in spectra, therefore we do not have a lot of data with which to compare our chemical evolution models and decide whether they are successful. We aim to compare our models with as broad a range of observations as possible and come to a conclusion on the dominant source of fluorine in the galaxy based on the success (or not) of our models. The origins of phosphorus are more clear, being primarily made in massive stars. However, there is a population of P-rich stars which are not currently able to be explained by any stellar models. We explore a massive star origin of this P-rich population, by including a range of massive star evolutionary scenarios in our chemical evolution modelling.

In Chapter 5 a new mode of operation for the OMEGA code is developed in which many zones are connected to create a multi-zone disc. The model, known as ALPHA, is used to develop a MW chemical evolution model both with and without radial gas flows. This extension allows us to take the flexibility and user-friendly nature of the OMEGA code to study more complex scenarios. Therefore, using these models, in Chapter 6 the evolution of ‘chemical clock’ ratios such as $[s/\alpha]$ are studied both with time and with galactocentric radius. Chemical clocks are currently an interesting field of study as they allow us to use ratios of chemical element abundances to calculate stellar ages. Determining stellar age is challenging and chemical clocks provides a novel way to age date populations of stars. In Chapter 7, the thesis is concluded and there is a discussion of further work that could be carried out in this field.

2. Galactic Chemical Evolution Code

Part of the information in section 2.2 has been published in the Monthly Notices of the Royal Astronomical Society as [Pignatari et al. \(2023\)](#), on which I am a co-author.

The main GCE code used in this work is OMEGA ([Côté et al., 2017](#)), the One-Zone Model for the Evolution of Galaxies, with the OMEGA+ ([Côté et al., 2018b](#)) extension. Both codes are available on GitHub in the NuGrid¹ NuPyCEE² and JINAPyCEE³ packages respectively.

2.1 OMEGA/OMEGA+

OMEGA, is a one-zone chemical evolution code that can be closed- or open-box in nature and simulates the evolution of several physical and chemical properties of a cold, star-forming galaxy. The time evolution of the galactic gas mass is defined as ([Tinsley 1980](#); [Pagel 1997](#); [Matteucci 2012](#))

$$\dot{M}_{\text{gas}}(t) = \dot{M}_{\text{inflow}}(t) + \dot{M}_{\text{ej}}(t) - \dot{M}_{\star}(t) - \dot{M}_{\text{outflow}}(t) \quad (2.1)$$

where \dot{M}_{inflow} is the rate of gas mass added by galactic inflows, \dot{M}_{ej} is the rate of gas mass added by stellar ejecta, \dot{M}_{\star} is the rate of gas mass removed from the reservoir by star formation and \dot{M}_{outflow} is the rate of gas mass lost by outflows. Gas inflows can be defined a few different ways in OMEGA and differently again in OMEGA+, this will be discussed later (see section 2.1.1). The star formation rate depends linearly on the mass of the cold gas in the galaxy (e.g [Springel et al. 2001](#), [Baugh 2006](#)) and is defined as:

$$\dot{M}_{\star}(t) = \frac{\epsilon_{\star}}{\tau_{\star}} M_{\text{gas}}(t) \quad (2.2)$$

where ϵ_{\star} and τ_{\star} are the dimensionless star formation efficiency (sfe) and star formation timescale, respectively. The outflow rate of gas from the galaxy is proportional to the star

¹<https://nugrid.github.io>

²<https://github.com/NuGrid/NUPYCEE>

³<https://github.com/becot85/JINAPyCEE>

formation rate (SFR) and is defined as

$$\dot{M}_{\text{outflow}}(t) = \eta \dot{M}_{\star}(t) \quad (2.3)$$

where η is the mass loading factor and controls the strength of the outflows. This assumption of outflows being entirely driven by stellar activity (e.g. the explosion of supernovae) and thus derived from the SFR is typical in semi-analytical modelling (e.g. [Murray et al. 2005](#)) and represents the idea that the outflow rate should be proportional to the rate of mechanical energy injected by stars. It was noted by [Côté et al. \(2017\)](#) that when the outflow rate is proportional to the SFR, a stellar population releases its ejecta after the outflow triggered by that population, however an outflow prescription which is proportional to \dot{M}_{ej} (see below) does not make a major difference to their results. To calculate the mass of gas added by stellar ejecta, the contribution of every stellar population formed by time t is summed so that

$$\dot{M}_{\text{ej}}(t) = \sum_j \dot{M}_{\text{ej}}^j(M_j, Z_j, t - t_j) \quad (2.4)$$

where \dot{M}_{ej}^j is the mass ejected by the j th stellar populations that formed at the time t_j , M_j is the initial mass of the population, Z_j is the initial metallicity of the population and $t-t_j$ is the age of the j th population at time t . The simple stellar populations (SSPs) are created at every time-step using SYGMA (Stellar Yields for Galactic Modelling Applications) ([Ritter et al., 2018a](#)). An SSP is defined as a population of stars with the same age and chemical composition, with the number of each type of star in the different evolutionary stages being weighted by an initial mass function (IMF). SYGMA includes ejecta from low- and intermediate-mass stars (AGB), massive stars, Type Ia supernovae and neutron star mergers. Additional sources can also be added manually by the user. The ejecta from the SSPs are then instantaneously and uniformly mixed into the gas reservoir. The chemical composition of the stellar ejecta is determined by the stellar yields that we employ. Each yield set provides abundances for a variety of chemical elements and isotopes (which isotopes are provided varies between authors) for a grid of stellar masses and metallicities. The initial mass function will determine how many stars of each mass are present at a given time, t and the metallicity of the stars depends on the metallicity of the gas in which they were born, which is tracked by the simulation.

SNe Ia are modelled by assuming a power-law delay-time distribution (DTD) similar to that of [Maoz & Mannucci \(2012\)](#) (see also [Freundlich & Maoz 2021](#), [Wiseman et al. 2021](#)) in the form $t^{-\beta}$ with $\beta = 1$. The minimum delay time of SNe Ia is set by the lifetime of intermediate-mass stars used in the GCE calculation. For every SSP, at any time t , the DTD used is multiplied by the fraction of progenitor white dwarfs ($f_{\text{WD}}(t)$) originating from stars in the mass range $3 - 8 M_{\odot}$ (see [Ritter et al. 2018a](#) for more details). $f_{\text{WD}}(t)$ smoothly evolves from 0 to 1 when the age of the SSP transits from the lifetime of an $8 M_{\odot}$ star to a $3 M_{\odot}$ star. The temporal evolution of the rate of SNe Ia is normalised such that 10^{-3} SNe occur per units of solar mass formed (see table 5 in [Côté et al. 2016](#) for references). For the modelling taking place in this work, we use the solar abundances of [Asplund et al. \(2009\)](#) throughout.

OMEGA+ is a single zone extension to OMEGA which surrounds the central cold star-forming galaxy (OMEGA object) with a non-star-forming external hot gas reservoir. The latter is considered as the circumgalactic medium (CGM). Not only can the evolution of the galaxy be followed (see above) but the evolution of the CGM can also be followed. This allows us to track the gas that has been previously ejected from the central galaxy, enriching the CGM, which can then be reintroduced to the galaxy as inflows at a later time. The time evolution of the mass of the gas in the CGM is defined as

$$\dot{M}_{\text{CGM}}(t) = \dot{M}_{\text{CGM,in}}(t) + \dot{M}_{\text{outflow}}(t) - \dot{M}_{\text{inflow}}(t) - \dot{M}_{\text{CGM,out}}(t) \quad (2.5)$$

where $\dot{M}_{\text{CGM,in}}$ is the inflow rate of gas from the intergalactic medium into the CGM, \dot{M}_{outflow} is the outflow rate of mass removed from the central galaxy and added to the CGM via outflows, \dot{M}_{inflow} is the rate of gas mass that flows into the central galaxy from the CGM, and $\dot{M}_{\text{CGM,out}}$ is the outflow rate of gas from the CGM into the intergalactic medium. The intergalactic medium represents the space outside the CGM and is defined as a sphere with radius equal to the virial radius of the dark matter halo that hosts the central galaxy. The mass of the CGM tends to increase if the mass of the dark matter halo also increases, as $\dot{M}_{\text{CGM,in}}$ can reach higher values due to a larger availability of gas in the environment; conversely, the CGM mass will decrease when the mass of the dark matter halo decreases, as gas can more efficiently leave the CGM, giving rise to higher values of $\dot{M}_{\text{CGM,out}}$. We can also decrease the mass of the gas in the CGM, even if the dark matter mass stays constant, by allowing the CGM

to have large-scale outflows. Details of all of these terms can be found in [Côté et al. \(2018b, 2019b\)](#) and references therein (see figure 7 of [Côté et al. \(2018b\)](#) for a visual representation of the workings of OMEGA+).

2.1.1 Defining Inflows

The prescription which defines the inflow rate of gas into the central galaxy differs between OMEGA and OMEGA+, as OMEGA+ allows for interaction with the CGM that OMEGA does not. There are a number of ways to define galactic gas inflow rate when using OMEGA including: the inflow/outflow model, the star-formation model and the mass assembly model. Details on how each of these models works can be found in [Côté et al. \(2017\)](#). However, they will not be described in this work as for the remainder of this thesis, we use OMEGA+ or ALPHA (the multi-zone code developed in Chapter 5) which use different mechanisms for defining gas inflow.

Gas inflow rate in OMEGA+ can be treated in four ways:

1. Exponential equations
2. Constant inflow timescale
3. Inflow timescale proportional to free-fall timescale
4. Input array.

Exponential equations: An exponential infall can be implemented using

$$\dot{M}_{\text{inflow}}(t) = N_{\text{norm}} e^{-\frac{(t-t_0)}{\tau}}. \quad (2.6)$$

where N_{norm} is the normalisation of the infall event, τ is the infall timescale and t_0 is the value of t at the first time-step. A number of exponential equations can also be combined, allowing for the replication of the [Chiappini et al. \(1997\)](#) two-infall model, this is the prescription that will be used in Chapters 3 and 4. As has been extensively discussed, the two-infall model assumes that the Milky Way forms by two separate gas infall episodes. The first infall episode forms the halo and thick disk while the second infall forms the thin disk. In OMEGA+ the

two-infall model is described as follows:

$$\dot{M}_{\text{inflow}}(t) = A_1 \exp\left(\frac{-t}{\tau_1}\right) + A_2 \exp\left(\frac{t_{\text{max}} - t}{\tau_2}\right). \quad (2.7)$$

where A_1 , A_2 , τ_1 , τ_2 and t_{max} are free parameters. A_1 and A_2 represent the normalisation of the first and second infall events, respectively, τ_1 and τ_2 are the time-scales for mass accretion for the first and second infall, and t_{max} is the time of maximum contribution to the second gas infall episode.

Constant inflow timescale: This defines the inflow rate by taking the mass of the gas inside the CGM and fixing the inflow timescale as follows:

$$\dot{M}_{\text{inflow}}(t) = \frac{M_{\text{CGM}}(t)}{\tau}. \quad (2.8)$$

Inflow timescale proportional to free-fall timescale: This option is more complex and relates the inflow timescale to the free-fall timescale of the dark matter halo, which in turn depends on redshift.

Input array: An arbitrary inflow can be set by using an array where each index is the total mass of the gas inflowing into the galaxy at each time-step.

The final aspect of galactic gas flows to consider are radial flows. The creation of a multi-zone version of OMEGA and the subsequent inclusion of radial gas flows can be found in Chapter 5.

2.2 Applications of OMEGA and OMEGA+

We exclusively use OMEGA and its developments in this Thesis due to its power as a chemical evolution code. Its semi-analytical nature allows one OMEGA+ ‘run’ to take less than 10 seconds, while an OMEGA run can happen in as little as a few seconds. This capability makes the code excellent as a flexible model for which a variety of parameters can be tested and changed allowing for comparisons between yield sets, galaxy properties and sensitivity studies (Côté et al., 2017). OMEGA has over a hundred parameters that can be activated or changed and their influence on chemical evolution explored. The flexibility of the code allows the user to model a variety of different types of galaxies; not just Milky-Way like galaxies but also dwarf spheroidal (dSph) galaxies like Sculptor (Pandey & West, 2022). OMEGA is also

made to be user-friendly, with both OMEGA and OMEGA+ easily accessible on GitHub and all tutorial material available as python notebooks. As the code is quick to run, flexible and user-friendly, it has also been adopted as a teaching tool for both school children ([Keegans et al., 2021](#)) and researchers (e.g. NPA-X School, CERN 2022).

Studies using OMEGA and OMEGA+ have greatly contributed to the field of GCE over the last few years. The initial study involving OMEGA ([Côté et al., 2017](#)) investigated the impact of the treatment of galactic inflows and outflows on GCE predictions. They modelled the dSph galaxy Sculptor using three different prescriptions of gas in- and outflows before using a Markov Chain Monte Carlo (MCMC) code to find the prescriptions which best reproduced the observed stellar abundances of nine chemical elements. They concluded that all three prescriptions could reproduce the stellar abundances but the values found for other galactic parameters such as SNe Ia rate or the strength of the outflows were significantly different between models. They ultimately concluded that it is insufficient for a model of chemical evolution to reproduce the chemical abundance trends and other constraints must also be used in order to understand and break the degeneracy between modelling assumptions. They found that the outcome of GCE modelling is predominantly driven by input stellar yield set rather than the complexity (or not) of the model itself.

When OMEGA+ was created ([Côté et al., 2018b](#)) the authors again explored dwarf galaxies in order to understand their formation and the origin of metal poor stars in the galactic halo. Using GAMMA, a merger tree code, they modelled the formation of the most massive galaxy in the Wise simulation ([Wise et al., 2012](#)) by considering its mass assembly history. OMEGA+ was used in order to model each of the dwarf galaxies as they formed, after being fed the initial conditions of the galaxy from GAMMA. They found they were able to reproduce the star formation history, metallicity distribution function and the later stages of the age metallicity relation using GAMMA coupled with the OMEGA+ galaxies.

In recent years, OMEGA+ has been used to investigate the evolution of the Milky Way. [Trueman et al. \(2022\)](#) used OMEGA+ to perform a study of short-lived radionuclides (SLRs) in the early solar system (ESS). By comparing data from the GCE models to abundances of primitive meteorites they find isolation times of between 9 - 26 Myr, this is the time the

protosolar gas was isolated from further enrichment before the birth of the sun. They also find chemical evolution models are missing a between 9 - 73% of ^{107}Pd and ^{108}Pd , suggesting a missing source of Pd in our models. This is a good example of the power of GCE modelling when considering stellar yield sets. By modelling the chemical evolution of the galaxy, using input stellar yields, it is clear when comparing to observations if sources of a particular element are missing or where we would expect a source to make more of an element through the evolution of a galaxy than we see in our models.

OMEGA has also been used as a powerful tool to study the conditions for planet formation. [Pignatari et al. \(2023\)](#) aimed to marry up our understanding of planetary system formation with chemical evolution models. We specifically studied C, N, O, Mg, Si and S as these elements are significant for planet formation; and planet formation and evolution simulations depend on their initial abundances. When modelling the solar neighbourhood, we considered the impact of both core collapse supernovae and faint supernovae on the evolution of the ratios of the above elements. We considered different fractions of faint supernovae and conventional CCSNe and found there is not one specific combination of yields which can reproduce all ratios considered. We also find that the fraction of faint supernovae does not have a strong impact for the elements of interest. However, the GCE results do provide an important benchmark for simulations of planet formation, especially when the elemental abundances of the host star are uncertain or unavailable.

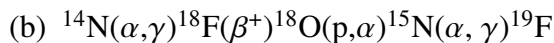
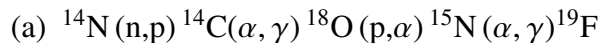
3. Chemical Evolution of Fluorine in the Milky Way

The information presented in this chapter has been published in the Monthly Notices of the Royal Astronomical society as [Womack et al. \(2023\)](#).

3.1 Introduction

For many years, understanding the origin and evolution of fluorine has posed a challenge for the scientific community. Fluorine has just one stable isotope, ^{19}F , with many different channels of production depending on the conditions in stars. ^{19}F is also fragile and can be easily destroyed by α captures (e.g. [Meynet & Arnould 2000](#)). This makes narrowing down a dominant site for fluorine production particularly difficult. There are five main sites that frequently appear in the literature as having the potential to contribute significantly to the chemical evolution of fluorine; these are the following.

1. **Asymptotic Giant Branch (AGB) stars:** Fluorine is produced in AGB stars during thermal pulses ([Forestini et al., 1992](#); [Straniero et al., 2006](#)). Secondary ^{19}F is made from ^{14}N seed nuclei via the following two chains of reactions:



([Lugaro et al., 2004](#)). In certain conditions, primary fluorine can also be made in AGB stars from the rapid burning of ^{13}C at high temperatures, which produces ^{15}N and allows for the nucleosynthesis of fluorine via $^{15}\text{N}(\alpha,\gamma)^{19}\text{F}$ ([Cristallo et al., 2014](#)). For a more detailed review of the ^{19}F production channels in AGB stars, see [Lucatello et al. \(2011\)](#). [Kobayashi et al. \(2011a\)](#) found that the dominant AGB mass range for fluorine production is $2-4 M_{\odot}$, over which temperatures do not get hot enough for hot

bottom burning to occur, preventing the destruction of fluorine via $^{19}\text{F}(\alpha, p)^{22}\text{Ne}$. However, it should be noted that the yield set used in [Kobayashi et al. \(2011a\)](#) favours ^{19}F production in this mass range (see figure 8 of [Karakas & Lattanzio 2007](#)). There is also observational evidence that AGB stars contribute to the galactic fluorine (see the pioneering works of [Jorissen et al. 1992](#)). However, it is still unclear if AGB stars can account for the total galactic abundance of fluorine.

2. **Wolf-Rayet (WR) stars:** Fluorine can be produced by WR stars during the helium burning phase. Again, the seed nuclei for ^{19}F production in these stars is ^{14}N . If the ^{14}N is of secondary origin, then the behavior of ^{19}F is also secondary and is, therefore, metallicity dependent. It is thought that WR winds can eject some of the fluorine before it is destroyed by α captures; this process is the result of a delicate balance between the rate at which mass is lost via winds and the efficiency of the $^{19}\text{F}(\alpha, p)^{22}\text{Ne}$ reaction. In one of their models, [Meynet & Arnould \(2000\)](#) predicted that WR stars can produce as much as $2 \times 10^{-3} M_{\odot}$ of ^{19}F . However, since then other studies have revealed that the ^{19}F yield in massive star winds may not be as high as this (e.g. [Stancliffe et al. 2005](#), [Palacios et al. 2005](#), [Brinkman 2022](#)). For example, when rotation is accounted for, [Palacios et al. \(2005\)](#) found that the WR fluorine yield falls significantly with respect to [Meynet & Arnould \(2000\)](#). Interestingly, [Brinkman \(2022\)](#) found negative net yields of ^{19}F in all their rotating and non-rotating models, with the exception of an $80 M_{\odot}$ model with an initial rotational velocity $v_{\text{rot}} = 150 \text{ km s}^{-1}$. All this raises the question - do WR stars contribute to the galactic fluorine budget at all, which will be addressed in later sections of this work.
3. **Rotating Massive stars:** Fluorine can be produced in massive stars in the He convective shell via the series of reactions $^{14}\text{N}(\alpha, \gamma)^{18}\text{F}(\beta^+)^{18}\text{O}(p, \alpha)^{15}\text{N}(\alpha, \gamma)^{19}\text{F}$ ([Goriely et al. 1989](#), [Choplin et al. 2018](#)). This chain of reactions becomes enhanced when rotation is induced, due to the increased abundance of CNO elements which arises as a result of rotation ([Limongi & Chieffi, 2018](#)).
4. **Core-collapse supernovae (CCSNe):** The ν -process in CCSNe is also a proposed site

for fluorine production (Woodsley & Haxton 1988, Kobayashi et al. 2011b). CCSNe are powered by neutrino heating mechanisms. These neutrinos can interact with some nuclides, including fluorine. ^{19}F is produced via the ν process in CCSNe by the following reaction: $^{20}\text{Ne}(\nu, \nu' p)^{19}\text{F}$. Exactly how much fluorine this process might produce in CCSN is unclear because there is uncertainty around the flux and energy of the neutrinos. However, given this production is a primary process, more observations at low metallicity might help us to constrain how much fluorine we might expect to be produced by this source.

5. **Novae:** José & Hernanz (1998) showed that fluorine can be produced by novae. The mechanism for novae to produce fluorine is as follows: $^{17}\text{O}(p, \gamma)^{18}\text{F}(p, \gamma)^{19}\text{Ne}(\beta^+)^{19}\text{F}$. Just as with the ν process, fluorine yields from novae are still highly uncertain. José & Hernanz (1998) found that fluorine was only significantly synthesised in their $1.35 M_{\odot}$ models. Therefore, we cannot be sure of their contribution to the galactic fluorine abundance.

Note that here and throughout this work we define AGB stars in the mass range $1 \leq M/M_{\odot} \leq 8$ and massive stars $8 < M/M_{\odot} \leq 120$.

Many chemical evolution studies have tried to disentangle this web and figure out which sources of fluorine are dominant in different metallicity ranges. There is not much agreement between authors. Renda et al. (2004) used the WR yields of Meynet & Arnould (2000) to show that WR stars can dominate fluorine production at solar and super-solar metallicities, while AGB stars were required in their models to reproduce the trends at lower metallicities. This is in contrast to the work of Olive & Vangioni (2019) who concluded that AGB stars dominate at high metallicity and that the ν process in CCSNe is required to reproduce low-metallicity observations. A combination of AGB stars and neutrino process was also used by Kobayashi et al. (2011b) to reproduce the observed behaviour of [F/O] in globular cluster and solar neighbourhood stars.

Timmes et al. (1995) was the first chemical evolution study to investigate fluorine, and they found that the inclusion of novae can reproduce [F/O] ratios in combination with AGB stars. The need for novae to reproduce [F/O] versus [O/H] ratios was also found by Spitoni

[et al. \(2018\)](#), who concluded that AGB and WR stars dominate galactic fluorine production. We note again that [Kobayashi et al. \(2011a\)](#) found that the dominant AGB mass range that contributes to fluorine is $2-4 M_{\odot}$ but this contribution can only be seen at $[\text{Fe}/\text{H}] \gtrsim -1.5$ dex.

By assuming that massive stars have, on average, increasingly faster initial rotational velocities at low metallicities, [Prantzos et al. \(2018\)](#) found that rotating massive stars can dominate the evolution of fluorine in the Solar Neighbourhood up to solar metallicity. A similar conclusion was reached by [Grisoni et al. \(2020\)](#), who investigated the chemical evolution of fluorine by separately modelling the thick and the thin disk of the Milky Way using the so-called ‘parallel model’ of [Grisoni et al. \(2017\)](#). In particular, [Grisoni et al. \(2020\)](#) concluded that rotating massive stars can dominate fluorine production up to solar metallicity but a boost in fluorine is also needed at higher metallicities in order to match the behaviour of the observations. They proposed that this boost could be obtained either by artificially enhancing the AGB yields or by including an additional contribution from novae in the models. The prescription for rotating massive stars in [Grisoni et al. \(2020\)](#) follows the assumptions of [Romano et al. \(2019\)](#) where all stars with $[\text{Fe}/\text{H}] < -1$ dex are given an initial rotational velocity $v_{\text{rot}} = 300 \text{ km s}^{-1}$ while all stars with $[\text{Fe}/\text{H}] \geq -1$ dex have $v_{\text{rot}} = 0 \text{ km s}^{-1}$. Rotating massive stars were first recognised as important at low metallicity by [Chiappini et al. \(2006\)](#) in relation to primary nitrogen production, which is the seed for fluorine production. This arose from the work of [Matteucci \(1986\)](#) who recognised the need for another primary component of nitrogen.

Fluorine has also recently become an element of interest for high redshift studies. [Franco et al. \(2021\)](#) were able to estimate the abundance of fluorine in a gravitationally lensed galaxy at a redshift of $z = 4.4$, determining that Wolf-Rayet stars must be responsible for the observed fluorine abundance enhancement. Though this is not a Milky Way observation, it can still give us an idea of the origins of fluorine in the early Universe and thus, presumably, at low metallicity.

Aside from the uncertainties in the dominant production site of fluorine, we must also contend with difficulty in gathering observations of fluorine. The majority of fluorine abundance determinations in the literature are obtained from the analysis of ro-vibrational HF lines

at $2.3 \mu\text{m}$ (Abia et al., 2015). This spectral range is contaminated by telluric lines, which prevent the use of many HF lines for fluorine abundance determinations. Recently, the first detection of an AIF line was obtained in 2 M-type AGB stars (Saber et al., 2022). Danilovich et al. (2021) also detected the AIF line towards an S-type AGB star, measuring an abundance of AIF 40% greater than solar.

Most fluorine observations for chemical evolution studies are available using HF lines as detected in both galactic and extra-galactic AGB stars (Abia et al., 2011, 2015, 2019), massive stars (e.g. Nandakumar et al. 2023, Brady et al. 2024) field stars (Lucatello et al. 2011, Li et al. 2013) and in the Galactic center (Guerço et al., 2022). There are also a variety observations of fluorine in open and globular clusters (e.g. Cunha et al. 2003; Cunha & Smith 2005, Smith et al. 2005, Yong et al. 2008, Nault & Pilachowski 2013, De Laverny & Recio-Blanco 2013, Maiorca et al. 2014, Seshashayana et al. 2024, Holanda et al. 2024). Since this work is mainly focused on the chemical evolution of fluorine in Milky Way field stars, the previously listed observations in open and globular clusters will not be included in our analysis.

The evolution of fluorine at low metallicity (e.g., $[\text{Fe}/\text{H}] \lesssim -1.5$ dex) poses a particular challenge because of a large contamination from telluric lines and blending of the HF lines with CO features (Lucatello et al., 2011). Despite those challenges, there are some measurements of fluorine abundances at low metallicities, which include a sample of red giants from Lucatello et al. (2011) and two red giants in Carina dwarf spheroidal (dSph) galaxy from Abia et al. (2015) among others (e.g. Li et al. 2013, Mura-Guzmán et al. 2020). Both the stellar sample of Lucatello et al. (2011) and the Carina stars from Abia et al. (2015) are considered in our work.

The structure of the Chapter is as follows: Section 3.2 lays out the sample of fluorine abundance measurements that are used in this work for different metallicity ranges, Section 3.3 introduces the main hypothesis and working assumptions of our galactic chemical evolution model and summarizes the different combinations of yields that are included in the model, Section 3.4 presents the main chemical evolution trends of interest as predicted by our model to reproduce observational data, and Section 3.5 explains how these results can help us to probe the chemical evolution of fluorine. Finally, in Section 3.6, we present the conclusions

of this Chapter.

3.2 Observations

The most recent set of fluorine abundance measurements are those of [Ryde et al. \(2020\)](#) who observed 66 red giants using the Immersion GRating INfrared Spectrometer (*IGRINS*) and the *Phoenix* infrared high-resolution spectrograph at the *Gemini* South Observatory. The metallicity range of these observations is $-1.1 < [\text{Fe}/\text{H}] < 0.4$ which extends the metallicity range of fluorine abundances in the solar neighbourhood that were available previous to this study (e.g. [Jönsson et al. 2017](#)).

Due to telluric lines and blending, much of the data we have at low $[\text{Fe}/\text{H}]$ are upper limits rather than absolute measurements. Though not as conclusive as absolute measurements, upper limits can still tell us about the range of fluorine abundances we might expect and can give us a preliminary idea of if our chemical evolution models can reproduce observations at low metallicity. The primary set of fluorine observations at low metallicity used in this work consists of a sample of eleven metal-poor red giant stars from [Lucatello et al. \(2011\)](#). The abundances were measured from the analysis of spectra obtained with the Cryogenic high-resolution InfraRed Echelle Spectrograph (*CRIFES*) on ESO's *VLT*. Of the 11 stars in the metallicity range $-3.4 < [\text{Fe}/\text{H}] < -1.3$, two have abundance measurements of fluorine, while the remaining nine have upper limits provided.

Eight red giants in the sample of [Lucatello et al. \(2011\)](#) are classified as CEMP-s stars (carbon-enhanced metal poor stars that are also enriched in s-process elements), whereas two stars are classified as CEMP-no star (not enriched with s-process or r-process elements). There is also one star in this sample classified as carbon normal. While the physical origin of CEMP-no stars is still unclear and debated ([Aoki et al., 2002](#); [Yoon et al., 2016](#); [Hansen, C. J. et al., 2016](#)), the s process and carbon enhancement as measured in the atmosphere of CEMP-s red giants likely results from binary mass transfer from an AGB companion that changed the initial surface abundances (e.g., [Lucatello et al. 2005](#); [Beers & Christlieb 2005](#); [Bisterzo et al. 2010](#); [Lugaro et al. 2012](#); [Starkenburg et al. 2014](#); [Hansen, T. T. et al. 2016](#); [Hempel et al. 2016](#)). Therefore, the predictions of our chemical evolution models at low

[Fe/H] solely provide a baseline for the average fluorine abundances at birth in CEMP-s red giants before mass transfer took place. We also include fluorine measurements as obtained in two stars of the Carina dSph galaxy by [Abia et al. \(2015\)](#). These measurements were obtained from spectra taken using the *Phoenix* infrared high-resolution spectrograph by [Abia et al. \(2011\)](#) and reanalysed by using the spectral synthesis code *Terbospectrum* by [Abia et al. \(2015\)](#). The formation of Carina occurred with low star formation efficiencies and a short infall timescale (e.g. [Lanfranchi et al. 2006](#), [Vincenzo et al. 2014](#)), as did the Milky Way halo. Therefore, observations in Carina dSph have been included in this work in order to further our understanding of how fluorine might behave at low metallicity in general. However, since these stars are not Milky Way stars we must be careful as they are not directly comparable with the chemical evolution models presented in this work or the other observations.

3.3 Galactic Chemical Evolution Model

We have used the chemical evolution code OMEGA+¹ ([Côté et al., 2018b](#)). This is a two-zone model where a central star forming region is modelled using the code OMEGA² ([Côté et al., 2017](#)), which simulates the evolution of several physical and chemical properties within a cold gas reservoir, surrounded by a non-star forming hot gas reservoir. The latter is considered as the circumgalactic medium (CGM) in our model. The details of how the code operates are in Chapter 2 of this work, here we will present the main equations that govern the evolution of the model.

We can follow both the evolution of the CGM and the internal star forming galaxy. The evolution of the mass of the gas in the CGM (M_{CGM}) is as follows:

$$\dot{M}_{\text{CGM}}(t) = \dot{M}_{\text{CGM,in}}(t) + \dot{M}_{\text{outflow}}(t) - \dot{M}_{\text{inflow}}(t) - \dot{M}_{\text{CGM,out}}(t) \quad (3.1)$$

where $\dot{M}_{\text{CGM,in}}$ is the inflow rate from the external intergalactic medium into the CGM, \dot{M}_{outflow} is the outflow rate of mass removed from the central galaxy and added to the CGM via outflows, \dot{M}_{inflow} is the rate of gas mass that flows into the central galaxy from the CGM

¹OMEGA+ is available online as part of the JINAPyCEE package <https://github.com/becot85/JINAPyCEE>

²OMEGA is available online as part of the NuPyCEE package <https://github.com/NuGrid/NUPYCEE>

and $\dot{M}_{\text{CGM,out}}$ is the outflow rate of gas from the CGM into the intergalactic medium. Details of all of these terms can be found in [Côté et al. \(2018b, 2019b\)](#) and references therein (see figure 7 of [Côté et al. \(2018b\)](#) for a visual representation of the workings of OMEGA+).

The evolution of the galactic gas mass \dot{M}_{gas} is defined as ([Tinsley 1980](#); [Pagel 1997](#); [Matteucci 2012](#)):

$$\dot{M}_{\text{gas}}(t) = \dot{M}_{\text{inflow}}(t) + \dot{M}_{\text{ej}}(t) - \dot{M}_{\star}(t) - \dot{M}_{\text{outflow}}(t) \quad (3.2)$$

where \dot{M}_{inflow} is the rate of gas mass added by galactic inflows from the CGM, \dot{M}_{ej} is rate of gas mass added by stellar ejecta, \dot{M}_{\star} is the rate of gas mass which is locked away by star formation and \dot{M}_{outflow} is the rate of the gas mass lost by outflows into the CGM. This equation is used at each timestep to track the evolution of the galaxy across 13 Gyr.

The infall prescription of gas from the CGM into the galaxy that we use here is a dual infall model based on [Chiappini et al. \(1997\)](#). It combines two episodes of exponential gas inflow and is described as follows:

$$\dot{M}_{\text{inflow}}(t) = A_1 \exp\left(\frac{-t}{\tau_1}\right) + A_2 \exp\left(\frac{t_{\text{max}} - t}{\tau_2}\right). \quad (3.3)$$

Where A_1 , A_2 , τ_1 , τ_2 , and t_{max} are free parameters, the values for which can be found in [Table 3.1](#). A_1 and A_2 represent the normalisation of the first and second infall events, respectively, τ_1 and τ_2 are the timescales for mass accretion for the first and second infall, and t_{max} is the time of maximum contribution of the second gas accretion episode, which is zero for the first episode.

The star formation rate is defined as

$$\dot{M}_{\star}(t) = \frac{\epsilon_{\star}}{\tau_{\star}} M_{\text{gas}}(t) \quad (3.4)$$

where ϵ_{\star} and τ_{\star} are the dimensionless star formation efficiency (sfe) and star formation timescale, respectively. The outflow rate is proportional to the star formation rate and is defined as

$$\dot{M}_{\text{outflow}}(t) = \eta \dot{M}_{\star}(t) \quad (3.5)$$

where η is the mass loading factor and controls the strength of the outflows. The values for ϵ_{\star} , τ_{\star} and η can also be found in [Table 3.1](#).

To calculate the mass of gas added by stellar ejecta, the contribution of every stellar population formed by time t is summed so that

$$\dot{M}_{\text{ej}}(t) = \sum_j \dot{M}_{\text{ej}}^j(M_j, Z_j, t - t_j) \quad (3.6)$$

where \dot{M}_{ej}^j is the rate of gas mass ejected by the j th stellar population, M_j is the initial mass of the population, Z_j is the initial metallicity of the population and $t - t_j$ is the age of the j th population at time t . The simple stellar populations (SSPs) are created at every timestep using SYGMA (Stellar Yields for Galactic Modelling Applications) (Ritter et al., 2018a). An SSP is defined as a population of stars with the same age and chemical composition, with the number of each type of star in the different evolutionary stages being weighted by an initial mass function (IMF). In this work we adopt the IMF of Kroupa (2001). SYGMA includes ejecta from low and intermediate mass stars, massive stars, Type Ia Supernovae (SNe Ia), neutron star mergers and additional sources can also be added manually by the user. The ejecta from the SSPs are then instantaneously and uniformly mixed into the gas reservoir.

We use the solar abundances of Asplund et al. (2009) throughout, where the ^{19}F solar abundance is $\log(\epsilon(\text{F})) = 4.56 \pm 0.30$.

3.3.1 Stellar Yields

Nine combinations of yields have been used throughout this work and are laid out in Table 3.2. We explore the following options for our AGB yields: (i) the Full-Network Repository of Updated Isotopic Tables & Yields (FRUITY) for AGB stars from Cristallo et al. (2015), that are available for metallicities $10^{-4} \leq Z \leq 2 \times 10^{-2}$ and masses in the range $1.3\text{-}6.0 M_{\odot}$; (ii) the Monash AGB yields from Lugaro et al. (2012); Karakas & Lugaro (2016), and Karakas et al. (2018) with metallicities $10^{-4} \leq Z \leq 3 \times 10^{-2}$ and masses in the range $0.9\text{-}8.0 M_{\odot}$; (iii) an extended version of the previous Monash yields that cover the same range of masses and metallicities as the previous set, where heavy elements (anything heavier than iron) are also included (Karakas & Lugaro, 2016; Karakas et al., 2018); finally, (iv) the AGB yields from Ventura et al. (2013, 2014, 2018) with metallicities $3 \times 10^{-4} \leq Z \leq 1.4 \times 10^{-2}$ and masses in the range $1.0\text{-}7.5 M_{\odot}$.

We consider the two following options for our massive star yields.

Parameter	Value
A_1 [$M_{\odot} \text{ yr}^{-1}$]	46
A_2 [$M_{\odot} \text{ yr}^{-1}$]	5.9
τ_1 [Gyr]	0.8
τ_2 [Gyr]	7.0
t_{max} [Gyr]	1.0
ϵ_{\star}	0.23
τ_{\star} [Gyr]	1.0
η	0.52

Table 3.1: Parameter values of the model, where A_1 , A_2 , τ_1 , τ_2 and t_{max} are all free parameters of Equation 3.3. ϵ_{\star} , the sfe, and τ_{\star} , the star formation timescale, are the free parameters of Equation 3.4 and η , the mass loading factor, is the free parameter of Equation 3.5. These values are equivalent to the values in the ‘best’ model of Côté et al. (2019a).

1. Set R of Limongi & Chieffi (2018), who developed stellar evolution models for massive stars by assuming three different initial rotation velocities as follows: $v_{\text{rot}} = 300 \text{ km s}^{-1}$, $v_{\text{rot}} = 150 \text{ km s}^{-1}$, and no rotation; all of these options will be explored in this work. For each rotational velocity, Limongi & Chieffi (2018) developed models with initial iron abundances $[\text{Fe}/\text{H}] = 0, -1, -2, \text{ and } -3$ dex in the mass range $13\text{-}120 M_{\odot}$. The chemical evolution models of Prantzos et al. (2018) assume a yield set which combines the massive star models of Limongi & Chieffi (2018) with different v_{rot} depending on metallicity, by assuming that lower metallicity stars rotate faster, on average, than higher metallicity stars, as illustrated in figure 4 of Prantzos et al. (2018). A similar mixture of rotating massive star models that varies as a function of $[\text{Fe}/\text{H}]$ will also be explored in this work. The logic for this combination comes about because Meynet & Maeder (1997) stated that in order to conserve angular momentum, low metallicity stars must rotate faster as they are more compact.
2. The yields of Nomoto et al. (2013, see also Kobayashi et al. 2006, 2011b, and Kobayashi et al. 2020) which do not include rotation. These yields use metallicities $10^{-3} \leq Z \leq$

Model Name	AGB yields	Massive Star Yields	SN Ia Yields
CLCmix	FRUITY	L&C $V_{\text{rot}} = \text{mix}$	Iwamoto
CLC000	FRUITY	L&C $V_{\text{rot}} = 0 \text{ kms}^{-1}$	Iwamoto
CLC150	FRUITY	L&C $V_{\text{rot}} = 150 \text{ kms}^{-1}$	Iwamoto
CLC300	FRUITY	L&C $V_{\text{rot}} = 300 \text{ kms}^{-1}$	Iwamoto
Mon18LCmix	Mon. 1	L&C $V_{\text{rot}} = \text{mix}$	Iwamoto
MonLCmix	Mon. 2	L&C $V_{\text{rot}} = \text{mix}$	Iwamoto
MonLC300	Mon. 2	L&C $V_{\text{rot}} = 300 \text{ kms}^{-1}$	Iwamoto
CNom	FRUITY	Nomoto	Iwamoto
VenLCmix	ATON	L&C $V_{\text{rot}} = \text{mix}$	Iwamoto

Table 3.2: Combination of yields used for the chemical evolution modelling in this work. Where FRUITY = [Cristallo et al. \(2015\)](#), Mon 1 = [Lugaro et al. \(2012\)](#) and [Karakas & Lugaro \(2016\)](#); [Karakas et al. \(2018\)](#), Mon 2 is the same as previous but with heavy elements included and ATON = [Ventura et al. \(2013, 2014, 2018\)](#). L&C are the massive star yields of [Limongi & Chieffi \(2018\)](#), Nomoto are the yields of [Nomoto, Kobayashi & Tominaga \(2013\)](#) and Iwamoto are the SN Ia yields of [Iwamoto et al. \(1999\)](#).

5×10^{-2} in the mass range 13-40 M_{\odot} .

Of these yield sets, we mainly consider the FRUITY AGB yields because they cover a large range of masses and metallicities. The code used to calculate these yields is also coupled to a full nuclear network up to the termination point of the s process, therefore it considers the full range of isotopes and reactions relevant to this work. For massive stars, we mainly use the yields of [Limongi & Chieffi \(2018\)](#) in order to investigate the impact of rotation. Finally, for all models we use the W7 SN Ia yields of [Iwamoto et al. \(1999\)](#). Here, we refer the reader to Appendix A where there is a brief discussion on how well model CLCmix can reproduce present day observational constraints and solar abundance ratios that are of interest in this Thesis.

3.4 Results

Figure 3.1a shows the abundance trend of [F/Fe] versus [Fe/H] for models assuming different combinations of yields, as summarised in Table 3.2. The predictions of our models are

compared with high metallicity observations of fluorine abundances in the red giant sample of [Ryde et al. \(2020\)](#), red points with error bars) and low metallicity observations in red giants from [Lucatello et al. \(2011\)](#), brown square symbols represent stars classified as CEMP-s whereas brown crosses are CEMP-no stars, the carbon normal star is represented by a brown point) and [Abia et al. \(2015\)](#), pink squares with error bars). We remind the readers that our models predict the evolution of the chemical abundances in the interstellar medium (ISM), hence how the birth abundances of stars change with time throughout the evolution of the Galaxy.

The two models which include massive stars with no rotation (*CLC000* and *CNom*) show an increasing trend in $[F/Fe]$ at higher metallicities that is in line with observations. However, these two models lie below the observed abundances. We note that, in the low metallicity regime from $-3.5 < [Fe/H] < -2$, the observational data are upper limits rather than absolute measurements, along with the high dispersion of the observational data in this metallicity range, which prevents us from drawing strong conclusions in this regime. The strongest constraint on our chemical evolution models is provided by observations in the metallicity range $-0.7 < [Fe/H] < 0.4$. We can still draw conclusions in the range $-2 < [Fe/H] < -0.7$ but we are limited by poor statistics. All models with rotating massive stars included cut through the middle of the upper limits, with the majority of the brown points sitting above the chemical evolution trend lines. This is important because we know that an upper limit means the value quoted has the potential to be lower than what is measured. We also see that the models including rotating massive stars are consistent with the bulk of the high-metallicity data. We note that models with higher v_{rot} can reach increasingly higher $[F/Fe]$ ratios at high metallicity. Nonetheless, no model with high v_{rot} reproduces the upward trend seen in observations at high $[Fe/H]$, which is only seen in the models with $v_{rot} = 0$.

Figure 3.1b shows the abundance trend of $[F/O]$ versus $[O/H]$ for the same set of models as in Figure 3.1a. These ratios are commonly plotted together when studying the chemical evolution of fluorine to trace the impact of the chemical enrichment from massive stars with minimal connection to the choice of the location of the mass cut in the massive star models. Looking at chemical evolution trends relative to oxygen is also useful because they do not

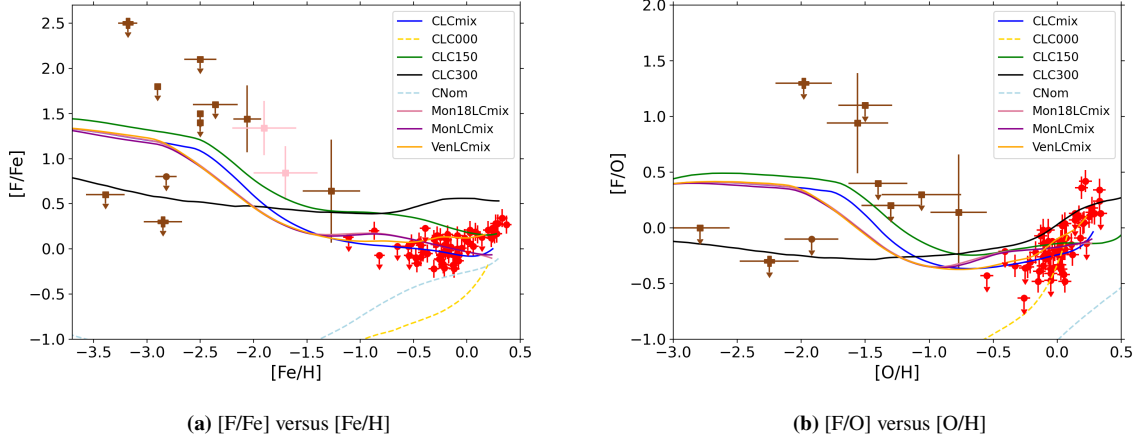


Figure 3.1: Left-hand panel: $[F/Fe]$ versus $[Fe/H]$ for models CLCmix, CLC000, CLC150, CLC300, CNom, Mon18LCmix and MonLCmix. The red points are observations of fluorine from Ryde et al. (2020), the brown points from Lucatello et al. (2011) and the pink squares are Carina data from Abia et al. (2015). CEMP-s stars in the sample of Lucatello et al. (2011) are represented by brown squares, CEMP-no stars by brown crosses and the carbon normal star by a brown point. Right-hand panel: the same but for $[F/O]$ versus $[O/H]$.

include the uncertainties associated with SNIa models. In Figure 3.1b the trajectories are again compared with observations from Ryde et al. (2020) and Lucatello et al. (2011). Again, some observations provide better constraints for our GCE models than others, with those at $[O/H] > -0.4$ providing the strongest constraint. We can see that all models which include any sort of prescription for rotation in massive stars cut through the low metallicity observations, including *VenLCmix*. Further discussion of this model can be found later in the section. Of the two models that do not include rotating massive stars (*CLC000* and *CNom*), only *CLC000* reproduces the abundance trends of the high metallicity observations.

In Figs 3.1a and 3.1b we also investigate the impact of different AGB stellar yields on the chemical enrichment of fluorine. Our model with the FRUITY stellar yields for AGB stars (*CLCmix*) predicts similar abundance trends as the models with the Monash stellar yields (*Mon18LCmix* and *MonLCmix*). The model with the AGB stellar yields of Ventura et al. (2013, 2014, 2018) (*VenLCmix*) predict higher final fluorine abundances in both Figs. 3.1a and 3.1b compared to the FRUITY and Monash yields but they still lie within the high metallicity observations.

The AGB stellar yields of Ventura et al. (2013, 2014, 2018) are explored in more detail

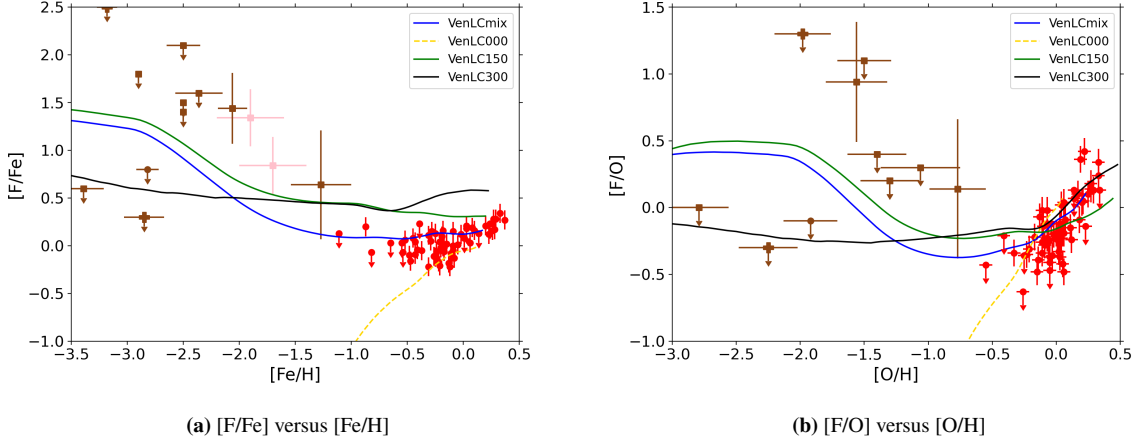


Figure 3.2: Panel a: [F/Fe] versus [Fe/H] for the Ventura et al. (2013, 2014, 2018) AGB yields in combination with each rotational prescription of the Limongi & Chieffi (2018) massive stars, compared with the same observational data as Figure 3.1a. Panel b: same as the Figure 3.2a but for [F/O] versus [O/H].

in Figure 3.2, which shows chemical evolution models combining those yields with massive star models with different initial v_{rot} from Limongi & Chieffi (2018). Figure 3.2a shows our results for [F/Fe] versus [Fe/H], whereas Figure 3.2b focuses on [F/O] versus [O/H]. In each figure, the chemical evolution trends for each massive star prescription are similar in shape to the trends we predict when assuming the FRUITY AGB yields. However, the final values for models *VenLCmix*, *VenLC000*, *VenLC150* and *VenLC300* for both [F/Fe] and [O/H] are systematically higher than *CLCmix*, *CLC000*, *CLC150* and *CLC300*.

The AGB stellar yields of Ventura et al. (2013, 2014, 2018) were the reference set adopted by Grisoni et al. (2020) in their ‘parallel’ chemical evolution model for the Solar Neighbourhood. However, when comparing our results with those in figure 1 of Grisoni et al. (2020), we caution the readers that we assume a different IMF and DTD for SNe Ia. In particular, Grisoni et al. (2020) assumed the IMF of Kroupa et al. (1993), which hosts much lower numbers of massive stars than the IMF of Kroupa (2001) which we use in our models (see also Vincenzo et al. 2016 for more details); secondly, while Grisoni et al. (2020) assumed the SN Ia single-degenerate model of Matteucci & Recchi (2001), here we assume a power-law DTD which is motivated by recent observational surveys (Maoz & Mannucci, 2012, see also Wiseman et al. 2021 for an observational perspective, and Vincenzo et al. 2017 for the impact of those two different DTDs on elemental abundance trends).

When we consider the [F/Fe] versus [Fe/H] abundance diagram (Figure 3.2a), our model with $v_{\text{rot}} = 0$ (*VenLC000*) predicts [F/Fe] ratios that are always ≈ 0.5 dex higher than model *Thin-V000* of Grisoni et al. (2020). Our models with $v_{\text{rot}} = 150$ and 300 km s^{-1} (*VenLC150* and *VenLC300*, respectively), instead, always lie below models *Thin-V150* and *Thin-V300* of Grisoni et al. (2020) for iron abundances between $-1.5 \lesssim [\text{Fe}/\text{H}] \lesssim -0.5$ but then move above them as metallicity increases. It is difficult to compare models with variable v_{rot} because we follow different prescriptions. We recall that Grisoni et al. (2020) chose the prescription of Romano et al. (2019) with a sharp transition from $v_{\text{rot}} = 300 \text{ km s}^{-1}$ to $v_{\text{rot}} = 0 \text{ km s}^{-1}$ at $[\text{Fe}/\text{H}] = -1$ dex, whereas our model uses a prescription from Prantzos et al. (2018) which employs a more gradual change to lower rotational velocities as the metallicity increases. The mix of rotational velocities adopted in the present work (*VenLCmix*) follows the observational trends much more closely than *Thin-Vvar* of Grisoni et al. (2020).

When we consider the [F/O] versus [O/H] abundance diagram (Figure 3.2b), our models with $v_{\text{rot}} = 0 \text{ km s}^{-1}$ always lie above model *Thin-V000* of Grisoni et al. (2020), being separated by a constant offset of ≈ 0.2 dex. Our model *VenLC150* appears to sit lower than *Thin-V150* of Grisoni et al. (2020) for $[\text{Fe}/\text{H}] \lesssim 0$ dex. Interestingly, the models with $v_{\text{rot}} = 300 \text{ km s}^{-1}$ follow a very similar shape in both this work and Grisoni et al. (2020). However, our model always lies below *Thin-V300* of Grisoni et al. (2020), being separated by an offset of ≈ 0.3 dex. Our model with a rotational mix (*VenLCmix*) can reproduce the observations at high metallicity more closely than the *Thin-Vvar* of Grisoni et al. (2020). However, we remind the reader once again that each of our works employs a different prescription for rotational mixing.

In summary, this discussion shows how careful we must be when we make chemical evolution models, and it further highlights the uncertainties we have in trying to best model the Milky Way.

3.4.1 Fluorine and s-process elements

The interplay between fluorine and s-process elements has been previously commented on in the literature (e.g. Lucatello et al. 2011, Abia et al. 2011, 2015, 2019). Fluorine and s-process

elements can be made together both in AGB stars and massive stars, especially when mixing is enhanced by rotation.

In massive stars, fluorine nucleosynthesis takes place in the helium convective shell via a series of reactions involving α -captures and proton captures. s-process elements in massive stars are synthesised via neutron captures, with the neutrons primarily coming from the $^{22}\text{Ne}(\alpha, n)^{25}\text{Mg}$ reaction. ^{22}Ne is synthesised from ^{14}N produced in the convective H-burning shell and brought into the He-burning core. Once in the core, two convective α -captures starting from ^{14}N produce ^{22}Ne . This process continues into the carbon burning phase (see [Pignatari et al. 2010](#); [Prantzos et al. 2018](#) for more details). In massive star models without rotation, we might expect to see s-process production up to the so-called ‘first-peak’ i.e. Sr, Y, Zr (e.g. [Limongi & Chieffi 2003](#)). However, [Frischknecht et al. \(2012\)](#) showed that the efficiency of the mixing processes described above can be greatly enhanced within rapidly rotating massive stars, leading to s-process production beyond the first peak.

In AGB stars, both fluorine and s-process elements are made during thermal pulses. Fluorine is made via a series of neutron, proton and α captures that use ^{14}N as the seed nucleus. s-process elements are made via neutron captures in the intershell region of the star (e.g. [Busso et al. 1999](#)). The primary neutron source here is the $^{13}\text{C}(\alpha, n)^{16}\text{O}$ reaction. Given the similar production sites of fluorine and s-process elements, it seems likely that where we find one we would likely find the other. This means there is a potential correlation between fluorine and s-process elements that needs to be explored.

Figure 3.3 shows the [s/Fe] versus [Fe/H] abundance trend for the models *CLCmix*, *CLC000*, *CLC150*, *CLC300*, *MonLCmix* and *MonLC300*, that are specified in Table 3.2. The models with the AGB yields of [Ventura et al. \(2013\)](#), the first set of Monash AGB yields (Mon.1), and the massive star yields of [Nomoto et al. \(2013\)](#) are not shown because they do not include heavy element abundances. In Figs 3.3 and 3.4, ‘s’ denotes the average s-process abundance for each of the models, where [s/Fe] is defined as follows ([Abia et al., 2002](#)):

$$[\text{s}/\text{Fe}] = ([\text{Sr}/\text{Fe}] + [\text{Y}/\text{Fe}] + [\text{Zr}/\text{Fe}] + [\text{Nb}/\text{Fe}] \\ + [\text{Ba}/\text{Fe}] + [\text{La}/\text{Fe}] + [\text{Ce}/\text{Fe}] + [\text{Pr}/\text{Fe}])/8.$$

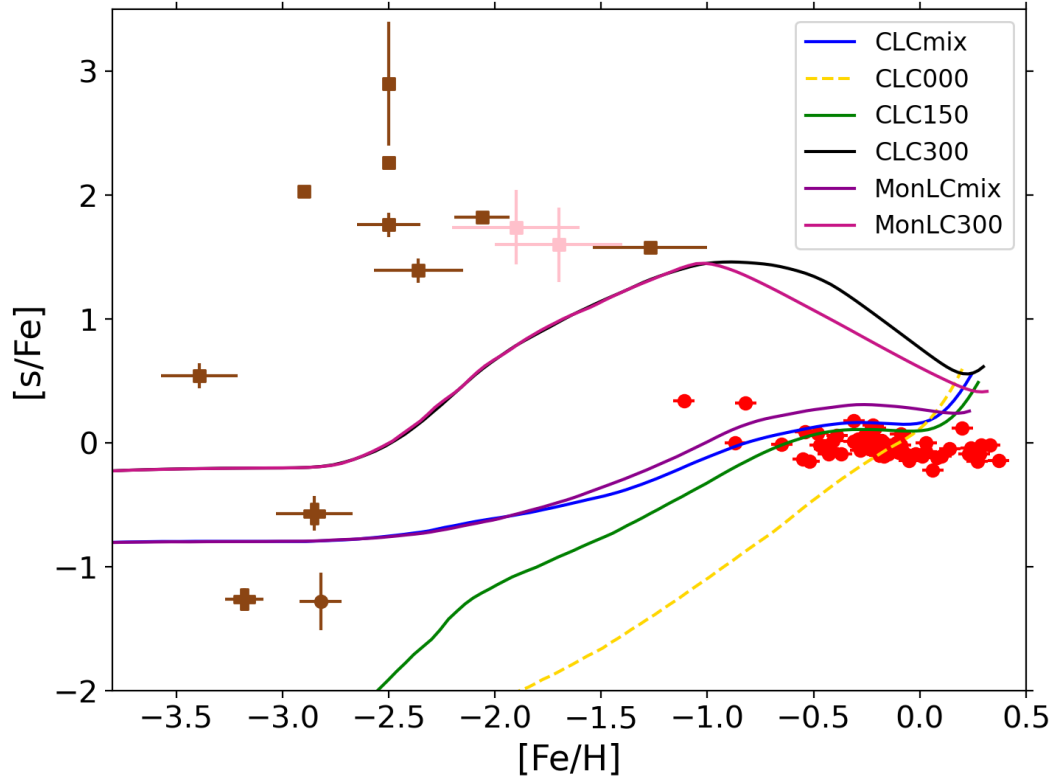


Figure 3.3: $[s/Fe]$ versus $[Fe/H]$ for models *CLCmix*, *CLC000*, *CLC150*, *CLC300*, *MonLCmix* and *MonLC300*. The observational data is the same as Figure 3.1a.

If we focus on the very low-metallicity regime, the only models that can reproduce the high upper limits on $[s/Fe]$ are those which include massive stars with $v_{\text{rot}} = 300 \text{ km s}^{-1}$. In the domain $-2.5 < [Fe/H] < -1$ the models *CLC300* and *MonLC300* underestimate the observations. These models also severely overestimate $[s/Fe]$ at high metallicity, disagreeing with the observations of [Ryde et al. \(2020\)](#). We note that a similar mismatch was also seen by [Vincenzo et al. \(2021\)](#) when comparing their models with the [Limongi & Chieffi \(2018\)](#) rotating massive star yields to the stellar abundance measurements of neutron-capture elements from the second data release of the GALactic Archaeology with HERMES (GALAH) survey ([Buder et al., 2018](#)). The rest of the models (those with a minor or absent contribution from stars with $v_{\text{rot}} = 300 \text{ km s}^{-1}$) provide a better explanation for the high metallicity observations, with *CLCmix* and *CLC150* reproducing the plateau in the data up to solar metallicity.

Figure 3.4 shows $[F/s]$ versus $[Fe/H]$ for the same models as Figure 3.3. By investigating

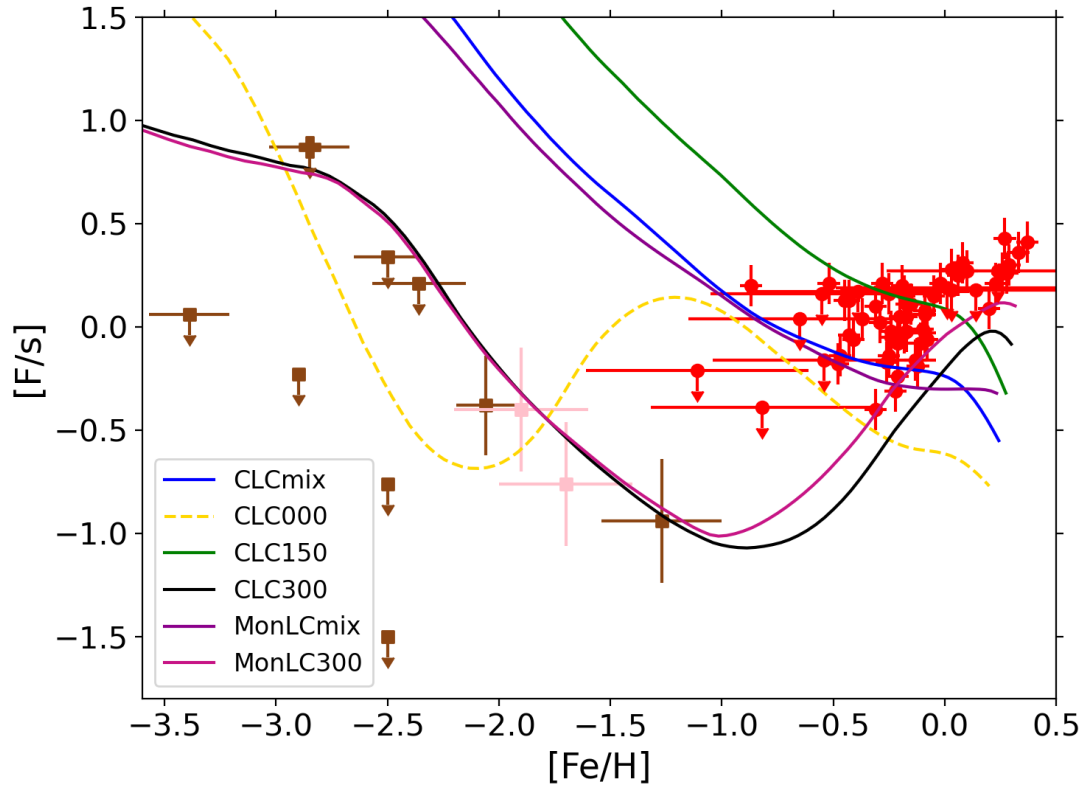


Figure 3.4: $[F/s]$ versus $[Fe/H]$ for models CLCmix, CLC000, CLC150, CLC300, MonLCmix and MonLC300. The observational data is the same as Figure 3.1a.

this ratio we can continue to probe the chemical evolution of fluorine. For comparison, Figure 3.5 shows $[F/Ba]$ versus $[Fe/H]$ for the same set of models. Since there is minimal change in the trajectory of the chemical evolution trends between $[F/s]$ in Figure 3.4 and $[F/Ba]$ in Figure 3.5, we can safely use the average s-process abundances for comparison with stellar observations by including a variety of s-process elements without loss of important information from tracking elements individually.

In the low metallicity regime ($-3.4 < [Fe/H] < -2.3$), the abundance of F and s-process elements for the CEMP stars in the figure has likely arisen due to accretion of material from an AGB companion (e.g. Busso et al. 2001, Sneden et al. 2008, Lucatello et al. 2011, Mura-Guzmán et al. 2020). Coupled with the fact that most of the observations in this region are upper limits, we cannot use these observations to constrain the GCE models. That being said, it is noteworthy that two scenarios seem to provide similar predictions for $[F/s]$ in

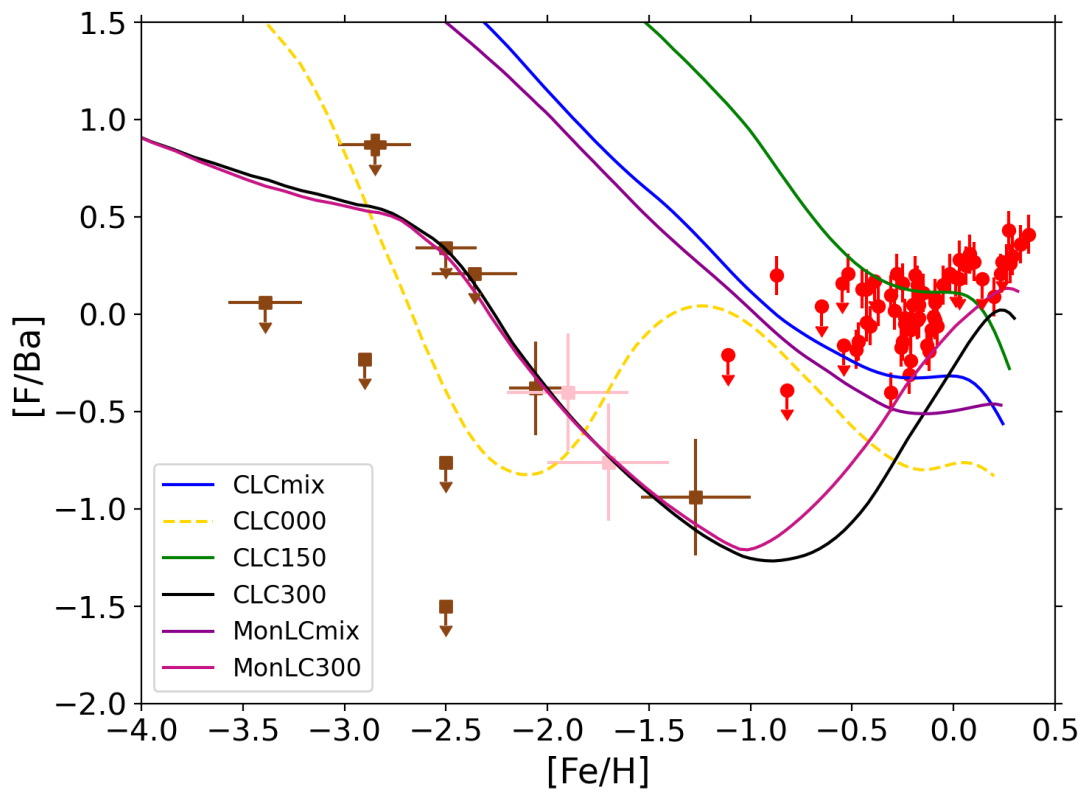


Figure 3.5: $[F/Ba]$ versus $[Fe/H]$ for models CLCmix, CLC000, CLC150, CLC300, MonLCmix and MonLC300.

The observational data is the same as Figure 3.1a.

Figure 3.4: (i) AGB + massive stars with $v_{\text{rot}} = 0$ (*CLC000*), and (ii) AGB + massive stars with $v_{\text{rot}} = 300 \text{ km s}^{-1}$ (*CLC300* and *MonLC300*). These two scenarios are potentially very different. For stars rotating as quickly as 300 km s^{-1} , the fluorine present on the surface will likely have been transported from the interior layers onto the surface due to the strong mixing from rotation. However, internal mixing is not as strong for non-rotating massive stars so there may not be as much fluorine transported from the interior layers to the surface. This could mean some of the surface fluorine is present due to accretion from a companion.

There are two key details in the figures presented in this work that can separate the two potentially different scenarios mentioned above.

1. In Figure 3.4, the solar and super-solar metallicity observations from Ryde et al. (2020) show an upturn in their [F/s] that is only predicted by the models with $v_{\text{rot}} = 300 \text{ km s}^{-1}$.
2. In Figure 3.1a, model *CLC000* is below all the observations, which means that solely including non-rotating massive stars is not enough to reproduce the observed fluorine abundance pattern.

Overall, this suggests that we need a contribution from rotating massive stars throughout the evolution of the Galaxy in order to reproduce the observations; in particular, Figure 3.4 shows that massive stars with $v_{\text{rot}} = 300 \text{ km s}^{-1}$ might play a crucial role in the chemical evolution of fluorine, especially when considering the simultaneous production of s-process elements.

Figs. 3.6 and 3.7 disentangle the contributions from massive stars, AGB stars and Type Ia SNe to ^{19}F , ^{56}Fe , ^{16}O , and ^{140}Ce as predicted by the model with $v_{\text{rot}} = 300 \text{ km s}^{-1}$ (*CLC300*). Here cerium is used as a proxy for the s-process elements. We can see that the massive star model with $v_{\text{rot}} = 300 \text{ km s}^{-1}$ dominates both ^{19}F and ^{140}Ce even when AGB stars kick in between $-1 < [\text{Fe}/\text{H}] < 0$. Figure 3.7 highlights this range in more detail.

By looking at the predictions of model *CLC300* in Figs. 3.6 and 3.7, both ^{19}F and ^{140}Ce abundances at $[\text{Fe}/\text{H}] = 0$ are higher than solar by a factor of ≈ 4 and ≈ 6 , respectively (the black dashed line on each panel corresponds to the solar fluorine and cerium abundances). Therefore, even though models *CLC300* and *MonLC300* are best at reproducing the observational trends of Figure 3.4, the fluorine and average s-process abundances that they generate at

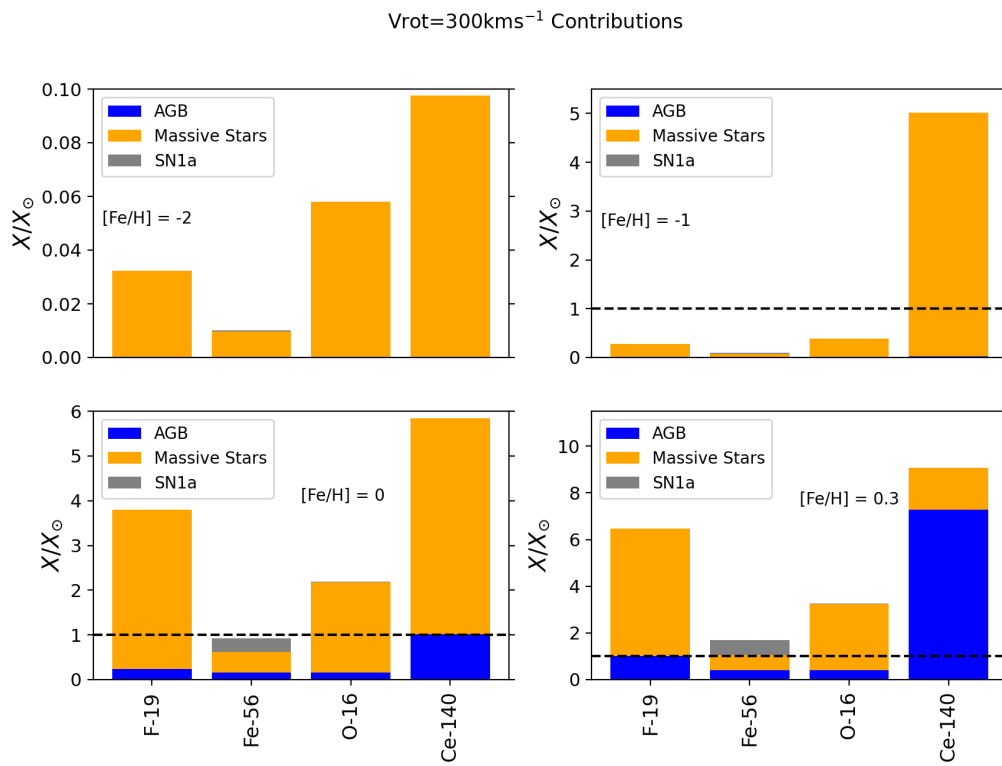


Figure 3.6: The contribution of each stellar source relative to solar for model CLC300 at metallicities $[Fe/H] = -2$ (top left), $[Fe/H] = -1$ (top right), $[Fe/H] = 0$ (bottom left) and $[Fe/H] = 0.3$ (bottom right - present). The contribution from massive stars is shown in orange, AGB stars in blue and SNe Ia in grey.

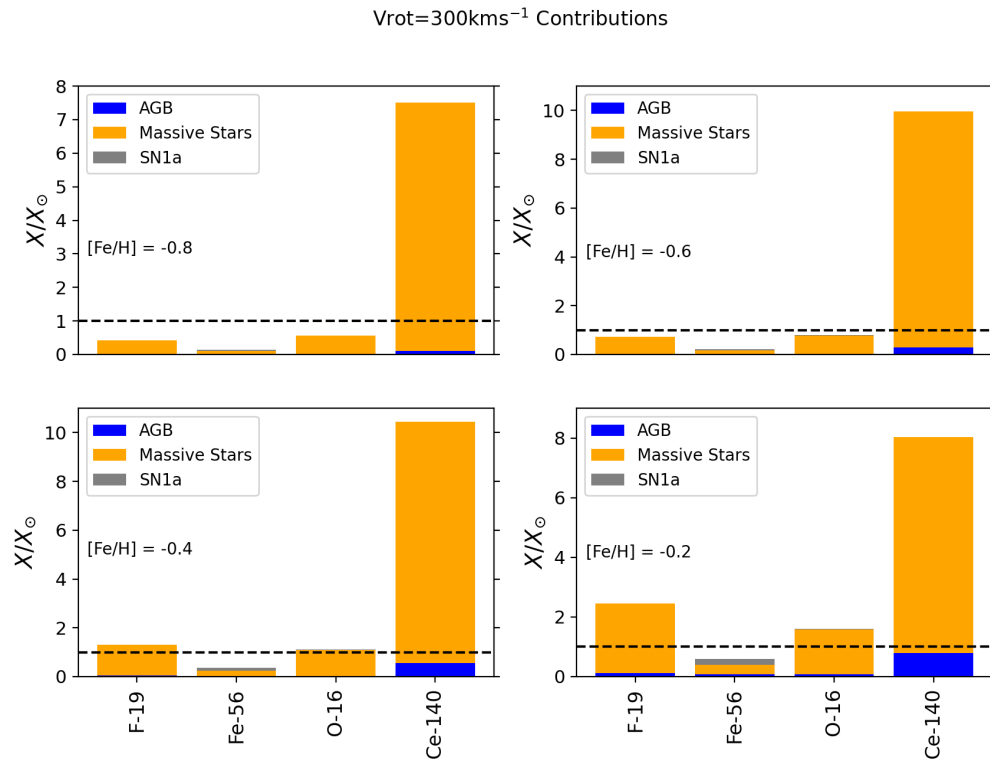


Figure 3.7: The contribution to each isotope from each stellar source relative to solar for model CLC300 at metallicities [Fe/H] = -0.8 (top left), [Fe/H] = -0.6 (top right), [Fe/H] = -0.4 (bottom left) and [Fe/H] = -0.2 (bottom right - present). The contribution from massive stars is shown in orange, AGB stars in blue and SNe Ia in grey.

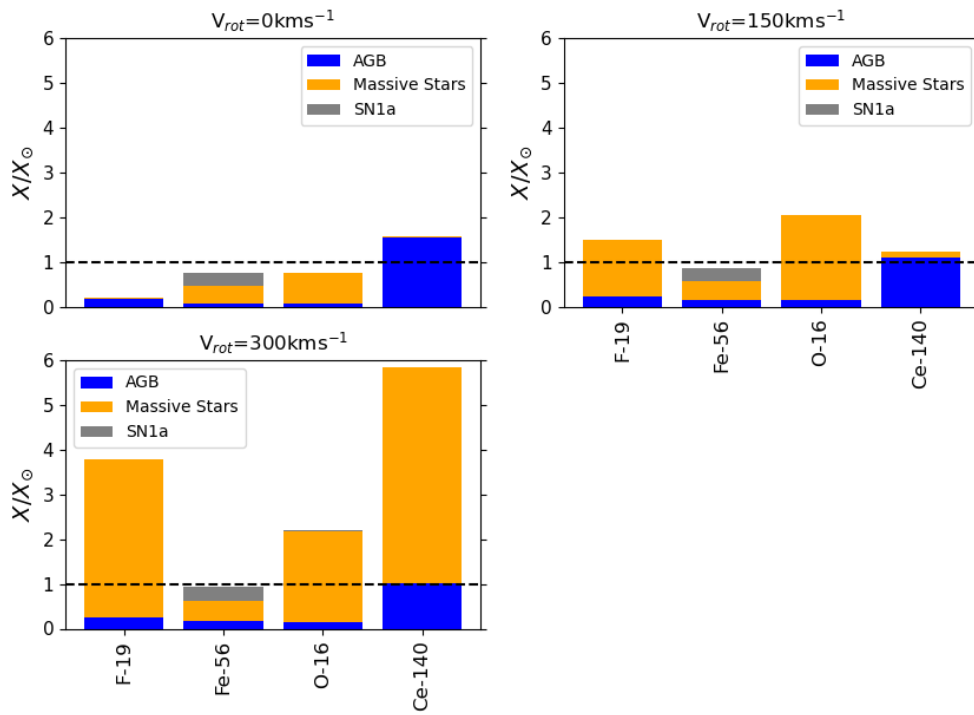


Figure 3.8: The contribution to each isotope from each stellar source relative to solar at $[Fe/H] = 0$ for models *CLC000* (top left), *CLC150* (top right) and *CLC300* (bottom). The contribution from massive stars is show in orange, AGB stars in blue and SNe Ia in grey.

solar metallicity are not physical, suggesting that a mix of massive star models with different v_{rot} should be assumed. The mix of rotational velocity we might expect will be discussed in the following section.

3.5 Discussion

At low metallicity, most red giants in the sample of [Lucatello et al. \(2011\)](#) are classified as CEMP-s, hence they likely had their surface fluorine abundances altered by binary mass transfer from an AGB companion. In Figs. [3.1a - 3.5](#) we also show CEMP-no stars, whose origin in the Milky Way halo is less clear. Our model predictions at low metallicity can solely be used as a baseline for the average ISM abundances at the point of birth of the stars, before any binary accretion has occurred, providing an empirical constraint on the degree of fluorine-enhancement for AGB stellar models. There is also a larger spread in the observed chemical abundance patterns at $[\text{Fe}/\text{H}] < -2.5$, which indicates a more inhomogeneous ISM at low metallicity, as stars formed out of gas enriched by a smaller number of CCSNe, whereas our models assume that the ISM is well mixed at all times, with the IMF being fully sampled starting from the turn-off mass. An additional source of scatter in the chemical abundances at $[\text{Fe}/\text{H}] < -2.5$, which is not included in our models, might be due to the fact that the Milky Way halo comprises several populations of stars that were born in different substructures and were later accreted by our Galaxy. We also note again that the observations in the metallicity range $-3.4 < [\text{Fe}/\text{H}] < -2.3$ are upper limits with a lot of dispersion. All this leads to uncertainty in our conclusions at $[\text{Fe}/\text{H}] < -2$.

At super-solar metallicity, there is a secondary behaviour of fluorine ([Ryde et al., 2020](#)). However, we must be careful about comparing our models to observations at this metallicity for a number of reasons. The first being that we do not have fluorine yields at super-solar metallicity, instead at $[\text{Fe}/\text{H}] > 0$ the model copies the yields from the final metallicity until the end of the simulation (when the age of the galaxy is 13 Gyr). Secondly, stars with super-solar metallicity are known to have formed in the inner disk and migrated so their composition is different to that of the local gas (see figure 10 of [Vincenzo & Kobayashi 2020](#) for an illustration of this). Therefore, the abundances of super-solar metallicity stars cannot be compared with a

one-zone model. Though we do not make strong conclusions about the evolution of fluorine above $[\text{Fe}/\text{H}] = 0$, these considerations should be kept in mind.

The models using massive stars with initial rotational velocities of 300 km s^{-1} are the only ones to reproduce both the slight downward trend of $[\text{F}/\text{s}]$ at low metallicity and upward trend of $[\text{F}/\text{s}]$ at high metallicities. Therefore, we need a contribution from rapidly rotating massive stars with initial rotational velocities of 300 km s^{-1} throughout the evolution of the Galaxy in order to match the full abundance pattern. Though models *CLC300* and *MonLC300* do not match the full abundance trend of the observations in the $[\text{F}/\text{Fe}]$ versus $[\text{Fe}/\text{H}]$ space (Figure 3.1a), there are many considerations to be made including the fact that the low metallicity observations are upper limits so there is a chance that those observations could sit lower than where they are placed, and we expect fewer massive stars rotating that quickly at higher metallicities (see [Meynet & Maeder 1997](#), [Prantzos et al. 2018](#)). Therefore, we should explore the possibility of a mix of initial rotational velocities, where stars with v_{rot} in the range $150\text{--}300 \text{ km s}^{-1}$ contribute throughout the evolution of the Galaxy. [Romano et al. \(2019\)](#) assumed a sharp transition for massive star rotation where massive stars have $v_{\text{rot}} = 300 \text{ km s}^{-1}$ for $[\text{Fe}/\text{H}] < -1$ and, suddenly, $v_{\text{rot}} = 0$ for $[\text{Fe}/\text{H}] \geq -1$. Meanwhile, [Rizzuti et al. \(2019\)](#) studied the rotating massive star yields of both [Frischknecht et al. \(2016\)](#) and [Limongi & Chieffi \(2018\)](#) compared with observations of the s-process elements Sr and Ba, agreeing that massive star rotational velocity varying as a function of metallicity is valid and effective in reproducing the observations. They suggest the nucleosynthesis of [Limongi & Chieffi \(2018\)](#) can be used by assuming initial massive star rotational velocity of 150 km s^{-1} at metallicities of $[\text{Fe}/\text{H}] < -2$ and very little or zero rotation above this metallicity. This strategy of a sharp change in initial rotational velocity at a given low metallicity is not appropriate for the situation we have here, as a contribution from models with v_{rot} in the range $150\text{--}300 \text{ km s}^{-1}$ needs to be assumed even above $[\text{Fe}/\text{H}] = -1$. Given we know that at higher metallicities massive stars should rotate more slowly, perhaps a combination of rotational velocities are present at higher metallicities, much like the approach employed by [Prantzos et al. \(2018\)](#).

The mixed-rotation scenario of [Prantzos et al. \(2018\)](#) assumes that rotating massive stars with $v_{\text{rot}} = 300 \text{ km s}^{-1}$ cease to contribute to the yields at around $[\text{Fe}/\text{H}] \approx -2$, failing to

reproduce the observed trend of $[F/s]$ as a function of $[Fe/H]$ (see model *CLCmix* in Figure 3.4). Therefore, a different combination of rotating massive star models needs to be employed, by including a metallicity-dependent contribution from models with $v_{\text{rot}} = 150 \text{ km s}^{-1}$ and 300 km s^{-1} up to solar metallicity. Figure 3.8 shows the contributions of each rotational velocity to the isotopes ^{19}F , ^{56}Fe , ^{16}O and ^{140}Ce relative to solar for models *CLC000*, *CLC150* and *CLC300* at $[Fe/H] = 0$. Model *CLC000* predicts $X(^{19}\text{F})/X_{\odot}(^{19}\text{F}) = 0.2$ and $X(^{140}\text{Ce})/X_{\odot}(^{140}\text{Ce}) = 1.5$, model *CLC150* predicts $X(^{19}\text{F})/X_{\odot}(^{19}\text{F}) = 1.4$ and $X(^{140}\text{Ce})/X_{\odot}(^{140}\text{Ce}) = 1.2$ and model *CLC300* predicts $X(^{19}\text{F})/X_{\odot}(^{19}\text{F}) = 3.7$, and $X(^{140}\text{Ce})/X_{\odot}(^{140}\text{Ce}) = 5.8$, at $[Fe/H] = 0$. In order to reproduce the fluorine solar abundance, we need to achieve $X(^{19}\text{F})/X_{\odot}(^{19}\text{F}) = 1.0$. This can be done with a 45% contribution from $v_{\text{rot}} = 0 \text{ km s}^{-1}$, a 50% contribution from $v_{\text{rot}} = 150 \text{ km s}^{-1}$ and a 5% contribution from $v_{\text{rot}} = 300 \text{ km s}^{-1}$. When employing these contributions, we achieve $[F/Fe] = 0.08$, $[F/O] = -0.033$ and $[F/s] = -0.45$. These percentage contributions are our suggestion for a mix of rotational velocities that are successful at reproducing fluorine abundances at solar metallicity. It is difficult to make a suggestion for combinations at other metallicities as we do not have a constraint for the abundances. We must be careful when suggesting a combination of rotational velocities as there are uncertainties in the yields that we must be aware of. Firstly, a change in the implementation of rotation may change the yields of elements affected by rotation. As discussed by Prantzos et al. (2018), another uncertainty associated with the Limongi & Chieffi (2018) yields in particular is the enhancement of fluorine in the $15 M_{\odot}$ and $20 M_{\odot}$ models with $v_{\text{rot}} = 150 \text{ km s}^{-1}$. In these models, a smaller He convective shell forms separately to the main He convective shell. When these two shells merge, the base of the new shell is deeper and thus, is exposed to higher temperatures which causes an enhancement in fluorine production. It is pointed out by Prantzos et al. (2018) that it is difficult to know if this scenario is ‘realistic’ given it only affects two of the stellar models. Other uncertainties such as reaction rates and nuclear networks will be discussed later in this work.

It has been proposed that a contribution from novae is needed in order to match the observed behaviour of $[F/O]$ versus $[O/H]$ (e.g. Timmes et al. 1995, Spitoni et al. 2018). The majority of the models in this work (*CLCmix*, *CLC150*, *CLC300*, *Mon18 LCmix*, and

MonLCmix) can reproduce the trends of [F/O] versus [O/H] without including any chemical enrichment of fluorine from novae (see Figure 3.1b). Therefore, it could be argued that we no longer need a contribution from novae to understand the chemical evolution of fluorine. That being said, it is important to understand the fluorine yields we might expect from novae and the consequences that could have on our results. It is unclear from the literature both how frequent the occurrence of novae are and the fluorine yields we might get from them. Kawash et al. (2021) suggests a nova rate of $\approx 30 \text{ yr}^{-1}$ while Shafter (2017) suggests a nova rate of $\approx 50 \text{ yr}^{-1}$ and recent results from Rector et al. (2022) suggest a rate of $\approx 40 \text{ yr}^{-1}$, however this result is for M31 rather than the Milky Way. Both Spitoni et al. (2018) and Grisoni et al. (2020) used the nova yields as predicted by José & Hernanz (1998), who found that fluorine is only significantly synthesised in their $1.35 M_{\odot}$ model, with a maximum yield of $5.4 \times 10^{-5} M_{\odot}$ and a minimum yield of $9.9 \times 10^{-7} M_{\odot}$. This gives a range of potential ^{19}F nova production rate that varies between $2.97 \times 10^{-5} M_{\odot} \text{ yr}^{-1}$ and $2.7 \times 10^{-3} M_{\odot} \text{ yr}^{-1}$. The upper bound here is so high due to the significant yield from the $1.35 M_{\odot}$ model. This wide range makes the contribution of novae to the galactic fluorine very uncertain. However, we can compare the potential nova yields to the yields we might expect from CCSNe. The CCSNe rate is variable with time in our model with an average rate of 0.025 yr^{-1} . The minimum ^{19}F yield from the Limongi & Chieffi (2018) massive star yields with $v_{\text{rot}} = 300 \text{ km s}^{-1}$ is $1.027 \times 10^{-5} M_{\odot}$ and the maximum is $1.025 \times 10^{-3} M_{\odot}$. This yields a potential range of ^{19}F production rate from CCSNe between $2.57 \times 10^{-7} M_{\odot} \text{ yr}^{-1}$ and $2.56 \times 10^{-5} M_{\odot} \text{ yr}^{-1}$. This range is lower than that of the potential nova yields. However, we must be aware that only the $1.35 M_{\odot}$ nova model is enhanced in fluorine, so there is the potential for the range of fluorine yield from novae to be lowered given that the enhancement only occurs at this one particular mass. Starrfield et al. (2020) looked at ^{19}F ejecta from novae for a $1.35 M_{\odot}$ star and found a range of $6.3 \times 10^{-11} M_{\odot}$ to $1.0 \times 10^{-6} M_{\odot}$, again demonstrating how uncertain fluorine yields from novae can be. Overall, we recognise that novae may indeed contribute to the galactic fluorine, though the yields are highly uncertain and several critical assumptions need to be made to include them in chemical evolution models, however, they are not required to reproduce the observational abundance patterns in this work.

3.5.1 Wolf-Rayet stars as a significant source of fluorine?

When massive stars rotate, they can, even if only for a brief period, enter into a Wolf-Rayet phase. Given that WR winds have been suggested as a dominant contributor to the chemical evolution of fluorine (Meynet & Arnould 2000, Renda et al. 2004), it is important to disentangle what portion of the rotating massive star yields comes from WR winds and what portion comes from the CCSN at the end of their evolution.

Meynet & Arnould (2000) found that WR stars could contribute significantly to the galactic fluorine content by calculating a series of WR yields and incorporating them in a chemical evolution model for the Milky Way. They found that the ^{19}F wind yield of a $60 M_{\odot}$ model could be a factor of 10-70 times higher than the initial stellar content of ^{19}F . These fluorine yields were subsequently used in the chemical evolution study of Renda et al. (2004), who explored three different scenarios for the nucleosynthesis of fluorine by using the chemical evolution code GEtool (Fenner & Gibson 2003, Gibson et al. 2003). The first scenario explored by Renda et al. (2004) used solely yields from CCSNe, the second CCSNe and WR stars, and the third used CCSNe, WR and AGB stars. Renda et al. (2004) concluded that, while AGB stars dominate fluorine production at low metallicity, WR stars are the dominant source of fluorine at solar and super-solar metallicities (see their figure 4). In the years since, many more massive star models have been created which include WR yields. This begs the question, do any of these studies find ^{19}F yields as high as those found by Meynet & Arnould (2000)?

Figure 3.9 shows a comparison of massive star wind yields from a variety of studies over the last couple of decades. The yields that are compared in the figure are from Limongi & Chieffi (2018), Ritter et al. (2018c), Brinkman et al. (2021); Brinkman (2022), Meynet & Arnould (2000), Ekström et al. (2012) and Sukhbold et al. (2016). Here, we look at non-rotating stars at solar metallicity in order to gain the widest comparison and to be able to compare with the non-rotating yields of Meynet & Arnould (2000). We can see that all considered wind yields sit at least 1 dex below the the Meynet & Arnould (2000) yields. This suggests that perhaps the Meynet & Arnould (2000) ^{19}F wind yields are unusually high compared to subsequent models. Therefore, there is potential that we may be able to rule out

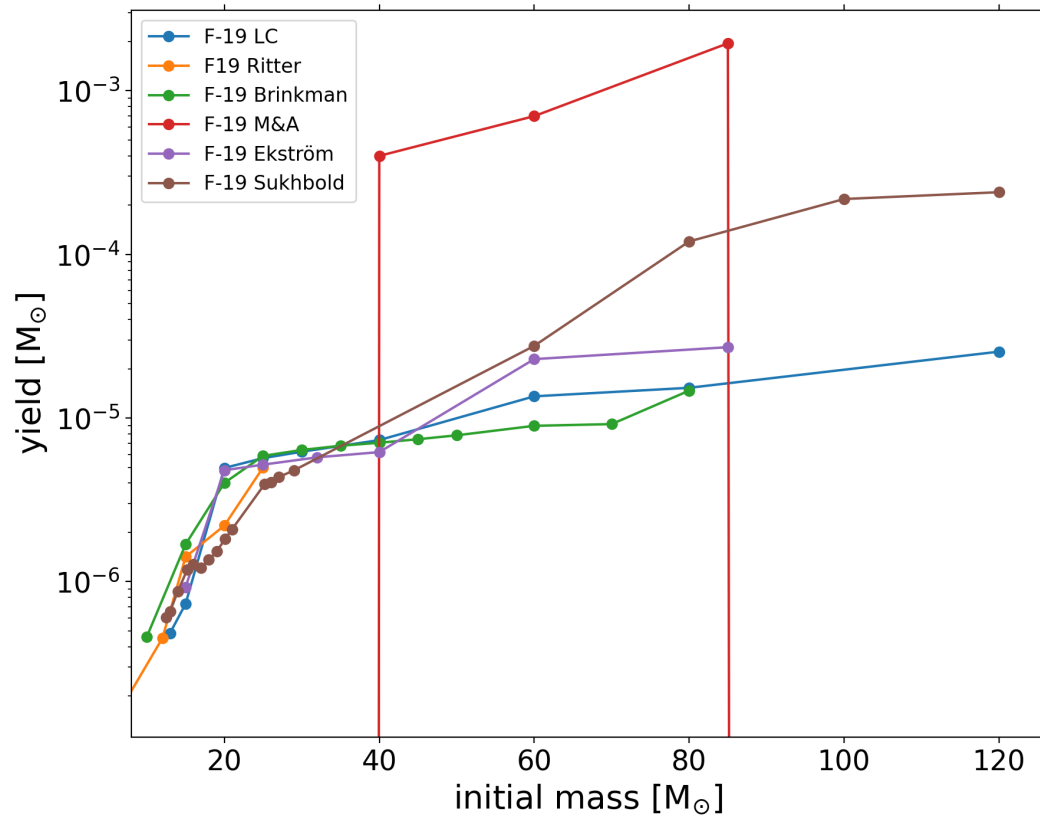


Figure 3.9: Non-rotating, solar metallicity wind yields from a range of studies over the last two decades. LC = Limongi & Chieffi (2018), Ritter = Ritter et al. (2018c), Brinkman = Brinkman et al. (2021); Brinkman (2022), M&A = Meynet & Arnould (2000), Ekström = Ekström et al. (2012), Sukhbold = Sukhbold et al. (2016)

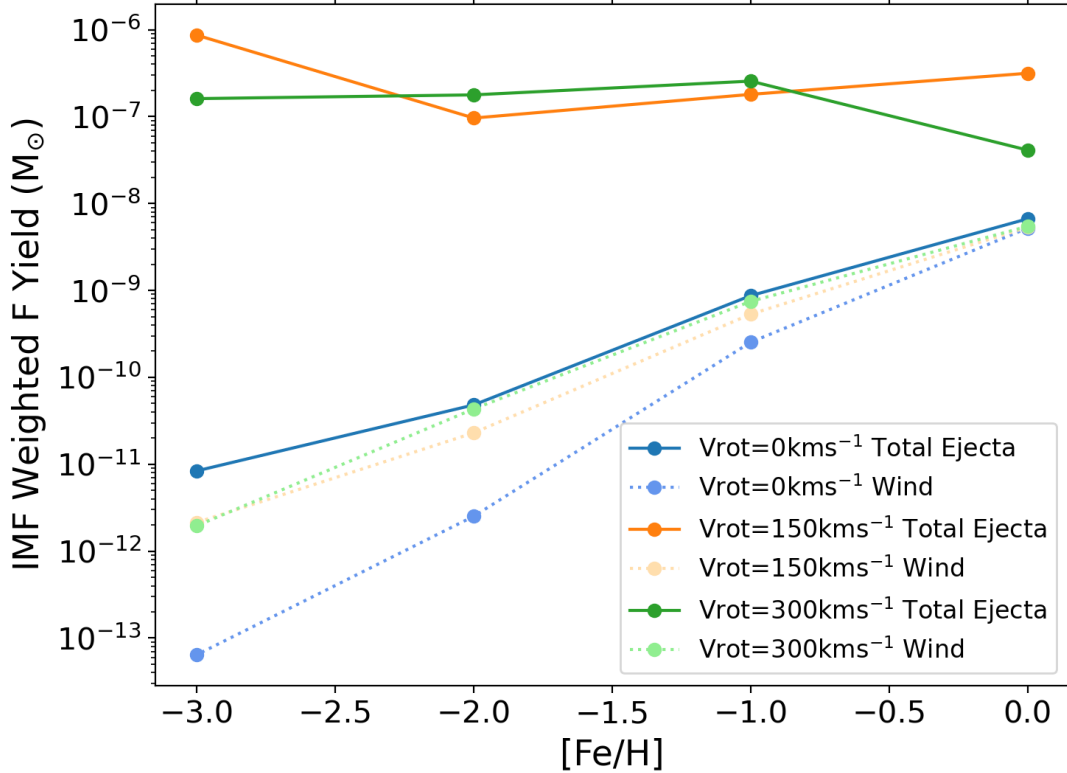


Figure 3.10: IMF weighted fluorine yield as a function of metallicity ($[\text{Fe}/\text{H}]$) for each rotational velocity prescription. The total yields are shown by a full line and darker colour while the wind yields are represented by dotted lines and lighter colours.

WR stars as a dominant contributor to the galactic fluorine budget.

To investigate this further, Figure 3.10 shows the IMF-weighted yield versus metallicity for the [Limongi & Chieffi \(2018\)](#) massive star yields used in this work. Here we see a comparison between the wind yield and the total ejecta for each rotational velocity. At low metallicity, the wind yields sit 4-6 dex lower than the total ejecta for the rotating models and around 2 dex lower for the non-rotating model. At higher metallicities, the gap between the wind contribution and total ejecta reduces due to enhanced mass loss, with the wind yields being around 2 dex lower than the total ejecta for the model rotating at 300 km s^{-1} and 1 dex lower for the model rotating at 150 km s^{-1} . For the non-rotating model, the yields are almost identical at high metallicity.

We conclude that we need a large contribution from rapidly rotating massive stars in order

to reproduce observations of fluorine in the Milky Way across the whole metallicity range. For $v_{\text{rot}} = 300 \text{ km s}^{-1}$, wind yields contribute a factor of around 10^{-2} less fluorine at high metallicities ($[\text{Fe}/\text{H}] \geq 0$) and a factor of around 10^{-6} less fluorine at the lowest metallicity ($[\text{Fe}/\text{H}] = -3$) than the explosive yield, for $v_{\text{rot}} = 150 \text{ km s}^{-1}$ wind yields contribute a factor of around 10^{-1} less fluorine at high metallicities and a factor of around 10^{-6} less fluorine at the lowest metallicity. We can, therefore, rule out Wolf-Rayet stars as a dominant source of fluorine. Being able to draw such conclusions is vital in untangling the web of possibilities for the origin and chemical evolution of fluorine.

3.5.2 Sources of Uncertainty in GCE

Like for any physical model, it is important to consider that there can be significant uncertainties concerning galactic chemical evolution (GCE) studies (e.g., [Romano et al. 2005, 2010](#)). For example, each choice for the parameters in [Table 3.1](#) can affect the behaviour of the chemical evolution models. [Côté et al. \(2016\)](#) explored some sources of GCE uncertainty, including: the IMF, DTD and number of SNe Ia, current stellar mass and star formation history.

We briefly explored the effect of changing both the IMF and the star formation efficiency of the models on our results. We found that:

1. using a [Kroupa et al. \(1993\)](#) IMF rather than [Kroupa \(2001\)](#) does not drastically change the results of the chemical evolution trends. Using the [Kroupa et al. \(1993\)](#) IMF produces more fluorine at lower metallicities which can produce a slightly better fit for $[\text{F}/\text{Fe}]$ versus $[\text{Fe}/\text{H}]$ trends but provides an overproduction of $[\text{F}/\text{O}]$ as a function of $[\text{O}/\text{H}]$ for the models which use the [Limongi & Chieffi \(2018\)](#) yields. However, a better fit to the observations is achieved by the model including the massive star yields of [Nomoto et al. \(2013\)](#).
2. using a higher star formation efficiency naturally exhausts the available gas more quickly, and thus does not produce as much fluorine at higher metallicities whereas a lower star formation efficiency sees a late increase in $[\text{F}/\text{Fe}]$. However, the shape of the chemical evolution trend is not significantly affected.

Another major source of uncertainty in GCE studies are the yield sets used (see, e.g., [Gibson 1997](#); [Mollá et al. 2015](#)). Each author will use a different code for stellar modelling which will in turn use a different reaction network. A reaction network specifies the reactions that will occur in a model and the rates at which such reactions will occur. Different modelling choices made by each author produce a layered effect when it comes to the uncertainty provided by stellar yields in chemical evolution modelling.

To better understand reaction rate uncertainties in the context of this work, we will look at the two reactions that can destroy fluorine: $^{19}\text{F}(\alpha, p)^{22}\text{Ne}$ and $^{19}\text{F}(p, \alpha)^{16}\text{O}$.

1. The most recent work on $^{19}\text{F}(p, \alpha)^{16}\text{O}$ was performed by [Zhang et al. \(2021b\)](#). By reanalysing experimental data, they found drastically different $^{19}\text{F}(p, \alpha)^{16}\text{O}$ rates than those recommended by the Nuclear Astrophysics Compilation of Reaction Rate (NACRE) ([Angulo et al., 1999](#)). They found rates larger by factors of 36.4, 2.3 and 1.7 for temperatures 0.01, 0.05 and 0.1 GK respectively. This increased rate naturally leads to the destruction of ^{19}F on a scale larger than previously thought. By performing a network calculation at solar metallicity with their recommended new rate for the reaction, the value of ^{19}F decreased by up to one order of magnitude. This reaction was directly measured by [Zhang et al. \(2021a\)](#) using the Jinping Underground Nuclear Astrophysics (JUNA) experimental facility. Though the rate they found deviated from the previous value by a factor of 0.2-1.3, it is still significantly higher than the accepted rate of [Spyrou et al. \(2000\)](#). Therefore, we will still expect a larger depletion of fluorine at solar metallicity using this reaction rate.
2. The most recent work to study $^{19}\text{F}(\alpha, p)^{22}\text{Ne}$ is [Palmerini et al. \(2020\)](#), who focused on the role that this reaction takes in AGB stars in particular. They found that during thermal pulses, ^{19}F can be easily destroyed by α -captures; in particular for a $5 M_{\odot}$ AGB star ^{19}F can be destroyed by a factor of 4.

These new discoveries related to the reactions that destroy fluorine could have implications for this work. If indeed, the destruction of fluorine is more enhanced in AGB stars than previously thought, the chemical evolution of fluorine at higher metallicities could be affected. The point

at which AGB stars begins to be significant is model dependent. For model *CLC300*, Figure 3.6 shows us that AGB stars begin to be significant in the production of fluorine around solar metallicity. Therefore, we might expect that the [F/Fe], [F/O] and [F/s] ratios studied in this work decrease from [Fe/H] = 0. Whether these reaction rates will also have a significant impact in the destruction of fluorine in rotating massive stars remains to be seen.

Uncertainties around reaction rates are a large source of uncertainty in stellar modelling and the yields we retrieve from those models. All this must be kept in mind when studying galactic chemical evolution. Especially given how uncertain each source's contribution to the galactic fluorine is, uncertainties around reaction rates add another piece to this complex puzzle.

3.6 Conclusions

We have studied the chemical evolution of fluorine in the Milky Way. We have used a range of yield sets to try to understand the dominant contributor to the galactic fluorine budget. In order to do this we compared our chemical evolution models to abundance determinations across a wide range of metallicities. The main conclusions of this work are as follows:

1. We investigated many combinations of yields with different prescriptions for the rotation of massive stars. Though we are limited by upper limits and poor statistics in the low metallicity regime, we found that in order to reproduce fluorine abundances across the whole metallicity range ($-3.4 < [\text{Fe}/\text{H}] < 0.4$), we need a contribution from rapidly rotating massive stars with initial rotational velocities as high as 300 km s^{-1} . We agree with the results of [Prantzos et al. \(2018\)](#) and [Grisoni et al. \(2020\)](#) that rotating massive stars play a crucial role in the fluorine production up to solar metallicities. We also suggest a combination of initial rotational velocities which can reproduce solar abundances.
2. We have investigated the contribution of massive star and WR winds to the galactic fluorine budget. We compared the winds of more recent massive star models to the winds of [Meynet & Arnould \(2000\)](#) and found that we expect to see significantly less fluorine in wind yields than we did 20 years ago.

3. From the initial study of wind yields, we then looked at the fluorine yields from the winds of the massive stars used in our chemical evolution models. We found that the wind yield can be up to six times lower than the ejecta from the core collapse. Thus, we have ruled out WR winds as a dominant contributor to the galactic fluorine.
4. We can rule out novae as an important source of galactic fluorine. Our models can successfully reproduce the observational pattern in $[F/O]$ versus $[O/H]$ space and as such we do not need a contribution from novae that others required in order to reproduce the pattern.
5. These conclusions, especially those related to the low metallicity regime, could be made stronger by additional observations of fluorine at low metallicity.

To conclude, our study into the chemical evolution of fluorine in the Milky Way has found that rapidly rotating massive stars are the dominant contributor to fluorine. We still need a contribution from AGB stars from $[Fe/H] \approx -1$. We have now been able to rule out Wolf-Rayet stars and novae as a significant contributor to the chemical evolution of fluorine.

4. Chemical evolution of Phosphorus in the Milky Way with a Focus on Phosphorus-Rich Stars

The theoretical aspects of the research findings presented in this chapter have been published in *Astronomy & Astrophysics* as [Brauner et al. \(2023\)](#). In particular, I contributed GCE modelling and analysis to section 5 of [Brauner et al. \(2023\)](#), which is the basis of what is presented here.

4.1 Introduction

Phosphorus, along with carbon, nitrogen, oxygen and sulphur, is an element that is key for life on Earth. It is important to understand the origin and evolution of phosphorus in nature as it plays a role in both DNA and in the exchange of energy to cells (e.g. [Gulick 1955](#)). Though this element is important scientifically, there is limited research on its origin and evolution. Our limited knowledge of this element is partly due to a difficulty obtaining observations. P_I absorption features in stellar spectra are intrinsically weak and therefore hard to detect (e.g. [Caffau et al. 2011](#)). Therefore, we do not have large stellar samples with which to compare our chemical evolution models so it is hard to draw meaningful conclusions about the evolution of phosphorus with current information.

Phosphorus has only one stable isotope (³¹P) and is primarily produced via neutron captures onto silicon during the carbon, oxygen and neon burning phases in massive stars ([Woosley et al. 2002](#); [Pignatari et al. 2016](#)). The P produced during these thermonuclear burning phases is subsequently ejected when the star eventually explodes as a core-collapse supernova. The explosive nucleosynthesis which occurs during CCSNe is not thought to contribute significantly to the overall phosphorus yield of the massive star progenitor ([Woosley & Weaver, 1995](#)), while the P yield from Type Ia supernovae ([Leung & Nomoto, 2018](#)) and from AGB stars is not expected to be significant ([Karakas & Lugaro, 2016](#)). Hence, galactic

chemical evolution studies tend to focus on the contribution of the massive star yields when modelling.

Most chemical evolution studies under-predict $[P/Fe]$ compared to observations. [Cescutti et al. \(2012\)](#) requires the P yield of the massive stars used in their models (these are the yields of [Woosley & Weaver 1995](#) and [Kobayashi et al. 2006](#)) to be multiplied by a factor of 3 in order to match the observations of [Caffau et al. \(2011\)](#) at all available metallicities in the galactic disc. Meanwhile, [Prantzos et al. \(2018\)](#) also underproduce P in the solar neighbourhood compared to observations ([Caffau et al. 2011](#), [Maas et al. 2017](#)), though including rotating massive stars does increase the $[P/Fe]$ ratio. However, the observational data they compare with is sparse compared to the data available for other elements in their study, with only minimal data around $-0.8 < [Fe/H] < 0.2$ so it is hard to draw strong conclusions. This underproduction, especially at sub-solar metallicities is reported by a number of authors (e.g. [Caffau et al. 2011](#), [Roederer et al. 2014](#), [Jacobson et al. 2014](#), [Maas et al. 2019](#)). However, [Kobayashi et al. \(2020\)](#) were able to reproduce the observations of $[P/Fe]$ ([Caffau et al. 2011](#), [Roederer et al. 2014](#), [Caffau et al. 2016](#)) in the solar neighbourhood with their chemical evolution model, using AGB yields primarily from the Monash group ([Lugaro et al. 2012](#), [Fishlock et al. 2014](#), [Karakas et al. 2018](#) and [Karakas & Lugaro 2016](#)) and massive star yields from [Kobayashi et al. \(2006\)](#) and [Kobayashi et al. \(2011a\)](#). The massive star yields used in [Kobayashi et al. \(2020\)](#) have the added source of hypernovae (HNe), these are CCSNe which have an explosion energy more than ten times that of regular supernovae, resulting in an increased production of iron and α elements. The fraction of HNe is set at 50 % for stars with $M \geq 20 M_{\odot}$, there is also a metallicity dependence with the fraction of HNe decreasing as metallicity increases. Though [Kobayashi et al. \(2020\)](#) are able to reproduce $[P/Fe]$ abundances, it should be noted that the number of observations used by [Kobayashi et al. \(2020\)](#) for comparison was still sparse, with many upper limits.

Phosphorus exhibits behaviour of a secondary element in massive stars (i.e. an element whose production requires an abundance of seed nuclei in order to be synthesised in a star). This secondary-like behaviour may explain why it is difficult for massive star models to produce sufficient P to match observations at sub-solar metallicities (e.g. [Goswami & Prantzos 2000](#)).

Recently, [Nandakumar et al. \(2022\)](#) showed that the behaviour of P is more consistent with α -element production in massive stars. This may suggest, contrary to the findings of [Woosley & Weaver \(1995\)](#), that CCSNe explosions indeed contribute to the overall phosphorus yield.

[Ritter et al. \(2018b\)](#) showed that a merger between the convective carbon and convective oxygen shells in massive stars, known as a CO shell merger, may increase the P yield (as well as other odd-Z elements) in the massive star and thus in the CCSNe ejecta. Initial GCE modelling using massive star yields with a CO shell merger suggests they could boost the [P/Fe] ratio to match or even overproduce compared to typical observations. However, the full impact of CO shell mergers on GCE is unknown it depends upon the frequency and nature of the shell mergers ([Griffith et al., 2021](#)).

Understanding the evolution of P became even more complex when P-rich stars were first identified by [Masseron et al. \(2020a\)](#). A group of 15 stars with $[P/Fe] \geq 1.2$ were discovered in the APOGEE-2 data release 14 (DR14) set ([Abolfathi et al., 2018](#)). These objects also appeared to be rich in O, Mg, Al, Si and Ce. GCE models already failed to reproduce ‘normal’ [P/Fe] ratios, therefore reproducing the abundances of stars enhanced in P as well as many other elements posed a problem. The stars in the sample are low mass giants, therefore [Masseron et al. \(2020a\)](#) suggested the P-rich stars did not produce the enhanced surface elemental abundances (including the P abundances) themselves and the abundance likely came from a progenitor which polluted the ISM out of which the stars were born, i.e. the abundances have arisen from local high inhomogeneity in the nucleosynthesis sources.

A detailed abundance pattern (including heavy elements) for two P-rich stars, one of which was from the original sample and the other newly identified, was analysed in detail by [Masseron et al. \(2020b\)](#). To find an origin for the enhanced P of the two stars, they compared the abundance patterns to a number of objects: two CH stars (with abundances of s-process origin), a CEMP-r/s star (enhanced in s-process and r-process elements due to mass transfer) and a metal-poor star with r-process element enhancement. After this comparison, they ultimately concluded that the abundance patterns of the P-rich stars could not be explained but could be as a result of new mode of operation for the s process. [Masseron et al. \(2020a\)](#) proposed the peculiar chemistry of P-rich stars could be explained by massive star rotation or

by CO shell mergers. We will explore this idea using GCE modelling later in this work.

The work of [Womack \(2021\)](#) proposed and investigated in detail the idea that the enhanced [P/Fe] in the two objects discussed above (2M13535604+4437076 and 2M22045404-1148287) could be as a result of i-process (intermediate neutron capture process) nucleosynthesis. The i process is a neutron capture process which occurs at intermediate neutron densities ($n \approx 10^{12} - 10^{15} \text{ cm}^{-3}$) to the s and r processes ([Cowan & Rose, 1977](#)), resulting in abundance patterns distinct from those which arise via the s or r process. The abundance patterns of Carbon Enhanced Metal Poor r/s (CEMP-r/s) stars are thought to arise from the i process as they display both enhanced s-process elements and an enhancement in europium, typically an r-process signature ([Hampel et al., 2016](#)). Hence, this could be the ‘new mode’ of operation of the s process that [Masseron et al. \(2020b\)](#) proposed to explain the P-rich stars abundance patterns. [Womack \(2021\)](#) compared both an AGB intershell model and a rapidly accreting white dwarf (RAWD) model, both promising sites for i-process nucleosynthesis (e.g. [Hampel et al. 2016](#), [Hampel et al. 2019](#), [Denissenkov et al. 2017, 2019](#)), to the abundance patterns of the two objects. Using ppn (post processing network), a code produced by the NuGrid collaboration ([Herwig et al., 2009](#)), the intershell region of a $1.65 M_{\odot}$ AGB star with metallicity, $Z = 1 \times 10^{-4}$ ($[\text{Fe}/\text{H}] \approx -2.26$) was modelled. The mass fractions of ^1H and ^{12}C were 0.0104 and 0.37 respectively. While, the RAWD model is model F of [Denissenkov et al. \(2019\)](#), which was created using the MESA stellar evolution code ([Paxton et al., 2011, 2013](#)) and post-processed by the NuGrid code mppnp ([Pignatari et al., 2016](#)). [Womack \(2021\)](#) found neither model could fully explain the abundance pattern of either of the two objects. For 2M13535604+4437076 neither model was able to reproduce the the abundances of all the s-process peak elements nor the unusually high P abundance. Therefore, [Womack \(2021\)](#) concluded that the abundances of this object are likely as a result of an unusual mode of the s process, in line with previous findings. For 2M22045404-1148287, the high P could be reproduced by both models. However, the RAWD model could not reproduce the most heavy element abundances. While, the AGB intershell model could reproduce the heavy element abundance pattern fairly well, with the exception of Ba, though the light element abundance pattern could not be replicated. In order to replicate all aspects of the abundance pattern,

Womack (2021) used a double i-process exposure using the AGB intershell model (see figure 5 in Koch et al. 2019) and found a statistically better fit to the observed abundances, as well as maintaining the enhancement in phosphorus.

Multi-object spectroscopic surveys have allowed us to determine the abundances of a large number of stars. This study uses data gathered in the infrared from the Apache Point Observatory Galactic Evolution Experiment (APOGEE) (Majewski et al., 2017) with the aim of finding a potential progenitor scenario for P-rich stars, improving our understanding of P production in the Milky Way. To follow this aim, we will compare models of galactic chemical evolution to both P-normal and P-rich stars. Section 4.2 details the observational samples used in this study and how the P-rich sample was selected, section 4.3 lays out the chemical evolution model and stellar yields we use, section 4.4 compares the observations with the models, in section 4.5 we set our results in context and in section 4.6 we conclude and look toward future work in this area.

4.2 Observational Data

This work uses two samples of stars, one has typical [P/Fe] and one has enhanced [P/Fe], we will call these the P-normal and P-rich samples, respectively. The P-normal sample is made up of main sequence solar neighbourhood stars from the Hypatia catalogue (Hinkel et al., 2014). The P-rich sample is data selected from the APOGEE survey (e.g. Majewski et al. 2017) and its extension APOGEE-2 (Blanton et al., 2017), here we use DR17 (Abdurro'uf et al., 2022). The detailed selection process for the P-rich sample is laid out in Brauner et al. (2023). However, the key elements of the selection process are described in the below section.

4.2.1 Sample selection

To put together a sample of P-rich stars, we first had to identify good candidates for P enhancement. The initial sample of P-rich stars are also enriched in Si suggesting they could form part of a larger Si rich population. Therefore, good candidates for P enhancement arise in the form of the Si rich sample ($[\text{Si}/\text{Fe}] \geq 0.5$) identified by Fernández-Trincado et al. (2019, 2020). After filtering out some stars with a potential binary companion, a sample of 53 Si-rich

stars become our first set of P-rich candidates. We add to the sample of P-rich candidate stars by also including the initial sample of 16 (Masseron et al., 2020a,b), bringing the total number of candidate objects to 69.

The elemental abundances of our stellar sample were derived using the *Brussels Automatic Code for Characterizing High accuracy Spectra* (BACCHUS, Masseron et al. 2016). The input data for the code are the APOGEE-DR17 spectra downloaded from the Sloan Digital Sky Survey (SDSS-IV) science archive server together with the calibrated parameters and abundances derived from the APOGEE Stellar Parameters and Chemical Abundance Pipeline (ASPCAP). For a full breakdown of how the synthetic spectra are obtained, the selection and processing of the spectral lines and determination of their uncertainties see section 3 of Brauner et al. (2023).

We obtain another set of candidates by utilising the Value Added Catalogue (VAC) called *BACCHUS analysis of Weak Lines in APOGEE Spectra* (BAWLAS, Hayes et al. 2022). This VAC explores elemental species with weak and blended lines (like P) and calculates their abundances using the BACCHUS code. This candidate selection process generated a total of 87 P-rich candidates for our chemical abundance analysis.

After analysing the spectra and calculating the stellar abundances, some stars in the sample were determined not to be P-rich. Out of the initial sample of 87, nine were excluded leaving a final sample of 78 P-rich ($[P/Fe] > 0.8$) giant stars. It should be noted here that P-rich stars in DR17 were not systematically searched for as Masseron et al. (2020b) did to get the initial sample from DR14, therefore we can regard this number as a lower limit with the expectation that there are more undiscovered P-rich stars present in DR17. Section 4.1 of Brauner et al. (2023) gives more detail on other features of the sample, as well as an overview of the objects that were rejected from the sample and why.

4.2.2 Notable features of the P-rich sample

Later on in this Chapter, we will discuss not only the abundance of P but also the abundance of other significant elements. Therefore, it is important to note some other key features of the sample related to the abundance of the α elements O, Mg, S and Si.

The O and Si abundances of the P-rich sample are enhanced compared with a background sample of field stars. The background sample was selected to have similar stellar parameters as the P-rich candidate stars so that a reasonable comparison can be made. There is also a slight enhancement in Mg compared with the background sample, however a clear overall enhancement in Mg for the P-rich stars is not observable within the error. S is not enhanced in the P-rich sample, which is surprising given that the production of S and Si is closely linked so we would expect that where Si is enhanced, so too is S but this is not the case. However, we must take the S abundance of the sample with caution as S lines in metal poor stars are subject to blends and temperature dependencies, making the calculated abundances potentially unreliable.

There are also some correlations between elements to be aware of. P and Si are positively correlated within the P-rich sample. Where we see a high P abundance, we also see enhancements in Si. There is also a weak positive correlation between Mg and P, suggesting the production of the two elements is somewhat linked and the behaviour of Mg could be coupled to the P-richness of a star.

4.3 Galactic Chemical Evolution Model

We once again use the chemical evolution code OMEGA+ (Côté et al., 2018b) for this work. The code has been described in section 2.1. The Milky Way model used is the same as that laid out in Chapter 3 (see section 3.3 for details) (Womack et al., 2023), with the same parameterisation as Table 3.1. The stellar yields used for the modelling are presented in the following section.

4.3.1 Stellar Yields

As it is accepted that AGB stars and SNe Ia do not significantly contribute to the galactic phosphorus abundance, the yields of these two stellar sources will be kept constant throughout. All models in this work use the FRUITY AGB yields (Cristallo et al., 2015) and SNe Ia yields of Iwamoto et al. (1999). The massive star yields are varied in order to investigate a range of progenitor scenarios, Table 4.1 summarises the options for massive star yields that are

Model Name	Massive Stars
CLC	L&C $V_{\text{rot}} = \text{mix}$
CRit(del)	Ritter delayed
CRit(rap)	Ritter rapid
CNom	Nomoto

Table 4.1: Combinations of yields used for the chemical evolution modeling. L&C $V_{\text{rot}} = \text{mix}$ are the rapidly rotating massive stars of [Limongi & Chieffi \(2018\)](#), Ritter delayed and Ritter rapid are from [Ritter et al. \(2018c\)](#), Nomoto is simply the yields of [Nomoto et al. \(2013\)](#)

employed in this work. Model *CLC* uses the rapidly rotating, massive star yields of [Limongi & Chieffi \(2018\)](#), where low-metallicity stars rotate faster than high-metallicity stars according to the mixed rotational velocity prescription of [Prantzos et al. \(2018\)](#). Both [Kobayashi et al. \(2011a\)](#) and [Prantzos et al. \(2018\)](#) have investigated the impact of rotating massive stars on the evolution of P, we investigate that for ourselves here. *CRit(del)* uses the massive star yields of [Ritter et al. \(2018c\)](#) with CO shell mergers and the delayed explosion prescription, while *CRit(rap)* uses the same yields, but with the rapid explosion prescription. Here, the terms ‘delayed’ and ‘rapid’ derive from the work of [Fryer et al. \(2012\)](#) who explains that an explosion is rapid if it occurs less than 250 ms after the halting of the initial collapse and is delayed if it occurs after that. [Fryer et al. \(2012\)](#) states if an explosion is rapid then it is more energetic thus, the remnant mass of the massive star is smaller, changing the ejecta of the CCSNe. Preliminary results from the study of CO shell mergers which are included in the yields of [Ritter et al. \(2018c\)](#) suggest they could boost production of P in CCSNe by up to an order of magnitude, and if 10 - 50% of CCSNe are affected by CO shell mergers, the evolution of $[P/Fe]$ and its dispersion could be reproduced. However, we need to be careful with the use of these yields as we are not certain of the frequency or nature of the CO shell mergers and we would require multi-dimensional hydrodynamics simulations to gain more clarity on this matter. Finally, *CNom* uses the massive star yields of [Nomoto et al. \(2013\)](#). Once again, we refer the reader to Appendix A where there is a brief discussion on how well model CLC can reproduce present day observational constraints and solar abundance ratios that are of interest

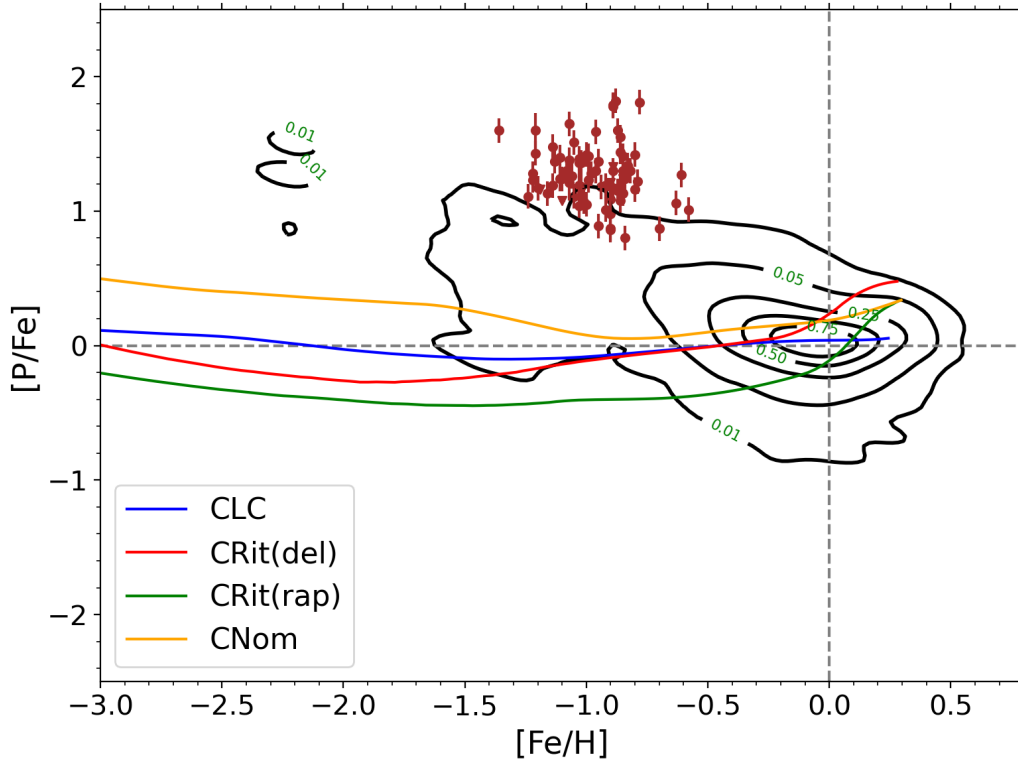


Figure 4.1: Evolution of $[P/Fe]$ versus $[Fe/H]$ using each of the four massive star yield sets. The observations of [Hinkel et al. \(2014\)](#) as representative of P-normal stars are shown as black contours while the P-rich sample generated in this work is shown as brown points. Upper limits in the P-rich sample are represented by downward triangles and lower limits by upward triangles. The solar abundance is shown as grey dashed lines.

in this Thesis.

4.4 Results

Figure 4.1 shows the evolution of $[P/Fe]$ versus $[Fe/H]$ for each massive star yield set we are exploring. The P-normal sample of stars ([Hinkel et al., 2014](#)) are represented by the black contours. The contours allow us to map the distribution density of the stellar abundances, with the numbers beside each contour showing the fraction of the observations enclosed in that annulus. The P-rich sample is represented by the brown points. The chemical evolution trends in Figure 4.1 confirm what has already been found in the literature. While we can reproduce the solar $[P/Fe]$ ratio, the models largely underproduce P compared to the observations at metallicities lower than solar. Though the yields of [Nomoto et al. \(2013\)](#) (yellow line) seem to cut through the contours better than the other models.

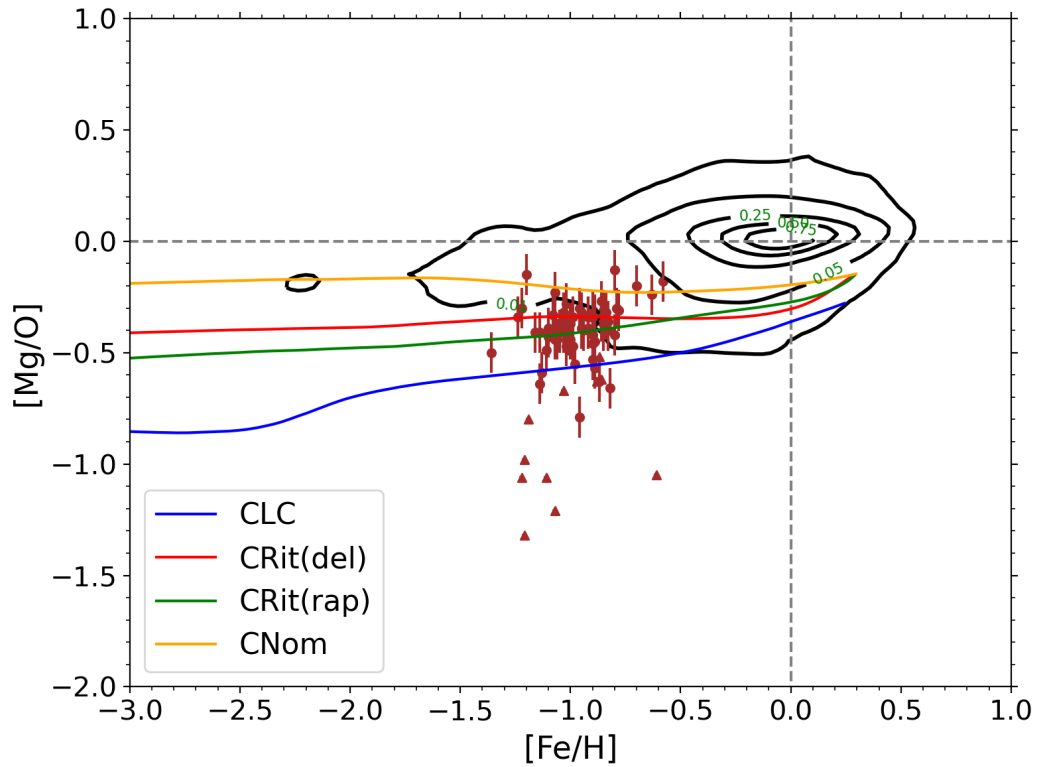


Figure 4.2: As Figure 4.1 but for the evolution of $[Mg/O]$ versus $[Fe/H]$.

Figure 4.2 shows the evolution of $[Mg/O]$ versus $[Fe/H]$. We study this ratio due to the enhancement in O and the slight enhancement in Mg that exists in the P-rich sample (see section 4.2.2). Though the P-rich sample may be enhanced in $[O/Fe]$ and $[Mg/Fe]$, it is clear this is not the case when the ratio $[Mg/O]$ is considered. The brown points sit in a similar region to the P-normal stars. Though some lower limits sit around 1 dex lower than the sample this is not concerning as their abundances, by nature of being a lower limit, could be higher. The $[Mg/O]$ ratio is well reproduced by all four GCE models.

Finally, Figure 4.3 shows the evolution of $[Si/S]$ versus $[Fe/H]$ for each of the four models. Again, we study this ratio because we know that the Si is enhanced in our sample and though we do not see a S enhancement in the P-rich sample, we expect there to be one due to the two element's similar sites of production. Therefore, it is intriguing to see how the chemical evolution models behave compared to the observations. We find the GCE models are consistently around solar $[Si/S]$ with a variation smaller than 0.1 dex between them. Therefore, the models are not wholly able to reproduce the observations. The P-rich sample is clearly

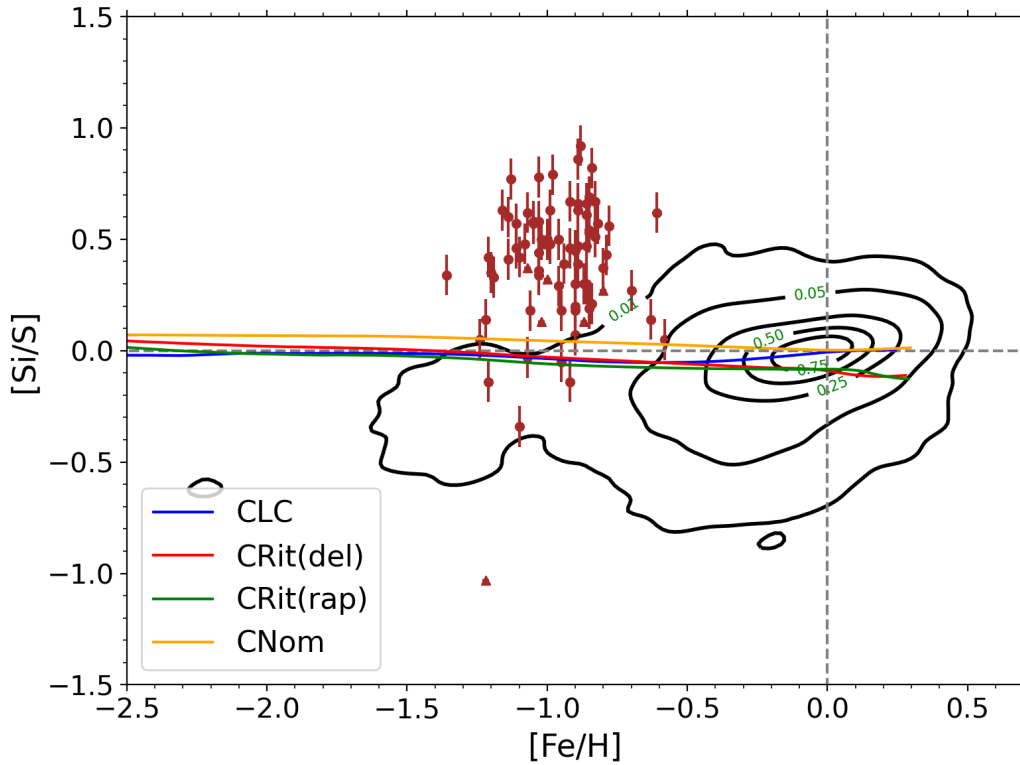


Figure 4.3: As Figure 4.1 but for the evolution of $[\text{Si}/\text{S}]$ versus $[\text{Fe}/\text{H}]$.

enhanced in $[\text{Si}/\text{S}]$ compared to the solar value. A larger $[\text{Si}/\text{S}]$ ratio is not exclusive to the P-rich population, with some P-normal stars in the sample (with $[\text{Fe}/\text{H}] \geq -0.5$) also exhibiting super-solar $[\text{Si}/\text{S}]$. Therefore, we show that there are a small number of P-normal stars which also display the anomalous $[\text{Si}/\text{S}]$ ratios that we expected from P-rich population.

4.5 Discussion

Here, we aim to explain the chemical evolution trends that we observe in Figures 4.1 to 4.3 and find out if these trends can help to narrow down a progenitor scenario for these anomalous P-rich stars.

The reason we are unable to reproduce the phosphorus enhancement of the P-rich sample is likely two-fold. Firstly, there is a lot of uncertainty around the P abundance of CCSNe yields. Phosphorus is made in the convective carbon shell of a massive star and in explosive carbon burning (e.g. Woosley & Weaver 1995, Woosley et al. 2002, Pignatari et al. 2016). Therefore, it is made in a different part of the CCSNe ejecta than iron, which makes the

CCSNe yields the dominant source of uncertainty for GCE models (e.g. [Romano et al. 2010](#)). Several uncertainties affect the last evolutionary stages of massive star progenitors in both one-dimensional models and multi-dimensional simulations of CCSNe. Given the two elements (P and Fe) are found in different parts of the ejecta at the end of life of a massive star, this makes the yields quite uncertain. Secondly, it could be the case that the P observed on the surface of these P-rich stars is not a GCE product but as a result of local nucleosynthesis. Therefore, P-rich stars have either been born from gas which is locally enriched in P or the P observed on the surface has been accreted from a companion object, though analysis would suggest the majority of the sample are not part of close binaries. However, we can still compare P-rich stars with GCE results for qualitative purposes.

We are able to reproduce the [Mg/O] ratios reasonably well with our GCE models because both elements are ejected from the O-rich stellar layers during the CCSNe of a massive star. Thus, we expect the GCE [Mg/O] ratio to be given by the relative ratios of the CCSNe yield set, especially given the production of ^{24}Mg relies on the production of ^{16}O via the α capture chain $^{16}\text{O}(\alpha, \gamma)^{20}\text{Ne}(\alpha, \gamma)^{24}\text{Mg}$. The models in [Figure 4.2](#) show a variation of approximately 0.2 dex between them at solar metallicities, which simply reflects the variation in the stellar yield sets. Overall, while Mg and O may be enhanced in P-rich stars, their relative ratio is consistent with theoretical ratios from CCSNe yields. However, note that for very massive stars, while Mg is not present in their winds, O is significantly enhanced causing an overproduction of O relative to Mg for stars with $M > 32 M_{\odot}$ (see sections 4.2 and 6.2 of [Griffith et al. 2021](#) for a discussion on this). The reader should note here that [Figure 4.2](#) also shows that the models are not wholly able to reproduce the ‘P-normal’ observations (black contours) as they do not reach solar abundance at solar metallicity. We also see an underproduction of Mg in [Chapter 6](#) later on in this work, therefore the low [Mg/O] of the models compared to solar may be due to an underproduction of Mg in the yield sets used. However, the models do still reproduce some of the sub-solar abundance ratios that we observe.

Si and S are produced in the same layers of a CCSNe and are ejected together, having been a direct product of explosive oxygen burning ([Pignatari et al., 2016](#)). There is also a

relevant contribution to the galactic Si and S abundances from SNe Ia (e.g. [Kobayashi et al. 2020](#)) where once again, Si and S are produced in the same parts of the ejecta. Therefore, we expect GCE models to carry the same [Si/S] ratios as are generated in the layers of the stars. Surprisingly, a significant fraction of P-rich stars have a super-solar [Si/S] abundance due to their enhancement in Si. This decoupling between models of nucleosynthesis and observations of P-rich stars is difficult to resolve, especially when we consider some P-normal stars also appear to show Si enhancement.

It is clear we have a long way to go to explain the anomalous abundances of P-rich stars using GCE models. Though we can reproduce the [Mg/O] abundances of the P-rich sample well, we are not able to explain the enhancement in P or Si with any of the massive star progenitor scenarios that we have considered.

4.6 Conclusions

From the GCE modelling performed in this chapter, we are not able to narrow down a progenitor scenario for the anomalous P-rich stars. Other methods were employed by [Brauner et al. \(2023\)](#) to try to narrow down a progenitor, these were: orbital analysis and a comparison to yields from models of other nucleosynthesis scenarios. The orbital analysis revealed that P-rich stars appear to belong primarily to the thick disc, with some belonging to the halo or accreted populations. The sample of P-rich stars could not be assigned to any one dynamical subgroup thus, they concluded the source of the P-richness could not be linked to peculiar orbital properties, different from the average values of the main Galaxy stellar populations.

Continuing the work started by [Masseron et al. \(2020a,b\)](#), [Brauner et al. \(2023\)](#) compared some of the elemental abundances of the P-rich sample to some other potential sources of P which may have caused the local enrichment of P in the ISM, which we assume the P-rich stars are born out from. They conclude that sub-Chandrasekhar (sub-Ch) mass SNe Ia are not the primary P polluter of the ISM as, though the Mn abundances matched well, the Ni abundance of the SNe Ia from [Sanders et al. \(2021\)](#) did not match the average abundance of the P-rich sample. Here, they used Mn and Ni as P abundances for sub-Ch SNe Ia were unavailable. Pair-instability supernovae (PISNe) could also be a potential progenitor for P-rich stars as

the sample of P-rich stars found so far exist in a narrow, low-metallicity range, as do PISNe. However, the stellar evolution simulations of [Kozyreva et al. \(2014\)](#) and [Takahashi et al. \(2018\)](#) show an odd-even effect (i.e. a deficiency in odd-Z elements compared to even-Z), which is not observed in the P-rich sample, ruling out PISNe as a progenitor.

Finally, [Brauner et al. \(2023\)](#) considered non-thermal nucleosynthesis. [Goriely \(2022\)](#) explored the idea of irradiation by stellar energetic particles (SEPs) and found that the enhancement in P observed in P-rich stars can be reproduced to a great extent. However, this non-thermal nucleosynthesis also creates an underprediction of both Al and Si abundances compared with P-rich stars. The occurrence of this process is also highly uncertain with no source, acceleration mechanism or target material for the SEPs having been reported.

There is much more work to be done in this area in order to determine a progenitor scenario for P-rich stars. More observations of P-rich stars are required, covering a wider range of elements. Availability of more s-process elements such as Ba, La and Pb would mean more analysis in the style of [Womack \(2021\)](#) can be performed, in which the full abundance patterns can be compared to the nucleosynthesis yields of a potential progenitor scenario. This would also allow us to confirm if the unusual abundances are as a result of a new operation of the s process or from a combination of massive star scenarios (e.g. rotation coupled with CO shell mergers). More work also needs to be done to study non-thermal nucleosynthesis and SEP interaction, following on from the work of [Goriely \(2022\)](#). The [Ba/La] ratio is underpredicted compared to solar by the spallation models. Therefore, Ba and La abundances of P-rich stars would be useful for comparison. A full study into how these SEPs interact with stellar atmospheres and the yields that the processes would generate would be useful so that a set of yields at a range of metallicities can be obtained. A wider range of yields would allow us to include this new form of nucleosynthesis in GCE models, so that its full impact can be studied. A range of i-process yields from AGB stars could also be useful here to see the GCE impact of this process, this could assist in confirming if the i process is a suitable progenitor.

In the meantime, we conclude that standard assumptions of GCE modelling are not able to match the observed abundances of the sample of 78 P-rich stars. Thus, we cannot on this occasion determine a viable progenitor scenario.

5. Developing Multi-zone OMEGA(ALPHA) for Chemical Evolution Modelling

“She felt fairly confident that with a great deal of practice and effort, she would succeed in the end.”

– Roald Dahl, *Matilda*

5.1 Introduction

By studying galactic chemical evolution (GCE) we develop our understanding of how the galaxy evolved. We can see footprints of the stellar generations that have come before through our observations of the stars and we can understand how their abundances have come to be through chemical evolution modelling. This allows us to paint a picture of how the galaxy has evolved chemically: the types of stars that must have formed and when and in what abundance have they produced the chemical elements, giving us key temporal information about galaxy evolution from a chemical perspective.

There are many different ways to model GCE. The most basic is modelling a galaxy as a single zone; this has been done by a number of authors (e.g. [Tinsley 1980](#), [Carigi et al. 2002](#), [Lanfranchi & Matteucci 2003](#), [2004](#), [2010](#), [Fenner et al. 2006](#) and more recently [Vincenzo et al. 2014](#), [Rybizki et al. 2017](#), [Romano et al. 2023](#)). Single-zone modelling is useful as it is often simpler and faster than more involved simulations. OMEGA ([Côté et al., 2017](#)), the single-zone semi-analytical code primarily used in this work, has been used in a variety of studies (e.g. [Côté et al. 2018a](#), [Trueman et al. 2022](#), [Womack et al. 2023](#), [Brauner et al. 2023](#), [Pignatari et al. 2023](#), [Lian et al. 2023](#)). These studies have broadened the field of GCE by giving us insight into a variety of topics from stellar nucleosynthesis, to planet formation, radioactive isotopes and galactic archaeology.

However, single-zone models, by nature, lack spatial information. By including a spatial

component, models of chemical evolution can become even more informative as we can use them to study radial profiles of a galactic disc. Studies of radial profiles and radial gradients in the Milky Way and beyond has been a topic of interest in the fields of galactic archaeology and galactic chemical evolution in recent years (e.g. [Mollá et al. 2019](#), [Arellano-Córdova et al. 2021](#), [Katz et al. 2021](#), [Da Silva et al. 2023](#), [Willett et al. 2023](#), [Magrini et al. 2023](#), [Pilyugin & Tautvaišienė 2024](#)). By modelling the disc we can compare our models to observed radial profiles, allowing us to gain a better understanding of how the abundance gradients may have originated, disc formation and chemical evolution in different regions of a galaxy.

One of the most important things to understand when studying radial gradients is how gas is accreted onto the disc. [Larson \(1976\)](#) pioneered the idea of the Milky Way disc forming via inside-out growth, while [Chiosi \(1980\)](#) introduced the first model of infalling gas onto the galactic disc. Following this, many models of gas accretion were proposed (e.g. [Lacey & Fall 1985](#), [Matteucci & Francois 1989](#), [Chiappini et al. 1997](#), [Dayal et al. 2013](#), [Peng & Maiolino 2014](#)), including the popular two-infall model ([Chiappini et al. 1997](#), [Chiappini et al. 2001](#)). The two-infall model assumes that the galaxy forms by two distinct accretion events, the first forms the halo and thick disc and the second, delayed, infall forms the thin disc. Many models of gas accretion rely on the idea that we have an exponentially declining accretion rate with both radius and time, regardless of how many infall episodes. For example, a single exponential infall was employed by [Belfiore et al. \(2019\)](#) and will also be utilised later in this work.

If a model comprises of more than one zone radially across the disc, regardless of the prescription for gas infall, we have a tool to study radial profiles as the gas is not evenly distributed over the galactic disc. Once there is radial information included in a model, some authors begin to explore radial gas migration. Radial motion of gas was proposed by [Tinsley & Larson \(1978\)](#) as a way to produce or enhance radial abundance gradients. They suggested that radial gas flows may be caused by loss of angular momentum of the galactic gas via either viscosity or interaction with a bar or spiral density wave. This idea was subsequently included in chemical evolution models by [Mayor & Vigroux \(1981\)](#). Their most successful model accounts for radial motion of gas driven by infall of gas with zero angular momentum.

Using the model, they were able to reproduce observed features of the Milky Way including the hydrogen (HI + HII) gas surface density, the SFR and oxygen abundance gradient. In order to constrain their models of chemical evolution, [Lacey & Fall \(1985\)](#) also included radial gas flows. They included 4 different prescriptions of radial flows based on a few different physical factors: angular momentum of the infalling gas, the viscosity of the gas and the gravitational interaction between the gas and the bar of the galaxy. By comparing with observations, they found that radial flows with a velocity as small as $|v_r| \approx 1 \text{ km s}^{-1}$ can impact the chemical evolution of the disc. They note that the inclusion of radial ‘inflows’ has a particularly strong impact on the solar neighbourhood metallicity distribution and the age-metallicity relation. While, [Edmunds & Greenhow \(1995\)](#) found that radial flows alone do not generate radial abundance gradients but must be coupled with a radially varying star formation rate.

More recently, radial gas flows have been studied by a variety of authors (e.g. [Spitoni & Matteucci 2011](#), [Bilitewski & Schönrich 2012](#), [Kubryk et al. 2015](#), [Prantzos 2016](#), [Grisoni et al. 2018](#), [Chen et al. 2023](#)). [Spitoni & Matteucci \(2011\)](#) uses the prescription of [Portinari & Chiosi \(2000\)](#) which treats the disc as a series of concentric shells and uses the flux through the boundaries to calculate the change in gas surface density in each shell. They found that in order to reproduce the observed gradients, the rate of radial gas flow should increase with galactocentric distance for both one and two-infall models. However, for some cases of the two-infall model, observed gradients could be replicated without radial flows. [Grisoni et al. \(2018\)](#) uses the radial flow prescription of [Spitoni & Matteucci \(2011\)](#) along with the chemical evolution models of [Grisoni et al. \(2017\)](#) to investigate $[\alpha/\text{Fe}]$ abundance gradients of the galactic disc. They found that introducing radial gas flows could be beneficial in reproducing radial gradients along the thin disc and found them particularly useful at higher metallicities in order to reproduce the observed $[\text{Mg}/\text{Fe}]$ vs $[\text{Fe}/\text{H}]$.

[Kubryk et al. \(2015\)](#) use a variable radial inflow profile by considering the gravitational interaction between the gas and the galactic bar. They constrain the averaged radial velocity of the gas to a few tenths of a km s^{-1} . The same prescription was employed by [Prantzos \(2016\)](#) to investigate the Milky Way age metallicity distribution and metallicity gradient. By also including stellar migration, they found a significant impact on several properties of the

disc including being able to reproduce the $[\alpha/\text{Fe}]$ vs $[\text{Fe}/\text{H}]$ of the disc.

From [Tinsley & Larson \(1978\)](#), we know that radial flows can be induced due to conservation of angular momentum. In this case, the angular momentum of the infalling gas differs from the circular motions of the disc, thus a radial flow will be induced due to conservation of angular momentum. However, this is difficult to model as the angular momentum of infalling gas is not known. [Bilitewski & Schönrich \(2012\)](#) performed a parameterised study into this effect. They calculated the change in angular momentum induced by gas falling onto a disc and used this to calculate the mass of gas flowing from one ring to the next. They found that inside-out formation alone could not explain the present-day metallicity gradient and concluded that radial flows must be required in order to do this. By using conservation of angular momentum, they were also able to constrain a rotational velocity of infalling material to approximately 160 km s^{-1} . Similarly, [Pezzulli & Fraternali \(2016\)](#) considered an analytical model of the disc to calculate accretion profiles, radial gradients and abundance gradients as a function of the angular momentum of the material accreted onto the disc. They found that the rotational velocity of the accreted material must be 70-80% that of the disc. This allows for gas accreted on the outskirts of the disc to be driven inward by radial flows. However, many works, including the present work, do not seek to conserve angular momentum due to the unknown angular momentum of the infalling gas.

This work aims to create a multi-zone model using many instances of the OMEGA chemical evolution code. In section 5.2, we will detail how the chemical evolution code and the multi-zone extension works, in section 5.3 we discuss the development of Milky Way models and in section 5.4 we investigate the sensitivity of the models to varying important parameters.

5.2 Methods and Simulations

5.2.1 Initial GCE model - OMEGA/+

OMEGA ([Côté et al., 2017](#)) is a single-zone chemical evolution code with gas inflows and outflows, it is available online as part of the NuPyCEE package¹. The evolution of the galactic

¹<https://github.com/NUGrid/NuPyCEE>

gas mass (\dot{M}_{gas}) is defined as: (Tinsley 1980; Pagel 1997; Matteucci 2012)

$$\dot{M}_{\text{gas}}(t) = \dot{M}_{\text{inflow}}(t) + \dot{M}_{\text{ej}}(t) - \dot{M}_{\star}(t) - \dot{M}_{\text{outflow}}(t) \quad (5.1)$$

where \dot{M}_{inflow} is the rate of gas mass added by galactic inflows, \dot{M}_{ej} is the rate of gas mass added by stellar ejecta, \dot{M}_{\star} is the rate of gas mass removed from the gas reservoir by star formation and \dot{M}_{outflow} is the rate of gas mass lost by outflows. The star formation rate is defined as

$$\dot{M}_{\star}(t) = \frac{\epsilon_{\star}}{\tau_{\star}} M_{\text{gas}}(t) \quad (5.2)$$

where ϵ_{\star} and τ_{\star} are the dimensionless star formation efficiency (SFE) and star formation timescale, respectively. The outflow rate is proportional to the star formation rate and is defined as

$$\dot{M}_{\text{outflow}}(t) = \eta \dot{M}_{\star}(t) \quad (5.3)$$

where η is the mass loading factor and controls the strength of the outflows. At each timestep, a simple stellar population (SSP) is created by SYGMA (Stellar Yields for Galactic Modelling Applications) (Ritter et al., 2018a). SYGMA includes ejecta from various stellar sources which is instantaneously and uniformly mixed into the gas reservoir. To calculate the gas mass injection rate due to stellar ejecta, the contribution of every stellar population formed by time t is summed so that

$$\dot{M}_{\text{ej}}(t) = \sum_j \dot{M}_{\text{ej}}^j(M_j, Z_j, t - t_j) \quad (5.4)$$

where \dot{M}_{ej}^j is the mass ejected by the j th stellar population, M_j is the initial mass of the population, Z_j is the initial metallicity of the population and $t - t_j$ is the age of the j th population at time t .

A subsequent development of OMEGA, called OMEGA+ (Côté et al., 2018b) includes a second zone acting as an external gas reservoir, the circumgalactic medium (CGM). Employing a CGM allows for more sophisticated prescriptions for infalling gas as well as the ability to keep track of the enrichment of the CGM so that galactic inflows can be enriched rather than pristine. A full description of OMEGA and OMEGA plus can be found in Chapter 2, though OMEGA+ will not be considered in this work.

5.2.2 Multi-zone extension

As discussed in section 5.1, the inclusion of radial information can be extremely beneficial for chemical evolution studies. Therefore, we have developed a multi-zone version of OMEGA (hereafter known as ALPHA) in order to provide this spatial dimension, while preserving the speed and usability of the original code.

To gain radial information, we connect many instances of OMEGA (single-zones) in order to simulate a multi-zone disc, which can be visualised as concentric rings (see Figure 5.2 later in this section). Connecting the zones takes advantage of the external control capabilities of OMEGA, which allow the user to control the behaviour of a zone at each timestep: specifying the star formation rate, mass lost and mass gained by the zone. More information on how this capability functions can be found in the online documentation of JINAPyCEE². In order to maintain the flexibility afforded by OMEGA, we allow the user to specify the number of zones that will comprise their galactic disc. The user is also able to specify the inner and outer radius of the disc. For example, if one wanted to simulate the Milky Way disc, they could specify the inner radius as ≈ 4 kpc and the outer as ≈ 16 kpc. It is important that the inner radius is not zero, as the model is not intended to have a complete central zone. Modelling the galactic bulge would require different physics as bulges do not form in the same way as discs (e.g. Eggen et al. 1962, Scannapieco & Tissera 2003; Immeli et al. 2004, Kormendy & Kennicutt 2004). For information on multi-zone modelling of the bulge, see Cavichia et al. (2023) and references therein.

In the following text, we will detail how the key equations and parameters have changed between OMEGA and ALPHA to make the multi-zone developments as usable and as physically motivated as possible.

Gas Inflows

The prescription for inflow rate follows similarly to the prescription detailed in Belfiore et al. (2019). We use an exponentially declining accretion rate with radius, with an infall timescale which increases with galactocentric radius, in order to achieve inside-out growth.

²https://github.com/becot85/JINAPyCEE/blob/master/DOC/Creating_multi_zone_models.ipynb

The infall rate of gas at radius (r) and at time (t) is defined as follows:

$$I(r, t) = I_0(r) e^{-\frac{t}{\tau_{\text{inf}}(r)}} \quad (5.5)$$

where $I_0(r)$ is the normalisation of the infall rate across the disc and the infall timescale τ_{inf} is defined as $\tau_{\text{inf}} = a + br$. The parameters a and b are the infall timescale at the galaxy centre and the linear gradient of the infall timescale respectively.

I_0 is then defined as follows:

$$I_0(r) = A e^{-\frac{r}{h}} \quad (5.6)$$

where h is a scale-length of the disc. The parameter, A , which governs how the total mass is distributed across the disc is defined as follows:

$$A = M_{\text{inf}} / \left(\int_{r_{\text{min}}}^{r_{\text{max}}} dr 2\pi r e^{-\frac{r}{h}} \int_0^T e^{-\frac{t}{\tau_{\text{inf}}(r)}} dt \right). \quad (5.7)$$

This allows for the total mass of gas in the galaxy at the end of the simulation (M) to be distributed in an inside-out manner across the disc throughout the length of the evolution of the galaxy.

Star Formation Rate

The star formation rate (SFR) is calculated in a similar manner as the base OMEGA code, using the Kennicutt-Schmidt law (Schmidt 1959, Kennicutt 1998). Here, we use surface gas density rather than absolute mass in order to account for the area of the zone for which we are calculating the SFR. The star formation rate density for a zone is defined as:

$$\Sigma_{\text{SFR}} = f_{\star} \left(\frac{\Sigma_{\text{gas}}}{1 \text{ M}_{\odot} \text{ pc}^{-2}} \right)^k \quad (5.8)$$

where f_{\star} is the star formation efficiency and k is a dimensionless exponent that controls the slope of the SFR.

Gas Outflows

Outflowing gas in the model, as with OMEGA, is driven by star formation. Again, we are considering surface densities. Outflow rate density of the model is defined as:

$$\dot{O} = \eta \Sigma_{\text{gas}} \quad (5.9)$$

where, η is again the mass loading factor.

Radial Gas Flows

In order to induce radial gas flows, a flow velocity (v_{rad}) must be specified. v_{rad} is constant regardless of zone. In this model, gas moves radially inward, so that the positive direction of flow is from each outer zone, into the next innermost zone.

To calculate the mass lost via radial flows from a given zone, n , to the next innermost zone ($n - 1$) at time t ($M_{\text{mig},n}(t)$) we need to know the proportion of that zone that is currently occupied by the mass it is about to lose for a given radial velocity. The blue shaded region in Figure 5.1 represents the mass that will be moved radially, which occupies a width, Δd . R_{out} represents the outer radius of the zone n , while R_{in} represents the inner radius.

For a fixed radial flow velocity, v_{rad} ,

$$\Delta d = v_{\text{rad}}\Delta t, \quad (5.10)$$

where Δt is the length of the current timestep in the simulation. The mass in the Δd region occupies an area:

$$A_{\text{mig}} = \pi(\Delta d + R_{\text{in}})^2 - \pi R_{\text{in}}^2, \quad (5.11)$$

while the area of the entire zone, n , is:

$$A_n = \pi R_{\text{out}}^2 - \pi R_{\text{in}}^2. \quad (5.12)$$

Therefore, we can also define the area A_{mig} as:

$$\begin{aligned} A_{\text{mig}} &= \rho A_n \\ A_{\text{mig}} &= \rho(\pi R_{\text{out}}^2 - \pi R_{\text{in}}^2), \end{aligned} \quad (5.13)$$

where ρ is the fraction of the area A_n being moved into the neighbouring zone.

Using equations 5.11 and 5.13:

$$\rho(\pi R_{\text{out}}^2 - \pi R_{\text{in}}^2) = \pi(\Delta d + R_{\text{in}})^2 - \pi R_{\text{in}}^2$$

We can simplify this and substitute equation 5.10 to achieve:

$$\rho(R_{\text{out}}^2 - R_{\text{in}}^2) = (v_{\text{rad}}\Delta t + R_{\text{in}})^2 - R_{\text{in}}^2.$$

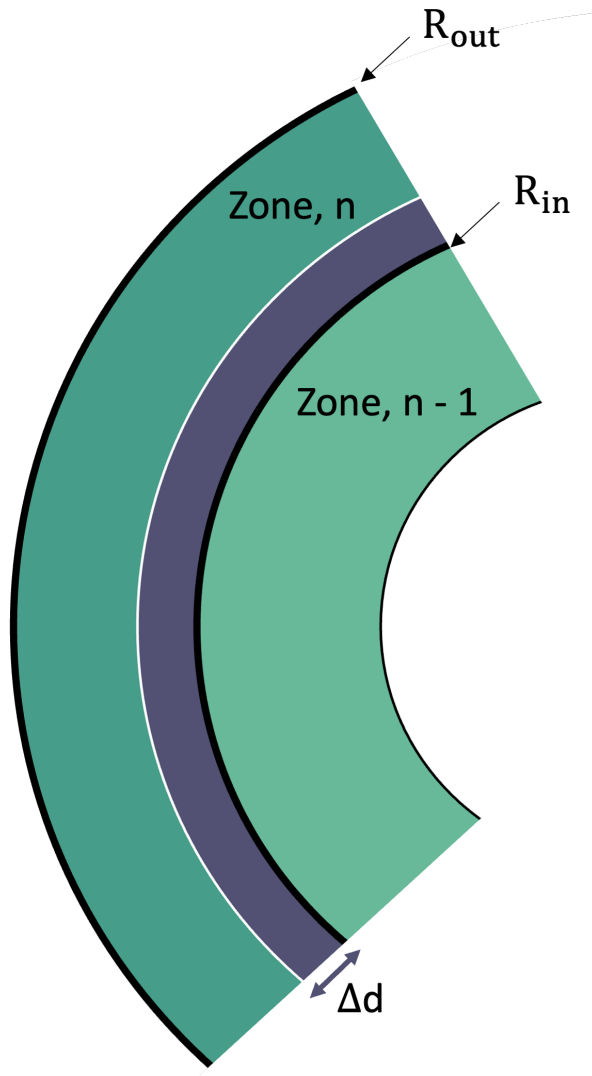


Figure 5.1: A slice of the galactic disc showing two zones n and $n - 1$, where $n - 1$ is the inner zone. The blue shaded region is the section of zone n , which will move into zone $n - 1$, moving a distance Δd . R_{out} and R_{in} are the outer and inner radii of zone n , respectively.

Thus, the fraction of gas mass in zone, n , transferred to zone $n - 1$ for a given timestep and v_{rad} is:

$$\rho = (v_{\text{rad}}\Delta t + R_{\text{in}})^2 - R_{\text{in}}^2 / (R_{\text{out}}^2 - R_{\text{in}}^2). \quad (5.14)$$

The fraction ρ is not constant (and must be between 0 and 1), varying with radius, time and v_{rad} . Therefore, for a given zone, n , at time t , the mass of gas moving into its neighbouring zone ($n - 1$) is:

$$M_{\text{mig},n}(t) = \rho M_{\text{gas}}(t). \quad (5.15)$$

The prescription for radial gas motion has been kept simple in order to preserve the nature of the model. By design, OMEGA runs quickly, allowing for simple chemical evolution modelling without the need for extensive, expensive computations. Once we introduce more complex prescriptions, we lose the ability to perform these quick computations, which is a key advantage of the code compared to others in the field. When using OMEGA or OMEGA+ to model galaxies, we do not calculate or need to preserve angular momentum due to the one-zone nature of the code. Therefore, we do not consider the preservation of angular momentum when considering the radial movement of gas as others may have done (e.g. [Bilitewski & Schönrich 2012](#)).

A pictorial representation of how gas moves in ALPHA can be found in [Figure 5.2](#). The figure shows gas flowing in and out of each zone (cream and brown arrows, respectively) as well as gas moving radially (pink arrows). The formation of SSPs is also illustrated in this figure by the red starred circles.

Overall, the evolution of the gas mass in an individual zone (n) is described as follows:

$$\dot{M}_{\text{gas}}(t) = \dot{M}_{\text{inflow}}(t) + \dot{M}_{\text{ej}}(t) + \dot{M}_{\text{mig}_{n+1}}(t) - \dot{M}_{\star}(t) - \dot{M}_{\text{outflow}}(t) - \dot{M}_{\text{mig}_n}(t) \quad (5.16)$$

where $n = 0$ for the innermost zone and increases with radius. When considering the innermost zone, the radial flow rate remains the same and we lose gas to the ‘bulge’, i.e. gas leaves the innermost zone, where it would flow into a region that we do not model. This happens in order to prevent gas piling up in the innermost zone, causing radial gradients to be steeper than is

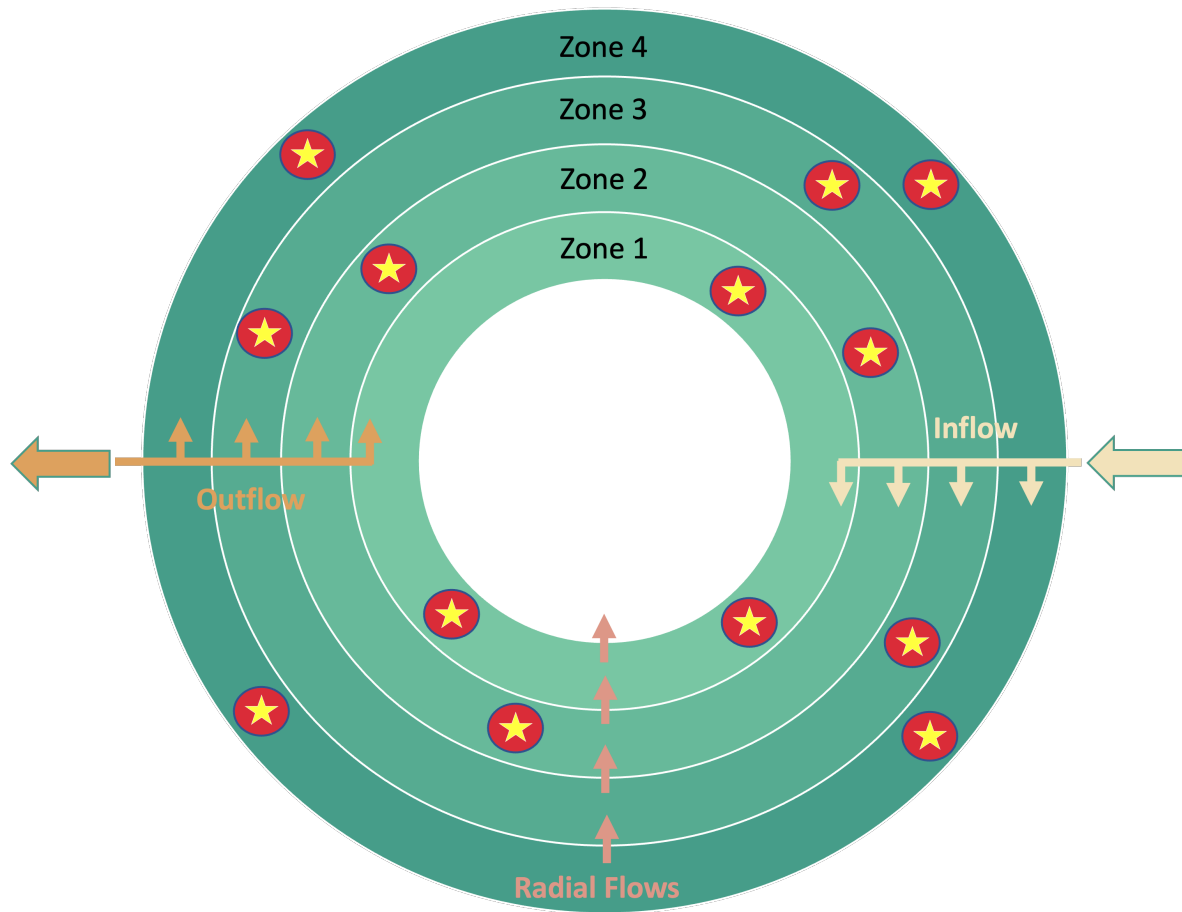


Figure 5.2: An example of a 4 zone model, with gas flows and star formation. The SSPs formed in each zone are represented by the red starred circles. The gas infalling onto each zone is represented by the cream arrows, the outflowing gas by the brown arrows and the radial gas flows by the pink arrows.

physical. Whereas, if we are considering the outermost zone then we gain no gas radially, so $\dot{M}_{\text{mig}_{n+1}}(t)$ is set to zero for this zone. This behaviour is shown in Figure 5.2. When gas is migrated radially from one zone to the next, we also take into account the chemical composition, calculating the abundances of the migrating gas and adding or subtracting the abundances of the gas in each zone as required.

User-Specified Parameters In the above equations, the parameters available to be specified by the user are:

1. Total infall mass, M_{inf}
2. Infall timescale at the galactic centre, a
3. Linear gradient of the infall timescale, b
4. Star formation efficiency, f_{\star}
5. Exponent of the surface gas density in the Kennicutt-Schmidt law, k .
6. Mass loading factor, η , see equation 5.9
7. Radial flow velocity, v_{rad}

As mentioned previously, the user can also specify the number of zones in the model as well as the inner and outer radii of the model.

All user-specified parameters that are available in OMEGA, for example: yield table, number of timesteps, age at the end of the simulation, to name some of the more commonly used, are also available in ALPHA. The parameters can be common across all zones or can be changed for individual zones, see the documentation provided in NuPyCEE for more information on the range of parameters available to the user in OMEGA. However, having different parameters across zones is not always appropriate, for example the yield table used should be kept constant across all zones.

5.3 Milky Way model development

In order to test and perform the first scientific study with ALPHA, we have developed a Milky Way (MW) model. In accordance with the Milky Way models of [Matteucci & Francois](#)

(1989), [Chiappini et al. \(1997\)](#), [Grisoni et al. \(2017\)](#) and others, we do not include gas outflows here but note that it is an option that could be explored in future work. For the initial study, radial migration of gas is also not included in the model. The effect of radial flow of gas on the galaxy properties is explored later (section 5.3.1).

To successfully develop a MW model, we performed a parameter study. This involved varying a selection of user-specified parameters: (i) the total mass of gas that is accreted by the galaxy over the course of the simulation (M_{inf}), (ii) the star formation efficiency parameter f_{\star} and (iii) the parameters which control the infall timescale of the gas, a and b (see section 5.2.2 for details on these parameters). The selected ranges used in the parameter study were as follows:

$$\begin{aligned} 2 \times 10^{10} &\leq M_{\text{inf}} \leq 2.5 \times 10^{10} M_{\odot} \\ 1.8 \times 10^{-4} &\leq f_{\star} \leq 2.5 \times 10^{-4} M_{\odot} \text{ yr}^{-1} \text{ kpc}^{-2} \\ -3 &\leq a \leq -1 \text{ Gyr} \\ 0.5 &\leq b \leq 2 \text{ Gyr kpc}^{-1} \end{aligned}$$

The range in M_{inf} arises as we expect the mass of the thin disc to be of the order of $10^{10} M_{\odot}$ (e.g. [Kafle et al. 2014](#), [Pouliasis et al. 2017](#)). We performed a small sensitivity study and found that $2 - 2.5 \times 10^{10} M_{\odot}$ is the optimal range for MW-like gas surface densities for this model. [Kennicutt \(1998\)](#) provides a range for f_{\star} of $2.5 \pm 0.7 \times 10^{-4}$ (their equation 4), again, after a small sensitivity study, we find the lower portion of this range to be ideal. Meanwhile, the range of a and b was determined by [Chiappini et al. \(2001\)](#), who use $a = -1.27$ and $b = 1.03$. Therefore, we select a range which encompasses these values.

Note that some aspects of the model remained fixed, we used: 10 zones with an inner radius of 4 kpc and an outer radius of 16.5 kpc and an exponent for Equation 5.8 of $k = 1.4$, again in accordance with [Kennicutt \(1998\)](#). To chose an appropriate yield set, we picked an arbitrary model with parameters $M_{\text{inf}} = 2.17 \times 10^{10} M_{\odot}$, $f_{\star} = 1.8 \times 10^{-4} M_{\odot} \text{ yr}^{-1} \text{ kpc}^{-2}$, $a = -1.5 \text{ Gyr}$ and $b = 2 \text{ Gyr kpc}^{-1}$ and studied the [O/H] gradient using a selection of yield sets including: AGB yields from FRUITY ([Cristallo et al., 2015](#)), Monash ([Karakas, 2010](#)) and NuGrid ([Pignatari et al., 2016](#)) and massive stars from NuGrid ([Ritter et al., 2018c](#)), Kobayashi and Nomoto ([Kobayashi et al. 2006](#), [Nomoto et al. \(2013\)](#)) and [Limongi & Chieffi \(2018\)](#) both with and

without rotation. We found that the slope of the Monash group AGB yields of [Karakas \(2010\)](#) in combination with the non-rotating massive star yields of [Limongi & Chieffi \(2018\)](#) and the W7 SNIa yields of [Iwamoto et al. \(1999\)](#) provided the closest value of the slope compared to stellar observations. More detail on the [O/H] gradient and the observations used can be found later in this section. In this work, we adopt the IMF of [Kroupa \(2001\)](#) for all models discussed.

We generated a set of 2000 models by evenly sampling across the selected ranges of the four parameters discussed above, selecting 10 values of M_{inf} and f_{\star} , five values of a and 4 values of b . To find the model which is most MW-like, a number of physical properties were explored. Firstly, in order for a model to be successful, it must have exponential disc scale length of the gas and solar neighbourhood gas surface densities in an appropriate range. We expect a successful model to have a disc scale length of 2.5 - 3.5 kpc (e.g. [Bovy et al. 2012](#), [Spitoni et al. 2017](#)) though some authors suggest the scale length could be outside of this range (e.g. [Bovy & Rix 2013](#)). [McKee et al. \(2015\)](#) determined the local average surface densities of the Milky Way by reanalysing data from the literature and found a total surface density (gas + stars) of $47.1 \pm 3.4 M_{\odot} \text{pc}^{-2}$. Therefore, we only select models with surface densities in this range for the solar neighbourhood annulus. Finally, we require a local surface gas density within 40% of the [McKee et al. \(2015\)](#) range. This narrowed our set down to 283 models.

We also required that the model match a number of known relations and properties. These are as follows:

1. Infall rate density at 4 kpc, 8 kpc and 12 kpc with similar shape to that of [Mollá et al. \(2016\)](#) figure 4 (i.e. exponential and flattening at outer radii),
2. SFR versus age of the galaxy with a typical curve shape, (i.e. a peak at early times followed by a decreasing slope as the galaxy evolves),
3. Stellar surface density profile which is similar to the models of [Johnson et al. \(2021\)](#), which fit MW observations (e.g. [Hayden et al. 2015](#)),

Property	No Flows Model	Flows Model
$M_{\text{inf}} (M_{\odot})$	2.4×10^{10}	3×10^{10}
$f_{\star} (M_{\odot} \text{ yr}^{-1} \text{ kpc}^{-2})$	2×10^{-4}	3.2×10^{-4}
a (Gyr)	-1.5	-1.5
b (Gyr kpc^{-1})	2	2

Table 5.1: Final properties of the models both with and without radial flows, after carrying out the parameter studies.

4. Present-day oxygen radial gradient ($[\text{O}/\text{H}]$ versus R) which reproduces observations of Cepheids used in [Mollá et al. \(2019\)](#) ([Luck & Lambert 2011](#), [Luck 2014](#), [Korotin et al. 2014](#), [Martin et al. 2015](#)),
5. Normalised SFR density versus R which can reproduce the observations of [Rana \(1991\)](#) and [Stahler & Palla \(2005\)](#), as followed by [Palla et al. \(2020\)](#),
6. Gas surface density profile which largely reproduces the averaged HI and HII observations of [Dame \(1993\)](#) and [Nakanishi & Sofue \(2003, 2006\)](#), as followed by [Palla et al. \(2020\)](#),
7. Solar neighbourhood metallicity distribution function (MDF) that follows the distribution of GALAH DR3 ([Buder et al., 2021](#)). For details on the selection criteria used to generate the GALAH MDF, refer to the discussion on ‘Panel g’ later in this section.
8. Local $[\text{Fe}/\text{H}]$ versus age (age-metallicity relation) which reaches solar abundance ($[\text{Fe}/\text{H}] = 0$) at the time $t \approx 8$ Gyr, corresponding to the formation of the sun.

Using these criteria, we filtered down to 90 acceptable models. Due to the interplay between the parameters, the acceptable models had values for M_{inf} and f_{\star} , across the full range of potential values, $-2 < a < -1$ and all 90 models had $b = 2$. In order to select a final model, we found the value for each parameter which appeared most frequently across the original 283 models reproducing only the exponential disc scale length and the solar neighbourhood gas surface density, assuming that combination was also included in the 90 acceptable models. The properties of the chosen model can be found in Table 5.1. The chosen MW-like model

with no radial flows has a solar neighbourhood total (gas + stars) mass surface density of $47.9 M_{\odot} \text{pc}^{-2}$ and a gas surface density of $8.7 M_{\odot} \text{pc}^{-2}$ at the present time.

Figure 5.3 shows the key relations detailed above for the chosen model. Here, we will reflect on the success of the model in reproducing the trends required in each panel of the figure. Where necessary, we can compare this to Figures B.2 to B.6, which show some diagnostic plots of models that were not chosen to illustrate how these plots aided in our model selection. Note that there is not one example of a ‘bad’ model, where none of the diagnostics could be reproduced. Thus, Figures B.2 to B.6 are not all from the same model and instead are an example of what a poor plot might look like for the diagnostic in question.

In the following description, we will frequently use the term ‘galactic age’, this refers to the age of the simulation. For example at an age of 8 Gyr, we are 8 Gyr through the evolution of the disc we are simulating.

Panel a

This plot shows the infall rate density of the gas as a function of galactic age, for annuli at approximately 4, 8 and 12 kpc. Here, we are looking for the model trends to replicate the curved profiles seen in Mollá et al. (2016). Therefore, we expect the trend at all annuli to be exponential, flattening at outer radii, which is the case in Figure 5.3. All 283 models were able to produce the curved shapes required at each annulus, this is due to the conservative range of the infall parameters a and b . If one were to increase a or b outside of the chosen range (with a becoming positive), we would see straighter, shallower slopes rather than curves. If a were to decrease, the curves become more pronounced, with some overlap between them, if b would decrease (becoming negative), we would see positive slopes rather than negative slopes. More detail on these effects can be found in section 5.4.

Panel b

Here, we show the global SFR of the model against galactic age. The global SFR is the SFR across the disc, calculated simply as the sum of the SFR in each zone. We are aiming to reproduce the classic curved shape of the SFR, with a peak at earlier times (2 - 4 Gyr) followed by a decreasing slope as the galaxy evolves (e.g. Revaz et al. (2016), Côté et al. 2019a). We can see the model does well at reproducing the expected shape, as do all the tested models.

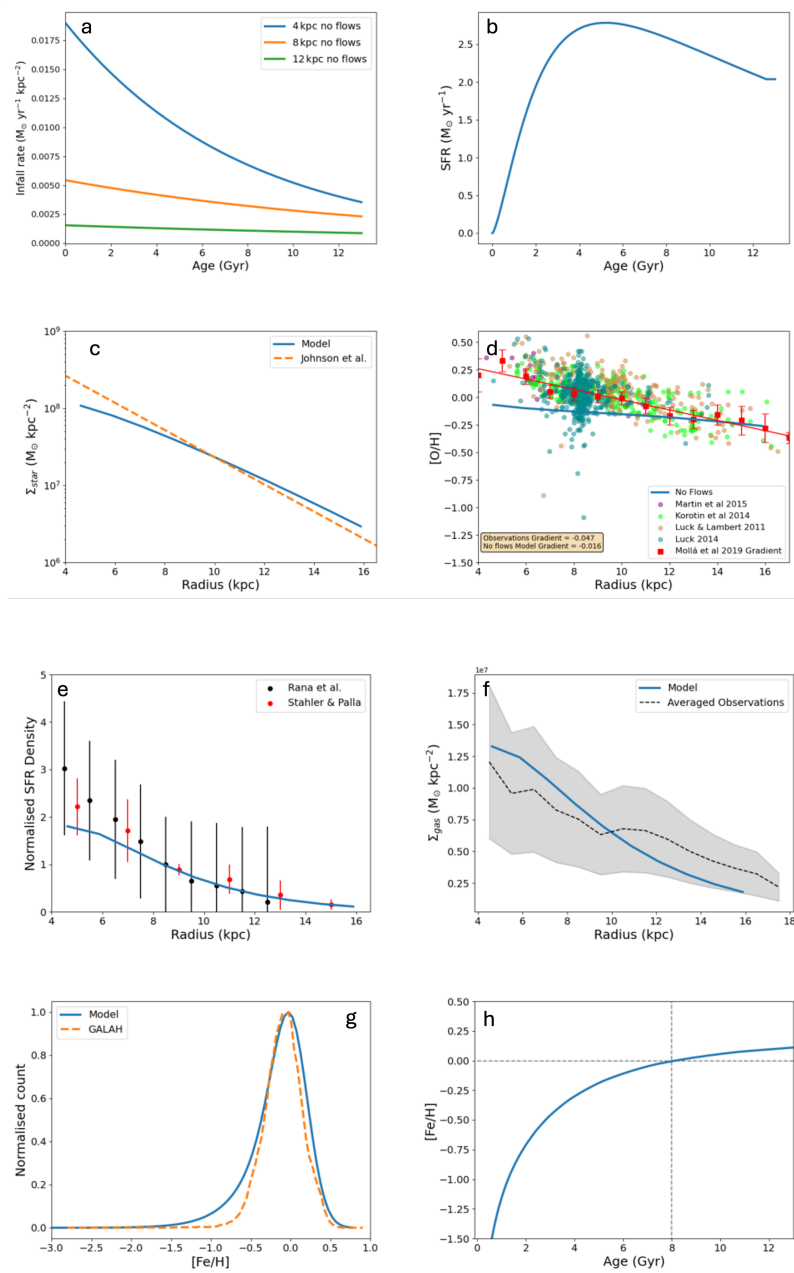


Figure 5.3: Key diagnostic plots when filtering for a good MW-like model. Panel a: Infall rate density versus galactic age at 4kpc (blue line), 8kpc (orange line) and 12kpc (green line), Panel b: SFR versus galactic age for the model, Panel c: Stellar surface density of the model (blue line) compared to Johnson et al. (2021) (orange dashed line), Panel d: [O/H] radial gradient for the model (blue line) compared to observations from Mollá et al. (2019) (see references therein), Panel e: Normalised SFR density gradient at the present time for the model compared with observations (Rana 1991, Stahler & Palla 2005), Panel f: Gas surface density of the model (blue line) compared with observations (black line is the averaged HI and HII abundance of Dame 1993, Nakanishi & Sofue 2003, 2006), Panel g: Metallicity distribution function of the model (blue line) compared to GALAH dwarfs (Buder et al., 2021) (orange line), Panel h: Age-metallicity relation of the model (blue line) compared to the solar abundance (grey dashed lines).

When determining if a model was successful, SFR was not a defining factor. We note here, that though the global SFR gives us an idea of the general trend across the disc, each annulus will have a different SFR, due to the differing gas surface density of each zone. This is illustrated in Figure B.1a which shows SFR versus galactic age for approximately the 4 kpc, 8 kpc and 12 kpc zones. As expected, the SFR in the inner zones (4 kpc and 8 kpc) is higher than in the outer zones. The SFR of the inner zones also peaks earlier, this is due to the way gas falls into the disc. Gas is accumulated more quickly in the inner zones at earlier times (see panel a), so we see an earlier peak in the star formation.

Panel c

The stellar surface density gradient was studied in panel c. The model is compared with the stellar surface density gradient calculated in Johnson et al. (2021). The solid black line in figure 6 of Johnson et al. (2021) is the stellar surface density gradient found by Bland-Hawthorn & Gerhard (2016) renormalised to their stellar mass. The slope of the Johnson et al. (2021) gradient is $-5.8 \times 10^7 M_{\odot} \text{kpc}^{-3}$, while the slope of the model displayed in Figure 5.3 is $-9.22 \times 10^6 M_{\odot} \text{kpc}^{-3}$. The approximate range of gradients across the 283 models is -9.22×10^6 to $-8.02 \times 10^6 M_{\odot} \text{kpc}^{-3}$. This narrow range of slopes compared to the slope of Johnson et al. (2021) means this was also not a strong diagnostic when determining the success of a model.

Panel d

The abundance gradient [O/H] vs R has been explored in detail by Mollá et al. (2019), who gathered [O/H] abundances from a variety of stellar sources (e.g. HII regions, open clusters, planetary nebulae), here we use the sample of Cepheids. Cepheids are an ideal object with which to compare our models because they are relatively short-lived. When we observe Cepheids, their abundances reflect the present-day composition of the galactic gas (Luck et al., 2013), which is ideal when studying ‘present-day’ radial gradients from the model. The gradient of the observations is $-0.047 \text{ dex kpc}^{-1}$, while the gradient of the model is $-0.016 \text{ dex kpc}^{-1}$. The model gradient is significantly shallower than the observations, which is also the case in Figure B.2 and across the board for all models tested. The range of oxygen abundance gradients for the 283 models tested was $-0.019 \text{ dex kpc}^{-1}$ to $-0.011 \text{ dex kpc}^{-1}$.

Therefore, we also could not use this as a strong diagnostic tool.

Panel e

Panel e shows the SFR density normalised to the SFR density of the solar neighbourhood annulus. We use the same approach as [Palla et al. \(2020\)](#), comparing with observations from [Rana \(1991\)](#) and [Stahler & Palla \(2005\)](#). The model used in [Figure 5.3](#) reproduces the observations well as it has both a similar shape and cuts through all the error bars from the observational data. In contrast, [Figure B.3](#) has a flat trend at inner radii, meaning it does not match the observations. This was also the case for other unsuccessful models, meaning this relation could be used to help determine which models were more MW-like than others.

Panel f

Once again using the approach of [Palla et al. \(2020\)](#), we compare the gas surface density from our model with observations from [Dame \(1993\)](#) and [Nakanishi & Sofue \(2003, 2006\)](#). We follow the prescription of [Palla et al. \(2020\)](#), taking the average of the three sets of observations, with the uncertainty going as either 50% of the average or half the difference between the minimum and maximum values in each radial bin, if larger. The averaged observations are represented by the black dashed line, while the uncertainty is represented by the grey shaded area. In [Figure 5.3](#), we see the model falls well within the observational uncertainty and is thus a successful model. However, the model in [Figure B.4](#) does not fall within the uncertainties, though it is close as all the models we rejected fell only slightly outside of the uncertainties at outer radii. Whether a model fell outside of the uncertainties gave us a strong diagnostic tool when deciding which models to reject.

Panel g

Panel g shows the metallicity distribution function of the solar neighbourhood zone of the model compared to that of GALAH ([Buder et al., 2021](#)). To generate the MDF from the GALAH data, we selected only dwarf stars using the following criteria: $4200 < T_{\text{eff}} < 6700$, $3.5 < \log(g) < 4.5$, $S/N > 40$ as well as the quality cuts $\text{flag_sp} = 0$, $\text{flag_fe_h} = 0$, $\text{flag_repeat} = 0$ in order to exclude any stars with flags on their stellar parameters or $[\text{Fe}/\text{H}]$ abundance. We select only dwarf stars in order to ensure reliable $\log(g)$ values (see [Griffith et al. \(2021\)](#) for an example of similar sample selection). After making the cuts, we removed any binaries

using information from [Traven et al. \(2020\)](#). The figure shows that the peaks match well with each other but the shape is different as the modelled MDF is slightly wider than the observations. The MDF of the model could be wider because we do not account for stellar migration, therefore, more metal poor stars that would have otherwise migrated out of the zone, remain in the zone in which they were born. We reject any models whose peaks do not align with the peak of the GALAH observational data, as seen in the distinctly separate peaks of [Figure B.5](#).

Panel h

The final panel (panel h) shows the age-metallicity relation of the solar neighbourhood. Ideally, the model should be able to reproduce the solar abundance, at the time of the formation of the sun - where the grey dashed lines intersect, as is the case for the chosen model. Whereas, [Figure B.6](#) shows a model which overproduces the solar abundance at the time of the sun's formation. This makes the age-metallicity relation a useful diagnostic.

From the comparison of the figures, it is clear that some diagnostics are more influential than others when determining the success of a model. The normalised star formation rate density (panel e), surface gas density (panel f), MDF (panel g) and age-metallicity relation (panel h) were the key diagnostics that we used to decide whether a model was an appropriate Milky Way-like choice. For a more detailed look at the model parameters that most strongly affected these diagnostics, see [section 5.4](#).

5.3.1 Effect of radial gas flows

Since radial gas flows are known as being important for galaxy evolution (e.g. [Mayor & Vigroux 1981](#), [Edmunds & Greenhow 1995](#), [Spitoni & Matteucci 2011](#), [Grisoni et al. 2018](#)), it is important to develop a MW-like model which includes this component. We use the multi-zone model described in [section 5.2](#) and apply a constant radial flow of 1 km s^{-1} (e.g. [Lacey & Fall 1985](#)). When we include this radial flow, there is a strong impact upon the majority of diagnostic plots presented in [Figure 5.3](#), with some exceptions. [Figure 5.4](#) shows the chosen MW-like model from the previous section both with and without radial gas flows.

We can see immediately that some diagnostics are more impacted than others by the addition of radial gas flows.

The most obvious similarity between the two models is illustrated by panel a. As none of the infall parameters have changed, the infall rate density for the flows remains identical to the no flows model, as the addition of radial gas flows does not have an impact on the infalling gas. From panel b, we can see the flows model has a reduced star formation rate compared with the no flows model. Though some regions of the disc will gain mass due to radial gas flows, most will see a decrease in gas surface density due to the addition of radial flows (as observed in panel f) - even the inner zone still loses some mass via radial flow. A decrease in gas surface density results in decreased star formation (see Equation 5.8), thus we see a decreased SFR. We can see the impact of a reduced SFR on the relations when we consider specific abundance ratios. Panel d shows the [O/H] abundance radial gradient, which is 0.2-1 dex lower for the flows model compared with the no flows model, due to the reduced SFR in combination with the movement of metal-rich material into the inner zones of the disc. This effect can also be observed in panel h, the solar neighbourhood age-metallicity relation, there is a reduction in the [Fe/H] abundance as the galaxy evolves. The impact of reduced [Fe/H] abundance can be seen in the MDF in panel g, as the peak is shifted by approx 0.5 dex. However, this effect is also due to the movement of metal-rich material into the inner zones. A proportion of any metal rich material generated in the solar neighbourhood zone in the later stages of the disc's evolution, will be carried into the inner zones by the radial gas flow, shifting the peak of the MDF to be slightly more metal poor than we would expect.

Panel c shows the stellar surface density gradient, which clearly becomes steeper at outer radii as the stellar density reduces. The sharp decline in gradient observed in both panel c and d is due to the outermost zone losing mass via radial flows but not gaining any to replenish the gas lost, causing a low surface density of material (as observed in panel f). Low surface density causes reduced star formation rate, hence both a reduced stellar density and abundance ratios (due to lack of stars producing those elements). As a result of the radial gas flow, 99% of the mass in the disc is contained within the first 9 zones therefore, when we calculate the slope of the radial gradients of any flow model, we do not include the final zone

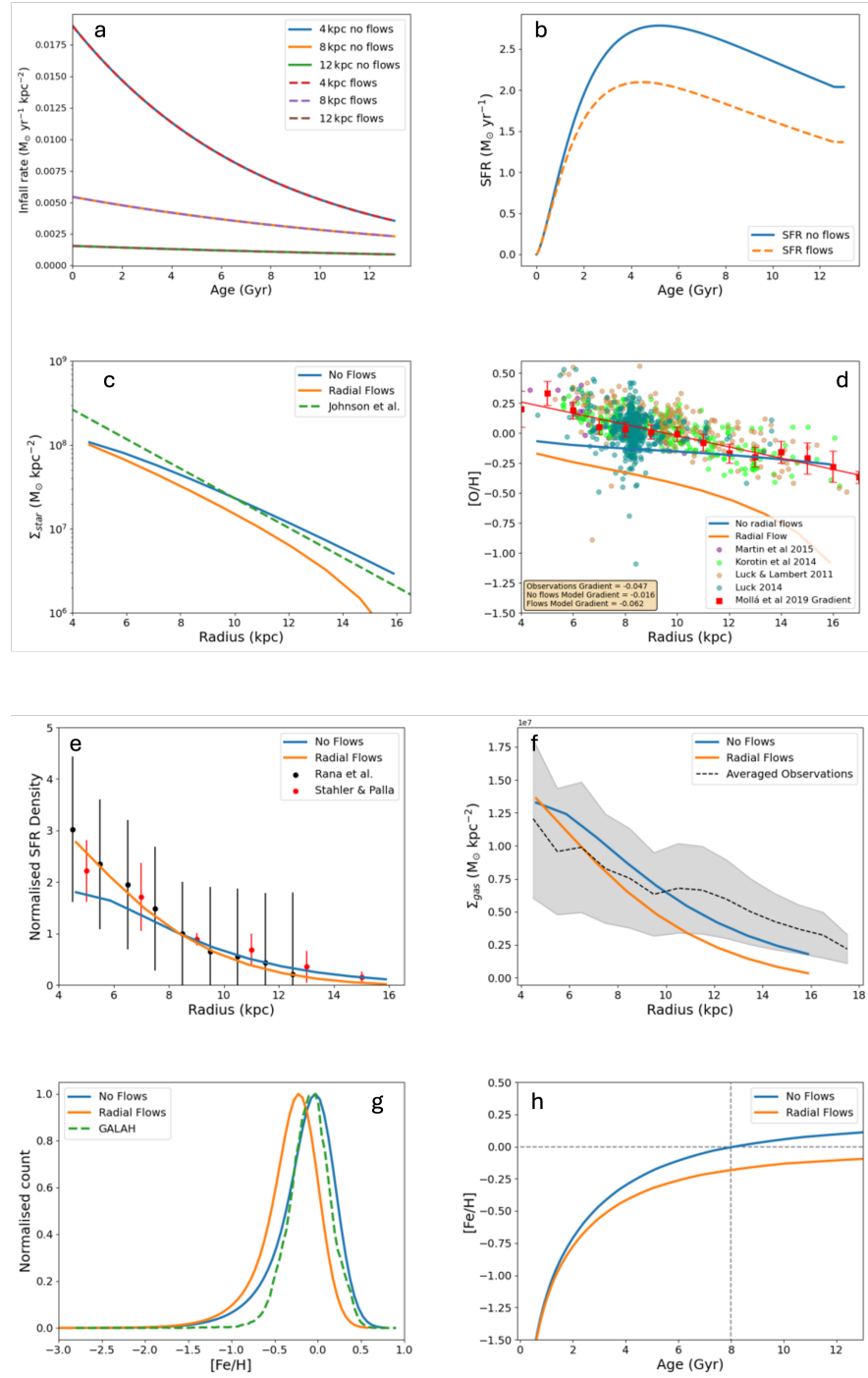


Figure 5.4: As Figure 5.3 but this time with the addition of a 1 km s^{-1} radial flows model which otherwise has the same properties as the no flows model. Panel a: Infall rate density versus galactic age at 4kpc (no flows: blue line, flows: red dashed), 8kpc (no flows: orange line, flows: purple dashed) and 12kpc (no flows: green line, flows: brown dashed), Panels b-h show the no flows model in blue and the flows model in orange. Panels c and g show the Johnson et al. (2021) and the GALAH data respectively in green dashed lines.

in the calculation. The gradient of the flows model in panel c is $-9.84 \times 10^6 M_{\odot} \text{ kpc}^{-3}$, this is steeper than the no flows model, and more in line with [Johnson et al. \(2021\)](#) (green dashed line). However, we can see the model sits much lower than the [Johnson et al. 2021](#) model, again likely due to the reduced SFR.

The gas surface density displayed in panel f drops below the observations of [Dame \(1993\)](#) and [Nakanishi & Sofue \(2003, 2006\)](#) at outer radii. This is due to the effect described above in which the outermost zone only loses gas via radial gas flows and does not receive any. As the simulation evolves, this causes the surface density in the outermost zone to reduce, meaning there is less gas in the zone that can be transported into the neighbouring inner zone via radial flow causing slightly reduced gas surface density in the next zone. Arguably the most successful panel of Figure 5.4 is panel e, the normalised SFR density gradient. The model produces a smooth curve, reproducing the data points, not just the error bars, as it is steeper at inner radii. The success of this diagnostic can again be attributed to the transport of material towards the inner zones.

Having looked at what happens when radial gas flow is added without changing the other parameters, it is clear that to better simulate the Milky Way, we need to alter the values of the parameters we are considering (M_{inf} , f_{\star} , a and b). Again, we found the most appropriate yield set for the model by finding the best fit to the [O/H] gradient using the no flows model as the fiducial set of parameters. In this instance, we found the AGB yields of [Cristallo et al. \(2015\)](#) in combination with the mixed rotation massive star yields of [Limongi & Chieffi \(2018\)](#), along with the same [Iwamoto et al. \(1999\)](#) SNIa yields worked well. We performed another parameter study to find a range of parameters that can be employed when including radial flows in the model. When using the original set of parameters, we find disc scale lengths and surface densities outside of the range that we require. As we are losing mass through the inner zone, we increase the range of M_{inf} that we are investigating to rectify this issue. The new range is $2.5 \times 10^{10} < M_{\text{inf}} < 3.5 \times 10^{10} M_{\odot}$. The range of f_{\star} is also expanded to encompass the full range of possibilities from [Kennicutt \(1998\)](#) ($1.8 \times 10^{-4} \leq f_{\star} \leq 3.2 \times 10^{-4} (M_{\odot} \text{ yr}^{-1} \text{ kpc}^{-2})$). We generate 450 models to be reduced using the same selection process outlined previously. After filtering for scale length and surface densities,

the number of models is reduced to 29. The criteria for a ‘good’ MW model when assessing the diagnostic plots also remain the same, however, note that for all viable models, the gas surface density Σ_{gas} , falls below the observations at outer radii. Once the the diagnostic plots were assessed, we found all 29 models are MW-like but take up a smaller range of the parameter space ($2.75 \times 10^{10} < M_{\text{inf}} < 3.1 \times 10^{10} M_{\odot}$, $2.5 \times 10^{-4} < f_{\star} < 3.2 M_{\odot} \text{ yr}^{-1} \text{ kpc}^{-2}$, $-2 < a < -1 \text{ Gyr}$ and $1.5 < b < 2 \text{ Gyr kpc}^{-1}$). We again settled on the model which used values of the parameters that appeared most frequently across the acceptable models, verifying that combination was also an acceptable model. Therefore, for the MW-like model including radial flows, we adopt a model with a solar-neighbourhood total mass surface density of $48.6 M_{\odot} \text{ pc}^{-2}$ and a gas surface density of $6.1 M_{\odot} \text{ pc}^{-2}$. The choices of M_{inf} , f_{\star} , a and b , can be found in Table 5.1.

The key diagnostic plots for the chosen model can be found in Figure 5.5 compared with the no flows model. It is immediately clear that allowing each model to have different parameters results in reaching a better agreement in both cases.

The three major changes between the no flows and the flows model is the increased infall mass across the length of the simulation, the increased star formation efficiency (and thus SFR) and the addition of the 1 kms^{-1} radial gas flow. Each of these three changes has a significant impact on the eight diagnostic plots. Firstly, the increased infall mass across the disc will naturally increase the amount of mass available in each zone and thus, the overall gas surface density. An increased gas surface density increases the star formation rate which, coupled with the increased star formation efficiency, will enhance the SFR in all zones. The effect of introducing radial gas flow has already been explored earlier in this section when comparing the models shown in Figure 5.4. However, the impact can be seen more profoundly in Figure 5.5 as the enhanced mass and SFR contribute to the the efficacy of introducing radial flows in developing a successful model. Introducing a radial flow increases the mass in the inner zones more than it will in the outer zones because the more mass that exists in a zone in general, the more mass there is available to be migrated inward via radial gas flow. As mass accumulates in the inner zones, the gas surface density increases, which increases the SFR, in turn increasing the stellar surface density. All of this contributes to more enhanced

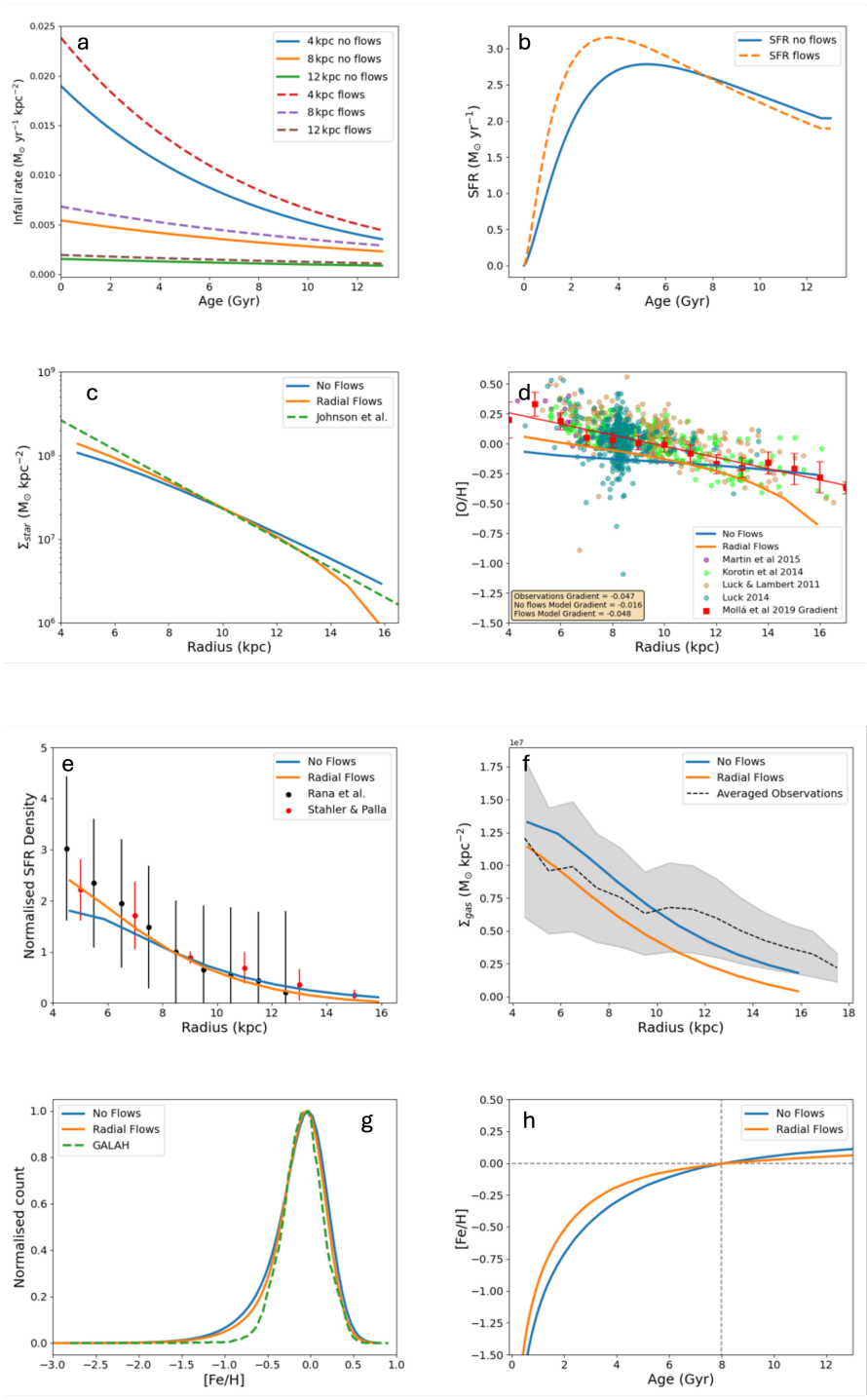


Figure 5.5: As Figure 5.4 but this time comparing the two final MW-like models both with (orange lines) and without (blue lines) radial gas flows.

abundance gradients (as seen in panel d, Figure 5.5), however, we remind the reader that a different yield set is employed between the two models, which may also have a secondary impact on the abundance ratios explored in panels d, g and h. The impact of these global trends can be observed in each of the eight panels of Figure 5.5.

Panel a

The infall rate density for the flows model shows a similar shape and trend to the no flows model but sits much higher for each radius. This change is solely due to the increased infall mass M_{inf} between the two models as more infalling mass will increase the infall rate density. The parameters controlling the infall, a and b , have remained unchanged between the two models and are thus not responsible for any differences which occur.

Panel b

In panel b, we see an increased star formation rate at earlier times for the flows model compared to the no flows model, the reason for this is likely two-fold. First, the star formation efficiency f_{\star} is increased, therefore we would expect enhanced SFR. Secondly, the reason the SFR peaks earlier is because more mass has fallen onto the disc at earlier times for the flows model in comparison with the no flows model due to the increased M_{inf} . The SFR of the flows model is slightly reduced at later times compared to the no flows model, this is likely due to the increased amounts of mass lost due to radial flows in all zones at later times. These trends are also largely replicated when we investigate the SFR for individual annuli. Figure B.1b shows the SFR of the no flows and flows models at approximately the 4 kpc, 8 kpc and 12 kpc zones. We see the SFR peak slightly earlier for each of the flows models compared to the no flows models and the SFR of the flows model at later times is less than that of the no flows model for both the 8 kpc and 12 kpc zones. However, this is not the case for the 4 kpc zone, where the SFR at later times remains greater than the no flows model. As the 4 kpc zone is the innermost zone, the gas surface density is consistently higher due to the concentrated mass from infall and the strong radial gas flows into this zone thus, the SFR remains higher than when radial flows are not included.

Panels c and d

These plots can both be explained by the same effect. The stellar surface density gradient and

the [O/H] gradient are both steeper due to the increased stellar density at inner radii as a result of higher gas surface density. In the case of panel c, the greater the SFR, the greater the stellar density, while for panel d, the more stars available in a zone, the more of an element will be produced. The [O/H] gradient also becomes steeper due to the movement of more metal-rich gas into the inner zones at later times.

The gradient of the stellar surface density in panel c is much closer to the [Johnson et al. \(2021\)](#) slope than the no flows model, with a gradient of $-1.37 \times 10^7 M_{\odot} \text{ kpc}^{-3}$. The [O/H] gradient of the flows model is significantly steeper than the no flows model and much more comparable to both slope and the data points of the [Mollá et al. \(2019\)](#) observational sample.

Panel e

The shape of the normalised SFR density follows the same physical explanation as panel e of Figure 5.4.

Panel f

In panel f, we see that the gas surface density is indeed greater in the inner zones. We also see that the gas surface density of the flows model is lower than the no flows model as a result of the radial gas migration carrying gas out of every zone. Hence, the flows model falls below the range of observations.

Panels g and h

We know from Figure 5.4 that an introduction of radial gas flows reduces the [Fe/H] abundance as metal rich material gets carried toward the inner zones. Previously, this meant the flows model sat lower than the no flows model in panel h (Figure 5.4). However with the addition of more mass via infall and an increased star formation rate, the flows model is able to successfully reproduce the MDF from GALAH (green dashed line) and the solar abundance at the time of the formation of the sun (solar neighbourhood age-metallicity relation).

Our model is also comparable with models in the literature. [Palla et al. \(2020\)](#) performed a similar study attempting to find a model which can match Milky Way abundance and SFR gradients. They found in order to reproduce observations, inside-out formation of the disc is not enough and radial gas flows or variable star formation efficiency (SFE) with radius must be included in the models. Their models E and F were found to reproduce the observational

constraints (O, N, Fe and Mg abundances and star formation rate) the best, with model E including a radial gas flow which varies with galactocentric radius and time. Meanwhile, model F uses an inward radial flow velocity of 1 km s^{-1} and variable SFE making it similar to the flows model developed in this section. Both our model and model F of [Palla et al. \(2020\)](#) can reproduce the same set of observations of SFR density in the disc (see panel e of Figure 5.5 above). The oxygen abundance gradient of model F is $-0.0734 \text{ dex kpc}^{-1}$, our gradient is $-0.047 \text{ dex kpc}^{-1}$, while the gradient of the observations is $-0.0539 \text{ dex kpc}^{-1}$ for the HII regions and $-0.0497 \text{ dex kpc}^{-1}$ for the Cepheids. Therefore, our model performs slightly better at reproducing the gradient of the oxygen abundance observations, though both models are able to well reproduce the observations when compared by eye.

Property	Observational Data	No Flows Model Value	Flows Model Value
SFR ($M_{\odot} \text{ yr}^{-1}$)	0.65 - 3.0	2.3	1.9
CCSNe rate (yr^{-1})	1.0×10^{-2} - 3.0×10^{-2}	1.9×10^{-2}	1.8×10^{-2}
SNe Ia rate (yr^{-1})	0.2×10^{-2} - 0.6×10^{-2}	0.2×10^{-2}	0.2×10^{-2}

Table 5.2: Present day SFR, and supernovae rate values from the model compared with observational constraints from [Kubryk et al. \(2015\)](#).

Our models also do well at reproducing present day observational constraints. Table 5.2 shows the present day SFR, CCSNe and SNe Ia rates from the models compared with observational constraints from [Kubryk et al. \(2015\)](#). We can see that both the no flows and flows model fall within the observational ranges for each of the three constraints, showing again that these are successful Milky Way like models.

5.4 Sensitivity Study

5.4.1 Varying the key parameters

In order to understand how the parameters that we varied affect the key diagnostic plots, we performed a sensitivity study. We present a series of eight-panel figures which investigate the impact of varying one parameter at a time. For this part of the sensitivity study, we use the no flows MW model described in the previous section. Using the no flows model minimises

the complexity of the discussion as we do not need to consider the impact of the radial gas flows on each of the diagnostic plots, allowing us to concentrate purely on the impact of the parameter in question.

In our discussion, for each parameter, we will focus on the diagnostics which show a large difference between each of the models to highlight where and how each parameter has the most profound influence. Therefore, there will be some panels of each figure (Figures 5.6 - 5.10) which will not be discussed in detail here.

First, we vary the mass of the infalling gas M_{inf} . We select four different values of M_{inf} : the extremes of the ranges used for the parameter studies and the two values used for both the no flows and flows models (see Table 5.1). The four M_{inf} values chosen are: 2×10^{10} , 2.4×10^{10} , 3×10^{10} and $3.5 \times 10^{10} M_{\odot}$. Figure 5.6 shows the eight-panel diagnostic plots for four models each using a different M_{inf} . The figure design is almost identical in nature to those presented in the previous section with the exception being panel a. Instead of panel a showing the infall rate density at three different radii, we show the infall rate density at approximately 4 kpc for each of the four models. This style of figure for infall rate density will be the same for the other figures presented in this section (Figures 5.7 - 5.10).

The most notable difference between each model in Figure 5.6 is the infall rate density (panel a). As we would expect, the models with larger M_{inf} sit higher in the plot, though they appear to have similar slopes as the infall parameters (a and b) have not changed. The SFR (panel b) is higher for those models with higher infall mass as there is more mass available to make stars. This results in a higher stellar surface density (panel c), than those with lower infall mass. An increased M_{inf} also results in higher surface gas density in each zone (panel f) as there is more gas distributed across the disc. The remaining panels d, e, g and h do not show a significant difference between each of the models. For panels d, g and h, there are minimal differences between each model as the yield table has not changed and the effect of the different infall masses is likely not strong enough to significantly impact the elemental ratios, even though the overall SFR is effected. Panel e shows the normalised SFR density, which, we remind the reader, means the SFR for each zone is normalised to the solar neighbourhood value. Again, though the infall mass does impact the overall SFR throughout the evolution of

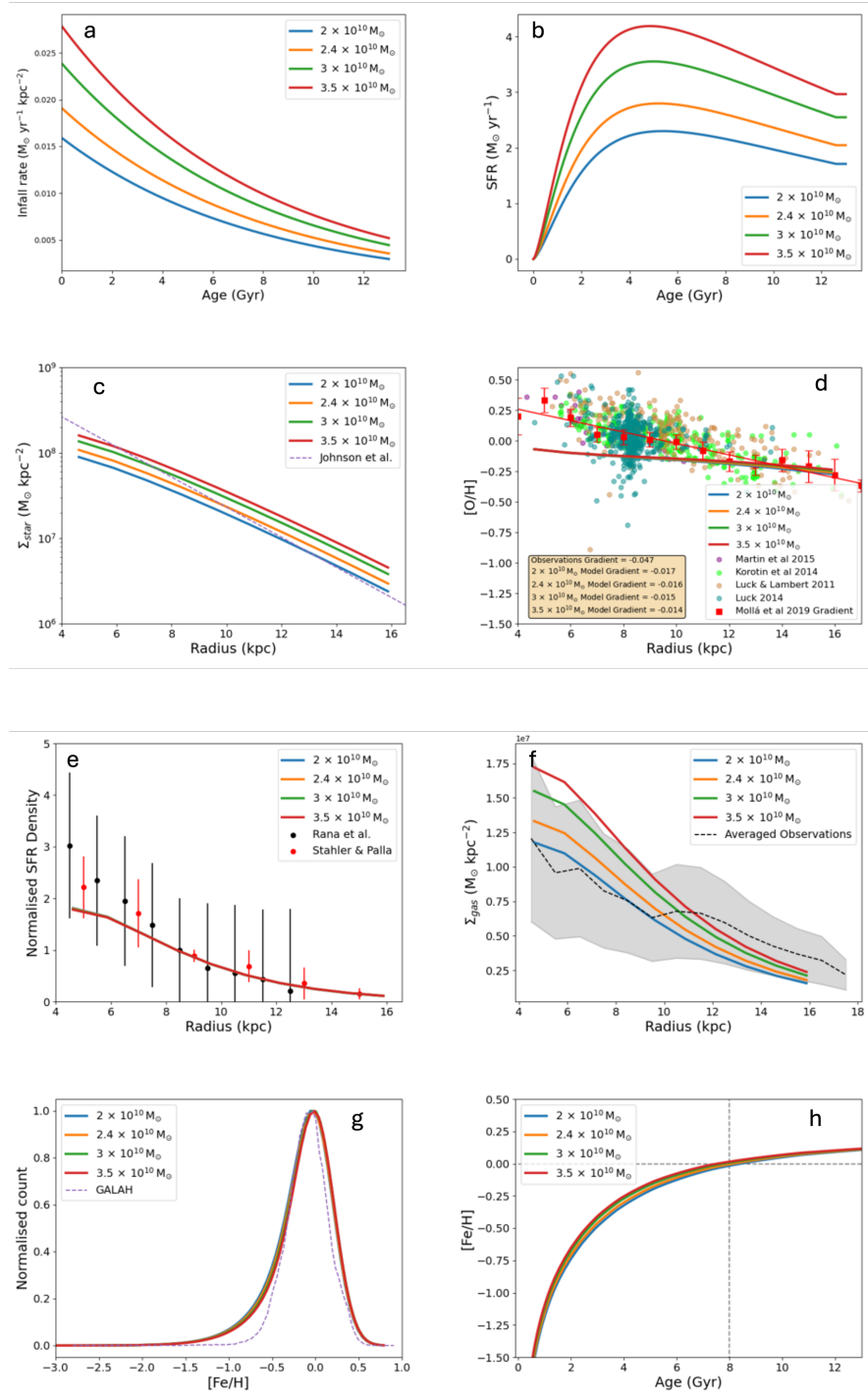


Figure 5.6: Key diagnostic plots when varying M_{inf} . All panels as Figure 5.3 with the exception of panel a, which instead shows the infall rate density of the 4 kpc zone for each model.

the disc, when it becomes normalised for each zone, we are able to match the observations.

The star formation efficiency is the next parameter to be varied. Again, we use the two extremes from the parameter study and the values used by the no flow and flows models (Table 5.1). However, the MW flows model uses the highest f_{\star} ($3.2 \times 10^{-4} \text{ M}_{\odot} \text{ yr}^{-1} \text{ kpc}^{-2}$) already, therefore, we select an intermediate value instead. The four f_{\star} values chosen are: 1.8×10^{-4} , 2×10^{-4} , 2.6×10^{-4} and $3.2 \times 10^{-4} \text{ M}_{\odot} \text{ yr}^{-1} \text{ kpc}^{-2}$. Figure 5.7 shows the diagnostic plots when varying f_{\star} . As there is no difference in infall between the models, their infall rate densities are identical (panel a). As expected, it is clear that varying the star formation efficiency has the most profound impact on the SFR trends shown in panel b. The model with the largest f_{\star} has a higher star formation rate, which peaks slightly earlier, in a similar fashion to Figure 5.5. However, this earlier peak cannot be attributed to a higher infall mass as previously and must purely be as a result of the increased star formation efficiency, as gas is consumed to make stars at an increased pace, shifting the SF peak to earlier epochs. The other more notable difference between the models is displayed in panel f, the surface gas density radial gradient. Here, we can see that the model with the lowest f_{\star} has the highest gas surface density. This arises as reduced star formation will leave more gas available in the disc. Similarly to the previous figure, we see minimal change in the normalised SFR density (panel e). There are more noticeable differences between the models in panels e, g and h. The MDF (panel g) is slightly shifted to the right for the models with higher f_{\star} , due to the more efficient star formation resulting in an increased [Fe/H] stellar yield. We see a similar effect in panel h, where the age metallicity relation shows that, particularly at earlier ages, high f_{\star} results in high [Fe/H] ratios. Finally in panel d, we see a separation between the models, particularly at outer radii. At the outer regions, there is generally less gas available, leading to reduced star formation and thus reduced stellar surface densities. We can see some separation in the stellar surface density of each of the tested models at the outer regions (panel c), which translates to the separation in panel d. The regions with higher stellar surface densities will yield increased [O/H].

We also study the effect of varying the infall timescale at the galaxy centre, a . Here, we use the two extremes of the range as well as two extremes outside the range to illustrate

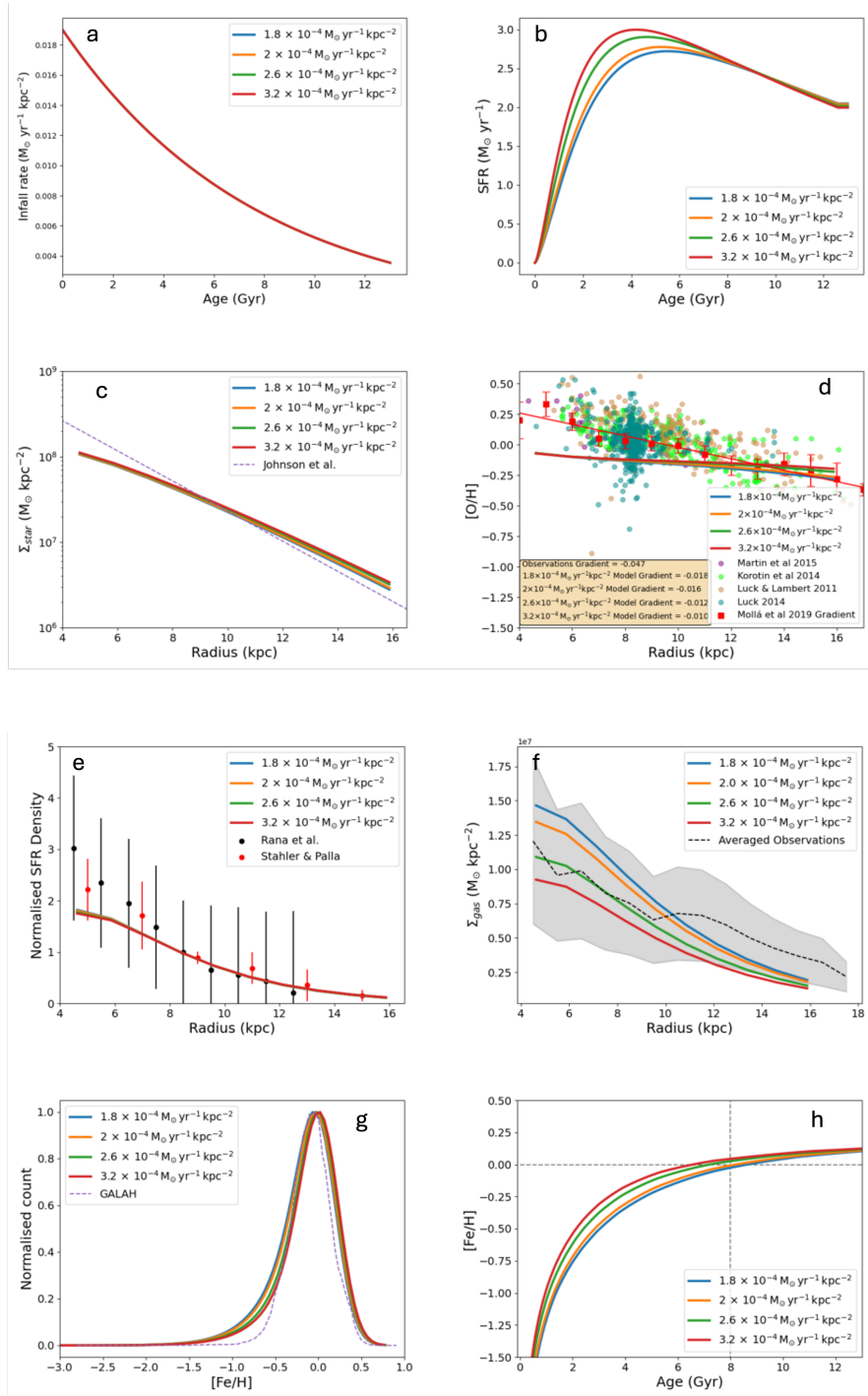


Figure 5.7: As Figure 5.6 but varying f_{\star} .

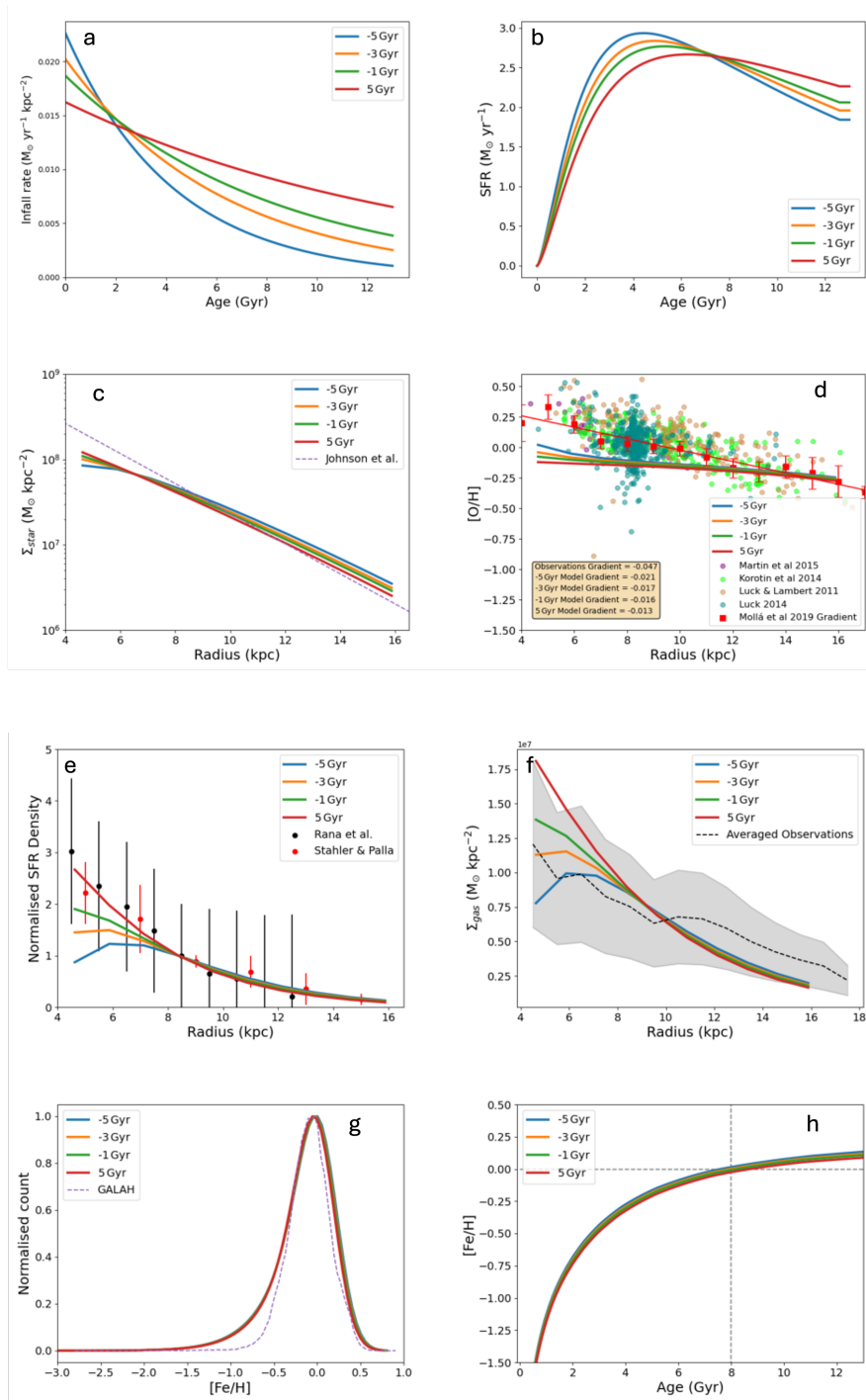


Figure 5.8: As Figure 5.6 but varying a.

the way in which this parameter controls the infall rate density. The chosen values were as follows: -5, -3, -1 and 5 Gyr. Figure 5.8 shows the eight diagnostic plots when varying a . As expected, varying a has the strongest impact on the infall rate density. We can see that the lowest value (blue line) has the steepest gradient at earlier ages. As a becomes less negative, the curve is shallower, meaning more mass is distributed across the disc at earlier ages. When a becomes positive (red line) there is a shallower and straighter trend. Again, we see some of the modelled SFR peaking more strongly and at earlier times due to having more gas in the disc at earlier ages. There are notable differences between the models in panels e and f, the normalised SFR density gradient and the gas surface density gradient, respectively. These radial gradients can be better explained if we also look at the infall rate density of some of the outer radii. The infall rate density of the models for the 8 kpc and 12 kpc zones are presented in Figure B.7. In panels e and f, there is a notable ‘bend’ in both the blue and orange model lines at inner radii, representing the two models with the lowest values for a . It is likely we see a reduced present-day gas surface density (and thus normalised SFR) due to the low infall rates at inner radii at later times in comparison with the other models. At outer radii (Figure B.7) we see the infall rate density increase for these models, while it decreases for those with larger values of a (green and red lines).

The final parameter to be individually varied is the gradient of the infall timescale, b . Larger absolute values of b mean that there is a larger difference in the infall timescale between two adjacent rings. Positive values of b mimic an inside-out formation of the disc as inner regions have shorter infall timescales than the outer ones, whereas negative values correspond to an outside-in formation. As above, we use the two extremes of the range as well as the two extremes outside the range. The chosen values were as follows: -5, 1, 2, 10 Gyr kpc⁻¹. Figure 5.9 shows the eight-panel diagnostic plots figure when varying b . Again, we see that increasing b causes straighter, shallower trends, as long as b remains positive. If b becomes negative (blue line) the slopes become positive, showing an outside-in formation as described above. The impact of this can be observed in panel b, where we can see that the lowest and highest values (blue and red lines respectively) mean the SFR does not follow the typical SFR curve. The blue line ($b = -5$ Gyr kpc⁻¹) shows what happens to the SFR when

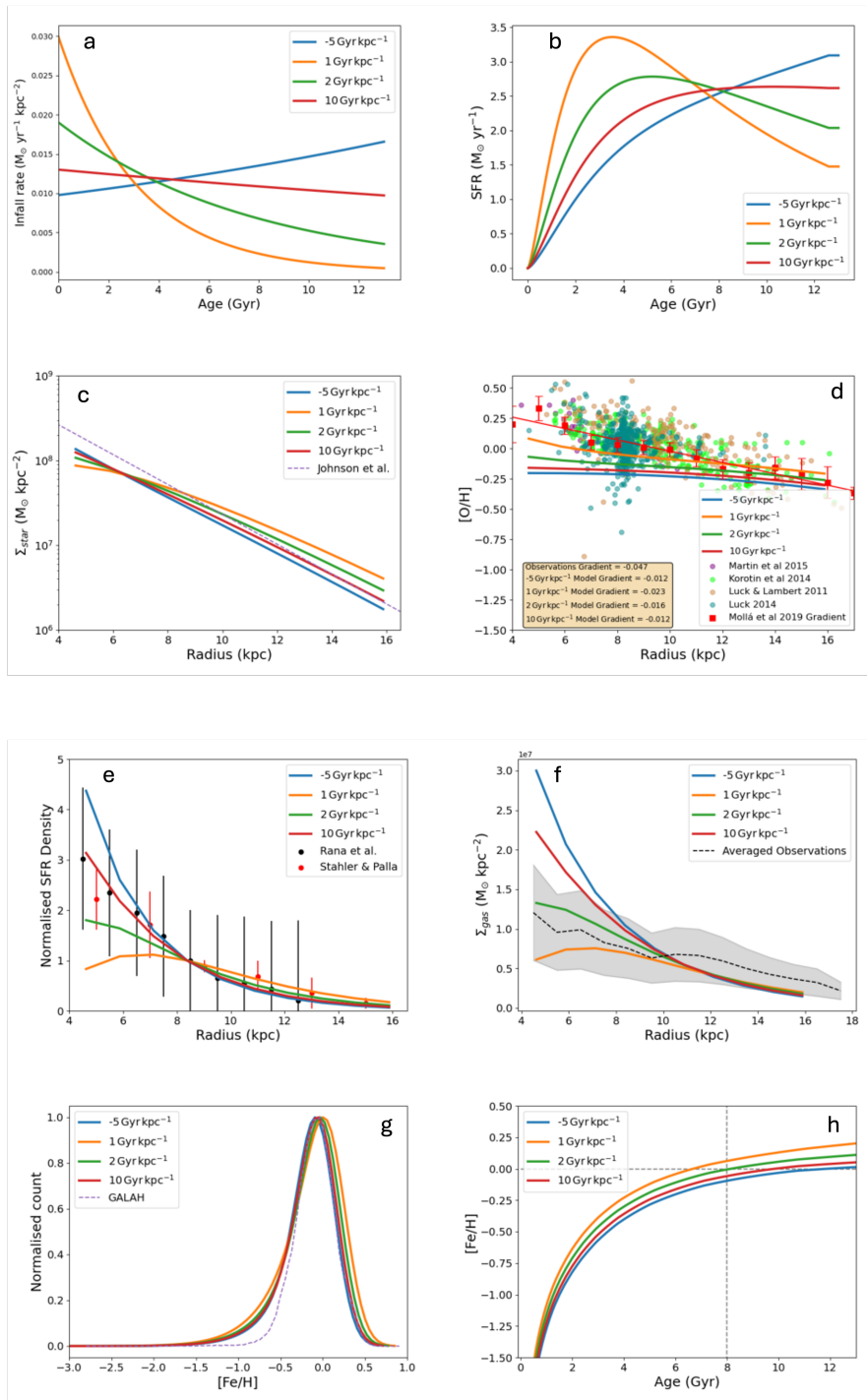


Figure 5.9: As Figure 5.6 but varying b.

we consider an outside-in scenario. We see a positive slope of the SFR, with an increased SFR at later times. This is due to the outside-in formation causing the infall rate to increase at later times, causing star formation to increase until the end of the simulation. The drastic differences in star formation rate have the most clear affect in panels g and h, where we can see a distinct difference in the [Fe/H] abundance. The model using 1 Gyr kpc^{-1} (orange line) has the greatest abundance of [Fe/H], likely due to the larger SFR at earlier times. We again observe the ‘bend’ in panels e and f due to the low infall rate density for the mid-range models (orange and green lines).

5.4.2 Varying radial flow velocity

We also want to investigate how a change in radial flow velocity can change the key diagnostic relations. Here, we will use the flows model described in the previous section and vary the v_{rad} parameter, keeping everything else constant (parameters can be found in Table 5.1). We choose four values for $v_{\text{rad}} = 0.5, 1, 2$ and 5 km s^{-1} , to illustrate halving and doubling the flows models $v_{\text{rad}} (1 \text{ km s}^{-1})$ and an extreme case in which we have a strong radial gas flow. Figure 5.10 shows the effect of varying v_{rad} for each diagnostic plot. Again, panel a uses infall rate densities for the 4 kpc region alone. The trends we observe here are similar to those considered in section 5.3 when comparing the model with and without flows. We see that a stronger flow (e.g. red line) carries too much gas out of the disc, reducing the gas surface density (panel f). A low gas surface density results in reduced SFR, which we can see in panel b, while the highest SFR arises from the model with the lowest radial flow velocity. Lower gas surface density results in lower stellar surface density (panel c) due to the lack of gas available to form stars. We can see this effect really strongly on the abundance ratios in panels d, g and h, where the metallicities [O/H] and [Fe/H] are significantly reduced for the models with the greater radial flow velocities (green and red lines). Finally, panel e the normalised SFR density shows a much steeper slope when the radial flow velocity is increased. This is likely because the SFR in the solar region will be greatly reduced compared to the inner regions of the disc as gas gets carried away from the solar neighbourhood meaning there is less available for star formation.

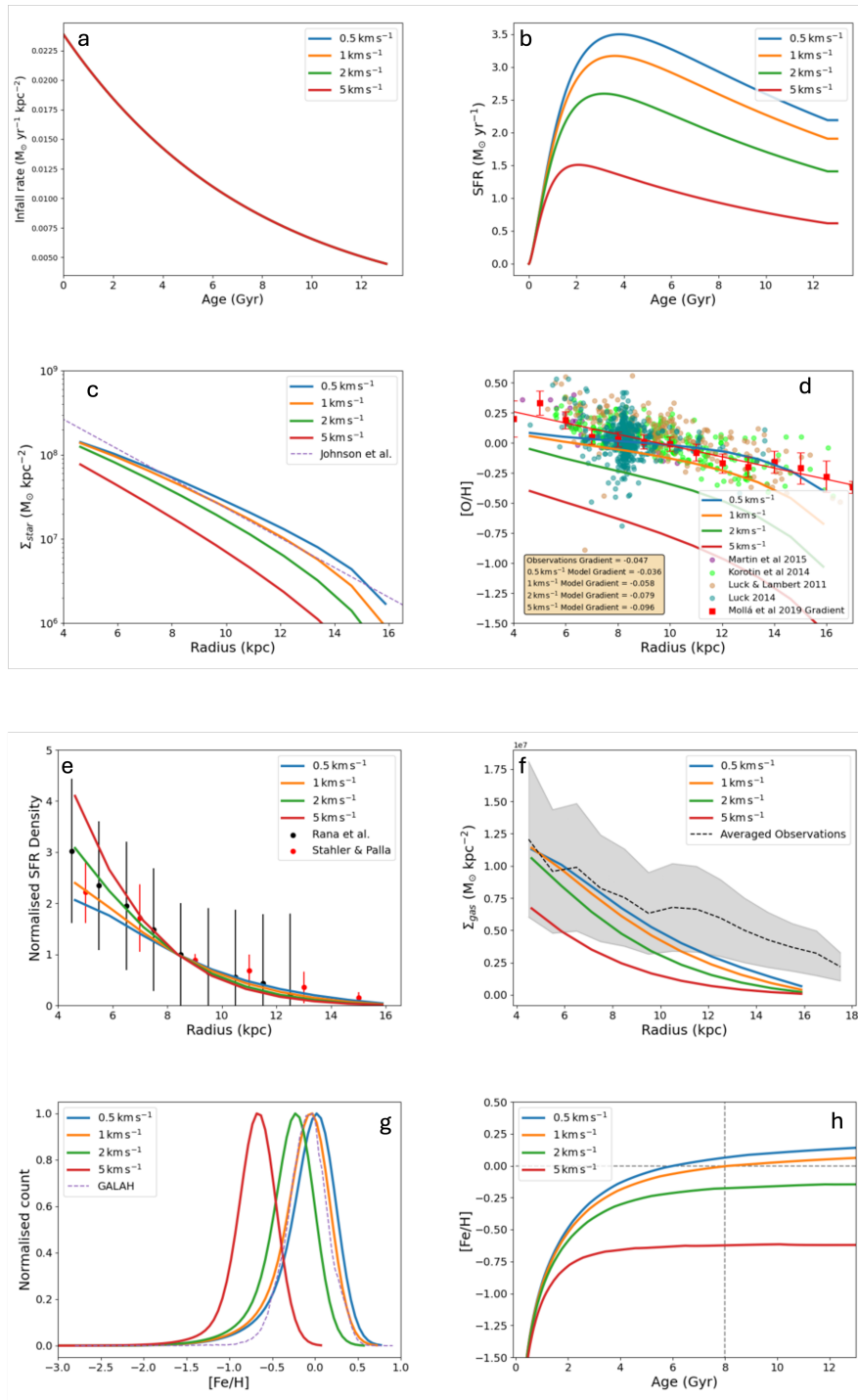


Figure 5.10: Key diagnostic plots for the flows model, varying v_{rad} . All panels as Figure 5.6.

5.5 Conclusions

We have developed ALPHA, a multizone version of OMEGA by connecting many instances of OMEGA and controlling the interactions between those zones to simulate adjacent ring-shaped annuli and including radial migration of gas between them. We have adapted the prescriptions for gas infall, star formation rate and outflow rate in order to create a model which includes a spatial information. Using the new spatial component of the model, we were able to develop a prescription for radial gas flows by allowing the user to specify a flow velocity and calculating what fraction of the mass in a zone has to migrate to the next innermost zone as a result of this flow velocity.

By employing ALPHA, we have developed a MW-like model both with and without radial flows. In both cases, we performed a parameter study to optimise the parameters chosen for each of the models. To select the final models, we used eight diagnostic plots that must reproduce MW constraints as well as possible (e.g. Figures 5.3 to 5.5). We also performed a sensitivity study to understand how varying our four key parameters (M_{inf} , f_{\star} , a and b) affects the diagnostic plots. Finally, as part of the sensitivity study, we investigated how the radial flow velocity impacted the diagnostic plots. We found the infall parameters a and b have the most profound effects on the diagnostic plots when we do not include radial gas flows, having an especially strong influence on the radial gradients of the SFR and gas surface density. However, when we include radial gas flows, we find that the flow velocity has the strongest impact on all the diagnostic plots, with the exception of gas infall rate, which naturally remains consistent between models.

The models developed in this work can now be used in order to study MW radial gradients, or specific regions on the MW disc. Beyond this work, the ALPHA code will be made publicly available to the astrophysics research community on GitHub so that other types of galaxies and models can be developed.

6. ‘Chemical Clocks’ and Milky Way Radial Gradients

6.1 Introduction

In recent years, ‘Chemical clocks’ or ‘cosmic chronometers’ have been an active field of research in galactic archaeology (e.g. [Haywood et al. 2013](#), [Bensby et al. 2014](#), [Nissen 2015](#), [Spina et al. 2016](#), [Hayden et al. 2017, 2022](#), [Casali et al. 2019, 2020](#), [Viscasillas Vázquez et al. 2022](#), [Ratcliffe et al. 2024](#)). A chemical clock is a ratio of two elements which has a tight relation with stellar age. Therefore, chemical clocks can be used to age-date stellar populations or inform us about formation timescales of different stellar populations (e.g. the thick and thin disc of the Milky Way). Determining stellar age from observations is not straightforward ([Soderblom, 2010](#)), however we can determine reliable stellar abundances. Therefore, using chemical abundance ratios to determine stellar age from observations can be a useful tool. For some stars, we can determine their ages using isochrone fitting/placement on the Hertzsprung-Russel diagram to determine their ages (e.g. [Edvardsson et al. 1993](#), [Nordström et al. 2004](#), [Holmberg et al. 2009](#), [Johnson et al. 2017](#)), this works particularly well for open clusters (OCs) and globular clusters (GCs) as well as single dwarf stars but it not so effective for single red giant stars. Red giant stars suffer from an age-metallicity degeneracy which means we cannot accurately measure their ages using isochrone fitting (e.g. [Monelli et al. 2014](#)).

Asteroseismology provided a new way to find stellar ages, especially for single, solar-like stars (e.g. [Mazumdar 2005](#), [Oti Floranes et al. 2005](#), [Kjeldsen et al. 2008](#), [Creevey et al. 2017](#), [Pinsonneault et al. 2018](#), [Miglio et al. 2021](#)). By detecting their oscillation modes, asteroseismology allows us to probe the interior of stars. However, we require accurate photometry and long baseline observations in a specific region of the sky in order to achieve accurate age determinations from asteroseismology.

The limitations of these age determination techniques mean we cannot provide ages for large samples of stars, and for those limited stars where we can, considerable effort is needed. Chemical clocks provide a way for us to determine the age of large samples of stars simply by evaluating their chemical compositions, which is much more straightforward to obtain from spectra.

A good chemical clock requires the two elements in the ratio to have different origins and to be released into the interstellar medium (ISM) on different timescales by their stellar sources. As the galaxy evolves, the ratio will also evolve and we can use the stellar abundances of a star as an indication of its age. One such example of this is $[\text{Mg}/\text{Fe}]$ (or $[\alpha/\text{Fe}]$ more generally). Magnesium, as well as other α elements, are largely produced by core collapse supernovae (CCSNe), while iron is primarily produced by Type Ia supernovae (SNIa). Stars undergoing CCSNe live and die on relatively short timescales compared to stars undergoing SNIa so there is an abundance of Mg at earlier times compared to Fe. The ratio of the two elements will decrease as more Fe is produced at later times (Nissen, 2015). There is also a bimodality of $[\alpha/\text{Fe}]$ in the MW disc, with the thick disc being α -enhanced compared to the thin disc. The $[\alpha/\text{Fe}]$ -age bimodality has been explored by a number of authors. Some suggest it is a product of two distinct infalls of gas which form the thick and thin discs respectively (i.e. the two infall model), with a period of minimal star formation as the galaxy accretes pristine gas (e.g. Chiappini et al. 1997, Spitoni et al. 2019, Palla et al. 2020, Lian et al. 2020). Other authors suggest that the thin disc low- α population arises as a result of migration, in which the end-points of different evolutionary tracks at various radii are mixed by stellar migration (e.g. Schönrich & Binney 2009b, Sharma et al. 2021). On the other hand, Clarke et al. (2019) proposes that the high- α population formed in the clumps of the gas-rich early disc and self enriched with the elements formed via CCSNe, similar effects are found in simulation (Vincenzo & Kobayashi 2020 and Khoperskov et al. 2021).

Both Haywood et al. (2013) and Bensby et al. (2014) find that $[\alpha/\text{Fe}]$ can be used as a proxy for stellar age for thick disc populations, older than around 8 Gyr. Bensby et al. (2014) use Ti as an α element to investigate this relation, while Haywood et al. (2013) use the mean abundance of Mg, Si and Ti. Haywood et al. (2013) also suggest that there is a weak correlation

between $[\alpha/\text{Fe}]$ and stellar age in younger, thin disc populations, as the dispersion in $[\alpha/\text{Fe}]$ is always less than 0.04 dex at any given age. [Nissen \(2015\)](#) use HARPS (High Accuracy Radial velocity Planet Searcher) ([Pepe et al., 2002](#)) spectra to calculate chemical abundances for a sample of solar-twin stars, they studied the relation between stellar abundances and elemental condensation temperature. They provide information on the correlation between elemental abundance ratios $[\text{X}/\text{Y}]$ and stellar age. For their sample of mainly thin disc stars, they find that $[\text{Mg}/\text{Fe}]$ increases with age (their figure 9), suggesting $[\text{Mg}/\text{Fe}]$ could be used as a cosmic chronometer for the thin disc as well as the thick disc. $[\text{Y}/\text{Fe}]$ is also studied and is found to decrease with stellar age, thus proposing that $[\text{Y}/\text{Mg}]$ could be an indicator of stellar age (their figure 10), which will be discussed later on in this work. [Hayden et al. \(2017\)](#) also found a relationship between enhanced $[\text{Mg}/\text{Fe}]$ and older stellar ages, with the oldest stellar populations belonging to high $[\text{Mg}/\text{Fe}]$ regions of their figure 2. However, below around 10 Gyr there is a large dispersion in $[\text{Mg}/\text{Fe}]$, though the older and younger populations can still be distinguished. The literature discussed finds that we can use $[\alpha/\text{Fe}]$ to split stellar populations into ‘older’ and ‘younger’ stars but there is not a tight correlation with age. For stars older than 8 Gyr, we can use the $[\alpha/\text{Fe}]$ -age relation as a chemical clock in the thick disc but this does not hold for all stellar ages, nor for the thin disc. Therefore, there is not a tight relation with age that we can exploit in order to determine the ages of stars using their chemical compositions.

Given $[\text{Mg}/\text{Fe}]$ as a chemical clock is not useful for thin disc populations, galactic archaeologists have turned their attention to ratios of neutron-capture elements and α -elements. Observations suggest $[\text{Y}/\text{Mg}]$ and $[\text{Y}/\text{Al}]$ abundance ratios are correlated with age (e.g. [Nissen 2015](#), [Spina et al. 2016](#), [Tucci Maia et al. 2016](#), [Spina et al. 2018](#), [Casali et al. 2020](#), [Berger et al. 2022](#), [Viscasillas Vázquez et al. 2022](#), [Storm & Bergemann 2023](#)), with $[\text{Ba}/\text{Mg}]$ also being investigated ([Ratcliffe et al., 2024](#)). S-process neutron capture elements (e.g. Sr, Y, Zr, Ba, La, Ce) are generally produced in the intershell regions of AGB stars and are ejected into the ISM via winds (e.g. [Busso et al. 1999](#)). The strongest s-process production comes from low mass AGB stars ($1.5 - 3 M_{\odot}$) with lifetimes of around a few hundred Myr ([Karakas & Lattanzio, 2014](#)). Low mass AGB lifetimes are much longer than the time it takes for a

massive star to explode as a CCSNe (a few tens of Myr) ejecting Mg, Al and other α elements. However, it should be noted that s-process elements can also be produced via neutron capture in massive stars, especially when those stars rotate. This idea has already been discussed in Chapter 3. Production of s-process elements in massive stars is, however, a metallicity dependent process and thus they still have distinct timescales of production. The production of alpha elements like Mg are largely not metallicity dependent, allowing $[s/\alpha]$ -age relations to still perform well as chemical clocks.

A wealth of observations in recent years provided more information about the $[s/\alpha]$ -age relation as a chemical clock. The work of [Nissen \(2015\)](#), suggested that $[Y/Mg]$ showed a sensitive correlation with stellar age for a sample of 21 solar neighbourhood, solar twin stars. Following on from this, [Tucci Maia et al. \(2016\)](#) analysed the abundances of 88 solar twins and again found a strong correlation between $[Y/Mg]$ and age. This result was echoed by [Spina et al. \(2016\)](#) who, similarly to [Nissen \(2015\)](#), found an increasing trend for $[\alpha/Fe]$ with age and a decreasing trend for $[s/Fe]$ with age; going on to suggest that $[Mg/Y]$ and $[Al/Y]$ can be a sensitive indicator of stellar age with $[Al/Y]$ showing the steepest dependence on age. Most follow-up work agrees that $[Y/Mg]$ -age as well as other $[s/\alpha]$ -age relations work well as chemical clocks for solar-twin stars (e.g [Spina et al. 2018](#), [Casali et al. 2020](#), [Titarenko et al. 2019](#), [Berger et al. 2022](#)). For example, [Spina et al. \(2018\)](#) confirmed the relation for solar twins, finding more negative slopes than previous studies. However, as different types of stars with a range of metallicities (i.e. non-solar) or originating from different regions of the disc (i.e. not the solar neighbourhood) have been probed, it appears the $[Y/Mg]$ -age relation is not consistent across the disc. [Feltzing et al. \(2017\)](#) studied a sample of solar neighbourhood dwarf stars with a wide range of $[Fe/H]$ and found that, though the relation held for solar analogues, it varied for other metallicities - even finding a flat trend for $[Fe/H] \approx -0.5$ dex. A metallicity dependence for $[s/\alpha]$ -age relations was also found by [Delgado Mena et al. \(2019\)](#). They required multivariable linear regression using a number of stellar properties including effective temperature, stellar mass and metallicity to explain the trends of a sample of FGK HARPS-GTO stars. Using a sample of OCs, [Casali et al. \(2020\)](#) suggests that there are different $[Y/Mg]$ -age relations depending on galactocentric radius due

to differing star formation histories and/or metallicity dependence of s-process element yields in different regions. Contrary to this, [Titarenko et al. \(2019\)](#) finds no metallicity dependence on the relation for thin disc stars. However, they observe a discontinuity in the relations between thick and thin disc stars at around 9 - 10 Gyr. Though the relation is not as strong for all types of stars, [Berger et al. \(2022\)](#) showed that the [Y/Mg]-age chemical clock is still statistically significant for non-solar FGK stars and can still be useful as an age diagnostic, as well as confirming the strong trend for solar-like stars. Authors have also studied the effect of non-local thermal equilibrium (NLTE) on the [Y/Mg] abundance ratio ([Storm & Bergemann, 2023](#)). NLTE effects are small for solar-like stars but strong for metal-poor red giant stars, reinforcing the idea that the relation works well for solar twin stars.

Open clusters are useful objects when studying radial dependencies of abundance ratios across a galactic disc because we are able to determine properties such as age and galactocentric distance more precisely from photometry compared to individual stars. As a result, they are often used as a reliable tracers of the evolution of the disc, especially as OCs cover the full disc of the Milky Way in both radius and age (e.g. [Spina et al. 2021](#)). [Viscasillas Vázquez et al. \(2022\)](#) utilises a sample of 62 OCs from the catalogue of the sixth internal data release of the Gaia-ESO survey to investigate the [s/ α]-age relation's radial dependency by splitting the sample into 'inner', 'solar' and 'outer' regions. In agreement with [Delgado Mena et al. \(2019\)](#), they find multivariate relations are needed to fit the trends with age for each region. They also note that [Ba/ α] is more sensitive to age for young disc stars, whose slopes vary less with galactocentric radius. We will employ the same sample of OCs later in this work to compare with our chemical evolution models (section [6.2.1](#)).

We have gained a depth of knowledge from the observations that does not extend to chemical evolution modelling, though some studies have started to probe the evolution of [s/ α]-age relations using GCE models. [Casali et al. \(2020\)](#) performed chemical evolution modelling to investigate how the multi-zone GCE model of [Magrini et al. \(2009\)](#) performs in reproducing [Y/Mg] abundances of solar twins and OCs. The model performs well at 9 and 16 kpc but is enhanced at 6 kpc due to the faster enrichment of s-process elements in the inner disc. In the high-metallicity regime of the inner disc, a depressed set of s-process

yields is required. Following on from this work, [Magrini et al. \(2021\)](#) also employed the GCE model of [Magrini et al. \(2009\)](#) to investigate s-process abundances at high metallicity in the inner disc. Rather than depressing the s-process yields, they use a set of AGB yields which include magnetic-buoyancy mixing (MAGN) ([Vescovi et al., 2020](#)). By replacing the Y yields with these new AGB yields, [Magrini et al. \(2021\)](#) were able to qualitatively explain the change in slope and intercept in the inner regions of the galactic disc (at approximately 6 kpc). However, they note that the MAGN yields currently exist for just one initial mass ($2 M_{\odot}$), thus the results should be taken with caution. The most recent work in this area comes from [Ratcliffe et al. \(2024\)](#). They investigated $[s/\alpha]$ -age relations with respect to stellar birth radius. As previous studies have done, [Ratcliffe et al. \(2024\)](#) used multivariate relations, finding a weaker $[s/\alpha]$ relation in the inner disc due to the negative $[s/\text{Mg}]$ radial abundance gradient. They also suggest that the tight $[s/\alpha]$ -age correlation of solar-like stars is due to stars of a similar age having similar birth radius. Part of their study also involved some chemical evolution modelling. A multi-zone model was used to study the evolution of the $[\text{Ba}/\text{Mg}]$ radial gradient, finding opposite trends from the modelling compared to the evolution of the observations. The model shows the $[\text{Ba}/\text{Mg}]$ abundance staying constant with time at outer radii while at inner radii, the abundance decreases, likely due to low AGB yields at high metallicity. If the model is modified to increase Ba yields by around a factor of two at high metallicities, the problems of the initial model are largely resolved, finding a $[\text{Ba}/\text{Mg}]$ abundance relatively constant with time after an initial increase.

As has been comprehensively discussed, by studying the radial dependence of chemical clocks we can gain information about the evolution of the disc. Some authors make comment on the differing SFH or the stellar sources at work in different regions of the disc and how this might play a role in the strength of the relation. Radial gradients have been extensively studied as they are not just important in the fields of galactic archaeology and GCE but in all areas which assist in our understanding of galaxy formation and evolution. For example, the oxygen radial gradient has been thoroughly studied (e.g. [Esteban et al. 2017](#), [Mollá et al. 2019](#), [Arellano-Córdova et al. 2021](#), [Da Silva et al. 2023](#)) as it can be used as a proxy for metallicity in ionised gas nebulae. We can also study radial gradients of galaxies other than

the Milky Way, for example M31 (Spitoni et al. 2014, La Barbera et al. 2024), M33 (Magrini et al., 2007) or elliptical galaxies (Pipino et al. 2008, Avila-Reese et al. 2023) amongst many others.

We aim to combine these two ideas of chemical clocks and radial abundance gradients to find out if the evolution of $[s/\alpha]$ ratios can strengthen its promise as a chemical clock. We will investigate the evolution of $[Y/Mg]$ and $[Ba/Mg]$ with age in comparison with open cluster observations, before moving on to study radial gradients and the evolution of the slope of radial abundance gradients with time. Section 6.2 presents the chemical evolution models used for this work and the observations with which will compare our models; section 6.3 is split into two parts, the first looks at age gradients of $[s/\alpha]$ as chemical clocks while the second part focuses on radial gradients of these ratios; section 6.4 presents a discussion and conclusions of this work.

6.2 Methods

In this work, we utilise ALPHA, the multi-zone chemical evolution code, which connects many instances of the single-zone GCE code OMEGA (Côté et al., 2017) to form a galactic disc. Chapter 5 explains in detail how ALPHA was developed and how we keep track of the gas in the model. Here, we will remind the reader of the key equations that we use to track the evolution of the gas in each zone of the disc. The evolution of the gas mass in a zone, n , is defined as:

$$\dot{M}_{\text{gas}}(t) = \dot{M}_{\text{inflow}}(t) + \dot{M}_{\text{ej}}(t) + \dot{M}_{\text{mig}_{n+1}}(t) - \dot{M}_{\star}(t) - \dot{M}_{\text{outflow}}(t) - \dot{M}_{\text{mig}_n}(t) \quad (6.1)$$

where, $\dot{M}_{\text{inflow}}(t)$ is the rate of gas mass falling into the galaxy, $\dot{M}_{\text{ej}}(t)$ is the rate of gas mass added by stellar ejecta, $\dot{M}_{\star}(t)$ is the rate of gas mass removed from the reservoir by star formation, $\dot{M}_{\text{outflow}}(t)$ is the rate of the gas mass lost from the zone via outflow, while $\dot{M}_{\text{mig}_{n+1}}(t)$ and $\dot{M}_{\text{mig}_n}(t)$ is the rate of gas mass gained and lost by radial gas flow respectively.

We use a single exponential infall of gas, where the infall rate is defined as:

$$I(r, t) = I_0(r) e^{-\frac{t}{\tau_{\text{inf}}(r)}} \quad (6.2)$$

where, $I_0(r)$ is the normalisation of the infall rate across the disc and the infall timescale τ_{inf}

Property	No Flows Model	Flows Model
$M_{\text{inf}} (M_{\odot})$	2.4×10^{10}	3×10^{10}
$f_{\star} (M_{\odot} \text{ yr}^{-1} \text{ kpc}^{-2})$	2×10^{-4}	3.2×10^{-4}
a (Gyr)	-1.5	-1.5
b (Gyr kpc $^{-1}$)	2	2

Table 6.1: Properties of the models.

is defined as $\tau_{\text{inf}} = a + br$. The parameters a and b are the infall timescale at the galaxy centre and the linear gradient of the infall timescale respectively.

At every timestep the stellar ejecta is calculated by summing the contribution of every stellar population formed by time, t so that:

$$\dot{M}_{\text{ej}}(t) = \sum_j \dot{M}_{\text{ej}}^j(M_j, Z_j, t - t_j) \quad (6.3)$$

where \dot{M}_{ej}^j is the rate of gas mass ejected by the j th stellar population, M_j is the initial mass of the population, Z_j is the initial metallicity of the population and $t - t_j$ is the age of the j th population at time t .

The SFR is defined as:

$$\Sigma_{\text{SFR}} = f_{\star} \left(\frac{\Sigma_{\text{gas}}}{1 M_{\odot} \text{ pc}^{-2}} \right)^k \quad (6.4)$$

where f_{\star} is the star formation efficiency, Σ_{gas} is the gas surface density of the zone and k is a dimensionless exponent that controls the slope of the SFR.

Finally, the mass which migrates via radial flow from the zone, n to its neighbouring zone, $n - 1$ is:

$$M_{\text{mig},n}(t) = \rho M_{\text{gas}}(t). \quad (6.5)$$

where ρ is the fraction of the mass in the zone (between zero and one) which gets moved as a result of the specified radial flow rate. A full definition of ρ and an explanation of the physical motivation can be found in 5.3.

We use two models which are almost identical to those introduced in the previous chapter. Each model consists of ten zones, with an inner radius of 4 kpc and an outer radius of 16.5 kpc. We use a [Kroupa \(2001\)](#) IMF and the exponent of Equation 6.4 is $k = 1.4$. We employ the

same yield set for both of the models, using the FRUITY AGB yields of [Cristallo et al. \(2015\)](#), the mixed rotation massive star yields of [Limongi & Chieffi \(2018\)](#) and [Iwamoto et al. \(1999\)](#) SNIa yields. This combination of yields is already used for the flows model, we employ it here for the no flows model for two reasons. First, for consistency between the two models when analysing the results of the study; second, we intend to study neutron capture elements, and the Monash AGB yields ([Karakas, 2010](#)) used by the no flows model developed in the previous chapter, do not include elements beyond iron. Again, in line with other similar works, we do not include outflowing gas in these models (e.g. [Matteucci & Francois 1989](#), [Chiappini et al. 1997](#), [Grisoni et al. 2017](#)). The important parameters for the evolution of the model M_{inf} , f_{\star} , a and b remain the same as the previous chapter and are repeated again in [Table 6.1](#) for clarity. For the flows model, we also use the same radial gas flow velocity of $v_{\text{rad}} = 1 \text{ km s}^{-1}$.

6.2.1 Observations

We use two catalogues of observations in this work, both are sets of open clusters. As we have already discussed, OCs are useful to compare with chemical evolution models as they have reliable age and distance determinations as such they can be used to probe the present-day radial abundance gradients. As the stars in open clusters form at the same time, at the same galactocentric distance and out of the same gas with the same chemical composition, we are able to really well constrain the radial profiles of the chemical abundances in the galactic ISM at different recent epochs, using OC stellar population abundances.

The first observations we use are the set of 62 OCs from [Viscasillas Vázquez et al. \(2022\)](#) which were briefly discussed in the introduction of this chapter. These open clusters are from IDR6 of the Gaia-ESO survey, with spectra obtained from UVES. As mentioned previously, [Viscasillas Vázquez et al. \(2022\)](#) separate these OCs by galactocentric distance, creating three groups of observations for the inner, solar and outer regions of the galactic disc. The inner region is defined as $R_{\text{GC}} < 7 \text{ kpc}$, the solar region as $7 \leq R_{\text{GC}} \leq 9 \text{ kpc}$ and the outer region as $R_{\text{GC}} > 9 \text{ kpc}$. We use the $[\text{Fe}/\text{H}]$, $[\text{Y}/\text{H}]$, $[\text{Ba}/\text{H}]$ and $[\text{Mg}/\text{H}]$ abundance ratios, age and galactocentric distances from this work. [Molero et al. \(2023\)](#) use this set of open

clusters to investigate the origin of neutron capture elements using radial gradients. They find their chemical evolution model cannot match the [Eu/H] gradient at all times but they can reproduce the limited evolution with time. Meanwhile, the model predicts radial [Y/H] and [Zr/H] gradients that appear to agree with the OC sample. Other authors have also taken advantage of this set of open clusters (e.g. [Randich et al. 2022](#), [Magrini et al. 2023](#), [Van der Swaelmen et al. 2023](#)), see these works for more information on the sample. We utilise this set of OCs to primarily study age gradients, and though we begin to use them to study radial gradients, we opt instead to use a different set when analysing the slopes of abundance ratios with respect to galactocentric radius.

The second set of observations we use are another sample of OCs from the recent work of [Carbajo-Hijarrubia et al. \(2024\)](#). The authors determine the atmospheric parameters and chemical abundances of 36 OCs as part of the Open Clusters Chemical Abundances from Spanish Observatories (OCCASO) project and add to the sample by including another 63 OCs from the literature (GES DR5, APOGEE DR17, GALAH DR3). The aspect of this study that we are interested in is the analysis of the slopes of the radial abundance gradients (their figure 18). By splitting the sample into age bins, the authors are able to study $\delta [X/Fe]/\delta R_{GC}$ to understand how radial gradients evolve with stellar age. This will be an important property with which to compare our models. In this work, we primarily focus on the evolution of the [Ba/Fe] slope.

6.3 Results

6.3.1 Age Gradients as Chemical Clocks

As the most commonly studied chemical clock, we first investigate the evolution of [Y/Mg] with age for our GCE models calculated with ALPHA. To be able to compare our models with observations, we must split them by region. For each zone of the multi-zone disc, we find the mid-point of it and assign it to one of the three groups (inner, solar, outer) using the same radii boundaries described in section 6.2.1. For a given ratio, to calculate the abundance of the models, we find the mean average of the abundance ratio for the zones included in each region, then we find upper and lower limits by finding the largest and smallest value that the

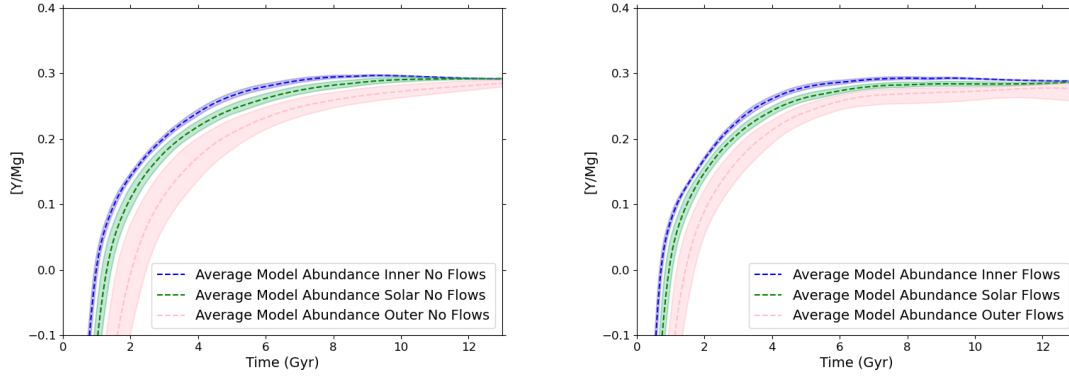
(a) Evolution of the $[Y/Mg]$ ratio for the no flows model.(b) Evolution of the $[Y/Mg]$ ratio for the flows model.

Figure 6.1: Evolution of $[Y/Mg]$ ratio for both the no flows and flows model, the abundances of the inner, solar and outer regions are shown in blue, green and pink respectively. A dashed line indicates the average abundance for that region, while the shaded area represents the upper and lower bounds.

given ratio can take for each region.

Figure 6.1 shows the evolution of $[Y/Mg]$ with time for the model with and without radial flows. The blue, green and pink areas represent the trends of the inner, solar and outer regions respectively with the dashed lines representing the average abundance and the shaded regions showing the possible range of abundance. For both the no flows (panel a) and flows models (panel b) there is clearly a steep increase in $[Y/Mg]$ until 4 Gyr when the abundance ratio plateaus, especially when the model includes radial gas flows. A plateau would suggest there is no significant change in either the Y or Mg abundances over the evolution of the disc after approximately 4 Gyr.

We compare the models to the open clusters of [Viscasillas Vázquez et al. \(2022\)](#) for each region. Figure 6.2 shows the no flows and flows models for each region along with the observations. The panels here show $[Y/Mg]$ versus time (i.e. the time through the evolution of the galaxy) therefore, the observations (Figure 6.2c) have been placed at their ‘birth time’ based on their ages (birth time = 13 Gyr - stellar age). As expected based on Figure 6.1, the trends are largely flat for the models in all regions, with no slopes being reproduced by the models. We also find a consistent over-production of $[Y/Mg]$ compared with the observations, regardless of region. This overproduction could arise due to an over abundance of Y, an under

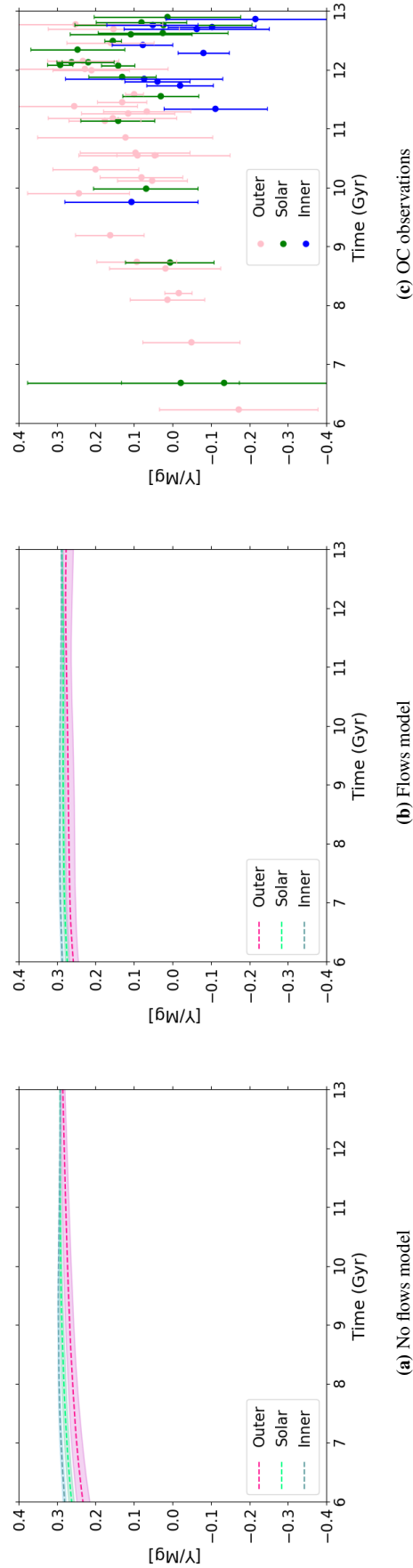


Figure 6.2: Average modelled $[Y/Mg]$ abundance ratio of both the no flows model (left) and flows model (right) compared to the observations of Viscasillas Vázquez et al. (2022) shown with their uncertainties (right).

abundance of Mg or a combination of both. To probe this further, we investigate the $[Y/Fe]$ and $[Mg/Fe]$ trends of the models in comparison with the OC sample.

Figure 6.3 presents the results for each region in a similar fashion as Figure 6.2 but this time we see the evolution of $[Y/Fe]$ (panels a to c) and $[Mg/Fe]$ (panels d to f). Figures 6.3a to 6.3c show we are able to reproduce some of the observed $[Y/Fe]$ abundance ratios but we are not able to reproduce the slopes that we see in the data from the outer region, for example. The modelled $[Y/Fe]$ abundances for the outer region cover a much wider range for the flows model than the no flows model because the outer regions lose mass via radial flow which is not replenished via infall or radial gas flows into the zone. This causes a wide range of abundance as the outermost zone loses more mass and therefore becomes metal-poorer than the inner regions. It is clear from Figures 6.3d to 6.3f that Mg is underproduced by the models by around 2 dex but that underproduction can be as high as 6 dex in some instances, with the models consistently sitting below the observations. The flows models are slightly less abundant in $[Mg/Fe]$ at later times as the iron that is produced by SNe Ias gets removed from the zones via radial flows.

As already discussed, in Figures 6.2 and 6.3 it is clear there are largely flat trends in the models (and in some of the observations e.g. $[Mg/Fe]$ in the solar region). Therefore, though for some ratios we can reproduce the observed abundances with the models (e.g. $[Y/Fe]$) we cannot use these ratios as chemical clocks as a flat trend does not allow us to determine the age of a star.

Given Viscasillas Vázquez et al. (2022) found the $[Ba/Mg]$ ratio was more sensitive to age than $[Y/Mg]$, we perform the same analysis for the $[Ba/Mg]$ -time relationship. Figure 6.4 shows the $[Ba/Mg]$ -time trends for the no flows (left panel) and flows (right panel) model. $[Ba/Mg]$ has a completely different evolution compared to $[Y/Mg]$. After an initial increase, we see a decrease in the ratio at approximately 4 Gyr rather than a plateau. Given we know the $[Mg/Fe]$ ratio remains largely flat (see Figure 6.3), we can assume this affect arises from the evolution of Ba (see the discussion of Figure 6.5 later in this section). The second clear feature is the widening of the band for the outer region. This suggests a wide range of Ba abundance across the disc compared with Y. The bands for each region are wider for the

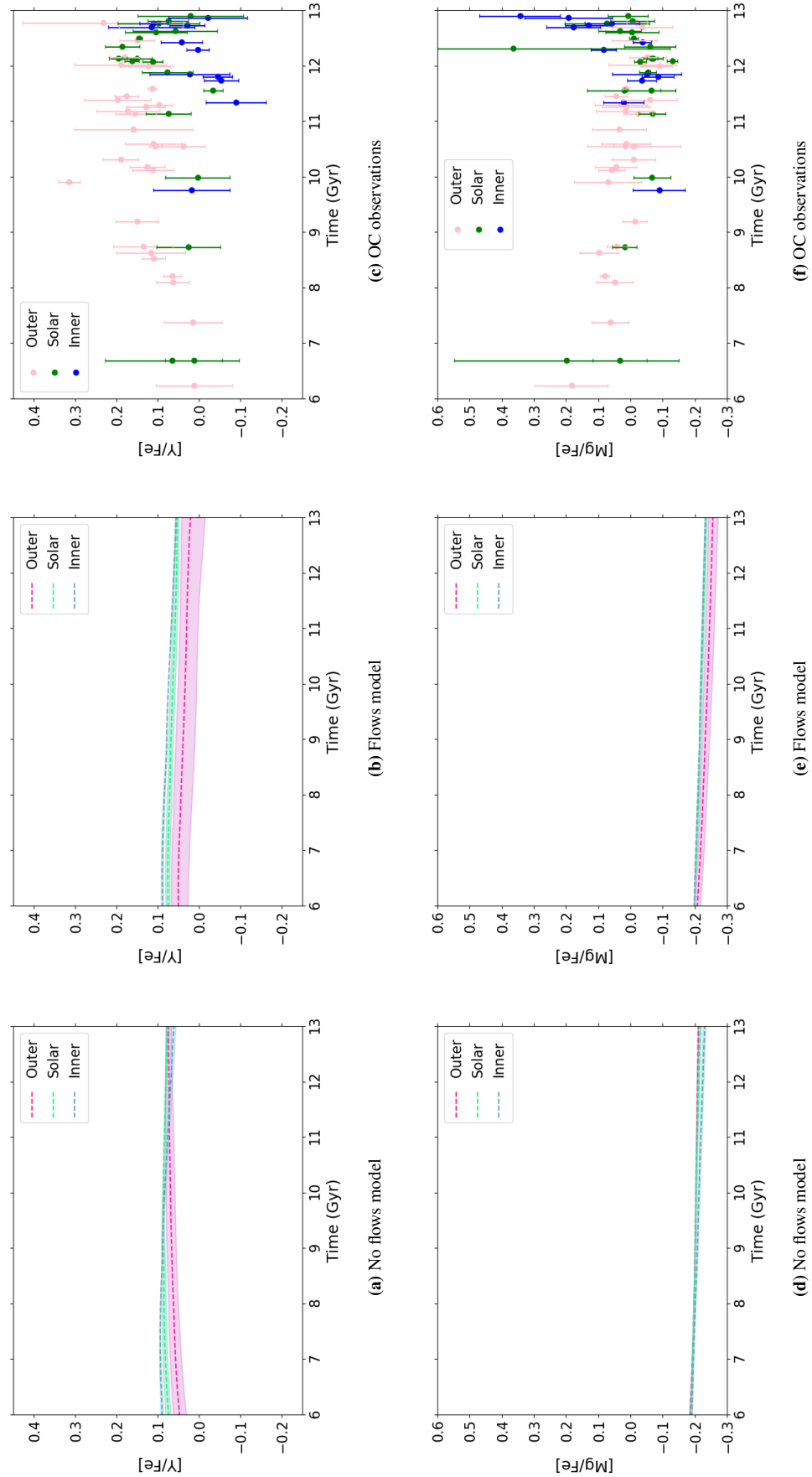
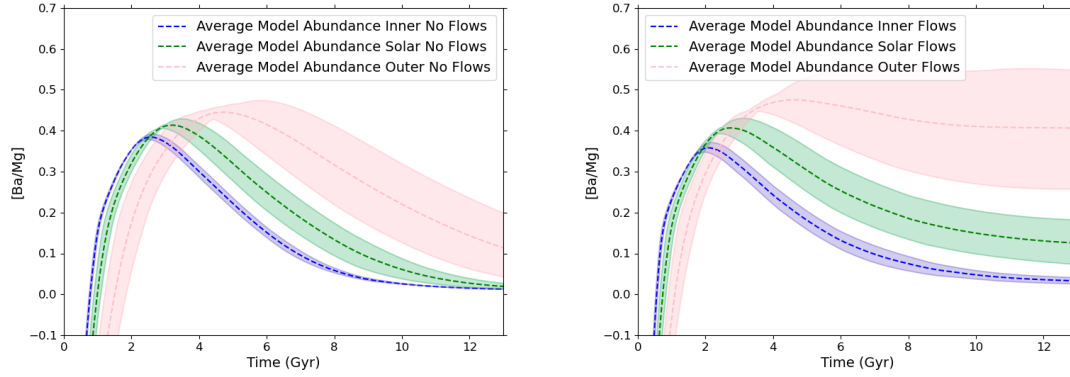


Figure 6.3: As Figure 6.2 but for $[Y/Fe]$ (panels a to c) and $[Mg/Fe]$ (panels d to f).



(a) Evolution of the [Ba/Mg] ratio for the no flows model.

(b) Evolution of the [Ba/Mg] ratio for the flows model.

Figure 6.4: As Figure 6.1 but following the evolution of the [Ba/Mg] ratio.

flows model (bottom panel), suggesting radial flows play an important role in the evolution of [Ba/Mg]. As radial flows carry gas away from the outer zone, the range of potential [Ba/Mg] abundance in that region increases. There is even a marked enhancement in [Ba/Mg] in the outer region, this is likely because Mg-rich gas gets carried away from the outer zones at earlier times, before Ba is ejected into the ISM.

Once again, in Figure 6.5 we compare the no flows and flows models with each other and with observations of [Ba/Mg] (panels a to c) and [Ba/Fe] (panels d to f). Again, we can see from Figures 6.5a to 6.5c that we can reproduce some of the observed abundance ratios, with the models covering the majority of the observed range. When we consider the differences between the no flows and flows models, we notice that the flows models show largely flat trends while the no flows models show slopes opposite to the observations, especially for the solar and outer regions. Again, this could be as a result of the regions on the outskirts of the disc losing Mg-rich gas at earlier times when flows are included so they are enhanced in [Ba/Mg] compared to the no flows models, where the material stays in the region into which it was ejected. A similar effect is found when studying the evolution of [Ba/Fe] in Figures 6.5d to 6.5f. The slopes of the models are again opposite to that of the observations and the slopes of the no flows model are steeper than the flows model. The wide range of possible modelled abundances allows the flows model in the outer region to reproduce some of the observed

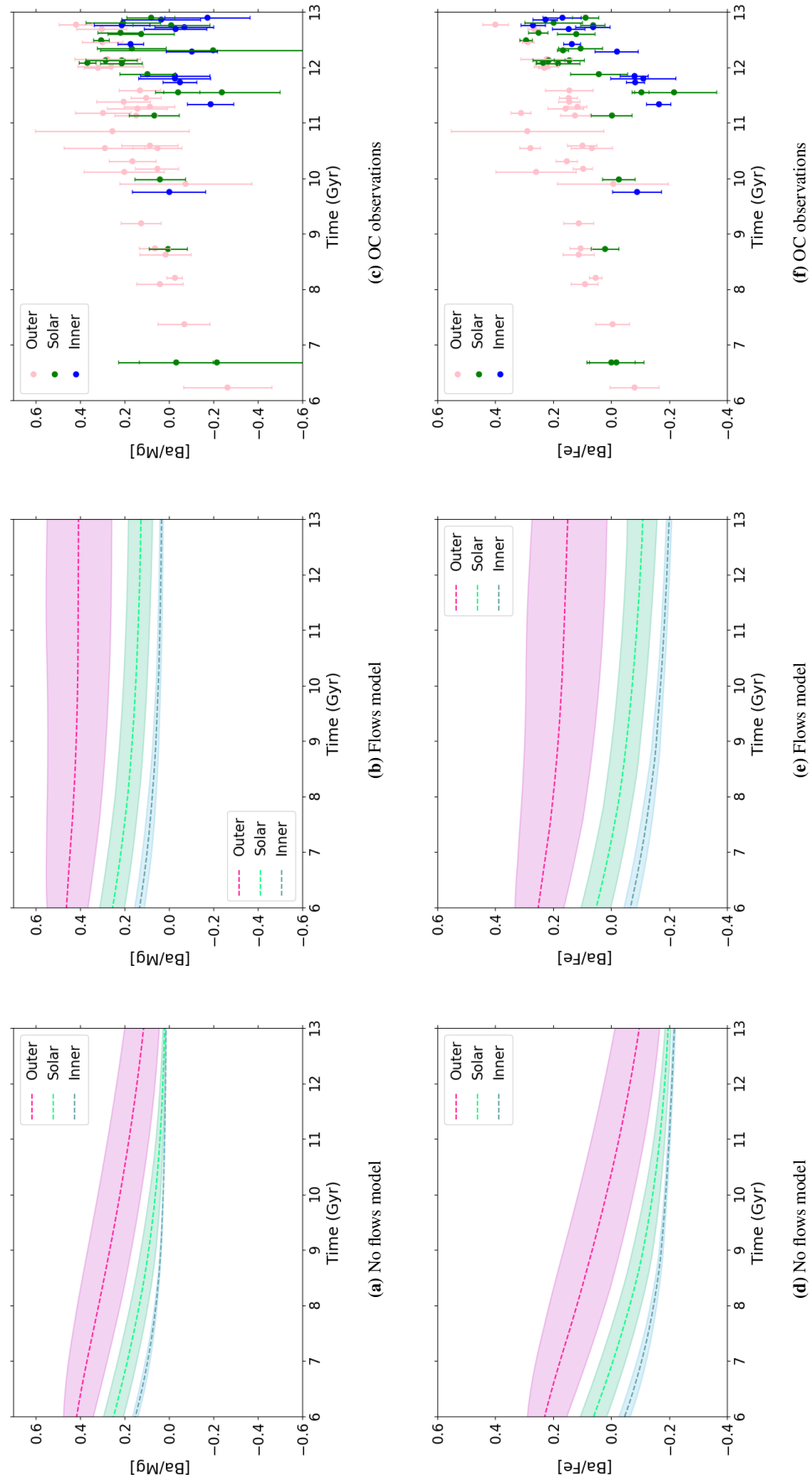


Figure 6.5: As Figure 6.2 but with [Ba/Mg] (panels a to c) and [Ba/Fe] (panels d to f).

Age Band	Stellar Age Range (Gyr)
Band 1	$0.1 \leq \text{Age} < 1$
Band 2	$1 \leq \text{Age} < 2$
Band 3	$2 \leq \text{Age} < 4$
Band 4	$4 \leq \text{Age} < 7$

Table 6.2: Age bands for the [Viscasillas Vázquez et al. \(2022\)](#) OCs.

ratios, however the inner and solar regions under produce [Ba/Fe] compared to observations.

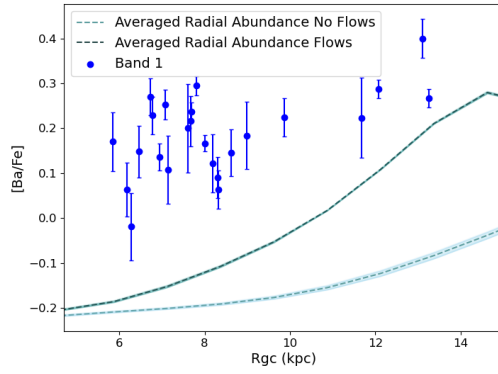
Again, we cannot draw any firm conclusions regarding these ratio's potential as a chemical clock as we are not able to reproduce any slopes in the observations using these models. However, we have been able to study the effect of radial flows on these ratios and we can see differences between the models that would suggest there is a strong effect on these abundance ratios when we include radial flows. Therefore, we move on to take advantage of the spatial information provided by the models and study the radial abundance gradients.

6.3.2 Abundance Gradients as a Function of Radius

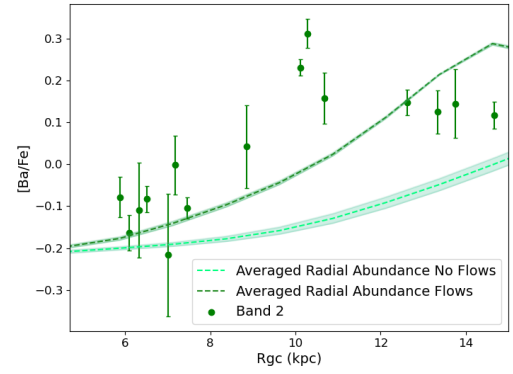
To study radial abundance gradients, we again split the data into groups, but this time by stellar age in Gyr. Table 6.2 shows the range of each band of stellar age.

For the radial gradients study, we will focus solely on the [Ba/Fe] ratio. We exclude Y and Mg from this part of the study due to largely flat abundances for [Y/Mg], [Y/Fe] and [Mg/Fe] with time and the minimal variation in abundances within regions, as we see narrow bands in Figures 6.2 and 6.3.

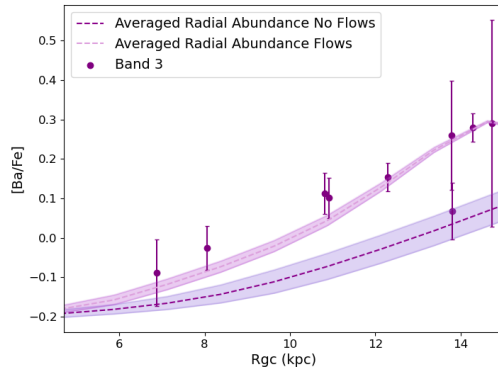
Though not a conventional chemical clock, we can still gain useful information from studying [Ba/Fe] ratios. The two elements still have different sites and timescales of production, with the production of Ba being metallicity dependent whereas the production of Fe is not. Figure 6.6 shows the radial abundance gradient for each age band. To calculate the abundances we go through a similar process as described previously when studying trends with time. For each age band, we find the mean average abundance of the model for that time period and use the lowest and highest values of the abundance during that time as the



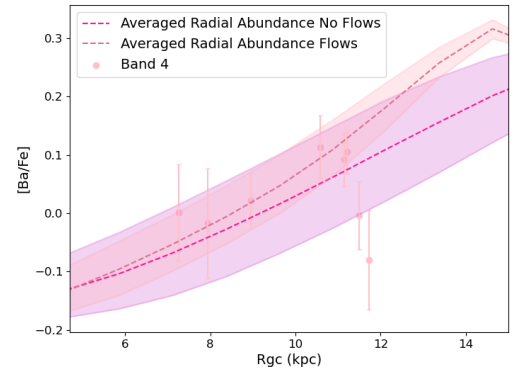
(a) $0.1 \leq \text{Stellar Age (Gyr)} < 1$



(b) $1 \leq \text{Stellar Age (Gyr)} < 2$



(c) $2 \leq \text{Stellar Age (Gyr)} < 4$



(d) $4 \leq \text{Stellar Age (Gyr)} < 7$

Figure 6.6: Radial abundance profiles for each stellar age band.

upper and lower bounds. For example, comparing the model with stars from age band 1, we calculate the average abundance of the model between 12 - 12.9 Gyr of evolution (i.e. we find the required abundances by calculating 13 Gyr - stellar age).

Each panel of Figure 6.6 shows the no flows and flows model besides the observations of Viscasillas Vázquez et al. (2022). The models perform especially well for the older three stellar ages (panels b - d). In panels b and c we can see good agreement between the trend of the observations and the flows model. In panel d, though the models appear to reproduce some of the observations, the range of potential values is too large to draw any firm conclusions. Though we underproduce [Ba/Fe] for the youngest stars (panel a), on visual inspection, the flows model appears to have a similar slope as the observations. To explore the trends with radius further, we investigate the impact of different stellar yield sets. Given that the massive star yield set used in Figure 6.6 is the mixed rotational velocity yields of Limongi & Chieffi (2018), we specifically study how the initial rotational velocity impacts the abundance trends of the models.

In Chapter 3, we studied the impact of massive star rotation on fluorine and s-process element yields. We found that varying the rotation prescription allowed us to match the observational trends at different metallicities, with a higher rotational velocity required at low metallicities, in agreement with the literature (e.g. Prantzos et al. 2018). We employ a similar idea here to investigate the impact of massive star rotation on the [Ba/Fe] radial gradient of the models.

Figures 6.7 and 6.8 show, for each one of the age bands, the impact of varying the massive star rotational velocity. For each figure, the panels on the left (a and d) show the impact of varying the rotational velocity prescription of the no flows model, the panels in the center (b and e) show the impact of varying the rotational velocity prescription of the flows model and the panels on the right (c and f) show the OC observations of Viscasillas Vázquez et al. (2022) covered by that age band. For each of the no flows and flows model we have investigated the impact of all options for massive star initial rotational velocity (Limongi & Chieffi, 2018): the mixed prescription, $v = 0 \text{ kms}^{-1}$, $v = 150 \text{ kms}^{-1}$ and $v = 300 \text{ kms}^{-1}$.

Figures 6.7a to 6.7c show the radial abundance profiles for the most recent time period (i.e.

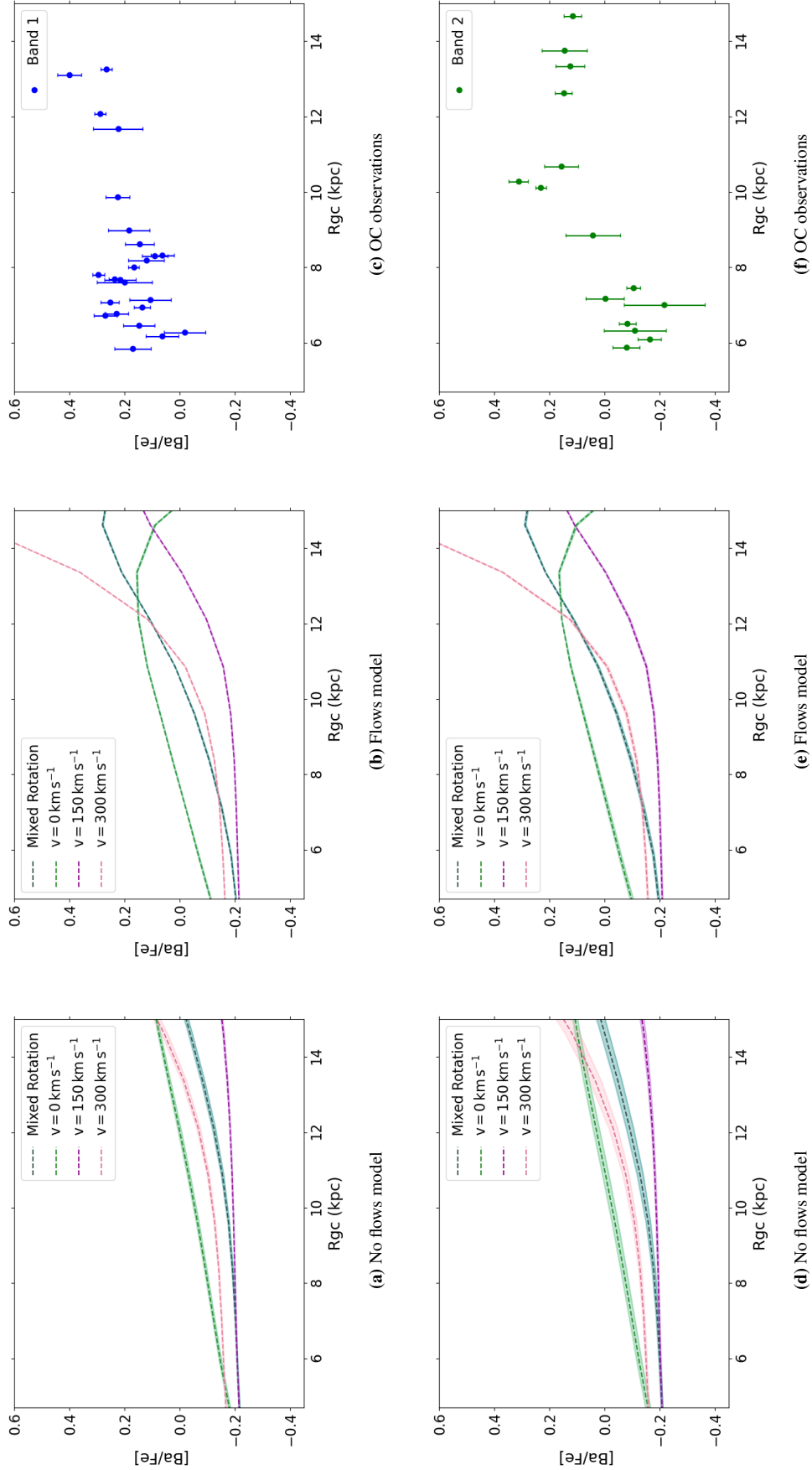


Figure 6.7: [Ba/Fe] radial gradients for both the no flows (left) and flows (middle) models alongside the observations of Vázquez et al. (2022) in age band 1 ($0.1 \leq \text{Stellar Age (Gyr)} < 1$, panels a to c) and band 2 ($1 \leq \text{Stellar Age (Gyr)} < 2$, panels d to f).

the youngest stellar ages). When radial gas flows are included, the slopes of the models which employ massive star rotation (i.e. not $v = 0 \text{ km s}^{-1}$, green lines) are much steeper than when radial gas flows are not included. This effect is likely because iron is produced on a shorter timescale than Ba so radial gas flows will carry more Fe away from the outer zones, causing a steepening of the slope with radius. When we do not include massive star rotation in the flows model, there is a decrease in slope at outer radii. As the Ba is being carried away from the outer regions in this model ($v = 0 \text{ km s}^{-1}$ with flows) it is not being replenished enough by the enhanced production of s-process elements in massive stars as they rotate. At inner radii, the slope of the observations appear to be reproduced by the mixed rotation model with radial flows and the two models using $v = 0 \text{ km s}^{-1}$ both with and without flows. This could be expected as the literature suggests that at high metallicities, we should not expect a strong contribution from rotating massive stars. In Chapter 3, we find we need a 45% contribution from $v = 0 \text{ km s}^{-1}$ massive stars at the time of the birth of the sun. The stars in this age band are 4-5 Gyr younger than the sun, thus we would perhaps expect an even stronger contribution from massive stars with zero rotational velocity at the time of their birth.

The radial profiles for the second age band are presented in Figures 6.7d to 6.7f. The models behave similarly to the previous figure, with a steepening of the slope as the massive star rotational velocity increases. Again, we see the zero rotational velocity flows model achieves good agreement with the observations, likely for the reasons outlined above, as these stars are younger than the sun.

Figures 6.8a to 6.8c show the radial gradients of the third age band for each massive star rotational velocity split by flows and no flows included in the models. As mentioned previously, the mixed rotational velocity model with radial flows does well reproducing the observations in this stellar age range. However, we also see that the no radial flows model with massive stars rotating at $v_{\text{rot}} = 300 \text{ km s}^{-1}$ also works well at reproducing the slope of the abundances. Again, this is consistent with the literature, which suggests we require rapidly rotating massive stars at low metallicities.

Finally, the oldest stars are compared with models representing the oldest age band in Figures 6.8d to 6.8f. Again, each of the models takes on similar shapes as the other age

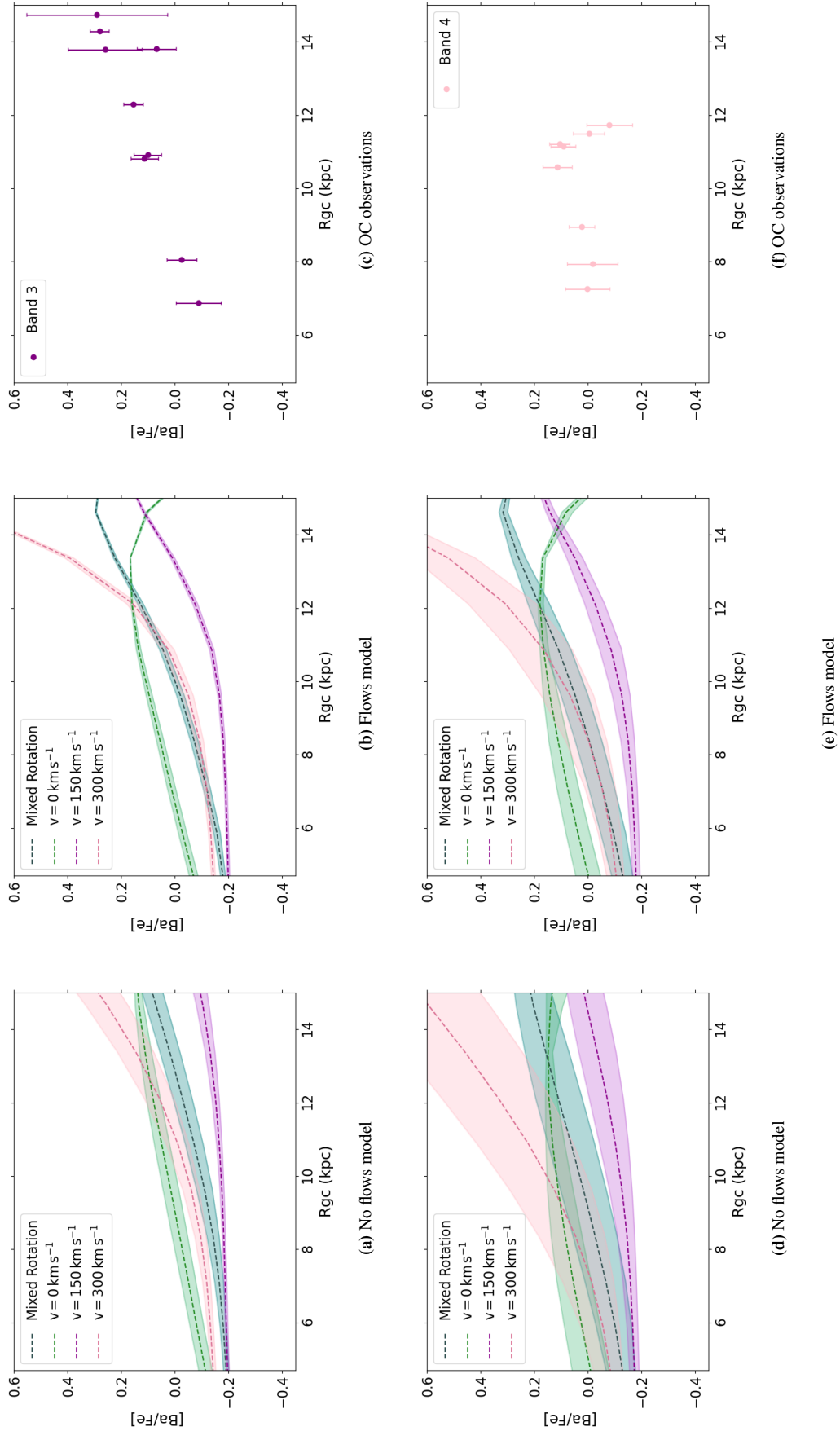


Figure 6.8: As Figure 6.7 but for age band 3 ($2 \leq \text{Stellar Age (Gyr)} < 4$, panels a to c) and band 4 ($4 \leq \text{Stellar Age (Gyr)} < 7$, panels d to f).

bands with the same rotational velocity prescription. Unfortunately, as discussed previously, the range of the models are too wide to draw any firm conclusions about their success in reproducing the observations.

When visually comparing the age bands represented in Figures 6.7 and 6.8, we know that the rotational velocity appears to have an impact on the slopes of the models. The slope of radial abundance gradients is a feature that has been recently explored by Carbajo-Hijarrubia et al. (2024) in their figure 18. Splitting their sample of OCs (see section 6.2.1) into age bands and calculating the slope, they study the change in slope with stellar age for a variety of elements including Ba. Therefore, we now use this set of observations to compare with our models. To be consistent with Carbajo-Hijarrubia et al. (2024), we alter our age bands so that the second oldest age band becomes narrower ($2 \leq \text{Stellar Age (Gyr)} < 3$) and the oldest age band becomes wider ($3 \leq \text{Stellar Age (Gyr)} < 7$). We once again investigate the radial abundance trends for each age band, however this time we calculate the slope of the radial gradient. We calculate the slope at the solar neighbourhood (between 7 kpc - 9.5 kpc) region for each radial gradient.

Figure 6.9 shows the slopes of the models in the style of Carbajo-Hijarrubia et al. (2024). For each age band, we plot the slope of each model which is calculated by first finding the weighted average [Ba/Fe] abundance in time and radius for each age band as follows:

$$\sum_i [Ba/Fe](t_i, R_k) \cdot \frac{SFR(t_i, R_k)}{\sum_i SFR(t_i, R_k)} \quad (6.6)$$

The slopes are then calculated by finding the gradient between 7 kpc and 9.5 kpc of the weighted average abundances. Models with radial gas flows are represented by triangles, while models without are represented by circles. Each massive star rotational velocity prescription is denoted by a different colour, mixed rotation by dark blue, zero rotation by green, 150 kms^{-1} by purple and 300 kms^{-1} by red. The stellar age bands are split by a grey dashed line, with age reading youngest to oldest for each panel left to right along the figure. The error bars on each point are calculated by finding the gradient between the midpoint (8.3 kpc) and each of the extremes of the solar neighbourhood annulus range. The observations of Carbajo-Hijarrubia et al. (2024) are represented by the wheat coloured box on each panel, they represent the range the observation could take from the lowest to highest error bars on the plot. Ideally, a single

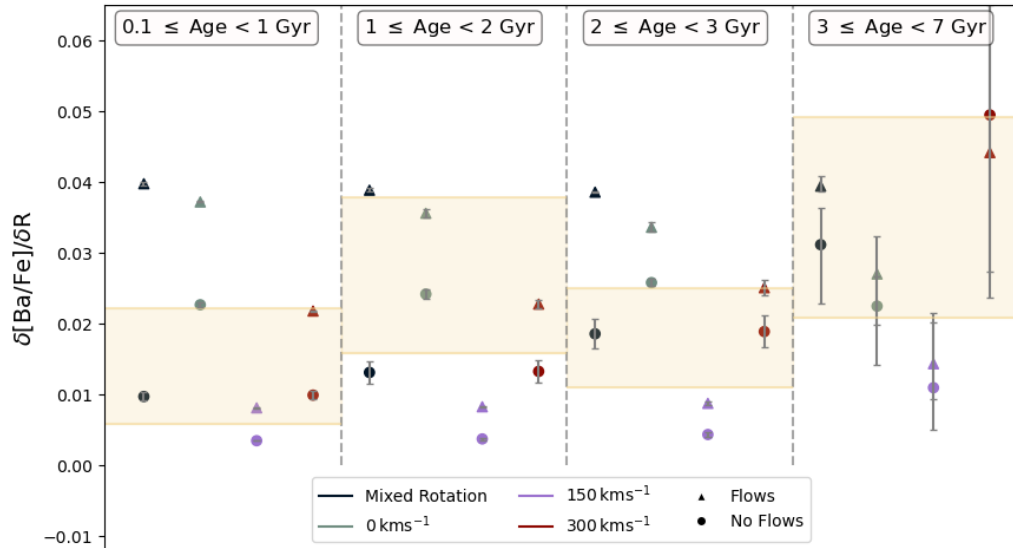


Figure 6.9: Slopes of the radial abundance profile for each model considered in this section, split by stellar age. Models which include radial gas flows are represented by triangles, while no radial gas flows are represented by circles. Each rotational velocity prescription is represented by a different colour: blue = mixed rotation, green = zero rotation, purple = 150 km s^{-1} and red = 300 km s^{-1} . The error bars on the model slopes are calculated by finding the gradient of the two extremes of the solar neighbourhood annulus, more information on how these are calculated can be found in the text. The observations of Carbajo-Hijarrubia et al. (2024) are represented by the wheat coloured box on each panel, they represent the range the observation could take from the lowest to highest error bars of the observations.

model would be able to replicate the slope of the observations at all ages, unfortunately, that is not the case. However, there are a set of models which are more successful than others, matching the observations in each age band most consistently (0 kms^{-1} no flows, 300 kms^{-1} and flows, mixed rotation no flows). We also see some interesting trends which are easily picked out in this format compared with viewing the models next to the observations as we did earlier in this section. It is clear that the models which use 150 kms^{-1} massive star rotational velocity produce the shallowest slopes. A flatter gradient in the solar neighbourhood suggests the Ba abundance in these models is not as enhanced as other models. For all models, except 300 kms^{-1} , the flows models produce consistently steeper slopes. This is likely because the iron produced at earlier times gets carried by radial flows into the inner regions, allowing for enhanced [Ba/Fe] in the outer regions, as Ba is released into the ISM. When radial flows do not occur, the iron stays in the region where it is ejected so the abundance ratio is lower than with radial flows. In each age band, we also see similar global trends: the models with mixed rotation and zero rotation have the steepest slopes, the 150 kms^{-1} rotation models have the shallowest slope and models with 300 kms^{-1} sit in the middle. This rule does not apply to the oldest age bands, where the models with 300 kms^{-1} massive star rotation have the steepest slopes in the panel. This is because at the oldest ages (i.e. low metallicity) Ba production is strongly enhanced in the 300 kms^{-1} models.

6.4 Discussion and Conclusions

We know from observations, that chemical clocks have been shown to be useful to determine stellar age, especially for solar-twins or in the solar neighbourhood region. However, we have found that these abundance-age(time) relations are not matched by our chemical evolution modelling. We find an underproduction of Mg and a flat Y production with time in the stellar yields prevent us from reproducing the ‘classical’ [Y/Mg] chemical clock. There are also large uncertainties in the observational data for this ratio. Therefore, even where we do see a slope in the OC abundances (e.g. for the outer region), the trend is not statistically significant so it is difficult to compare our models with these observations and draw firm conclusions. We also find we produce opposite gradients than the observations for [Ba/Mg] and [Ba/Fe]

abundance ratios. We also may not be able to reproduce the age gradient relations due to the uncertainties involved in chemical evolution modelling. Stellar yield sets are often uncertain and rely on up to date and reliable reaction rates to be included in the stellar models. The radial flow velocity used in our flows models is also uncertain as we do not have accurate predictions of radial flow velocity of the gas in the Milky Way. Therefore, our gradients may be improved by improved stellar yields or knowledge of Milky Way dynamics.

As we struggle to reproduce $[s/\alpha]$ or $[s/Fe]$ ratios with age, we instead studied radial gradients of these ratios. We find the gradients vary both by age and by massive star rotational velocity. Analysing the gradients using their solar neighbourhood slopes, we find we are somewhat able to reproduce slopes from the observations (Carbajo-Hijarrubia et al., 2024).

Though we cannot draw any firm conclusions by naming one model as the most successful at reproducing observed gradients, we may be able to use this data to make predictions. The slopes we have generated using our chemical evolution models are indicative of the slopes we may see in observations. If we can make predictions of the radial gradients we may observe in galaxies, this may assist in determining the age, plausible range of rotational velocity of massive stars or gas dynamics of the galaxy based on the slopes.

Overall, we find chemical evolution models struggle to confirm the ‘chemical clock’ trends we see in observations, even for solar neighbourhood regions. We can go some way to reproducing radial gradients of open cluster observations using our models. We find some models are more successful than others, though no model is perfectly able to reproduce the slopes. In future, the predictions made by the models may help us to determine galaxy properties based on the radial abundance gradients.

7. Conclusions and Future Work

“Anticipating problems and figuring out how to solve them is actually the opposite of worrying: it’s productive.”

– Chris Hadfield, *An Astronaut’s Guide to Life on Earth*

In this work, we have taken a deeper look at the chemical evolution of the Milky Way. We have used the chemical evolution code, OMEGA+, with a single-zone surrounded by a circumgalactic medium to perform single element studies of fluorine and phosphorus. We have developed OMEGA, increasing the scope of its capability by including a spatial component for studying specific regions of a galaxy or galactic radial profiles. The new development is called ALPHA. Using ALPHA, we have created two Milky Way like models, one with and one without radial gas flows, performing a parameter study to develop the models and a sensitivity study to understand how the key parameters play a role in the model’s evolution. The first scientific study using ALPHA is performed in this work, studying $[s/a]$ element ratios to investigate both age and radial gradients of the Milky Way.

In Chapter 3, when studying the chemical evolution of fluorine, we utilised a variety of stellar yield tables, recognising the importance of stellar yields when modelling chemical evolution. By considering a range of stellar yields, we were able to agree with some literature that suggests rotating massive stars play an important role in the chemical evolution of fluorine, while also being able to rule out Wolf-Rayet stars as a dominant contributor to the chemical evolution of fluorine. In this Chapter, there is also an in depth discussion of the uncertainties surrounding galactic chemical evolution modelling (see section 3.5.2), which applies to the GCE modelling throughout this work. As seen in Chapter 5, changing any one parameter can have a profound effect on the chemical evolution trends, especially as there is an interplay between many of the parameters in chemical evolution modelling (e.g. the mass of the galaxy, will effect the star formation rate, which effects the abundances of the stellar ejecta and the ISM). Stellar yield set can also be a large source of uncertainty in GCE modelling, with

each author choosing different stellar modelling techniques and reaction rates. These choices impact the yields of the stellar models which are fed into chemical evolution models.

The second, single-element study was performed in Chapter 4. This work attempted to explain the origin of the phosphorus-rich nature of a sample of stars from APOGEE using chemical evolution modelling. Using OMEGA+, we varied only the massive star yield set to investigate four different massive star scenarios. We compared each of the models to the ratios $[P/Fe]$, $[Mg/O]$ and $[Si/S]$ for a sample of P-rich and P-normal stars and found, though the models could reproduce some ratios, we could not reach the high P abundances of the P-rich sample. We ultimately concluded that the origin of P-rich stars cannot currently be explained by chemical evolution modelling. However, this may change in the future with more observations across more elements or with yield sets for rarer nucleosynthesis events such non-thermal nucleosynthesis or different modes of operation of the s or i process.

We have added an extra layer of complexity to chemical evolution modelling with OMEGA by creating ALPHA (Chapter 5). ALPHA connects many instances (zones) of OMEGA and allows interaction between them in the form of radial gas flows. To develop MW-like models both with and without radial gas flows, we performed a parameter study, varying the key parameters which most strongly influence the evolution of the disc. Following this study, we find models which can largely reproduce key values and expected MW trends. In order to appreciate how each parameter may affect the key MW trends, we performed a sensitivity study, varying each parameter within a given range and observing how the trends changed with each one. We found the infall parameters, a and b , to have the most profound impact on the evolutionary trends of the disc when we do not consider radial gas flows. However, when radial gas flows are included in the models, it is the radial flow velocity that most strongly impacts the evolutionary trends.

In Chapter 6, we utilise our new multi-zone chemical evolution models to perform some novel science using the active field of chemical clocks. We study both age and radial gradients of our MW model to understand how the popular $[s/\alpha]$ chemical clocks may vary by age and region. The models were able to go some way to reproducing observed abundances, but we could not reproduce some of the observed trends with age and radius, especially when

considering Y and Mg. Thus, we cannot draw firm conclusions on the ‘chemical clock’ nature of these ratios. However, we were able to take advantage of the spatial component of the model and begin to study radial gradient slopes. This was recently done by [Carbajo-Hijarrubia et al. \(2024\)](#) using observations but has yet to be tackled in the literature using chemical evolution modelling. We compare our modelled slopes to the slopes in the literature and find that the models are not able to fully constrain the observations. However, the models do give us a prediction of the slopes we may observe in a galaxy. This could help us in the future to determine the age, massive star rotational velocity or gas dynamics of a galaxy.

We believe the future of this work lies in continuing to study radial profiles and radial abundance gradients using ALPHA. We have seen already that ALPHA can be a powerful tool in making predictions of slopes of the abundance gradient in the galactic disc, we expect to be able to continue on that trajectory, perhaps exploring stronger radial gas flows which would simulate a more turbulent system. Given that chemical clock trends appear to be the most strong in the solar neighbourhood or with solar twin stars, one could also isolate the solar neighbourhood zone in models using ALPHA. Or one could use ALPHA to model just the solar neighbourhood region but using many zones to increase the resolution of the model in that region. More observations of stars with a large range of available elements (especially neutron capture elements) as well as galactocentric distances would be useful for a comparison to these models, so that the observations can constrain the models and conclusions can be as firm as possible.

There is still plenty of opportunity for development of the ALPHA code and the Milky Way models which arise from it. We selected the parameters M_{inf} , f_{\star} , a and b as the main parameters to be investigated in this work due to their strong influence on the evolution of the models. However, the number of zones used, the starting and ending radius of the disc and the value of the SFR exponent, k , will all play a role in the evolution of the models, with their own dependencies. Therefore, an even more in depth study, or perhaps a Monte-Carlo approach could be taken to develop new and different Milky Way-like models using ALPHA. ALPHA could also be used for the modelling of other disc galaxies.

Bibliography

- Abate C., Pols O. R., Izzard R. G., Karakas A. I., 2015, [A&A](#), **581**, A22
- Abbott B. P., et al., 2017a, [Phys. Rev. Lett.](#), **119**, 161101
- Abbott B. P., et al., 2017b, [ApJL](#), **848**, L12
- Abdurro'uf et al., 2022, [ApJS](#), **259**, 35
- Abia C., et al., 2002, [ApJ](#), **579**, 817
- Abia C., Cunha K., Cristallo S., de Laverny P., Domínguez I., Recio-Blanco A., Smith V. V., Straniero O., 2011, [ApJL](#), **737**, L8
- Abia C., Cunha K., Cristallo S., de Laverny P., 2015, [A&A](#), **581**, A88
- Abia C., Cristallo S., Cunha K., de Laverny P., Smith V. V., 2019, [A&A](#), **625**, A40
- Abolfathi B., et al., 2018, [ApJS](#), **235**, 42
- Alexander R. K., Vincenzo F., Ji A. P., Richstein H., Jordan C. J., Gibson B. K., 2023, [MNRAS](#), **522**, 5415
- Andrews B. H., Weinberg D. H., Schönrich R., Johnson J. A., 2017, [ApJ](#), **835**, 224
- Angulo C., et al., 1999, [Nucl. Phys. A](#), **656**, 3
- Aoki W., Norris J. E., Ryan S. G., Beers T. C., Ando H., 2002, [ApJL](#), **576**, L141
- Arai A., Tajitsu A., Kawakita H., Shinnaka Y., 2021, [ApJ](#), **916**, 44
- Arcones A., Thielemann F.-K., 2023, [A&AR](#), **31**, 1
- Arellano-Córdova K. Z., Esteban C., García-Rojas J., Méndez-Delgado J. E., 2021, [MNRAS](#), **502**, 225
- Argast D., Samland M., Gerhard O. E., Thielemann F. K., 2000, [A&A](#), **356**, 873
- Argast D., Samland M., Thielemann F. K., Gerhard O. E., 2002, [A&A](#), **388**, 842
- Asplund M., Lambert D. L., Kipper T., Pollacco D., Shetrone M. D., 1999, [A&A](#), **343**, 507
- Asplund M., Grevesse N., Sauval A. J., Scott P., 2009, [ARA&A](#), **47**, 481

- Avila-Reese V., Ibarra-Medel H., Lacerna I., Rodríguez-Puebla A., Vázquez-Mata J. A., Sánchez S. F., Hernández-Toledo H. M., Cannarozzo C., 2023, [MNRAS](#), **523**, 4251
- Battino U., et al., 2019, [MNRAS](#), **489**, 1082
- Baugh C. M., 2006, [Reports on Progress in Physics](#), **69**, 3101
- Beers T. C., Christlieb N., 2005, [ARA&A](#), **43**, 531
- Belfiore F., Vincenzo F., Maiolino R., Matteucci F., 2019, [MNRAS](#), **487**, 456
- Belokurov V., Erkal D., Evans N. W., Koposov S. E., Deason A. J., 2018, [MNRAS](#), **478**, 611
- Bensby T., et al., 2013, [A&A](#), **549**, A147
- Bensby T., Feltzing S., Oey M. S., 2014, [A&A](#), **562**, A71
- Berger T. A., van Saders J. L., Huber D., Gaidos E., Schlieder J. E., Claytor Z. R., 2022, [ApJ](#), **936**, 100
- Bilitewski T., Schönrich R., 2012, [MNRAS](#), **426**, 2266
- Bisterzo S., Gallino R., Straniero O., Cristallo S., Käppeler F., 2010, [MNRAS](#), **404**, 1529
- Bland-Hawthorn J., Gerhard O., 2016, [ARA&A](#), **54**, 529
- Blanton M. R., et al., 2017, [AJ](#), **154**, 28
- Bovy J., Rix H.-W., 2013, [ApJ](#), **779**, 115
- Bovy J., Rix H.-W., Liu C., Hogg D. W., Beers T. C., Lee Y. S., 2012, [ApJ](#), **753**, 148
- Brady K. E., Pilachowski C. A., Grisoni V., Maas Z. G., Nault K. A., 2024, [AJ](#), **167**, 291
- Brauner M., Masseron T., García-Hernández D. A., Pignatari M., Womack K. A., Lugaro M., Hayes C. R., 2023, [A&A](#), **673**, A123
- Brinkman H., 2022, Short-lived radioactive isotopes from massive single and binary stellar winds, PhD Thesis, University of Szeged
- Brinkman H. E., den Hartogh J. W., Doherty C. L., Pignatari M., Lugaro M., 2021, [ApJ](#), **923**, 47
- Buder S., et al., 2018, [MNRAS](#), **478**, 4513
- Buder S., et al., 2021, [MNRAS](#), **506**, 150
- Burbidge E. M., Burbidge G. R., Fowler W. A., Hoyle F., 1957, [Reviews of Modern Physics](#), **29**, 547

- Bureau M., Freeman K. C., 1999, *AJ*, **118**, 126
- Busso M., Gallino R., Wasserburg G. J., 1999, *ARA&A*, **37**, 239
- Busso M., Gallino R., Lambert D. L., Travaglio C., Smith V. V., 2001, *ApJ*, **557**, 802
- Cabrera-Lavers A., Hammersley P. L., González-Fernández C., López-Corredoira M., Garzón F., Mahoney T. J., 2007, *A&A*, **465**, 825
- Caffau E., Bonifacio P., Faraggiana R., Steffen M., 2011, *A&A*, **532**, A98
- Caffau E., Andrievsky S., Korotin S., Origlia L., Oliva E., Sanna N., Ludwig H. G., Bonifacio P., 2016, *A&A*, **585**, A16
- Campbell S. W., Lugaro M., Karakas A. I., 2010, *A&A*, **522**, L6
- Carbajo-Hijarrubia J., et al., 2024, *A&A*, **687**, A239
- Carigi L., Hernandez X., Gilmore G., 2002, *MNRAS*, **334**, 117
- Carollo D., et al., 2007, *Nature*, **450**, 1020
- Carollo D., et al., 2010, *ApJ*, **712**, 692
- Casali G., et al., 2019, *A&A*, **629**, A62
- Casali G., et al., 2020, *A&A*, **639**, A127
- Castro-Ginard A., Jordi C., Luri X., Cantat-Gaudin T., Balaguer-Núñez L., 2019, *A&A*, **627**, A35
- Castro-Ginard A., et al., 2020, *A&A*, **635**, A45
- Cavichia O., Mollá M., Bazán J. J., 2023, *MNRAS*, **520**, 402
- Cescutti G., 2008, *A&A*, **481**, 691
- Cescutti G., Matteucci F., Caffau E., François P., 2012, *A&A*, **540**, A33
- Chabrier G., 2003, *PASP*, **115**, 763
- Chen B., Hayden M. R., Sharma S., Bland-Hawthorn J., Kobayashi C., Karakas A. I., 2023, *MNRAS*, **523**, 3791
- Chiappini C., Matteucci F., Gratton R., 1997, *ApJ*, **477**, 765
- Chiappini C., Matteucci F., Romano D., 2001, *ApJ*, **554**, 1044

- Chiappini C., Hirschi R., Meynet G., Ekström S., Maeder A., Matteucci F., 2006, [A&A](#), **449**, L27
- Chieffi A., Limongi M., Straniero O., 1998, [ApJ](#), **502**, 737
- Chieffi A., et al., 2021, [ApJ](#), **916**, 79
- Chiosi C., 1980, [A&A](#), **83**, 206
- Chopin A., Hirschi R., Meynet G., Ekström S., Chiappini C., Laird A., 2018, [A&A](#), **618**, A133
- Clarke A. J., et al., 2019, [MNRAS](#), **484**, 3476
- Clarkson O., Herwig F., Pignatari M., 2018, [MNRAS](#), **474**, L37
- Clayton D., 2003, *Handbook of Isotopes in the Cosmos*. Cambridge University Press
- Colavitti E., Cescutti G., Matteucci F., Murante G., 2009, [A&A](#), **496**, 429
- Côté B., Ritter C., O’Shea B. W., Herwig F., Pignatari M., Jones S., Fryer C. L., 2016, [ApJ](#), **824**, 82
- Côté B., O’Shea B. W., Ritter C., Herwig F., Venn K. A., 2017, [ApJ](#), **835**, 128
- Côté B., Denissenkov P., Herwig F., Ruiter A. J., Ritter C., Pignatari M., Belczynski K., 2018a, [ApJ](#), **854**, 105
- Côté B., Silvia D. W., O’Shea B. W., Smith B., Wise J. H., 2018b, [ApJ](#), **859**, 67
- Côté B., Lugaro M., Reifarth R., Pignatari M., Világos B., Yagüe A., Gibson B. K., 2019a, [ApJ](#), **878**, 156
- Côté B., Yagüe A., Világos B., Lugaro M., 2019b, [ApJ](#), **887**, 213
- Cowan J. J., Rose W. K., 1977, [ApJ](#), **212**, 149
- Creevey O. L., et al., 2017, [A&A](#), **601**, A67
- Cristallo S., Di Leva A., Imbriani G., Piersanti L., Abia C., Gialanella L., Straniero O., 2014, [A&A](#), **570**, A46
- Cristallo S., Straniero O., Piersanti L., Gobrecht D., 2015, [ApJS](#), **219**, 40
- Cunha K., Smith V. V., 2005, [ApJ](#), **626**, 425
- Cunha K., Smith V. V., Lambert D. L., Hinkle K. H., 2003, [AJ](#), **126**, 1305
- Da Silva R., et al., 2023, [A&A](#), **678**, A195
- Dame T. M., 1993, in *Back to the Galaxy*. AIP, pp 267–278, [doi:10.1063/1.43985](#)
- Danilovich T., et al., 2021, [A&A](#), **655**, A80

- Dayal P., Ferrara A., Dunlop J. S., 2013, [MNRAS](#), 430, 2891
- De Laverny P., Recio-Blanco A., 2013, [A&A](#), 555, A121
- Deason A. J., Belokurov V., Sanders J. L., 2019, [MNRAS](#), 490, 3426
- Delgado Mena E., et al., 2019, [A&A](#), 624, A78
- Denissenkov P. A., Herwig F., Battino U., Ritter C., Pignatari M., Jones S., Paxton B., 2017, [ApJL](#), 834, L10
- Denissenkov P. A., Herwig F., Woodward P., Andrassy R., Pignatari M., Jones S., 2019, [MNRAS](#), 488, 4258
- Di Matteo P., et al., 2014, [A&A](#), 567, A122
- Doherty C. L., Gil-Pons P., Siess L., Lattanzio J. C., Lau H. H. B., 2015, [MNRAS](#), 446, 2599
- Edmunds M. G., Greenhow R. M., 1995, [MNRAS](#), 272, 241
- Edvardsson B., Andersen J., Gustafsson B., Lambert D. L., Nissen P. E., Tomkin J., 1993, [A&A](#), 275, 101
- Eggen O. J., Lynden-Bell D., Sandage A. R., 1962, [ApJ](#), 136, 748
- Ekström S., et al., 2012, [A&A](#), 537, A146
- Esteban C., Fang X., García-Rojas J., Toribio San Cipriano L., 2017, [MNRAS](#), 471, 987
- Feltzing S., Howes L. M., McMillan P. J., Stonkutė E., 2017, [MNRAS](#), 465, L109
- Fenner Y., Gibson B. K., 2003, [PASA](#), 20, 189
- Fenner Y., Gibson B. K., Gallino R., Lugaro M., 2006, [ApJ](#), 646, 184
- Fernández-Alvar E., et al., 2018, [ApJ](#), 852, 50
- Fernández-Trincado J. G., et al., 2019, [ApJL](#), 886, L8
- Fernández-Trincado J. G., Beers T. C., Minniti D., 2020, [A&A](#), 644, A83
- Ferrini F., Penco U., Palla F., 1990, [A&A](#), 231, 391
- Ferrini F., Matteucci F., Pardi C., Penco U., 1992, [ApJ](#), 387, 138
- Ferrini F., Molla M., Pardi M. C., Diaz A. I., 1994, [ApJ](#), 427, 745
- Fishlock C. K., Karakas A. I., Lugaro M., Yong D., 2014, [ApJ](#), 797, 44
- Forestini M., Goriely S., Jorissen A., Arnould M., 1992, [A&A](#), 261, 157

- Fragkoudi F., Di Matteo P., Haywood M., Khoperskov S., Gomez A., Schultheis M., Combes F., Semelin B., 2017, *A&A*, **607**, L4
- Franco M., et al., 2021, *Nature Astronomy*, **5**, 1240
- Frebel A., Norris J. E., 2015, *ARA&A*, **53**, 631
- Freundlich J., Maoz D., 2021, *MNRAS*, **502**, 5882
- Frischknecht U., Hirschi R., Thielemann F. K., 2012, *A&A*, **538**, L2
- Frischknecht U., et al., 2016, *MNRAS*, **456**, 1803
- Fröhlich C., Martínez-Pinedo G., Liebendörfer M., Thielemann F. K., Bravo E., Hix W. R., Langanke K., Zinner N. T., 2006, *Phys. Rev. Lett.*, **96**, 142502
- Fryer C. L., Belczynski K., Wiktorowicz G., Dominik M., Kalogera V., Holz D. E., 2012, *ApJ*, **749**, 91
- Fuhrmann K., 1998, *A&A*, **338**, 161
- Gallart C., et al., 2024, *A&A*, **687**, A168
- García Pérez A. E., et al., 2018, *ApJ*, **852**, 91
- Ghosh S., Fragkoudi F., Di Matteo P., Saha K., 2024, *A&A*, **683**, A196
- Gibson B. K., 1997, *MNRAS*, **290**, 471
- Gibson B. K., Fenner Y., Renda A., Kawata D., Lee H.-C., 2003, *PASA*, **20**, 401
- Gilmore G., Reid N., 1983, *MNRAS*, **202**, 1025
- Gilmore G., et al., 2012, *The Messenger*, **147**, 25
- Goriely S., 2022, *A&A*, **658**, A197
- Goriely S., Jorissen A., Arnould M., 1989, in *Nuclear Astrophysics*. p. 60
- Goswami A., Prantzos N., 2000, *A&A*, **359**, 191
- Gratton R. G., Carretta E., Matteucci F., Sneden C., 2000, *A&A*, **358**, 671
- Greggio L., Renzini A., 1983, *Mem Soc Astron Ital*, **54**, 311
- Griffith E. J., Sukhbold T., Weinberg D. H., Johnson J. A., Johnson J. W., Vincenzo F., 2021, *ApJ*, **921**, 73

- Grisoni V., Spitoni E., Matteucci F., Recio-Blanco A., de Laverny P., Hayden M., Mikolaitis Š., Worley C. C., 2017, *MNRAS*, **472**, 3637
- Grisoni V., Spitoni E., Matteucci F., 2018, *MNRAS*, **481**, 2570
- Grisoni V., Romano D., Spitoni E., Matteucci F., Ryde N., Jönsson H., 2020, *MNRAS*, **498**, 1252
- Guerço R., Ramírez S., Cunha K., Smith V. V., Prantzos N., Sellgren K., Daflon S., 2022, *ApJ*, **929**, 24
- Gulick A., 1955, *American Scientist*, **43**, 479
- Hampel M., Stancliffe R. J., Lugaro M., Meyer B. S., 2016, *ApJ*, **831**, 171
- Hampel M., Karakas A. I., Stancliffe R. J., Meyer B. S., Lugaro M., 2019, *ApJ*, **887**, 11
- Hansen, C. J. et al., 2016, *A&A*, **588**, A37
- Hansen, T. T. Andersen J., Nordström B., Beers T. C., Placco V. M., Yoon J., Buchhave L. A., 2016, *A&A*, **586**, A160
- Hartwick F. D. A., 1976, *ApJ*, **209**, 418
- Hartwick F. D. A., 1987, in *The Galaxy*, NATO Advanced Study Institute (ASI) Series C. p. 281
- Hayden M. R., et al., 2015, *ApJ*, **808**, 132
- Hayden M. R., Recio-Blanco A., de Laverny P., Mikolaitis S., Worley C. C., 2017, *A&A*, **608**, L1
- Hayden M. R., et al., 2022, *MNRAS*, **517**, 5325
- Hayes C. R., et al., 2018, *ApJ*, **852**, 49
- Hayes C. R., et al., 2022, *ApJS*, **262**, 34
- Haywood M., Di Matteo P., Lehnert M. D., Katz D., Gómez A., 2013, *A&A*, **560**, A109
- Helmi A., Babusiaux C., Koppelman H. H., Massari D., Veljanoski J., Brown A. G. A., 2018, *Nature*, **563**, 85
- Herwig F., et al., 2009, in *Proceedings of 10th Symposium on Nuclei in the Cosmos — PoS(NIC X)*. Sissa Medialab, Trieste, Italy, p. 023
- Herwig F., Pignatari M., Woodward P. R., Porter D. H., Rockefeller G., Fryer C. L., Bennett M., Hirschi R., 2011, *ApJ*, **727**, 89
- Hill V., et al., 2011, *A&A*, **534**, A80

- Hinkel N. R., Timmes F. X., Young P. A., Pagano M. D., Turnbull M. C., 2014, [AJ](#), **148**, 54
- Holanda N., Roriz M. P., Drake N. A., Junqueira S., Daflon S., da Silva J. R. P., Pereira C. B., 2024, [MNRAS](#), **527**, 1389
- Holmbeck E. M., Andrews J. J., 2024, [ApJ](#), **963**, 110
- Holmberg J., Nordström B., Andersen J., 2009, [A&A](#), **501**, 941
- Hunt E. L., Reffert S., 2024, [A&A](#), **686**, A42
- Iben I. J., Tutukov A. V., 1984, [ApJ](#), **282**, 615
- Iben I. J., Tutukov A. V., 1987, [ApJ](#), **313**, 727
- Iliadis C., 2015, Nuclear physics of stars. Wiley-VCH
- Immeli A., Samland M., Gerhard O., Westera P., 2004, [A&A](#), **413**, 547
- Iwamoto K., Brachwitz F., Nomoto K., Kishimoto N., Umeda H., Hix W. R., Thielemann F.-K., 1999, [ApJS](#), **125**, 439
- Izzo L., et al., 2022, [MNRAS](#), **510**, 5302
- Jacobson H. R., Thanathibodee T., Frebel A., Roederer I. U., Cescutti G., Matteucci F., 2014, [ApJL](#), **796**, L24
- Johnson J. A., et al., 2017, [AJ](#), **154**, 108
- Johnson J. W., et al., 2021, [MNRAS](#), **508**, 4484
- Jones S., Ritter C., Herwig F., Fryer C., Pignatari M., Bertolli M. G., Paxton B., 2016, [MNRAS](#), **455**, 3848
- Jönsson H., Ryde N., Spitoni E., Matteucci F., Cunha K., Smith V., Hinkle K., Schultheis M., 2017, [ApJ](#), **835**, 50
- Jorissen A., Smith V. V., Lambert D. L., 1992, [A&A](#), **261**, 164
- José J., Hernanz M., 1998, [ApJ](#), **494**, 680
- Jurić M., et al., 2008, [ApJ](#), **673**, 864
- Kafle P. R., Sharma S., Lewis G. F., Bland-Hawthorn J., 2014, [ApJ](#), **794**, 59
- Kappeler F., Beer H., Wisshak K., 1989, [Reports on Progress in Physics](#), **52**, 945
- Karakas A. I., 2010, [MNRAS](#), **403**, 1413

- Karakas A., Lattanzio J. C., 2007, [PASA](#), *24*, 103
- Karakas A. I., Lattanzio J. C., 2014, [PASA](#), *31*, e030
- Karakas A. I., Lugaro M., 2016, [ApJ](#), *825*, 26
- Karakas A. I., García-Hernández D. A., Lugaro M., 2012, [ApJ](#), *751*, 8
- Karakas A. I., Lugaro M., Carlos M., Cseh B., Kamath D., García-Hernández D. A., 2018, [MNRAS](#), *477*, 421
- Katz D., Gómez A., Haywood M., Snaith O., Di Matteo P., 2021, [A&A](#), *655*, A111
- Kauffmann G., White S. D. M., Guiderdoni B., 1993, [MNRAS](#), *264*, 201
- Kauffmann G., Colberg J. M., Diaferio A., White S. D. M., 1999, [MNRAS](#), *303*, 188
- Kawash A., et al., 2021, [ApJ](#), *922*, 25
- Keegans J. D., et al., 2021, [Physics Education](#), *56*, 035001
- Keegans J. D., et al., 2023, [ApJS](#), *268*, 8
- Kemp A. J., Karakas A. I., Casey A. R., Côté B., Izzard R. G., Osborn Z., 2022, [ApJL](#), *933*, L30
- Kennicutt Robert C. J., 1998, [ApJ](#), *498*, 541
- Khoperskov S., Haywood M., Snaith O., Di Matteo P., Lehnert M., Vasiliev E., Naroenkov S., Berczik P., 2021, [MNRAS](#), *501*, 5176
- Kjeldsen H., Bedding T. R., Christensen-Dalsgaard J., 2008, [ApJL](#), *683*, L175
- Kobayashi C., Umeda H., Nomoto K., Tominaga N., Ohkubo T., 2006, [ApJ](#), *653*, 1145
- Kobayashi C., Karakas A. I., Umeda H., 2011a, [MNRAS](#), *414*, 3231
- Kobayashi C., Izutani N., Karakas A. I., Yoshida T., Yong D., Umeda H., 2011b, [ApJL](#), *739*, L57
- Kobayashi C., Karakas A. I., Lugaro M., 2020, [ApJ](#), *900*, 179
- Koch A., Reichert M., Hansen C. J., Hampel M., Stancliffe R. J., Karakas A., Arcones A., 2019, [A&A](#), *622*, A159
- Kormendy J., Kennicutt Robert C. J., 2004, [ARA&A](#), *42*, 603
- Korotin S. A., Andrievsky S. M., Luck R. E., Lépine J. R. D., Maciel W. J., Kovtyukh V. V., 2014, [MNRAS](#), *444*, 3301

- Kozyreva A., Yoon S. C., Langer N., 2014, [A&A](#), **566**, A146
- Kromer M., et al., 2015, [MNRAS](#), **450**, 3045
- Kroupa P., 2001, [MNRAS](#), **322**, 231
- Kroupa P., Tout C. A., Gilmore G., 1993, [MNRAS](#), **262**, 545
- Kruijssen J. M. D., Pfeffer J. L., Reina-Campos M., Crain R. A., Bastian N., 2019, [MNRAS](#), **486**, 3180
- Kubryk M., Prantzos N., Athanassoula E., 2015, [A&A](#), **580**, A126
- Kuijken K., Merrifield M. R., 1995, [ApJL](#), **443**, L13
- La Barbera F., Vazdekis A., Pasquali A., Heidt J., Gargiulo A., Eftekhari E., 2024, [A&A](#), **687**, A156
- Lacey C. G., Fall S. M., 1985, [ApJ](#), **290**, 154
- Lanfranchi G. A., Matteucci F., 2003, [MNRAS](#), **345**, 71
- Lanfranchi G. A., Matteucci F., 2004, [MNRAS](#), **351**, 1338
- Lanfranchi G. A., Matteucci F., 2010, [A&A](#), **512**, A85
- Lanfranchi G. A., Matteucci F., Cescutti G., 2006, [A&A](#), **453**, 67
- Larson R. B., 1972, [Nature Physical Science](#), **236**, 7
- Larson R. B., 1976, [MNRAS](#), **176**, 31
- Leung S.-C., Nomoto K., 2018, [ApJ](#), **861**, 143
- Li H. N., Ludwig H. G., Caffau E., Christlieb N., Zhao G., 2013, [ApJ](#), **765**, 51
- Lian J., et al., 2020, [MNRAS](#), **494**, 2561
- Lian J., Storm N., Guiglion G., Serenelli A., Cote B., Karakas A. I., Boardman N., Bergemann M., 2023, [MNRAS](#), **525**, 1329
- Limongi M., Chieffi A., 2003, [ApJ](#), **592**, 404
- Limongi M., Chieffi A., 2018, [ApJS](#), **237**, 13
- Loebman S. R., Debattista V. P., Nidever D. L., Hayden M. R., Holtzman J. A., Clarke A. J., Roškar R., Valluri M., 2016, [ApJL](#), **818**, L6

- Lucatello S., Tsangarides S., Beers T. C., Carretta E., Gratton R. G., Ryan S. G., 2005, [ApJ](#), **625**, 825
- Lucatello S., Masseron T., Johnson J. A., Pignatari M., Herwig F., 2011, [ApJ](#), **729**, 40
- Lucey M., Pearson S., Hunt J. A. S., Hawkins K., Ness M., Petersen M. S., Price-Whelan A. M., Weinberg M. D., 2023, [MNRAS](#), **520**, 4779
- Luck R. E., 2014, [AJ](#), **147**, 137
- Luck R. E., Lambert D. L., 2011, [AJ](#), **142**, 136
- Luck R. E., Andrievsky S. M., Korotin S. N., Kovtyukh V. V., 2013, [AJ](#), **146**, 18
- Lugaro M., 2005, *Stardust From Meteorites: An Introduction to Presolar Grains*. World Scientific
- Lugaro M., Ugalde C., Karakas A. I., Görres J., Wiescher M., Lattanzio J. C., Cannon R. C., 2004, [ApJ](#), **615**, 934
- Lugaro M., Campbell S. W., de Mink S. E., 2009, [PASA](#), **26**, 322
- Lugaro M., Karakas A. I., Stancliffe R. J., Rijs C., 2012, [ApJ](#), **747**, 2
- Lugaro M., et al., 2022, [Universe](#), **8**, 130
- Lynden-Bell D., 1975, [Vistas in Astronomy](#), **19**, 299
- Maas Z. G., Pilachowski C. A., Cescutti G., 2017, [ApJ](#), **841**, 108
- Maas Z. G., Cescutti G., Pilachowski C. A., 2019, [AJ](#), **158**, 219
- Magrini L., Corbelli E., Galli D., 2007, [A&A](#), **470**, 843
- Magrini L., Sestito P., Randich S., Galli D., 2009, [A&A](#), **494**, 95
- Magrini L., et al., 2021, [A&A](#), **646**, L2
- Magrini L., et al., 2023, [A&A](#), **669**, A119
- Maiorca E., Uitenbroek H., Uttenthaler S., Randich S., Busso M., Magrini L., 2014, [ApJ](#), **788**, 149
- Majewski S. R., et al., 2017, [AJ](#), **154**, 94
- Maoz D., Mannucci F., 2012, [PASA](#), **29**, 447
- Martin R. P., Andrievsky S. M., Kovtyukh V. V., Korotin S. A., Yegorova I. A., Saviane I., 2015, [MNRAS](#), **449**, 4071

- Maschberger T., 2013, [MNRAS](#), **429**, 1725
- Masseron T., Johnson J. A., Plez B., van Eck S., Primas F., Goriely S., Jorissen A., 2010, [A&A](#), **509**, A93
- Masseron T., Merle T., Hawkins K., 2016, BACCHUS: Brussels Automatic Code for Characterizing High accUracY Spectra, Astrophysics Source Code Library, record ascl:1605.004
- Masseron T., García-Hernández D. A., Santoveña R., Manchado A., Zamora O., Manteiga M., Dafonte C., 2020a, [Nature Communications](#), **11**, 3759
- Masseron T., García-Hernández D. A., Zamora O., Manchado A., 2020b, [ApJL](#), **904**, L1
- Matteucci F., 1986, [MNRAS](#), **221**, 911
- Matteucci F., 2012, Chemical evolution of the Galaxy. Springer
- Matteucci F., Francois P., 1989, [MNRAS](#), **239**, 885
- Matteucci F., Greggio L., 1986, [A&A](#), **154**, 279
- Matteucci F., Recchi S., 2001, [ApJ](#), **558**, 351
- Matteucci F., Tornambe A., 1985, [A&A](#), **142**, 13
- Matteucci F., Grisoni V., Spitoni E., Zulianello A., Rojas-Arriagada A., Schultheis M., Ryde N., 2019, [MNRAS](#), **487**, 5363
- Mayor M., Vigroux L., 1981, [A&A](#), **98**, 1
- Mazumdar A., 2005, [A&A](#), **441**, 1079
- McKee C. F., Parravano A., Hollenbach D. J., 2015, [ApJ](#), **814**, 13
- Meynet G., Arnould M., 2000, [A&A](#), **355**, 176
- Meynet G., Maeder A., 1997, [A&A](#), **321**, 465
- Miglio A., et al., 2021, [A&A](#), **645**, A85
- Miller G. E., Scalo J. M., 1979, [ApJS](#), **41**, 513
- Milone A. P., 2015, [MNRAS](#), **446**, 1672
- Molaro P., Izzo L., Mason E., Bonifacio P., Della Valle M., 2016, [MNRAS](#), **463**, L117
- Molaro P., Izzo L., Bonifacio P., Hernanz M., Selvelli P., della Valle M., 2020, [MNRAS](#), **492**, 4975

- Molero M., Magrini L., Matteucci F., Romano D., Palla M., Cescutti G., Viscasillas Vázquez C., Spitoni E., 2023, *MNRAS*, **523**, 2974
- Mollá M., Cavichia O., Gavián M., Gibson B. K., 2015, *MNRAS*, **451**, 3693
- Mollá M., Díaz Á. I., Gibson B. K., Cavichia O., López-Sánchez Á.-R., 2016, *MNRAS*, **462**, 1329
- Mollá M., Díaz Á. I., Cavichia O., Gibson B. K., Maciel W. J., Costa R. D. D., Ascasibar Y., Few C. G., 2019, *MNRAS*, **482**, 3071
- Monelli M., et al., 2014, *ApJ*, **796**, 90
- Mura-Guzmán A., Yong D., Abate C., Karakas A., Kobayashi C., Oh H., Chun S. H., Mace G., 2020, *MNRAS*, **498**, 3549
- Murray N., Quataert E., Thompson T. A., 2005, *ApJ*, **618**, 569
- Nakanishi H., Sofue Y., 2003, *PASJ*, **55**, 191
- Nakanishi H., Sofue Y., 2006, *PASJ*, **58**, 847
- Nandakumar G., Ryde N., Montelius M., Thorsbro B., Jönsson H., Mace G., 2022, *A&A*, **668**, A88
- Nandakumar G., Ryde N., Mace G., 2023, *A&A*, **676**, A79
- National Nuclear Data Centre B. N. L., 2021, <https://www.nndc.bnl.gov/nudat2/>
- Nault K. A., Pilachowski C. A., 2013, *AJ*, **146**, 153
- Ness M., Freeman K., 2016, *PASA*, **33**, e022
- Nishimura N., Takiwaki T., Thielemann F.-K., 2015, *ApJ*, **810**, 109
- Nishimura N., Sawai H., Takiwaki T., Yamada S., Thielemann F. K., 2017, *ApJL*, **836**, L21
- Nissen P. E., 2015, *A&A*, **579**, A52
- Nissen P. E., Schuster W. J., 2010, *A&A*, **511**, L10
- Nomoto K., Kobayashi C., Tominaga N., 2013, *ARA&A*, **51**, 457
- Nordström B., et al., 2004, *A&A*, **418**, 989
- Olive K. A., Vangioni E., 2019, *MNRAS*, **490**, 4307
- Ono M., Hashimoto M., Fujimoto S., Kotake K., Yamada S., 2012, *Progress of Theoretical Physics*, **128**, 741

- Otí Floranes H., Christensen-Dalsgaard J., Thompson M. J., 2005, [MNRAS](#), **356**, 671
- Pagel B. E. J., 1989, *Rev. Mex. Astron. Astrofis.*, **18**, 161
- Pagel B. E. J., 1997, *Nucleosynthesis and Chemical Evolution of the Galaxies*. Cambridge University Press
- Pagel B. E. J., Patchett B. E., 1975, [MNRAS](#), **172**, 13
- Palacios A., Arnould M., Meynet G., 2005, [A&A](#), **443**, 243
- Palla M., Matteucci F., Spitoni E., Vincenzo F., Grisoni V., 2020, [MNRAS](#), **498**, 1710
- Palmerini S., Busso M., Vescovi D., 2020, in *Journal of Physics Conference Series*. IOP, p. 012032, [doi:10.1088/1742-6596/1668/1/012032](https://doi.org/10.1088/1742-6596/1668/1/012032)
- Pandey K., West C., 2022, [MNRAS](#), **517**, 1071
- Paxton B., Bildsten L., Dotter A., Herwig F., Lesaffre P., Timmes F., 2011, [ApJS](#), **192**, 3
- Paxton B., et al., 2013, [ApJS](#), **208**, 4
- Peng Y.-j., Maiolino R., 2014, [MNRAS](#), **443**, 3643
- Pepe F., et al., 2002, *The Messenger*, **110**, 9
- Pezzulli G., Fraternali F., 2016, [MNRAS](#), **455**, 2308
- Pignatari M., Gallino R., Heil M., Wiescher M., Käppeler F., Herwig F., Bisterzo S., 2010, [ApJ](#), **710**, 1557
- Pignatari M., et al., 2013, [ApJ](#), **762**, 31
- Pignatari M., et al., 2016, [ApJS](#), **225**, 24
- Pignatari M., et al., 2023, [MNRAS](#), **524**, 6295
- Pilyugin L. S., Tautvaišienė G., 2024, [A&A](#), **682**, A41
- Pinsonneault M. H., et al., 2014, [ApJS](#), **215**, 19
- Pinsonneault M. H., et al., 2018, [ApJS](#), **239**, 32
- Pipino A., D'Ercole A., Matteucci F., 2008, [A&A](#), **484**, 679
- Poggio E., et al., 2021, [A&A](#), **651**, A104
- Portail M., Gerhard O., Wegg C., Ness M., 2017, [MNRAS](#), **465**, 1621

- Portinari L., Chiosi C., 2000, [A&A](#), **355**, 929
- Pouliasis E., Di Matteo P., Haywood M., 2017, [A&A](#), **598**, A66
- Prantzos N., 2016, [Astronomische Nachrichten](#), **337**, 953
- Prantzos N., Abia C., Limongi M., Chieffi A., Cristallo S., 2018, [MNRAS](#), **476**, 3432
- Rana N. C., 1991, [ARA&A](#), **29**, 129
- Randich S., et al., 2022, [A&A](#), **666**, A121
- Ratcliffe B., Minchev I., Cescutti G., Spitoni E., Jönsson H., Anders F., Queiroz A., Steinmetz M., 2024, [MNRAS](#), **528**, 3464
- Recchi S., Wunsch R., Palouš J., Dinnbier F., 2017, [Astrophysics and Space Science](#), **362**, 183
- Recio-Blanco A., et al., 2023, [A&A](#), **674**, A29
- Rector T. A., et al., 2022, [ApJ](#), **936**, 117
- Renda A., et al., 2004, [MNRAS](#), **354**, 575
- Revaz Y., Arnaudon A., Nichols M., Bonvin V., Jablonka P., 2016, [A&A](#), **588**, A21
- Ritter C., Côté B., Herwig F., Navarro J. F., Fryer C. L., 2018a, [ApJS](#), **237**, 42
- Ritter C., Andrassy R., Côté B., Herwig F., Woodward P. R., Pignatari M., Jones S., 2018b, [MNRAS](#), **474**, L1
- Ritter C., Herwig F., Jones S., Pignatari M., Fryer C., Hirschi R., 2018c, [MNRAS](#), **480**, 538
- Rizzuti F., Cescutti G., Matteucci F., Chieffi A., Hirschi R., Limongi M., 2019, [MNRAS](#), **489**, 5244
- Robin A. C., Marshall D. J., Schultheis M., Reylé C., 2012, [A&A](#), **538**, A106
- Roederer I. U., Jacobson H. R., Thanathibodee T., Frebel A., Toller E., 2014, [ApJ](#), **797**, 69
- Romano D., Chiappini C., Matteucci F., Tosi M., 2005, [A&A](#), **430**, 491
- Romano D., Karakas A. I., Tosi M., Matteucci F., 2010, [A&A](#), **522**, A32
- Romano D., Matteucci F., Zhang Z.-Y., Ivison R. J., Ventura P., 2019, [MNRAS](#), **490**, 2838
- Romano D., et al., 2023, [ApJ](#), **951**, 85
- Rosswog S., Korobkin O., Arcones A., Thielemann F. K., Piran T., 2014, [MNRAS](#), **439**, 744

- Rupke D. S. N., 2018, [Galaxies](#), **6**, 138
- Rybizki J., Just A., Rix H.-W., 2017, [A&A](#), **605**, A59
- Ryde N., et al., 2020, [ApJ](#), **893**, 37
- Saberi M., Khouri T., Velilla-Prieto L., Fonfría J. P., Vlemmings W. H. T., Wedemeyer S., 2022, [A&A](#), **663**, A54
- Salpeter E. E., 1955, [ApJ](#), **121**, 161
- Sanders J. L., Belokurov V., Man K. T. F., 2021, [MNRAS](#), **506**, 4321
- Scannapieco C., Tissera P. B., 2003, [MNRAS](#), **338**, 880
- Schmidt M., 1959, [ApJ](#), **129**, 243
- Schmidt M., 1963, [ApJ](#), **137**, 758
- Schönrich R., Binney J., 2009a, [MNRAS](#), **396**, 203
- Schönrich R., Binney J., 2009b, [MNRAS](#), **399**, 1145
- Searle L., Zinn R., 1978, [ApJ](#), **225**, 357
- Selvelli P., Molaro P., Izzo L., 2018, [MNRAS](#), **481**, 2261
- Semczuk M., Dehnen W., Schönrich R., Athanassoula E., 2022, [MNRAS](#), **509**, 4532
- Seshashayana S. B., et al., 2024, [A&A](#), **683**, A218
- Shafter A. W., 2017, [ApJ](#), **834**, 196
- Sharma S., Hayden M. R., Bland-Hawthorn J., 2021, [MNRAS](#), **507**, 5882
- Silva Aguirre V., et al., 2018, [MNRAS](#), **475**, 5487
- Smith V. V., Cunha K., Ivans I. I., Lattanzio J. C., Campbell S., Hinkle K. H., 2005, [ApJ](#), **633**, 392
- Snedden C., Kraft R. P., Shetrone M. D., Smith G. H., Langer G. E., Prosser C. F., 1997, [AJ](#), **114**, 1964
- Snedden C., Cowan J. J., Gallino R., 2008, [ARA&A](#), **46**, 241
- Soderblom D. R., 2010, [ARA&A](#), **48**, 581
- Somerville R. S., Davé R., 2015, [ARA&A](#), **53**, 51

- Spina L., Meléndez J., Karakas A. I., Ramírez I., Monroe T. R., Asplund M., Yong D., 2016, [A&A](#), **593**, [A125](#)
- Spina L., et al., 2018, [MNRAS](#), **474**, [2580](#)
- Spina L., et al., 2021, [MNRAS](#), **503**, [3279](#)
- Spitoni E., Matteucci F., 2011, [A&A](#), **531**, [A72](#)
- Spitoni E., Matteucci F., Sozzetti A., 2014, [MNRAS](#), **440**, [2588](#)
- Spitoni E., Romano D., Matteucci F., Ciotti L., 2015, [ApJ](#), **802**, [129](#)
- Spitoni E., Gioannini L., Matteucci F., 2017, [A&A](#), **605**, [A38](#)
- Spitoni E., Matteucci F., Jönsson H., Ryde N., Romano D., 2018, [A&A](#), **612**, [A16](#)
- Spitoni E., Silva Aguirre V., Matteucci F., Calura F., Grisoni V., 2019, [A&A](#), **623**, [A60](#)
- Spitoni E., Verma K., Silva Aguirre V., Calura F., 2020, [A&A](#), **635**, [A58](#)
- Spitoni E., et al., 2023, [A&A](#), **670**, [A109](#)
- Springel V., White S. D. M., Tormen G., Kauffmann G., 2001, [MNRAS](#), **328**, [726](#)
- Spyrou K., Chronidou C., Harissopulos S., Kossionides S., Paradellis T., Rolfs C., Schulte W., Borucki L., 2000, [The European Physical Journal A](#), **7**, [79](#)
- Stahler S. W., Palla F., 2005, *The Formation of Stars*. WILEY-VCH Verlag GmbH & Co. KGaA., Weinheim
- Stancliffe R. J., Lugaro M., Ugalde C., Tout C. A., Görres J., Wiescher M., 2005, [MNRAS](#), **360**, [375](#)
- Starkenburger E., Shetrone M. D., McConnachie A. W., Venn K. A., 2014, [MNRAS](#), **441**, [1217](#)
- Starrfield S., Bose M., Iliadis C., Hix W. R., Woodward C. E., Wagner R. M., 2020, [ApJ](#), **895**, [70](#)
- Storm N., Bergemann M., 2023, [MNRAS](#), **525**, [3718](#)
- Straniero O., Gallino R., Cristallo S., 2006, [Nucl. Phys. A](#), **777**, [311](#)
- Sukhbold T., Ertl T., Woosley S. E., Brown J. M., Janka H. T., 2016, [ApJ](#), **821**, [38](#)
- Tajitsu A., Sadakane K., Naito H., Arai A., Aoki W., 2015, [Nature](#), **518**, [381](#)
- Tajitsu A., Sadakane K., Naito H., Arai A., Kawakita H., Aoki W., 2016, [ApJ](#), **818**, [191](#)
- Takahashi K., Yoshida T., Umeda H., 2018, [ApJ](#), **857**, [111](#)

- Talbot Raymond J. J., Arnett W. D., 1971, [ApJ](#), 170, 409
- Talbot Raymond J. J., Arnett W. D., 1973, [ApJ](#), 186, 51
- Timmes F. X., Woosley S. E., Weaver T. A., 1995, [ApJS](#), 98, 617
- Tinsley B. M., 1968, [ApJ](#), 151, 547
- Tinsley B. M., 1974, [ApJ](#), 192, 629
- Tinsley B. M., 1980, [Fundamentals of Cosmic Physics](#), 5, 287
- Tinsley B. M., Larson R. B., 1978, [ApJ](#), 221, 554
- Titarenko A., Recio-Blanco A., de Laverny P., Hayden M., Guiglion G., 2019, [A&A](#), 622, A59
- Tosi M., 1982, [ApJ](#), 254, 699
- Townsley D. M., Miles B. J., Timmes F. X., Calder A. C., Brown E. F., 2016, [ApJS](#), 225, 3
- Traven G., et al., 2020, [A&A](#), 638, A145
- Trueman T. C. L., Côté B., Yagüe López A., den Hartogh J., Pignatari M., Soós B., Karakas A. I., Lugaro M., 2022, [ApJ](#), 924, 10
- Tucci Maia M., Ramírez I., Meléndez J., Bedell M., Bean J. L., Asplund M., 2016, [A&A](#), 590, A32
- Valenti E., et al., 2016, [A&A](#), 587, L6
- Van den Bergh S., 1958, [AJ](#), 63, 492
- Van den Bergh S., 1962, [AJ](#), 67, 486
- Van der Swaelmen M., et al., 2023, [A&A](#), 670, A129
- Ventura P., Di Criscienzo M., Carini R., D'Antona F., 2013, [MNRAS](#), 431, 3642
- Ventura P., di Criscienzo M., D'Antona F., Vesperini E., Tailo M., Dell'Agli F., D'Ercole A., 2014, [MNRAS](#), 437, 3274
- Ventura P., Karakas A., Dell'Agli F., García-Hernández D. A., Guzman-Ramirez L., 2018, [MNRAS](#), 475, 2282
- Vescovi D., Cristallo S., Busso M., Liu N., 2020, [ApJL](#), 897, L25
- Vincenzo F., Kobayashi C., 2020, [MNRAS](#), 496, 80

- Vincenzo F., Matteucci F., Vattakunnel S., Lanfranchi G. A., 2014, [MNRAS](#), **441**, 2815
- Vincenzo F., Matteucci F., Belfiore F., Maiolino R., 2016, [MNRAS](#), **455**, 4183
- Vincenzo F., Matteucci F., Spitoni E., 2017, [MNRAS](#), **466**, 2939
- Vincenzo F., Spitoni E., Calura F., Matteucci F., Silva Aguirre V., Miglio A., Cescutti G., 2019, [MNRAS](#), **487**, L47
- Vincenzo F., Thompson T. A., Weinberg D. H., Griffith E. J., Johnson J. W., Johnson J. A., 2021, [MNRAS](#), **508**, 3499
- Viscasillas Vázquez C., et al., 2022, [A&A](#), **660**, A135
- Wasserburg G. J., Qian Y. Z., 2000, [ApJL](#), **529**, L21
- Weinberg D. H., Andrews B. H., Freudenburg J., 2017, [ApJ](#), **837**, 183
- Whelan J., Iben Icko J., 1973, [ApJ](#), **186**, 1007
- Willett E., et al., 2023, [MNRAS](#), **526**, 2141
- Winteler C., Käppeli R., Perego A., Arcones A., Vasset N., Nishimura N., Liebendörfer M., Thielemann F. K., 2012, [ApJL](#), **750**, L22
- Wise J. H., Abel T., Turk M. J., Norman M. L., Smith B. D., 2012, [MNRAS](#), **427**, 311
- Wiseman P., et al., 2021, [MNRAS](#), **506**, 3330
- Womack K., 2021, Signatures of i-process nucleosynthesis, MSc Thesis, University of Hull
- Womack K. A., Vincenzo F., Gibson B. K., Côté B., Pignatari M., Brinkman H. E., Ventura P., Karakas A., 2023, [MNRAS](#), **518**, 1543
- Woosley S. E., Haxton W. C., 1988, [Nature](#), **334**, 45
- Woosley S. E., Weaver T. A., 1994, [ApJ](#), **423**, 371
- Woosley S. E., Weaver T. A., 1995, [ApJS](#), **101**, 181
- Woosley S. E., Heger A., Weaver T. A., 2002, [Reviews of Modern Physics](#), **74**, 1015
- Yong D., Meléndez J., Cunha K., Karakas A. I., Norris J. E., Smith V. V., 2008, [ApJ](#), **689**, 1020
- Yoon J., et al., 2016, [ApJ](#), **833**, 20

Zhang L. Y., et al., 2021a, [Phys. Rev. Lett.](#), **127**, 152702

Zhang L. Y., López A. Y., Lugaro M., He J. J., Karakas A. I., 2021b, [ApJ](#), **913**, 51

Zoccali M., Valenti E., 2016, [PASA](#), **33**, e025

Zoccali M., et al., 2017, [A&A](#), **599**, A12

A. Appendix - Extra Model Information

This appendix includes information regarding the success of the model in Chapters 3 and 4 at reproducing present day Milky Way constraints and solar abundances. Here, we use the model with the FRUITY AGB yields of [Cristallo et al. \(2015\)](#) and the rotating massive star yields of [Limongi & Chieffi \(2018\)](#) as this model is common across both chapters, as well as being successful in reproducing a large amount of the observations across both works.

Figure A.1 shows the evolution of the SFR, inflow rate, gas mass and supernovae rates (CCSNe and SNe Ia) with galactic age. The shaded bars at the present time represent observational constraints from [Kubryk et al. \(2015\)](#). We can see that the model is able to reproduce the observational constraints for all properties. Table A.1 shows the present day value of each of the properties from the models and compares them with the data from [Kubryk et al. \(2015\)](#), again showing that the model is within the observed range for these parameters.

Property	Observational Data	Model Value
SFR ($M_{\odot} \text{ yr}^{-1}$)	0.65 - 3.0	2.5
Inflow rate ($M_{\odot} \text{ yr}^{-1}$)	0.6 - 1.6	1.3
Gas mass (M_{\odot})	3.6×10^9 - 12.6×10^9	9.4×10^9
CCSNe rate (yr^{-1})	1.0×10^{-2} - 3.0×10^{-2}	2.7×10^{-2}
SNe Ia rate (yr^{-1})	0.2×10^{-2} - 0.6×10^{-2}	0.3×10^{-2}

Table A.1: Present day SFR, inflow rate, gas mass and supernovae rate values from the model compared with observational constraints from [Kubryk et al. \(2015\)](#).

We also find that the model does well at reproducing solar abundances at the time of the formation of the sun for the elements of interest in Chapters 3 and 4. The elements of interest in Chapter 3 are: F, O, Fe and Ce, while in Chapter 4 they are: P, O, Mg, Si, S and Fe. Table A.2 shows the abundance $[X/\text{Fe}]$ or $[\text{Fe}/\text{H}]$ for each of the elements at 8 Gyr through the evolution of the model (the time of the formation of the sun). If the model reproduces

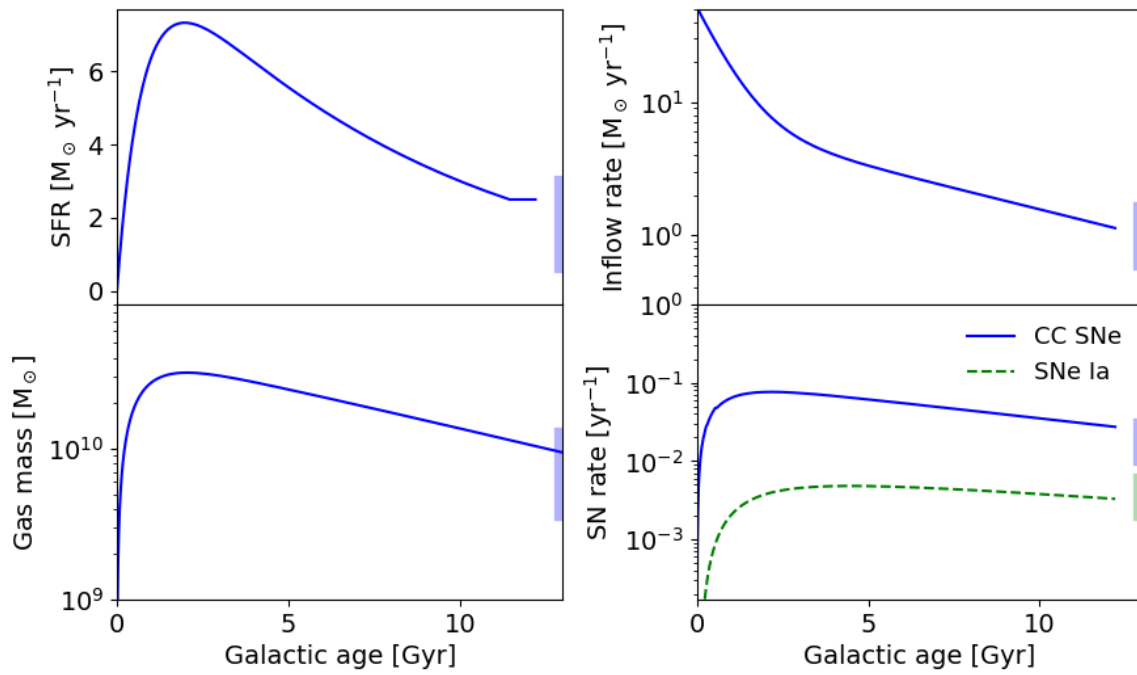


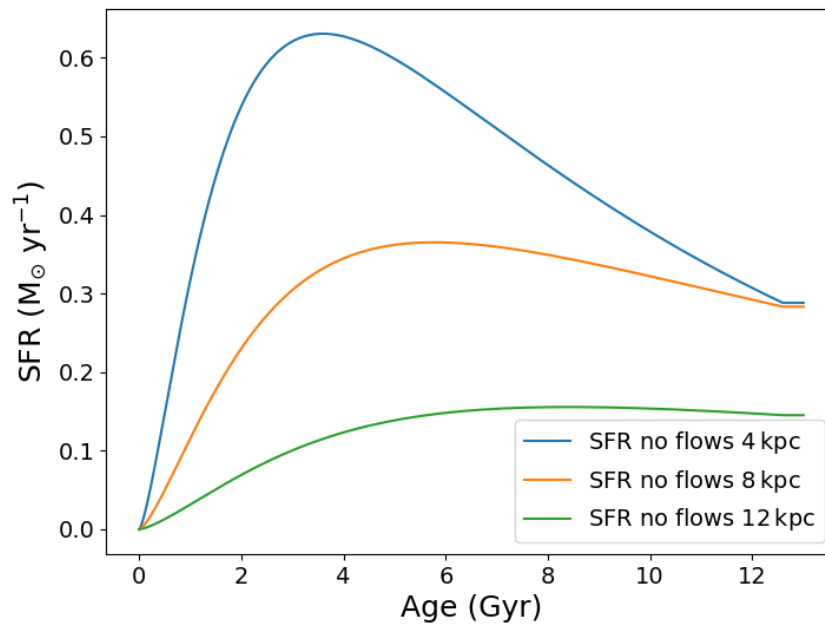
Figure A.1: Evolution of star formation rate, inflow rate, gas mass and supernovae rates with galactic age for the model. The shaded regions are present day observational constraints from [Kubryk et al. \(2015\)](#).

solar abundance exactly, we would expect $[X/Fe]$ (or $[Fe/H]$ in the case of iron) to be zero at 8 Gyr. We can see that some abundance ratios are closer to zero than others, with fluorine and phosphorus performing particularly well. However, all abundance ratios are within less than 0.3 dex of solar.

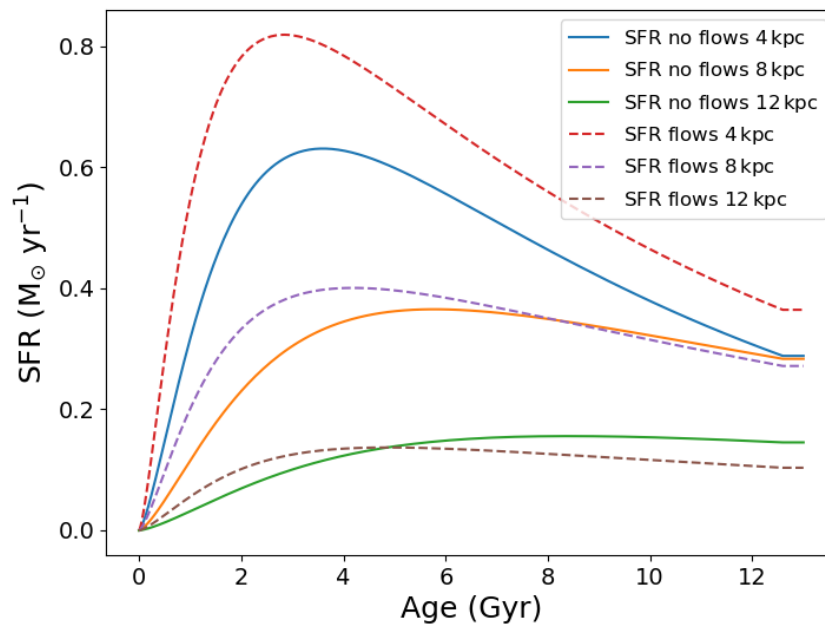
Element Ratio	Abundance
$[F/Fe]$	-0.08
$[P/Fe]$	0.04
$[O/Fe]$	0.11
$[Mg/Fe]$	-0.23
$[Si/Fe]$	0.13
$[S/Fe]$	0.14
$[Ce/Fe]$	0.27
$[Fe/H]$	0.05

Table A.2: $[X/Fe]$ or $[Fe/H]$ abundance ratios for the model using [Asplund et al. \(2009\)](#) solar abundances.

B. Appendix - Multi-zone Development



(a) SFR versus galactic age for the no radial gas flows model.



(b) SFR versus galactic age for both the no flows and flows models.

Figure B.1: SFR versus galactic age for the 4 kpc, 8 kpc and 12 kpc zones.

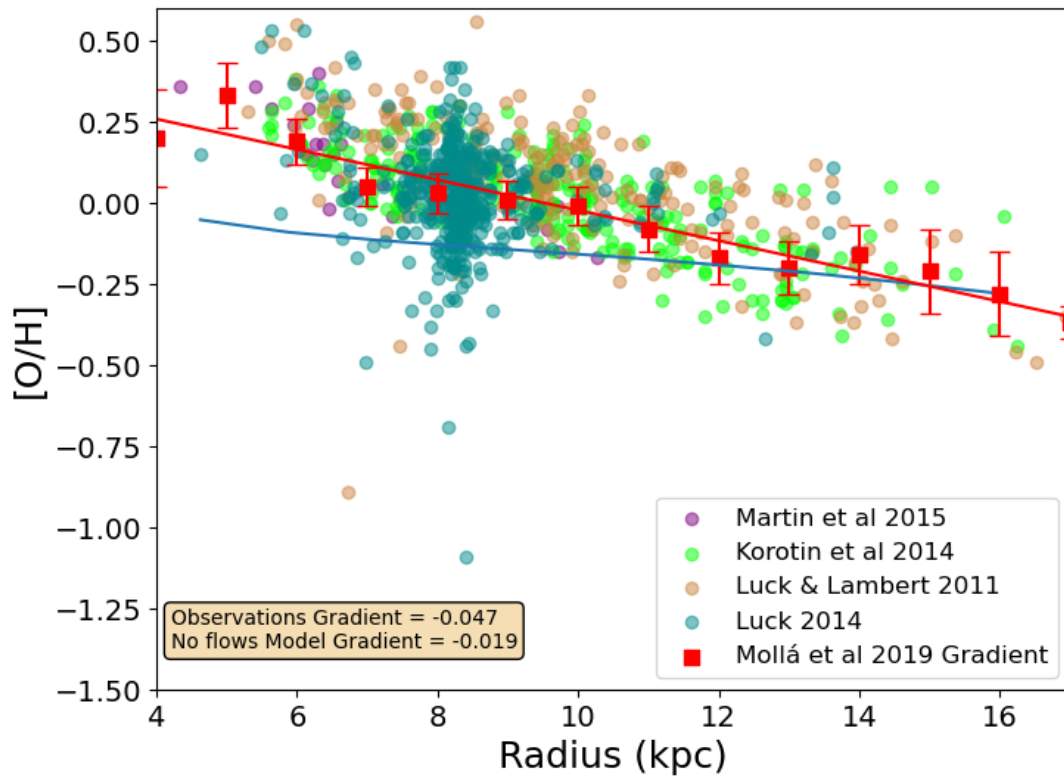


Figure B.2: An example of an $[O/H]$ gradient that we rejected when selecting a MW-like model. The model has properties: $M_{\text{inf}} = 2.5 \times 10^{10} M_{\odot}$, $f_{\star} = 1.8 \times 10^{-4} M_{\odot} \text{ yr}^{-1} \text{ kpc}^{-2}$, $a = -2.5 \text{ Gyr}$ and $b = 2 \text{ Gyr kpc}^{-1}$.

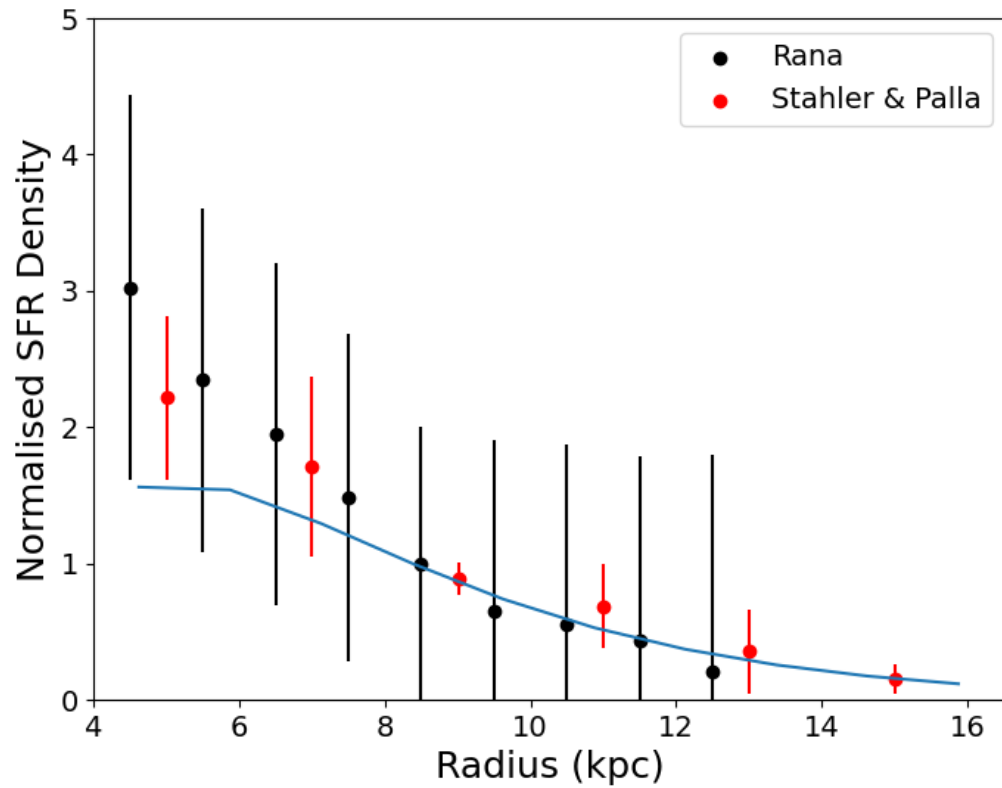


Figure B.3: An example of an unacceptable normalised star formation rate density when selecting a MW-like model. The model has properties: $M_{\text{inf}} = 2.17 \times 10^{10} M_{\odot}$, $f_{\star} = 2.34 \times 10^{-4} M_{\odot} \text{ yr}^{-1} \text{ kpc}^{-2}$, $a = -2.5 \text{ Gyr}$ and $b = 2 \text{ Gyr kpc}^{-1}$.

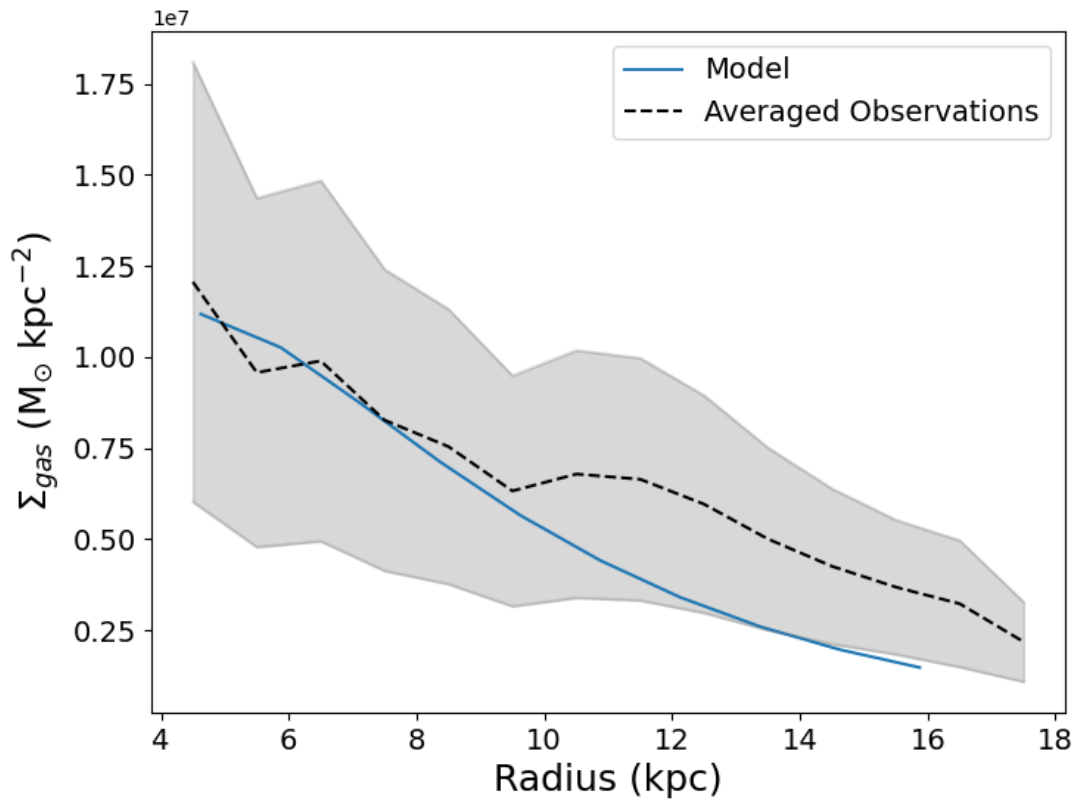


Figure B.4: An example of a rejected surface gas density gradient. The model has properties: $M_{\text{inf}} = 2.22 \times 10^{10} M_{\odot}$, $f_{\star} = 2.5 \times 10^{-4} M_{\odot} \text{yr}^{-1} \text{kpc}^{-2}$, $a = -1 \text{ Gyr}$ and $b = 2 \text{ Gyr kpc}^{-1}$.

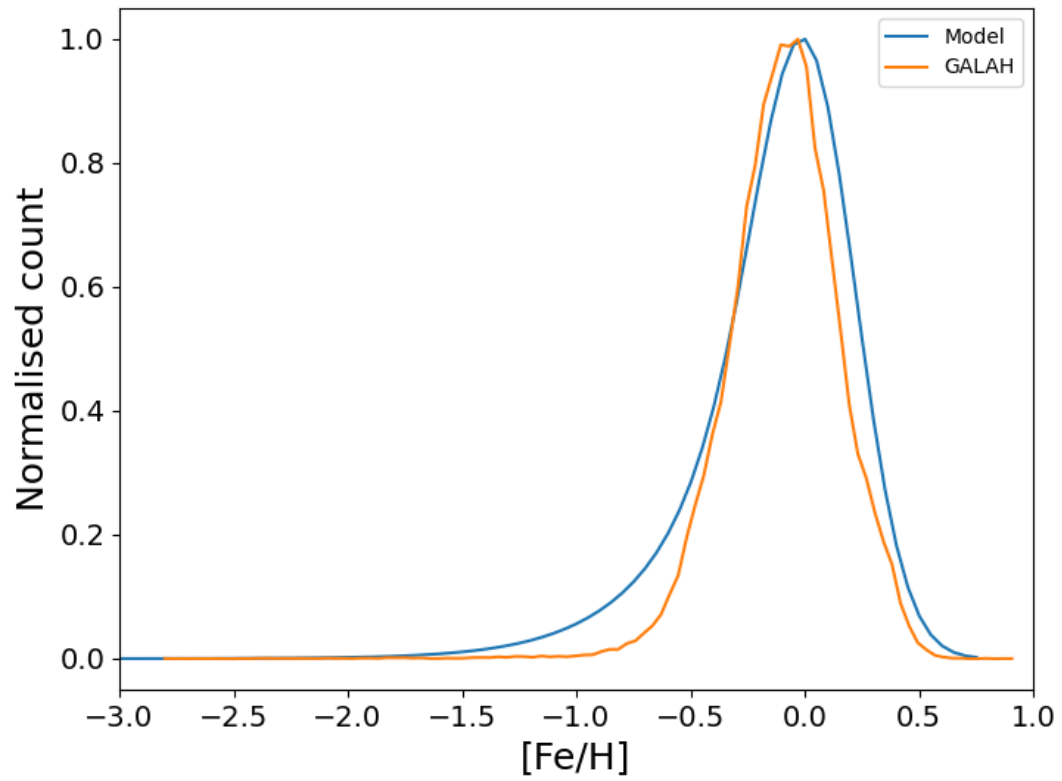


Figure B.5: An example of a metallicity distribution function that we rejected when selecting a MW-like model. The model has properties: $M_{\text{inf}} = 2.27 \times 10^{10} M_{\odot}$, $f_{\star} = 2.5 \times 10^{-4} M_{\odot} \text{ yr}^{-1} \text{ kpc}^{-2}$, $a = -1 \text{ Gyr}$ and $b = 2 \text{ Gyr kpc}^{-1}$.

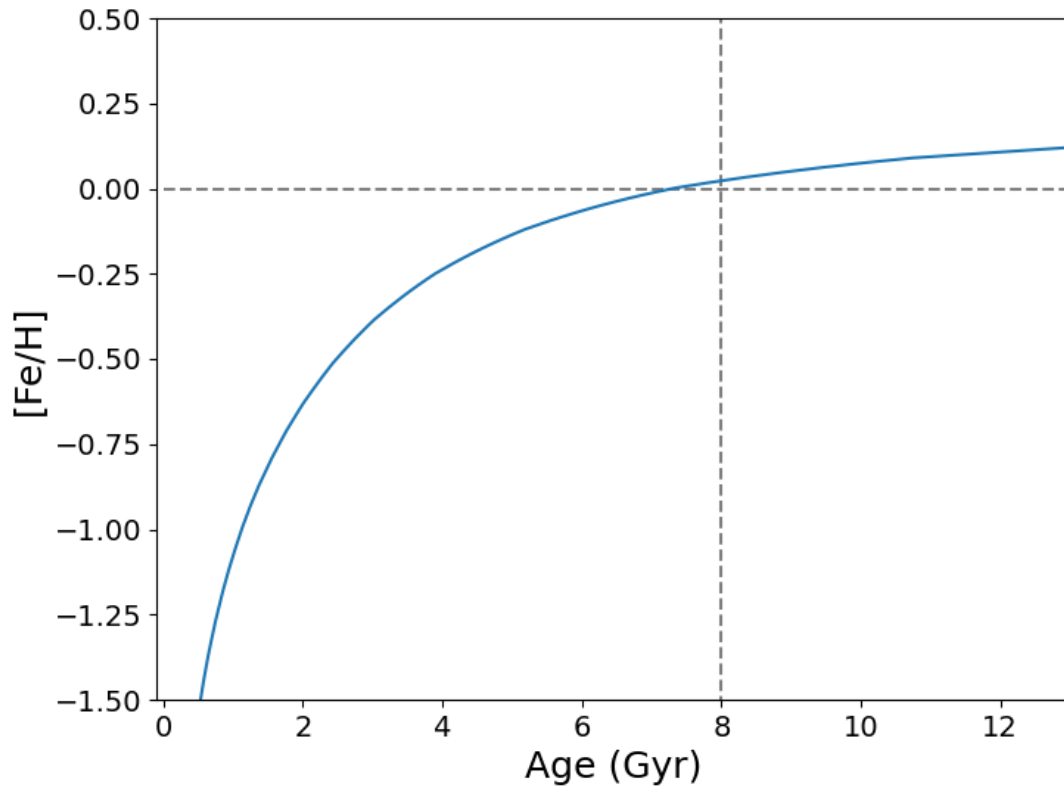
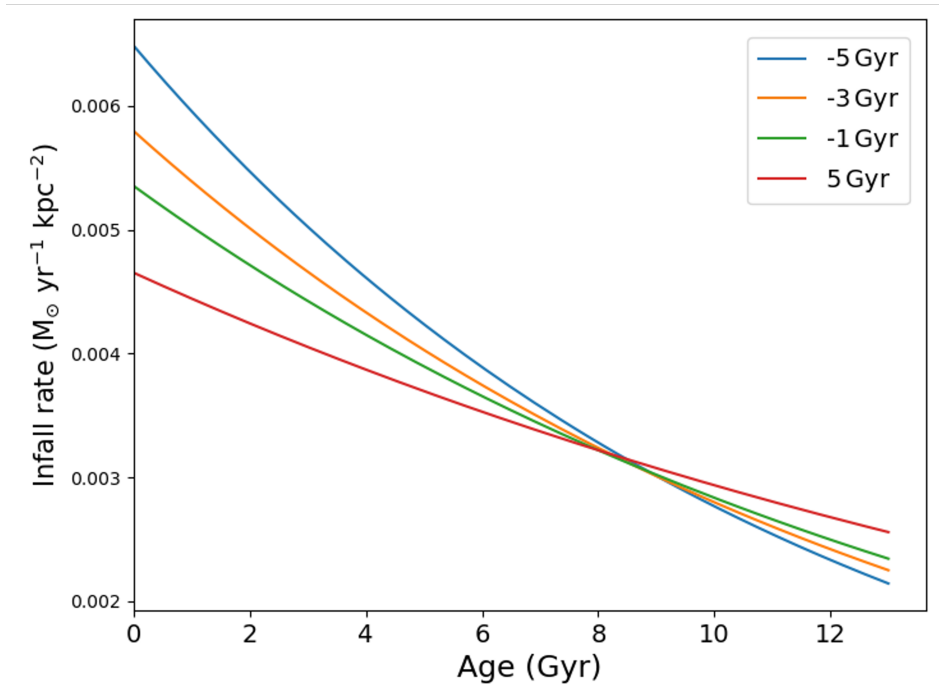
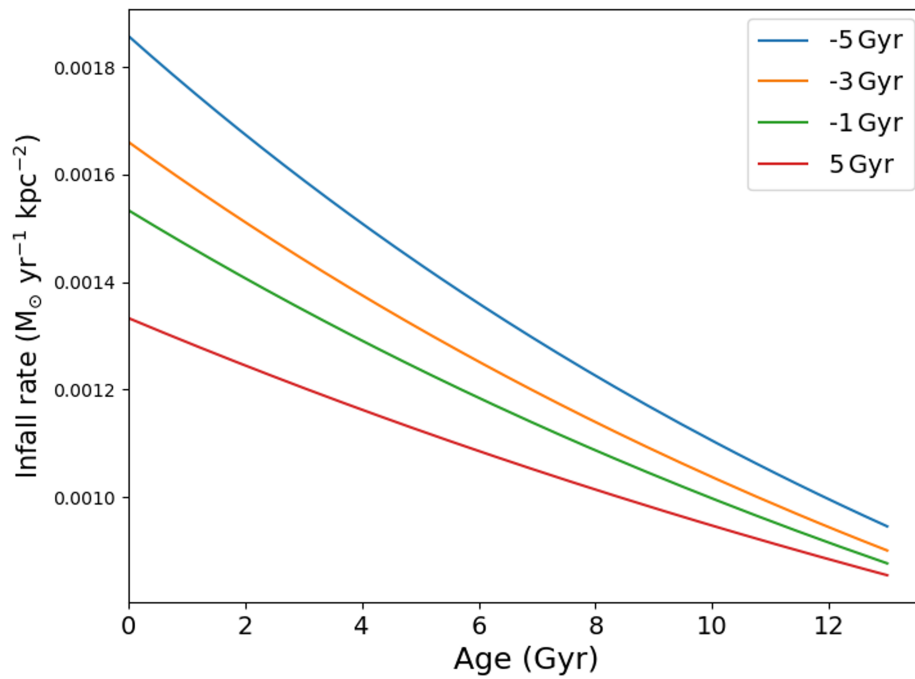


Figure B.6: An example of an unacceptable age-metallicity relation that we rejected when selecting a MW-like model. The model has properties: $M_{\text{inf}} = 2.33 \times 10^{10} M_{\odot}$, $f_{\star} = 2.5 \times 10^{-4} M_{\odot} \text{ yr}^{-1} \text{ kpc}^{-2}$, $a = -2 \text{ Gyr}$ and $b = 2 \text{ Gyr kpc}^{-1}$.

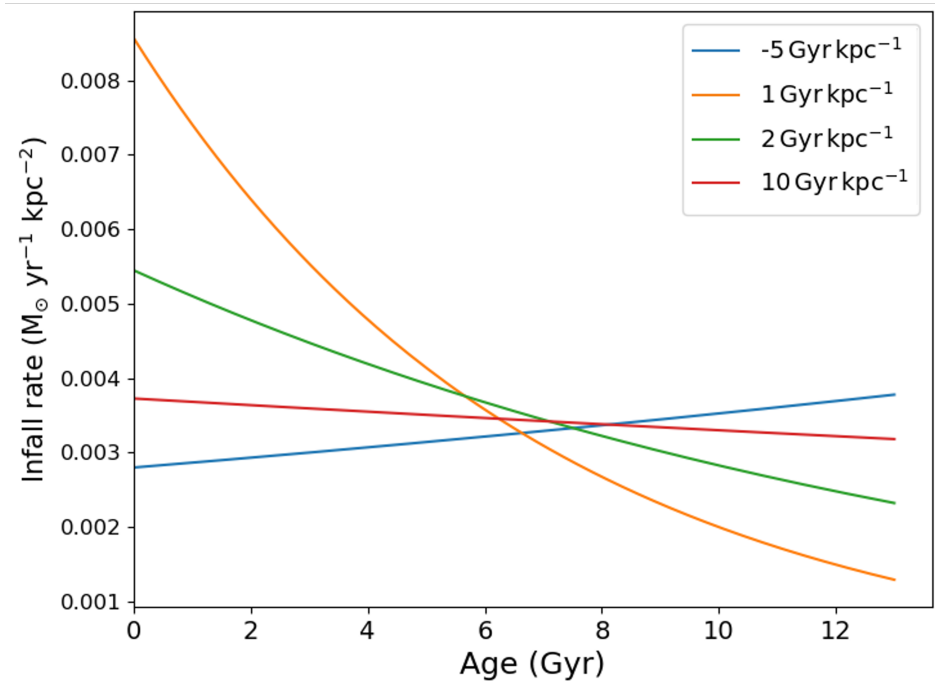


(a) Infall rate density for each model at 8 kpc

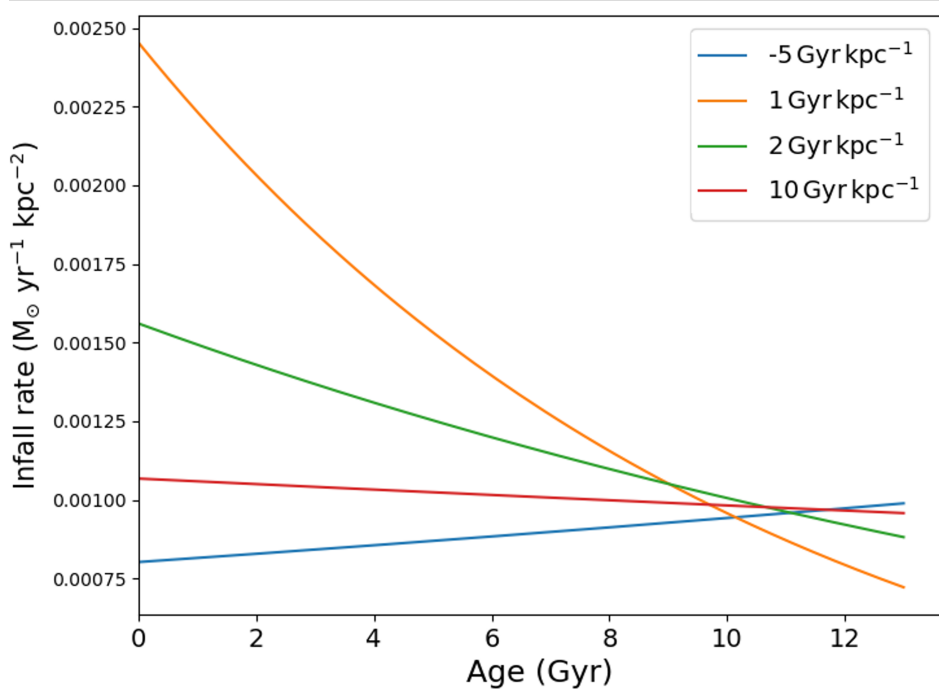


(b) Infall rate density for each model at 12 kpc

Figure B.7: Infall rate density at 8 kpc and 12 kpc for four models varying the infall parameter a .



(a) Infall rate density for each model at 8 kpc



(b) Infall rate density for each model at 12 kpc

Figure B.8: Infall rate density at 8 kpc and 12 kpc for four models varying the infall parameter b.